ISSN 2518-7198 (Print)
ISSN 2663-5089 (Online)

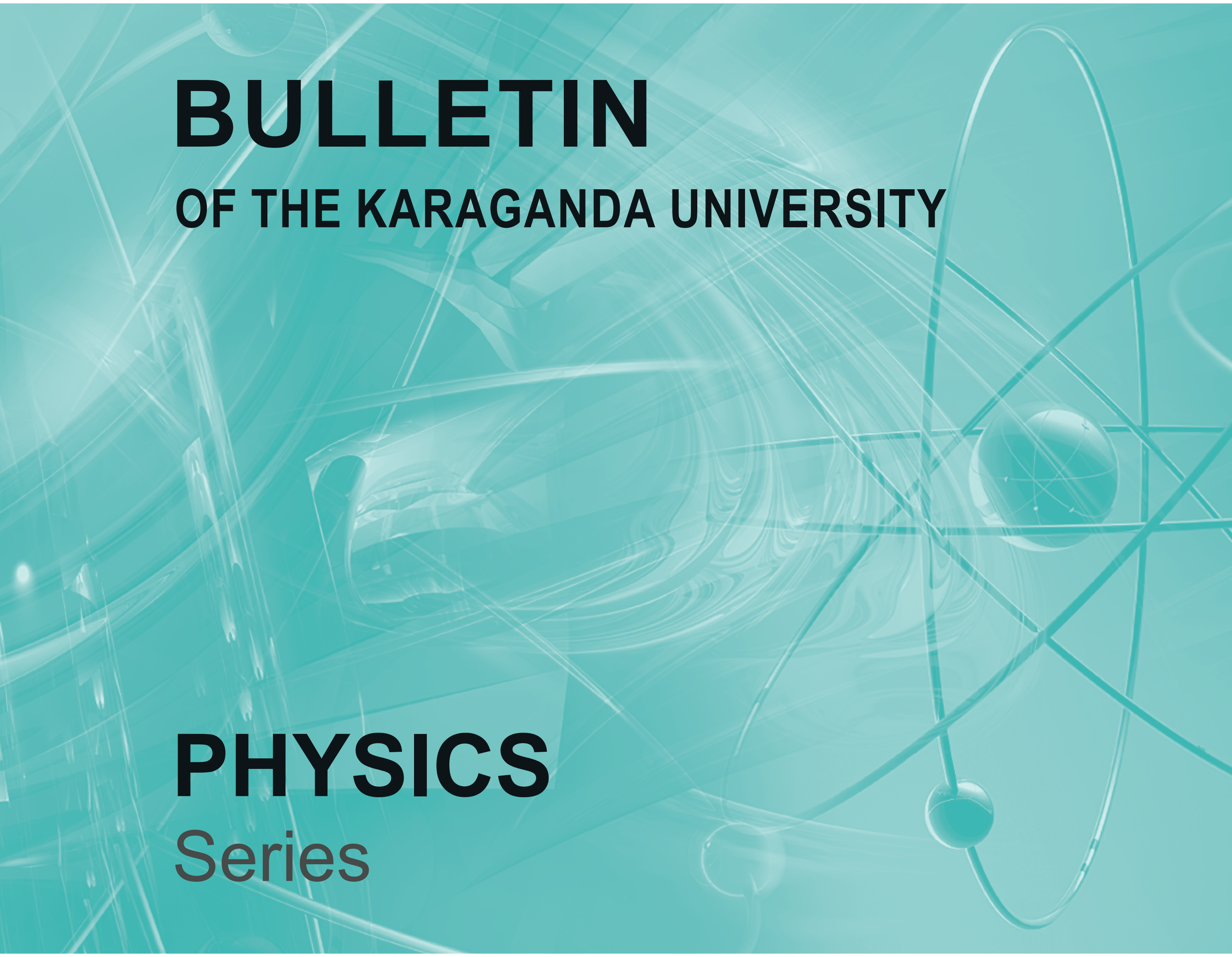

BULLETIN
OF THE KARAGANDA UNIVERSITY

PHYSICS
Series

№ 3(103)/2021

ISSN 2663-5089 (Online)
ISSN-L 2518-7198 (Print)
Индексі 74616
Индекс 74616

ҚАРАҒАНДЫ УНИВЕРСИТЕТІНІҢ ХАБАРШЫСЫ

ВЕСТНИК КАРАГАНДИНСКОГО УНИВЕРСИТЕТА

BULLETIN OF THE KARAGANDA UNIVERSITY

ФИЗИКА сериясы

Серия ФИЗИКА

PHYSICS Series

№ 3(103)/2021

Шілде–тамыз–қыркүйек
30 қыркүйек 2020 ж.

Июль–август–сентябрь
30 сентября 2020 г.

July–August–September
September, 30th, 2020

1996 жылдан бастап шығады
Издается с 1996 года
Founded in 1996

Жылына 4 рет шығады
Выходит 4 раза в год
Published 4 times a year

Қарағанды, 2021
Караганда, 2021
Karaganda, 2021

Бас редакторы

PhD д-ры
А.К. Хасенов

Жауапты хатшы

PhD д-ры
Д.Ж. Қарабекова

Редакция алқасы

Б.Р. Нүсіпбеков,	техн. ғыл. канд., Акад. Е.А. Бөкетов ат. Қарағанды университеті (Қазақстан);
Т.Ә. Көкетайтегі,	физ.-мат. ғыл. д-ры, Акад. Е.А. Бөкетов ат. Қарағанды университеті (Қазақстан);
Н.Х. Ибраев,	физ.-мат. ғыл. д-ры, Акад. Е.А. Бөкетов ат. Қарағанды университеті (Қазақстан);
А.О. Сәулебеков,	физ.-мат. ғыл. д-ры, М.В. Ломоносов атындағы ММУ-дың Қазақстан филиалы, Нұр-Сұлтан (Қазақстан);
И.В. Брейдо,	техн. ғыл. д-ры, Қарағанды техникалық университеті (Қазақстан);
И.П. Курытник,	техн. ғыл. д-ры, Освенцимдегі В. Пилецкий атындағы Мемлекеттік жоғары кәсіптік мектебі (Польша);
М. Стоев,	PhD д-ры, инженерия докторы, «Неофит-Рилски» Оңтүстік-Батыс университеті (Болгария);
З.Ж. Жаңабаев,	физ.-мат. ғыл. д-ры, Әл-Фараби атындағы Қазақ ұлттық университеті, Алматы (Қазақстан);
С.Е. Көмеков,	физ.-мат. ғыл. д-ры, Қ.И.Сәтбаев атындағы Қазақ ұлттық техникалық университеті, Алматы (Қазақстан);
В.М. Лисицын,	физ.-мат. ғыл. д-ры, Томск политехникалық университеті (Ресей);
И.Н. Огородников,	физ.-мат. ғыл. д-ры, Ресейдің Тұңғыш Президенті Б.Н. Ельцин атындағы Орал федералдық университеті, Екатеринбург (Ресей);
О.П. Пчеляков,	физ.-мат. ғыл. д-ры, РҒА Сібір бөлімшесінің А.В. Ржанов атындағы Жартылай өткізгіштер физикасы институты, Новосибирск (Ресей);
А.Т. Акылбеков,	физ.-мат. ғыл. д-ры, Л.Н.Гумилев атындағы Еуразия ұлттық университеті, Нұр-Сұлтан (Қазақстан);
А.Ж. Тұрмұхамбетов,	физ.-мат. ғыл. д-ры, Қ.И. Сәтбаев атындағы Қазақ ұлттық техникалық университеті, Алматы (Қазақстан);
К.Ш. Шүңкеев,	физ.-мат. ғыл. д-ры, Ақтөбе мемлекеттік педагогикалық институты (Қазақстан);
В.Ю. Кучерук,	техн. ғыл. д-ры, Винница ұлттық техникалық университеті (Украина);
В.А. Кульбачинский,	физ.-мат. ғыл. д-ры, М.В. Ломоносов атындағы Москва мемлекеттік университеті (Ресей);
А.Д. Погребняк,	физ.-мат. ғыл. д-ры, Сумск мемлекеттік университеті (Украина);
А.П. Суржиков,	физ.-мат. ғыл. д-ры, Томск политехникалық университеті (Ресей)

Редакцияның мекенжайы: 100024, Қазақстан, Қарағанды қ., Университет к-сі, 28
Тел.: +7 701 531 4758; факс: (7212) 35-63-98.
E-mail: vestnikku@gmail.com; karabekova71@mail.ru
Сайты: physics-vestnik.ksu.kz

Редакторлары

Ж.Т. Нурмуханова, С.С. Балкеева, Д.В. Волкова

Компьютерде беттеген

Г.Қ. Жаносова

Қарағанды университетінің хабаршысы. «Физика» сериясы.

ISSN-L 2518-7198 (Print). ISSN 2663-5089 (Online).

Меншік иесі: «Академик Е.А. Бөкетов атындағы Қарағанды университеті» КЕАҚ.

Қазақстан Республикасы Ақпарат және қоғамдық даму министрлігімен тіркелген. 30.09.2020 ж. № KZ38VPY00027378 қайта есепке қою туралы куәлігі.

Басуға 29.09.2021 ж. қол қойылды. Пішімі 60×84 1/8. Қағазы офсеттік. Көлемі 15,5 б.т. Таралымы 200 дана. Бағасы келісім бойынша. Тапсырыс № 71.

«Акад. Е.А. Бөкетов ат. Қарағанды ун-ті» КЕАҚ-тың баспасының баспаханасында басылып шықты.
100024, Қазақстан, Қарағанды қ., Университет к-сі, 28. Тел. (7212) 35-63-16. E-mail: izd_kargu@mail.ru

© Академик Е.А. Бөкетов атындағы Қарағанды университеті, 2021

Главный редактор
д-р PhD
А.К. Хасенов

Ответственный секретарь
д-р PhD
Д.Ж. Карабекова

Редакционная коллегия

Б.Р. Нусупбеков,	канд. техн. наук, Карагандинский университет им. акад. Е.А. Букетова (Казахстан);
Т.А. Кокетайтеги,	д-р физ.-мат. наук, Карагандинский университет им. акад. Е.А. Букетова (Казахстан);
Н.Х. Ибраев,	д-р физ.-мат. наук, Карагандинский университет им. акад. Е.А. Букетова (Казахстан);
А.О. Саулебеков,	д-р физ.-мат. наук, Казахстанский филиал МГУ им. М.В. Ломоносова, Нур-Султан (Казахстан);
И.В. Брейдо,	д-р техн. наук, Карагандинский технический университет (Казахстан);
И.П. Курытник,	д-р техн. наук, Государственная высшая профессиональная школа им. В. Пилецкого в Освенциме (Польша);
М. Стоев,	д-р PhD, доктор инженерии, Юго-Западный университет им. Неофита Рильского, Благоевград (Болгария);
З.Ж. Жанабаев,	д-р физ.-мат. наук, Казахский национальный университет им. аль-Фараби, Алматы (Казахстан);
С.Е. Кумеков,	д-р физ.-мат. наук, Казахский национальный технический университет им. К. Сатпаева, Алматы (Казахстан);
В.М. Лисицын,	д-р физ.-мат. наук, Томский политехнический университет (Россия);
И.Н. Огородников,	д-р физ.-мат. наук, Уральский федеральный университет им. Первого Президента России Б.Н. Ельцина, Екатеринбург (Россия);
О.П. Пчеляков,	д-р физ.-мат. наук, Институт физики полупроводников им. А.В. Ржанова Сибирского отделения РАН, Новосибирск (Россия);
А.Т. Акылбеков,	д-р физ.-мат. наук, Евразийский национальный университет им. Л.Н. Гумилева, Нур-Султан (Казахстан);
А.Ж. Турмухамбетов,	д-р физ.-мат. наук, Казахский национальный технический университет им. К. Сатпаева, Алматы (Казахстан);
К.Ш. Шункеев,	д-р физ.-мат. наук, Актюбинский государственный педагогический институт (Казахстан);
В.Ю. Кучерук,	д-р техн. наук, Винницкий национальный технический университет (Украина);
В.А. Кульбачинский,	д-р физ.-мат. наук, Московский государственный университет им. М.В. Ломоносова (Россия);
А.Д. Погребняк,	д-р физ.-мат. наук, Сумский государственный университет (Украина);
А.П. Суржиков,	д-р физ.-мат. наук, Томский политехнический университет (Россия)

Адрес редакции: 100024, Казахстан, г. Караганда, ул. Университетская, 28
Тел.: +7 701 531 4758. Факс: (7212) 35-63-98.
E-mail: vestnikku@gmail.com; karabekova71@mail.ru
Сайт: physics-vestnik.ksu.kz

Редакторы
Ж.Т. Нурмуханова, С.С. Балкеева, Д.В. Волкова

Компьютерная верстка
Г.Қ. Жанбосова

Вестник Карагандинского университета. Серия «Физика».

ISSN-L 2518-7198 (Print). ISSN 2663-5089 (Online).

Собственник: НАО «Карагандинский университет имени академика Е.А. Букетова».

Зарегистрирован Министерством информации и общественного развития Республики Казахстан. Свидетельство о постановке на переучет № KZ38VPY00027378 от 30.09.2020 г.

Подписано в печать 29.09.2021 г. Формат 60×84 1/8. Бумага офсетная. Объем 15,5 п.л. Тираж 200 экз. Цена договорная. Заказ № 71.

Отпечатано в типографии издательства НАО «Карагандинский университет им. акад. Е.А. Букетова».
100024, Казахстан, г. Караганда, ул. Университетская, 28. Тел. (7212) 35-63-16. E-mail: izd_kargu@mail.ru

© Карагандинский университет им. акад. Е.А. Букетова, 2021

Main Editor
PhD
A.K. Khassenov

Responsible secretary
PhD
D.Zh. Karabekova

Editorial board

B.R. Nussupbekov,	Cand. of techn. sciences, Karagandy University of the name of acad. E.A. Buketov (Kazakhstan);
T.A. Kuketaev,	Doctor of phys.-math. sciences, Karagandy University of the name of acad. E.A. Buketov (Kazakhstan);
N.Kh. Ibrayev,	Doctor of phys.-math. sciences, Karagandy University of the name of acad. E.A. Buketov (Kazakhstan);
A.O. Saulebekov,	Doctor of phys.-math. sciences, Kazakhstan branch of Lomonosov Moscow State University, Nur-Sultan (Kazakhstan);
I.V. Breido,	Doctor of techn. sciences, Karaganda Technical University (Kazakhstan);
I.P. Kurytnik,	Doctor of techn. sciences, The State School of Higher Education in Oświęcim (Auschwitz) (Poland);
M. Stoev,	PhD, doctor of engineering, South-West University “Neofit Rilski” (Bulgaria);
Z.Zh. Zhanabaev,	Doctor of phys.-math. sciences, Al-Farabi Kazakh National University, Almaty (Kazakhstan);
S.E. Kumekov,	Doctor of phys.-math. sciences, Kazakh National Technical University named after K. Satpayev, Almaty (Kazakhstan);
V.M. Lisitsyn,	Doctor of phys.-math. sciences, Tomsk Polytechnic University (Russia);
I.N. Ogorodnikov,	Doctor of phys.-math. sciences, Ural Federal University named after the first President of Russia B.N. Yeltsin, Yekaterinburg (Russia);
O.P. Pchelyakov,	Doctor of phys.-math. sciences, Rzhanov Institute of Semiconductor Physics of Siberian branch of Russian Academy of Sciences, Novosibirsk (Russia);
A.T. Akylbekov,	Doctor of phys.-math. sciences, L.N. Gumilyov Eurasian National University, Nur-Sultan (Kazakhstan);
A.Zh. Turmuhambetov,	Doctor of phys.-math. sciences, Satbayev Kazakh National Technical University, Almaty (Kazakhstan);
K.Sh. Shunkeyev,	Doctor of phys.-math. sciences, Aktobe State Pedagogical Institute (Kazakhstan);
V.Yu. Kucheruk,	Doctor of techn. sciences, Vinnytsia National Technical University, Vinnitsa (Ukraine);
V.A. Kulbachinskii,	Doctor of phys.-math. sciences, Lomonosov Moscow State University (Russia);
A.D. Pogrebnjak,	Doctor of phys.-math. sciences, Sumy state University (Ukraine);
A.P. Surzhikov,	Doctor of phys.-math. sciences, Tomsk Polytechnic University (Russia)

Postal address: 28, University Str., 100024, Karaganda, Kazakhstan
Tel.: +7 701 531 4758; Fax: (7212) 35-63-98.
E-mail: vestnikku@gmail.com; karabekova71@mail.ru
Web-site: physics-vestnik.ksu.kz

Editors
Zh.T. Nurmukhanova, S.S. Balkeyeva, D.V. Volkova

Computer layout
G.K. Zhanbossova

Bulletin of the Karaganda University. “Physics” series.

ISSN-L 2518-7198 (Print). ISSN 2663-5089 (Online).

Proprietary: NLC “Karagandy University of the name of academician E.A. Buketov”.

Registered by the Ministry of Information and Social Development of the Republic of Kazakhstan. Rediscount certificate No. KZ38VPY00027378 dated 30.09.2020.

Signed in print 29.09.2021. Format 60×84 1/8. Offset paper. Volume 15,5 p.sh. Circulation 200 copies. Price upon request. Order № 71.

Printed in the Publishing house of NLC “Karagandy University of the name of acad. E.A. Buketov”.
28, University Str., Karaganda, 100024, Kazakhstan. Tel. (7212) 35-63-16. E-mail: izd_kargu@mail.ru

© Karagandy University of the name of academician E.A. Buketov, 2021

МАЗМҰНЫ — СОДЕРЖАНИЕ — CONTENTS

ТЕХНИКАЛЫҚ ФИЗИКА
ТЕХНИЧЕСКАЯ ФИЗИКА
TECHNICAL PHYSICS

КОНДЕНСАЦИЯЛАНҒАН КҮЙДІҢ ФИЗИКАСЫ
ФИЗИКА КОНДЕНСИРОВАННОГО СОСТОЯНИЯ
PHYSICS OF THE CONDENSED MATTER

ТЕХНИКАЛЫҚ ФИЗИКА
ТЕХНИЧЕСКАЯ ФИЗИКА
TECHNICAL PHYSICS

DOI 10.31489/2021Ph3/6-16
UDC 620.179.18

A.A. Bespalko, D.D. Dann*, M.V. Petrov, E.K. Pomishin

National Research Tomsk Polytechnic University, Russia,
*(*E-mail: dddann@tpu.ru)*

Acoustic-electrical testing of defects in the cement-sand and cement-glass model samples

A complex method of acoustic-electrical testing of defects in dielectric samples made from cement-sand and cement-glass mixtures is discussed. The paper reports the results of studies of changes in the parameters of electromagnetic responses and their spectra under pulsed deterministic acoustic excitation of model samples with defects in the form of solid-state inclusions. The results of mathematical calculations of the time variation in the stress-strain state induced in a defective dielectric model sample by deterministic acoustic pulse are presented. The relationship is shown between the parameters of the acoustic excitation and the electromagnetic response to the impact in a magnetic field. The study revealed that the specific electrical resistance of the cement-sand and cement-glass mixtures differs significantly. Excitation of electrical double layers by acoustic pulses causes an electromagnetic signal, parameters of which depend on the parameters of the acoustic impact and acoustic and electrical properties of the material. As a result, a reduced specific electrical resistance of the mixture increases its conductivity. The numerical calculation of the propagation of the deterministic acoustic pulse showed that its parameters change when it passes through a defect with acoustic impedance different from that of the mixture used.

Keywords: non-destructive testing, dielectrics, acoustic impact, electromagnetic radiation, magnetic field, modeling.

Introduction

At present the increasing number of products is manufactured from solid dielectric materials and composites. These products are used in various conditions, including extreme ones. Insulators, structural dielectrics, concrete structures and other practically used dielectrics require regular non-destructive testing to be environmentally friendly. Early detection of defects in dielectric products is crucial to maintaining their mechanical and electric strength. The defects in solid materials and products are detected using well-proven non-destructive testing methods: ultrasonic, acoustic pulse and acoustic emission; electrical and electromagnetic; magnetic; X-ray and other methods [1–10]. This variety of non-destructive methods is not always efficient for testing of dielectric materials and structures. This is due to close values of the acoustic impedance of the media of the product and the defect during ultrasonic sounding and during acoustic emission testing of the fracture development; lack of magnetic properties in the majority of composites, including dielectric materials; high X-ray permeability in organic and some inorganic dielectrics, and dangerous effect of radiation on the operator's health. Therefore, complex destructive testing methods should be employed based on well-proven algorithms and newly developed ones. Mechanoelectric or acoustic-electrical [11–19] conversions in solid-state structures can be successfully used to develop such complex testing techniques. The acoustic-electrical test uses contact acoustic sounding of the test object and contactless recording of the electromagnetic response to this impact with further amplitude-frequency analysis of the electromagnetic signal. External acoustic deterministic pulses or acoustic pulses arising in the material during fracture development induced by mechanical load can be used as a source of vibrations [11, 12]. As a result of this action, charges or electrical double layers at the interfaces of media, inclusions or blocks, on crack sides or on other structural defects of the dielectric materials emit electromagnetic signals.

A mathematical and physical rationale for testing dielectric heterogeneous materials by electromagnetic signal parameters is reported in [20]. It is shown that mechanical vibrations induced by a normalized single impact cause a displacement current. Experimental studies [21, 22] also indicate that the passage of acoustic waves causes EMS generation, which is associated with vibrations of electrical double layers. In this case, EMS amplitude-frequency parameters depend on the characteristics of acoustic pulses and the charge state of the defects in the form of inclusions.

Thus, under an external deterministic acoustic impact, defects in the form of solid inclusions or voids can be successfully tested with regard to the parameters of electromagnetic responses to this perturbation. The paper discusses the applicability of the acoustic-electric method of non-destructive testing for defective model composite dielectric materials made from cement-sand (CSM) and cement-glass (CGM) mixtures. Solid materials with acoustic impedance different from the impedance of the used CSM and CGM composites were used as defects.

Methods of conducting experiments

For experimental studies of the acoustic-electrical conversion samples were made from a cement-sand and cement-glass mixture with a size of $(50\times50\times95)\times10^{-9}$ m^3 with artificial solid parallelepiped inclusions of different size (Fig. 1). The samples were fabricated in accordance with [22]. The moisture content of the samples did not exceed 1.5 % of the sample weight, the sand grain size was $(2.5–8.0)\times10–^{4}$ m, and the size of glass fractions varied in the range of $(1.5–2.5)\times10^{-4}$ m. For EMS measurements, the side sample surface of $(50\times95)\times10^{-6}$ m^2 was laid out into 15 sites. The width of the EMS measurement sites depended on the size of the capacitive sensor lobe of the electromagnetic receiver.

A point impact with a ball weighing 8.59×10^{-4} kg was applied to the center of the sample end face with the area of $(50\times50)\times10^{-6}$ m^2. The materials used as inclusions to simulate defects, are presented in Table 1. The materials were chosen to have their acoustic impedance and electrical resistivity greater or less than z and ρ of CSM or CGM.

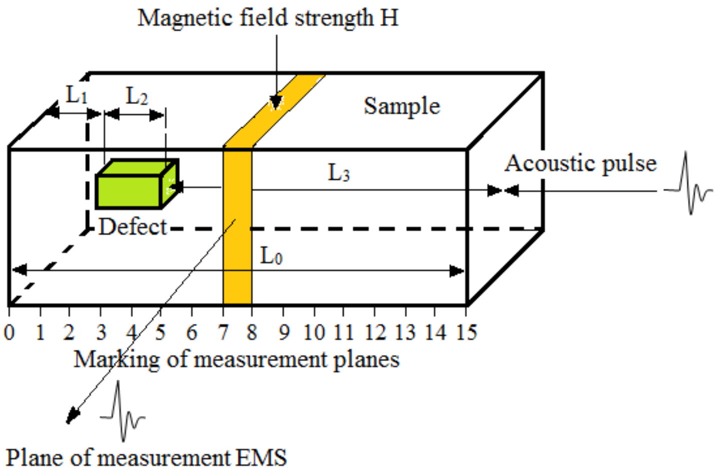

Figure 1. A model sample made from the cement-sand or cement-glass mixture with a solid rectangular inclusion with a magnetic field of strength H applied to the mixture material–defect contact

Four sizes of the rectangular defects used were $(1.0\times1.0\times1.5)\times10^{-6}$ m^3, $(1.5\times1.5\times2.0)\times10^{-6}m^3$, $(2.0\times2.0\times3.0)\times10^{-6}m^3$, and $(2.5\times2.5\times3.8)\times10^{-6}m^3$. The axes of the defects were coaxial with the sample axes. The largest faces of the defects were parallel to the larger surfaces of the model samples. The sand/glass–cement ratio was two parts to one part by weight, and the water-cement ratio was 0.7. Before pouring the solution, the inclusions were fixed in the mold in the desired position using an elastic dielectric thread. After solidification, the samples were stored at (20–22) °C for 28 days. The position of the inclusion in the sample was monitored by digital radiography using the PerkinElmer XRD 0822 detector [23]. Changes in the electrical resistance *R* of the samples were measured at frequencies of (1–100) kHz using an LCR-819 immittance meter [24].

Table 1

Acoustic and electrical parameters of the materials used

No.	Defect material	Specific gravity of the material ρ_v, kg/m^3	Longitudinal sound speed c_l, m/s	Acoustic impedance $z{\cdot}10^6$, kg/s·m^2	Specific electrical resistance ρ, Ohm·m
1	Cement-sand mixture (CSM)	1900	2765	5.25	38.4×10^{3}
2	Cement-glass mixture (CGM)	1973	3240	6.39	14.7×10^{3}
2	Plexiglas (PMMA)	1200	2700	3.24	10^{17}–10^{18}
3	Fluoroplastic (PTFE)	2200	1340	2.95	10^{15}–10^{17}
4	Ebonite	1150	2400	2.76	10^{12}–10^{14}
5	Glass, flint	2500	4560	11.4	10^{9}–10^{12}
6	Magnetite Ore (75 %)	4150	5870	24.34	10–^{3}-10^{2}
7	Duralumin, D16T	2700	6400	17.28	2.8×10^{-8}
8	Brass, L59	8500	4600	39.10	6.5×10^{-8}
9	Carbon steel	7800	5890	45.94	1.3×10^{-7}

The resistance measurement error was 0.05 %. The specific electrical resistance of the mixtures was calculated by the formula

$$\rho = \frac{RS}{L}, \qquad (1)$$

where *R* is the sample resistance, *S* is the area of the channel through which the current flows, *L* is the channel length. Graphs of ρ changes versus frequency for CSM and CGM are shown in Figure 2. Table 1 presents the value $\rho_s = 38.4\times10^{3}$ Ohm·m, which corresponds to the frequency of the highest amplitude in the EMS spectrum. At equal frequency CGM samples exhibit electrical resistivity $\rho_g = 14.7\times10^{3}$ Ohm·m.

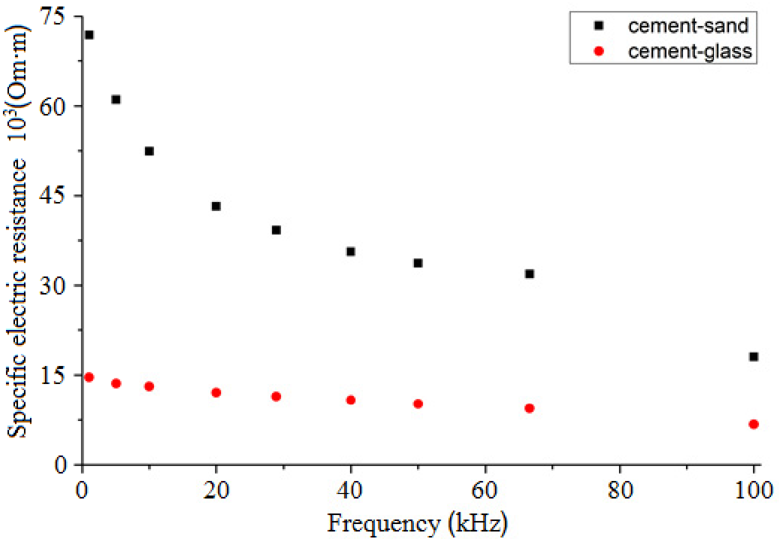

Figure 2. Changes in the specific electrical resistance of CSM and CGM samples

Figure 2 shows that the specific electrical resistance of CSM is lower than that of CGM in the entire range of the frequencies used. As shown below, this range corresponds to the frequency range of the recording capacitive differential sensor (EDS). The block diagram of the stand used for acoustic excitation and recording of the sample electromagnetic response to this impact is shown in Figure 3. It includes a dynamic acoustic pulse excitation system AP, a system for receiving and measuring the parameters of electromagnetic responses EMS. The energy of the acoustic pulse was monitored by measuring the velocity of the impact ball flight through two optical pairs that consisted of LED and a photodiode. The AP shape was monitored using a broadband piezoelectric receiver [25]. The measurement data were transmitted from the NI BNC 2120 unit

[26] or from the Tektronix 2024B oscilloscope to the computer for further amplitude-frequency analysis using the developed and standard programs.

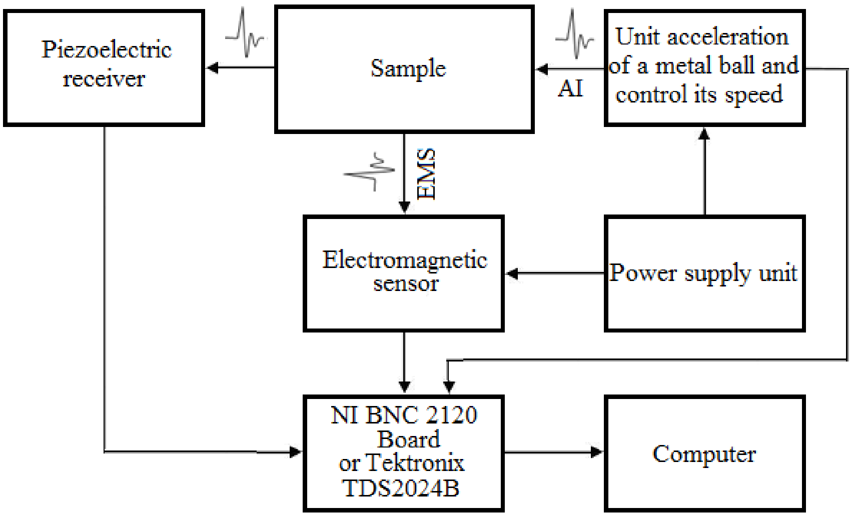

Figure 3. Block diagram of the stand for acoustic excitation
of electromagnetic signals in the test model samples

In the dynamic acoustic pulse excitation system, a spring device was used to accelerate the ball. The ball hit a hardened steel plate 2.5×10^{-3} m thick with an acoustic impedance z and hardness close to z_b of the ball, which was in acoustic contact with the sample. The velocities of the flight and rebound of the ball were determined using two optical pairs that included a light emitting diode LED and a photodiode PD installed at a distance of 5×10^{-2} m from each other. The impact excited an acoustic signal of certain amplitude and time parameters in the plate. From the plate, the acoustic pulse passed through a layer of mineral oil into the test sample. Mineral oil was also used to provide the acoustic contact of the sample with a piezoelectric receiver of the acoustic signals transmitted through the sample. The primary acoustic pulse excited by the ball was close to a bell-shaped one, and its base duration was 50×10^{-6} seconds. Analog signals from the measuring system of the ball flight were fed to the measuring eight-channel NI BNC-2120 module. After that, the EMS was transmitted to the computer. The battery pack provided 6V voltage across the LED and PD of the measuring system. The ball velocity at the moment of impact V_i^2 and that of the rebound from the target V_b^2 were calculated with regard to the time of the ball flight and the distance between the optoelectronic pairs. The obtained values of the velocity and the ball mass (m), as well as the approximation of elastic collision of the ball with the grounded metal plate were used to calculate the acoustic impact energy transmitted to the sample as

$$E_{exc} = \frac{m}{2}\left(V_i^2 - V_b^2\right), \tag{2}$$

where E_{exc} is the energy induced in the sample upon ball impact. The energy losses of the acoustic pulse in the plate were not considered. The spring compression was changed to induce the acoustic impact energy in the test sample within (8–30)×10^{-3} J. The longitudinal speed of sound was measured with a piezoelectric emitter using the same stand (Fig. 3).

EDS operating in the range from 1 to 100 kHz was used as a receiver of electromagnetic signals. At the output of the capacitive sensor, the signal could be amplified 10 or 100 fold. The EDS input sensitivity was 5×10^{-4} V. The size of the receiving plates of the sensor was (0.5×3.0)×10^{-4} m^2. During the experiments, the distance from the surface of the test samples to the nearest plate of the electromagnetic sensor was set within (1–2)×10^{-3} m. The electromagnetic sensor for measuring electromagnetic signals along the entire sample length was enabled to move along its central axis sequentially over the measurement sites from 0–1 to 14–15 and backwards. The initially set distance between the receiving plate of the electromagnetic sensor and the sample surface was maintained stable during EMS measurements using the optical stage dials and the control plate of a given thickness. A special program was used to normalize EMS to the perturbation created by the ball impact, and the fast Fourier transform (FFT) program was used to perform its spectral analysis.

Theoretical and experimental research

Numerical and experimental modeling was carried out for testing CSM and CGM model samples, including those with rectangular defects. Initially, numerical modeling was performed using the concept of continuum mechanics for elastic wave propagation in a dielectric sample under excitation by deterministic acoustic pulses. The computational algorithm for determining the parameters of the stress-strain state (SSS) of the model sample is based on the relations of the mechanics of the deformed body. In the general case, a system of equations was used, describing the behavior of a deformable solid in space and includes well-known equations, continuities, and relations between the components of the total strain rate tensor. In addition, the calculations employed the constitutive relations that specify the relationship between the components of the stress and strain tensors:

$$\sigma_{ij} = f(\varepsilon_{ij}), \tag{3}$$

$$\varepsilon_{ij} = \frac{\Delta x_{ij}}{x_{ij}}, \tag{4}$$

where x_{ij} is spatial coordinates; σ_{ij} is stress tensor components; ε_{ij} is total strain tensor components.

The numerical implementation was carried out according to a noncentral difference scheme of the second order of accuracy with respect to the space and time steps [27]. The accuracy of the numerical results was assessed by the internal convergence of the results when changing the parameters of the finite-difference grid and time integration steps [28]. The boundary conditions were set in accordance with the laboratory experiments. In calculations, the excitation corresponded to the experiment acoustic pulse in shape, amplitude, and duration. The calculations were performed for the sample $(5.0\times5.0\times9.5)\times10^{-6}$ m^3 in size with real elastic properties. For calculations, the following values of CGM properties were set: density of $(1.9–2.3)\times10^3$ kg/m^3; modulus of elasticity of 4×10^{10} N/m^2; Poisson's ratio of 0.2; longitudinal wave velocity of 3.2×10^3 m/s. The calculation was performed for the impact onto the center of the sample end face. An elastic calculation model was used. The numerical simulation results were visualized using a special graphics package.

Figure 4 presents the results of modeling the perturbation propagation over the simulated region. The results were visualized as isosurfaces. At time 5×10^{-6} s (Fig. 4a), perturbation propagates over the homogeneous region in the form of a hemisphere, which corresponds to the general concepts of the mechanics of acoustic wave propagation. For clarity, the interaction between the wave front and a carbon steel insert with sizes of $(2.5\times2.5\times3.8)\times10^{-6}$ m^3 was considered. Figure 4b shows how the leading edge of the wave meets a harder insert and bends it at lateral sides. At the next propagation stage, the wave front moves faster along a more elastic insert, Figure 4c.

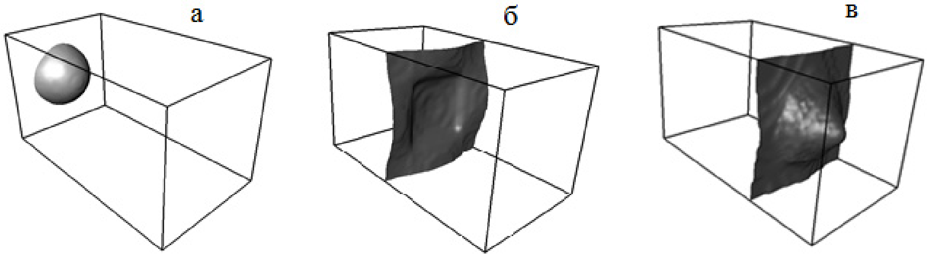

Figure 4. Propagation of elastic perturbation in the model in time:
a) 5×10^{-6} s; b) 10×10^{-6} s; c) 12×10^{-6} s.

Thus, the inserts with elastic properties different from those of the base material change the of the wave process pattern. Changes in the elasticity modulus and material density produce the greatest effect. For example, the ratio of the elasticity moduli of carbon steel and the base material differs more than 10 fold. The smaller the difference in elasticity moduli, the less sensitive the wave process to inhomogeneities. The sums of rates were calculated for carbon steel, fluoroplastic, magnetite ore, and glass (flint) defects of various sizes. Figure 5 presents the example of the calculated changes in the integral characteristics of the sums of displacement rates in layers of CSM (Fig. 5, a, b, c) and CGM (Fig. 5, d, e, f) that are close to 75 % magnetite ore defects of sizes: $(1.0\times1.0\times1.5)\times10^{-6}$ m^3, $(2.0\times2.0\times3.0)\times10^{-6}$ m^3, $(2.5\times2.5\times3.8)\times10^{-6}$ m^3. The figure shows that the displacement rates change significantly in layers close to defects of different sizes. As reported in [10–22], the parameters of acoustic excitation and electromagnetic response to this type of impact are uniquely related, therefore, the parameters of the recorded EMS will be close to the changes in the sums of rates shown in Figure 5.

The calculations in Figure 5 show that an increase in the defect size shifts the spectrum towards the high-frequency region.

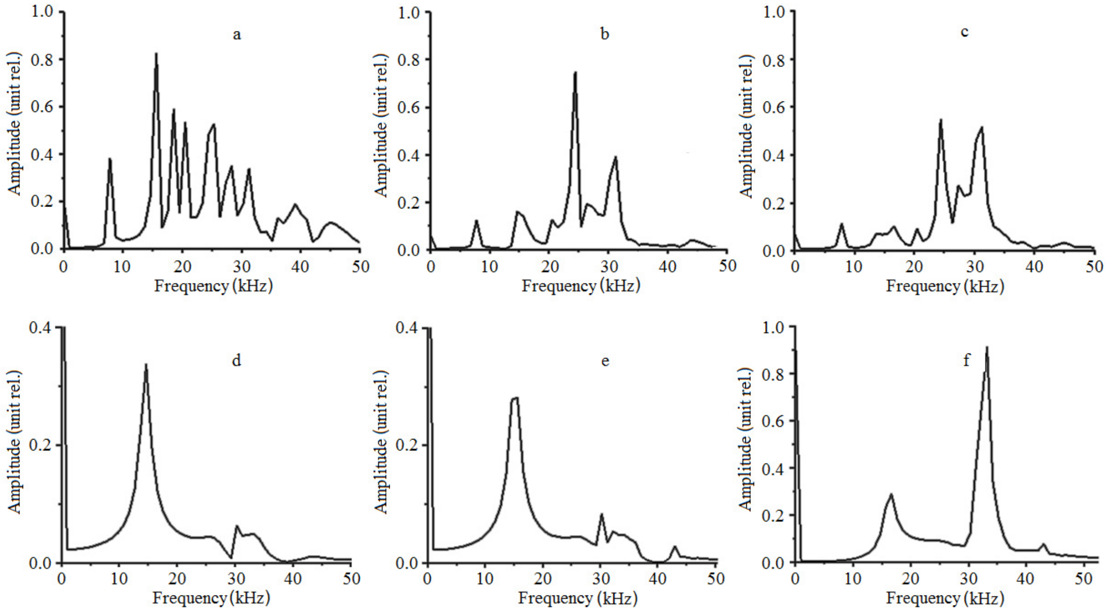

Figure 5. Calculated integral characteristics of the sums of displacement rates in layers close to 75 % magnetite ore defects of different sizes: a, d) $(1.0\times1.0\times1.5)\times10^{-6}$ m^3; b, e) $(2.0\times2.0\times3.0)\times10^{-6}$ m^3; c, f) $(2.5\times2.5\times3.8)\times10^{-6}$ m^3; a, b, c for CSM; d, e, f for CGM

Further experimental studies were performed for electromagnetic signals and their spectra excited by deterministic acoustic pulses in CSM and CGM samples with steel, carbon steel, fluoroplastic, magnetite ore, and glass (flint) defects. In the experiments an acoustic pulse was applied to the center of the sample end face, and the receiving electric sensor was located near the lateral surface at a distance of at least 10^{-2}m from the impact point at a height of 2×10^{-3} m. A magnetic field was applied to samples with magnetizable defects, which corresponded to strength $H = 1.45\times10^5$ A/m on the sample surface (Fig. 1). The magnetic field was applied to samples made from different model mixtures (CSM and CGM) to reveal its effect on the amplitude of EMS from magnetizable defects. Previous experiments on the 75 % magnetite ore samples [29] showed that under acoustic excitation the applied magnetic field significantly affects the electromagnetic responses.

Initially, the studies were conducted for CSM and CGM samples with a ferrite magnet defect $(1.0\times1.0\times1.5)\times10^{-6}$ m^3 in size without magnetic field and with magnetic field of 1.45×10^5 A/m applied to the sample surface. Figure 6 shows electromagnetic signals and their spectra under deterministic acoustic excitation of the CSM sample with a ferrite magnet defect with sizes of $(1.0\times1.0\times1.5)\times10^{-6}$ m^3 without magnetic field (Fig. 6 a, c) and with magnetic field of 1.45×10^5 A/m applied to the sample surface (Fig. 6 c, d). The figure shows that when magnetic field is applied, the EMS amplitude and spectral components increase by more than 20 %. That increase was observed in all EMS measurements during excitation with acoustic pulses with similar acoustic pulse amplitudes. In addition, the figure shows a good correlation between the EMS spectra in both cases.

Figure 7 shows changes in the EMS amplitude and spectra for CGM samples, which have a lower specific electrical resistance (Fig. 2) with the defect similar to that in CSM samples. In Figure 7 the EMS amplitude and spectra of CGM samples are significantly lower than the amplitude and spectra of CSM samples. Moreover, magnetization decreases the amplitudes and spectral components of the signal.

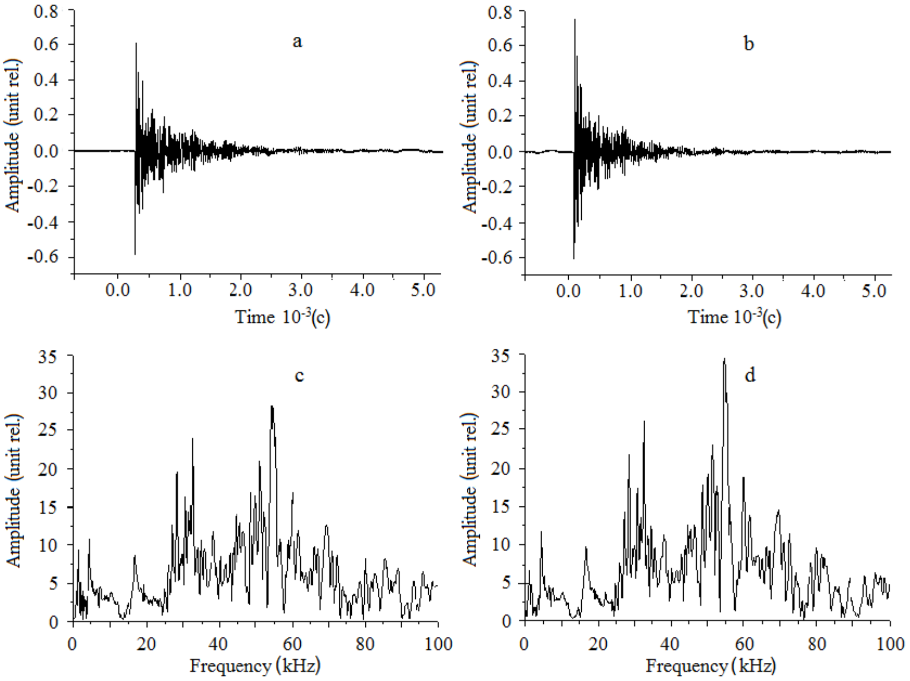

Figure 6. Electromagnetic signals and their spectra upon deterministic acoustic excitation of CSM sample with a ferrite magnet defect with sizes of $(1.0\times1.0\times1.5)\times10^{-6}$ m^3 without magnetic field (a, c) and with magnetic field of 1.45×10^5 A/m applied to the sample surface (b, d)

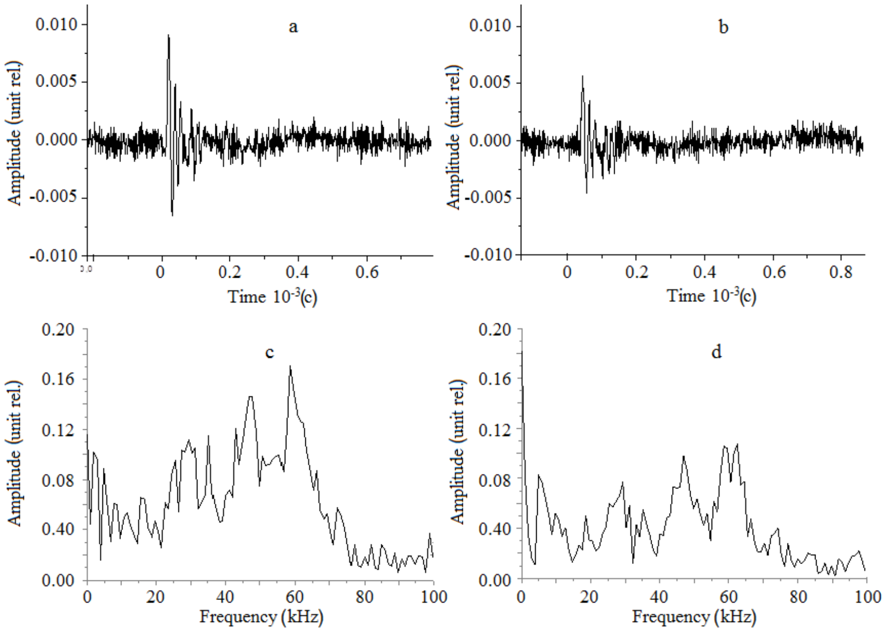

Figure 7. Electromagnetic signals and their spectra upon deterministic acoustic excitation of the CGM sample with a ferrite magnet defect $(1.0\times1.0\times1.5)\times10^{-6}$ m^3 in size without magnetic field (a, c) and with magnetic field of 1.45×10^5 A/m applied to the sample surface (b, d)

Addition of a 75 % magnetite ore defect in the CSM sample showed that the EMS amplitude and spectra in these samples without magnetic field and with magnetic field applied tend to decrease (Fig. 8) similar to previous experiments.

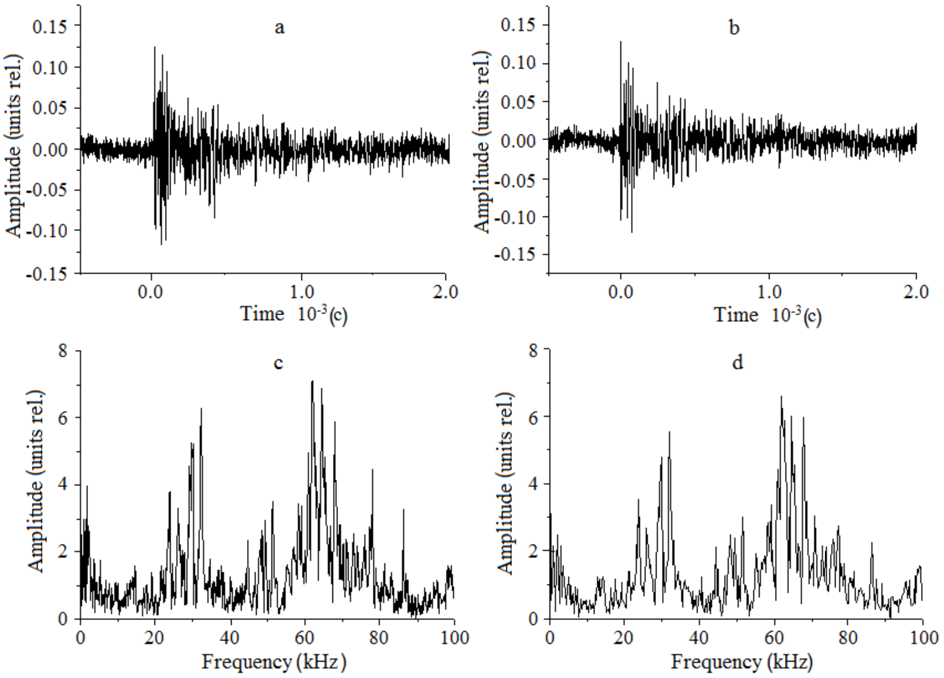

Figure 8. Electromagnetic signals and their spectra upon deterministic acoustic excitation of the CSM sample with magnetite defect with s of $(1.0\times1.0\times1.5)\times10^{-6}$ m^3 without magnetic field (a, c) and with magnetic field of 1.45×10^5 A/m (b, d) applied to the sample surface

Discussion and conclusions

The study revealed that the specific electrical resistance of the cement-sand ρ_{csm} and cement-glass ρ_{cgm} mixtures differs significantly (Fig. 2). In addition, the acoustic impedance z of mixtures and defects in the mixture differs (Table 1). This has a significant effect on the parameters and propagation of deterministic acoustic pulses in defective samples and on the parameters of the electromagnetic responses excited at the contact between the sample and the defect materials during acoustic-electrical conversions [19]. Excitation of electrical double layers (EDL) by acoustic pulses causes an electromagnetic signal, parameters of which depend on the parameters of the acoustic impact and acoustic and electrical properties of the material [10–19]. As a result, a reduced ρ of the mixture increases its conductivity. In turn, increased conductivity facilitates the drainage of the EDL charge generated at the contact between the materials of the mixture and the defect. Then, the EMS amplitude decreases proportionally under the acoustic impact on the electrical double layer. In this case, the applied magnetic field leads to the polarization of magnetic dipoles and, therefore, to the drainage of a weakly fixed EDL charge under the action of Lorentz forces. The results of weakening of the EMS signal amplitudes and its frequency components were significant for CGM samples with a ferrite magnet defect (Fig. 7) and insignificant for CSM samples with a 75 % magnetite ore defect (Fig. 8). At the same time, the amplitude of EMS and its spectral components in CSM samples with a ferrite magnet increased significantly. This can be attributed to better dielectric properties of CSM as compared to CGM (Table 1) and, as a result, an increased EDL charge.

Thus, the numerical calculation of the propagation of the deterministic acoustic pulse showed that its parameters change when it passes through a defect with acoustic impedance different from that of the mixture used. The obtained integral characteristics of the sums of the displacement rates in layers close to carbon steel defects with sizes of $(1.0\times1.0\times1.5)\times10^{-6}$ m^3, $(2.0\times2.0\times3.0)\times10^{-6}$ m^3, and $(2.5\times2.5\times3.8)\times10^{-6}$ m^3 differ significantly.

Experimental studies of EMS and its spectral components in CSM and CGM samples showed that samples with high electrical resistivity show more stable amplitude-frequency characteristics of electromagnetic signals under similar deterministic acoustic excitation. An increase or retention of EMS characteristics can also be observed when a magnetic field is applied to defective CSM samples.

Acknowledgements

This study was supported by the Russian Science Foundation, project No. 20–79–10156.

References

1 Mason W.P. Physical Acoustics. — V. 1 / W.P. Mason. — New York: Academic Press, 1964. — 532 p.

2 Клюев В.В. Неразрушающий контроль. / В.В. Клюев. — Т. 3 — М.: Машиностроение, 2008. — 864 с.

3 Blitz J. Electrical and Magnetic Methods of Non-destructive Testing / J. Blitz. — Springer Netherlands, 1997. — 261 p.

4 Ida N. Numerical Modeling for Electromagnetic Non-Destructive Evaluation / N. Ida. — Springer US, 1995. — 511 p.

5 Михеев М.Н. Магнитные методы структурного анализа и неразрушающего контроля / М.Н. Михеев, Э.С. Горкунов. — М.: Наука, 1993. — 266 с.

6 Ficilli F. Non-Destructive Testing by Magnetic Techniques / F. Ficilli. — LAP Academic Publishing, 2012. — 140 p.

7 Yurov V.M. X-ray computed tomography-based analysis of impact damage propagation in composite materials / V.M. Yurov, V.I. Goncharenko, S.L. Vasiliev, S.A. Dmitriev, S.A. Yurgenson // Eurasian Phys. Tech. J. — 2019. — V. 16(2). — P. 31–35.

8 Surzhikov A.P. Influence of solid-phase ferritization method on phase composition of lithium-zinc ferrites with various concentration of zinc / A.P. Surzhikov, A.M. Pritulov, E.N. Lysenko, A.N. Sokolovskii, V.A. Vlasov, E.A. Vasendina // Journal of Thermal Analysis and Calorimetry. — 2012. — V. 109. — No. 1. — P. 63–67.

9 Carnì D.L. Damage analysis of concrete structures by means of acoustic emissions technique / D.L. Carnì, C. Scuro, F. Lamonaca, R.S. Olivito, D. Grimaldi // Compos. Part B: Engineering. — 2017. — V. 115. — 79–86.

10 Yamada I. Electromagnetic and acoustic emission associated with rock fracture / I. Yamada, K. Masuda, H. Mizutani // Phys. Earth Planet. Int. — 1989. — V. 57(1–2). — P. 157–168.

11 Nazarov K.M. Study of water infiltration into cement-based mortars using real-time thermal neutron radiography / K.M. Nazarov, S.E. Kichanov, A. El Abd, M. Taman, D.P. Kozlenko // Eurasian Phys. Tech. J. — 2020. — V. 17(1). — P. 39–45.

12 O'Keefe S.G. A mechanism for the production of electromagnetic radiation during fracture of brittle materials / S.G. O'Keefe, D.V. Thiel // Phys. Earth Planet. Int. — 1995. — V. 89(11). — P. 127–135.

13 Dann D.D. Changes in the Parameters of the Electromagnetic Response of Model Dielectric Samples with Air Cavity Defects under External Deterministic Acoustic Impact / D.D. Dann, M.V. Petrov, P.I. Fedotov, E.A. Sheveleva // Bulletin of the University of Karaganda-Physics. — 2021. — V.101(1). — P. 12–17.

14 Lacidogna G. Acoustic and electromagnetic emissions as precursor phenomena in failure processes / G. Lacidogna, A. Carpinteri, A. Manuello, G. Durin, A. Schiavi, G. Niccolini, A. Agosto // Strain. — 2010. — V. 47. — P. 144–152.

15 Fursa T.V. Theoretical investigations of the influence of defects under pulsed mechanical excitation of concrete / T.V. Fursa, B.A. Lyukshin, G.E. Utsyn // Russian Physics Journal. — 2015. — V. 57(12). — P. 1658–1661.

16 Kyriazopoulos A. Non-destructive evaluation of cement-based materials from pressure-stimulated electrical emission. Preliminary results. / A. Kyriazopoulos, C. Anastasiadis, D. Triantis, C.J. Brown // Construction and Building Materials. — 2011. — V. 29(4). — P. 1980–1990.

17 Koktavy P. Experimental study of electromagnetic emission signals generated by crack generation in composite materials / P. Koktavy // Measurement Science and Technology. — V. 20(1). — 015704.

18 Stergiopoulos C. Electrical and Acoustic Emissions in cement mortar beams subjected to mechanical loading up to fracture / C. Stergiopoulos, I. Stavrakas, G. Hloupis, D. Triantis, F. Vallianato // Engineering Failure Analysis. — V. 35. — 454–461.

19 Bespal'ko A.A. Transformation of acoustic pulses into electromagnetic response in stratified and damaged structures / A.A. Bespal'ko, Y.N. Isaev, L.V. Yavorovich // J. Min. Sci. — 52(2). — P. 279–285.

20 Bespal'ko A.A. Modelling of Infrared Glow in Rock Holes / A.A. Bespal'ko, V.A. Shtirts, P.I. Fedotov, A.O. Chulkov, L.V. Yavorovich // J. Nondestr. Eval. — 2019. — V. 38. — P. 30–29.

21 Fursa T.V. Experimental and theoretical investigation of the characteristics of an electric response to an elastic impact excitation of piezo-containing heterogeneous materials / T.V. Fursa, B.A. Lyukshin, G.E. Utsyn // Russian Journal of Nondestructive Testing. — V.47(10). — P. 675–679.

22 Bespal'ko A.A. Modelling Acoustic–Electric Nondestructive Testing for Defects in Dielectric Materials / A.A. Bespal'ko, A.P. Surzhikov, D.D. Dann, G.E. Utsyn, M.V. Petrov, E.K. Pomishin // Rus. J. Nondestr. Test. — 2021. — V. 57(2). — P. 85–95.

23 X-ray flat panel detector PerkinElmer XRD 0822 [Electronic resource]. — Access mode: www.perkinelmer.com.

24 Immittance's meter LCR-819 [Electronic resource]. — Access mode: www.electronpribor.ru/catalog/53/lcr-819.htm#specification

25 Королев В.М. Апериодический пьезодатчик для ультразвуковых дефектоскопов / В.М. Королев // Дефектоскопия. — 1973. — № 4. — С. 12–18.

26 Installation guide BNC-2120 [Electronic resource]. — Access mode: https://www.ni.com/pdf/manuals/372123d.pdf

27 Warming R.F. Non-central difference schemes of the II and III order of accuracy for solving nonlinear hyperbolic equations / R.F. Warming, P. Kutler, G. Lomax // Rocket Technol. Cosmonautics. — 1973. — V. 11(2). — P. 76–85.

28 Barashkov V.N. Predicting the destruction of industrial installations / V.N. Barashkov, A.V. Gerasimov, B.A. Lyukshin // Russian Physics Journal. — 1998. — No. 10. — P. 657–661.

29 Bespal'ko A.A. Investigation and control of magnetization of magnetite ore samples by electromagnetic signal parameters / A.A. Bespal'ko, P.I. Fedotov, L.V. Yavorovich // Test. Diagn. — 2013. — No. 13. — P. 221–224.

А.А. Беспалько, Д.Д. Данн, М.В. Петров, Е.К. Помишин

Цемент-құм және цемент-шыны модельдік үлгілерінің ақауын акустикалық-электрлік тестілеу

Цемент-құм және цемент-шыны қоспаларының диэлектрлік үлгілерінің ақауларын акустикалық-электрлік тестілеудің кешенді әдісі талқыланған. Мақалада қатты күйдегі қосылыстар түріндегі ақаулары бар модельдік үлгілердің импульсті детерминирленген акустикалық қозуы кезінде электромагниттік дабылдардың параметрлері мен олардың спектрлерінің өзгеруін зерттеу нәтижелері қарастырылды. Детерминирленген акустикалық импульспен қозған кезде ақаулы диэлектрлік модельдік үлгінің кернеулі-деформацияланған күйінің уақыттық өзгеруінің математикалық есептеулерінің нәтижелері келтірілген. Сынақ объектісінің акустикалық қозу параметрлері мен магнит өрісіндегі осындай әсерге электромагниттік дабыл арасындағы байланыс көрсетілген. Зерттеу барысында цемент-құм және цемент-шыны қоспаларының электрлік кедергісі айтарлықтай ерекшеленетіні анықталды. Қос электр қабаттарының акустикалық импульстарының қозуы электромагниттік дабылдың шығарылуына әкеледі, оның параметрлері акустикалық әсер ету параметрлерімен, сондай-ақ материалдың акустикалық және электрлік қасиеттерімен анықталады. Нәтижесінде, егер қоспаның меншікті кедергісі азайтылса, онда оның өткізгіштігі артады, детерминирленген акустикалық импульстің таралуын сандық есептеу пайдаланылған үлгінің қоспасының кедергісінен өзгеше акустикалық кедергісі бар ақаудан өткен кезде оның параметрлерінің өзгеруін көрсетті.

Кілт сөздер: беріктік бақылау, диэлектриктер, акустикалық әсер, электромагниттік эмиссия, магнит өрісі, модельдеу.

А.А. Беспалько, Д.Д. Данн, М.В. Петров, Е.К. Помишин

Акустико-электрическое тестирование дефектности цементно-песчаных и цементно-стекольных модельных образцов

Обсужден комплексный метод акустико-электрического тестирования дефектности диэлектрических образцов из цементно-песчаной и цементно-стекольной смесей. Рассмотрены результаты исследований изменения параметров электромагнитных откликов и их спектров при импульсном детерминированном акустическом возбуждении модельных образцов с дефектами в виде твердотельных включений. Представлены результаты математических расчетов изменения во времени напряженно-деформированного состояния дефектного диэлектрического модельного образца при его возбуждении детерминированным акустическим импульсом. Показана связь параметров акустического возбуждения объекта тестирования и электромагнитного отклика на такое воздействие в магнитном поле. В процессе исследований установлено, что удельные электрическое сопротивление цементно-песчаной и цементно-стекольной смесей существенно отличается. Возбуждение акустическими импульсами двойных электрических слоев приводит к излучению электромагнитного сигнала, параметры которого определяются параметрами акустического воздействия, а также акустическими и электрическими свойствами материала. В результате, если уменьшить удельное сопротивление смеси, то увеличится ее проводимость. Численный расчет распространения детерминированного акустического импульса показал изменение его параметров при прохождении через дефект с отличающимся акустическим импедансом от импеданса используемой смеси образца.

Ключевые слова: неразрушающий контроль, диэлектрики, акустическое воздействие, электромагнитная эмиссия, магнитное поле, моделирование.

References

1 Mason, W.P. (1964). *Physical Acoustics. V. 1.* New York: Academic Press.

2 Klyuev, V.V. (2008). *Nerazrushaushchii kontrol [Non-Destructive Testing].* Moscow: Mashinostroenie [in Russian].

3 Blitz, J. (1997). *Electrical and Magnetic Methods of Non-destructive Testing.* Springer Netherlands.

4 Ida, N. (1995). *Numerical Modeling for Electromagnetic Non-Destructive Evaluation.* Springer US.

5 Mikheev, M.N. & Gorkunov, E.S. (1993). *Magnitnye metody strukturnogo analiza i nerazrushaiushchego kontrolia [Magnetic methods of structural analysis and non-destructive testing].* Moscow: Nauka [in Russian].

6 Ficilli, F. (2012). *Non-Destructive Testing by Magnetic Techniques.* LAP Lambert Academic Publishing.

7 Yurov, V.M., Goncharenko, V.I., Vasiliev, S.L., Dmitriev, S.A., & Yurgenson, S.A. (2019). X-ray computed tomography-based analysis of impact damage propagation in composite materials. *Eurasian Phys. Tech. J.*, 16(2), 31–35.

8 Surzhikov, A.P., Pritulov, A.M., Lysenko, E.N., Sokolovskii, A.N., Vlasov, V.A., & Vasendina, E.A. (2012) Influence of solid-phase ferritization method on phase composition of lithium-zinc ferrites with various concentration of zinc. *Journal of Thermal Analysis and Calorimetry*. V. 109, No. 1, pp. 63–67.

9 Carnì, D.L., Scuro, C., Lamonaca, F., Olivito, R.S., & Grimaldi, D. (2017). Damage analysis of concrete structures by means of acoustic emissions technique. *Composites Part B: Engineering*. 115, 79–86.

10 Yamada, I., Masuda, K., & Mizutani, H. (1989). Electromagnetic and acoustic emission associated with rock fracture. *Phys. Earth Planet. Int.*, 57.

11 Nazarov, K.M., Kichanov, S.E., El Abd, A., Taman, M., & Kozlenko, D.P. (2020). Study of water infiltration into cement-based mortars using real-time thermal neutron radiography. *Eurasian Phys. Tech. J.*, 17(1), 39–45.

12 O'Keefe, S.G., & Thiel, D.V. (1995). A mechanism for the production of electromagnetic radiation during fracture of brittle materials. *Phys. Earth Planet. Int.*, 89(11), 127–135.

13 Dann, D.D., Petrov, M.V., Fedotov, P.I., & Sheveleva, E.A. (2021). Changes in the Parameters of the Electromagnetic Response of Model Dielectric Samples with Air Cavity Defects under External Deterministic Acoustic Impact. *Bulletin of the University of Karaganda-Physics,* 101(1), 12–17.

14 Lacidogna, G., Carpinteri, A., Manuello, A., Durin, G., Schiavi A., Niccolini G., et al.(2010). Acoustic and electromagnetic emissions as precursor phenomena in failure processes. *Strain*, 47, 144–152.

15 Fursa, T.V., Lyukshin, B.A., & Utsyn, G.E. (2015). Theoretical investigations of the influence of defects under pulsed mechanical excitation of concrete. *Russian Physics Journal*, 1658–1661.

16 Kyriazopoulos, A., Anastasiadis, C., Triantis, D., & Brown, C.J. (2011). Non-destructive evaluation of cement-based materials from pressure-stimulated electrical emission. Preliminary results. *Construction and Building Materials*, 29(4), 1980–1990.

17 Koktavy, P. (2009). Experimental study of electromagnetic emission signals generated by crack generation in composite materials. *Measurement Science and Technology*, 20(1), 015704.

18 Stergiopoulos, C., Stavrakas, I., Hloupis, G., Triantis, D., & Vallianato, F. (2013). Electrical and Acoustic Emissions in cement mortar beams subjected to mechanical loading up to fracture. *Engineering Failure Analysis* 35, 454–461.

19 Bespal'ko, A.A., Isaev, Y.N., & Yavorovich, L.V. (2016). Transformation of acoustic pulses into electromagnetic response in stratified and damaged structures. *J. Min. Sci.*, 52(2), 279–285.

20 Bespal'ko, A.A., Shtirts, V.A., Fedotov, P.I., Chulkov, A.O., & Yavorovich, L.V. (2019). Modelling of Infrared Glow in Rock Holes. *J. Nondestr. Eval.*, 38, 30–29.

21 Fursa, T.V., Lyukshin, B.A., & Utsyn, G.E. (2011). Experimental and theoretical investigation of the characteristics of an electric response to an elastic impact excitation of piezo-containing heterogeneous materials. *Russian Journal of Nondestructive Testing*. 47 (10), 675–679.

22 Bespal'ko, A.A., Surzhikov, A.P., Dann, D.D., Utsyn, G.E., Petrov, M.V., & Pomishin, E.K. (2021) Modelling Acoustic–Electric Nondestructive Testing for Defects in Dielectric Materials. *Russian Journal of Nondestructive Testing*, 57(2), 85–95.

23 X-ray flat panel detector PerkinElmer XRD 0822. *perkinelmer.com.* Retrieved from www.perkinelmer.com

24 Immittance's meter LCR-819. *electronpribor.ru.* Retrieved from www.electronpribor.ru/catalog/53/lcr-819.htm#specification

25 Korolev, V. M. (1973). Aperiodicheskii pezodatchik dlia ultrazvukovykh defektoskopov [Aperiodic piezoelectric sensor for ultrasonic flaw detectors]. *Defectoscopy*, 4, 12–18 [in Russian].

26 Installation guide BNC-2120. *ni.com.* Retrieved from https://www.ni.com/pdf/manuals/372123d.pdf

27 Warming, R.F., Kutler, P., & Lomax, G. (1973). Non-central difference schemes of the II and III order of accuracy for solving nonlinear hyperbolic equations. *Rocket Technol. Cosmonautics*, 11(2), 76–85.

28 Barashkov, V.N., Gerasimov, A.V., & Lyukshin, B.A. (1998). Predicting the destruction of industrial installations. *Russian Physics Journal,* 10, 657–661.

29 Bespal'ko, A.A., Fedotov, P.I., & Yavorovich, L.V. (2013). Investigation and control of magnetization of magnetite ore samples by electromagnetic signal parameters. *Test. Diagn*., 13, 221–224.

DOI 10.31489/2021Ph3/17-24
UDC 537.226

S. Shevelev[1*], E. Sheveleva[1], O. Stary[2]

[1]*National Research Tomsk Polytechnic University, Russia;*
[2]*Czech Technical University in Prague, Czech Republic*
(*[*]E-mail: wevelev@tpu.ru*)

Investigation of the influence of the mode of heat treatment of the initial powder on the efficiency of sintering zirconium ceramics by dilatometry

Using methods of synchronous thermal and X-ray structural analyzes applied to zirconium dioxide powders partially stabilized with yttrium obtained by chemical coprecipitation the processes of dehydration of these powders during annealing in air have been investigated. Using the dilatometry method the regularities of compaction of powder compacts have been investigated with thermal sintering. It was found that the resulting powders mainly consist of the tetragonal modification zirconium dioxide and are nano-sized. The average particle size was 25 nm. The resulting powders are characterized by a high degree of agglomeration. It is shown that an increase in the thermal annealing temperature from 500 to 700 ºC leads to partial baking of individual particles inside the agglomerate, and causes the formation of hard agglomerates, the presence of which complicates the processes of compaction and subsequent sintering. The presence of such agglomerates prevents the production of ceramics with high mechanical characteristics: density and porosity. Thermal annealing temperature increase leads to a decrease in the density of the sintered ceramic and a decrease in its hardness.

Keywords: zirconium dioxide, dilatometry, co-precipitation, chlorides, microscopy, agglomeration.

Introduction

Ceramic materials based on partially yttrium-stabilized zirconium dioxide are increasingly used in various fields of science and technology. High hardness allows the use of zirconium ceramics for the production of cutting and abrasive tools; high melting point and low thermal conductivity are used in thermal insulation and refractory materials. Zirconium ceramics are used for the production of adsorption-semiconductor gas sensors [1, 2], thin-film coatings [3, 4], ion-exchange materials, and chemical reaction catalysts [5–7].

All stages of the technological cycle are important to obtain high-quality ceramics [8]. At the stage of synthesis of initial powders the features of their structure are formed, such as grain size, interface surface and their state, porosity and other defects [9–14]. Therefore, method of obtaining initial powder play an important role in obtaining ceramics with high values of mechanical properties [15–21].

Currently, a large number of methods for obtaining nanosized zirconium dioxide powders exists [22–25]. Many of these methods allow to obtain very high quality powders, but are of little use in conditions of mass production. Among them, the so-called methods of soft chemistry which lead to the formation of a crystalline or semi-crystalline structure without high-temperature treatment, stand out [26], for example, the coprecipitation method [27]. It is applicable in mass production environment, and at the same time has a low cost of the finished product. The main disadvantage of this method is a high degree of agglomeration [28].

The purpose of this work is to study of the effect of agglomeration of zirconium dioxide powders, partially stabilized with yttrium, obtained by coprecipitation on the kinetics of the sintering process of powder compacts.

The method of the experiment

For the production of ceramic material based on partially stabilized zirconium dioxide composition (ZrO_2 + 3 mol.% Y_2O_3) a chemical method of co-precipitation of zirconium and yttrium hydroxides from an aqueous solution of zirconium and yttrium salts is used: zirconium oxide-dichloride YCl_3x6H_2O and yttrium chloride 6-water YCl_3x6H_2O by adding a 25 % aqueous solution of ammonia to pH 9.5. The hydroxide mixture is washed, dried at a temperature of 90 °C for 12 hours and then annealed at a temperature of no more than 700 °C. Annealing time is 1 hour. BET analysis of the obtained powders was carried out on the device “Sorbtometer-M” (Catakon, Russia). Studies were carried out for the initial powders obtained by sol-gel technology without annealing (type P1) and for P1 powders subjected to annealing in air at temperatures of 500 °C (type P2) and 700 °C (type P3) at a heating rate of 20 °C per minute isothermal exposure for 60 minutes. Press samples were made by uniaxial static pressing on a hydraulic press PGR-10 (Lab Tools, Russia). The pressing pressure was varied in the range of 70–960 MPa. The ceramics were sintered in a dilatometer furnace DIL 402 C (NETZSCH, Germany) in an air atmosphere. The air purge rate was 20 mm/min. Electron microscopy was performed on a JEM-2100 scanning electron microscope (Japan). X-ray diffraction analysis was performed on an ARL'xtra diffractometer (ThermoFisher Scientific, Switzerland) with a semiconductor Si (Li) Peltier detector using monochromatized CuKα-radiation. The diffractograms were measured in the angle range 2θ = (90–120)° at a speed of 0.02 ° c^{-1}. The phase analysis was performed using the PDF-4+ powder database of the International Centre for Diffraction Data (ICDD). The diffractograms were processed by the full-profile Ritveld method using the Powder Cell 2.4 software package. The density and porosity of the ceramic samples were determined by hydrostatic weighing in distilled water on a Shimadzu AUW-220 D (Shimadzu Corporation, Japan) scale with a special prefix. The microhardness was measured using a Zwick (Germany) ZHV1M microhardness meter. The thermal analysis of the powders was performed on a synchronous thermal analysis device STA-449 combined with a mass spectrometer QMS 403 D (NETZSCH, Germany).

Experimental results and discussion

Microstructure research. The results of electron microscopy of P1-P3 powders are shown in Figure 1. From the analysis of the presented results it can be seen that the P1 powder consists of agglomerates of small primary particles. The small size of the primary particles leads to a significant increase in the surface energy of the powder system. In combination with the close location of individual particles under the action of Van Der Waals forces, the formation of multiparticle clusters of individual particles — agglomerates, the shape and size of which vary very widely [29].

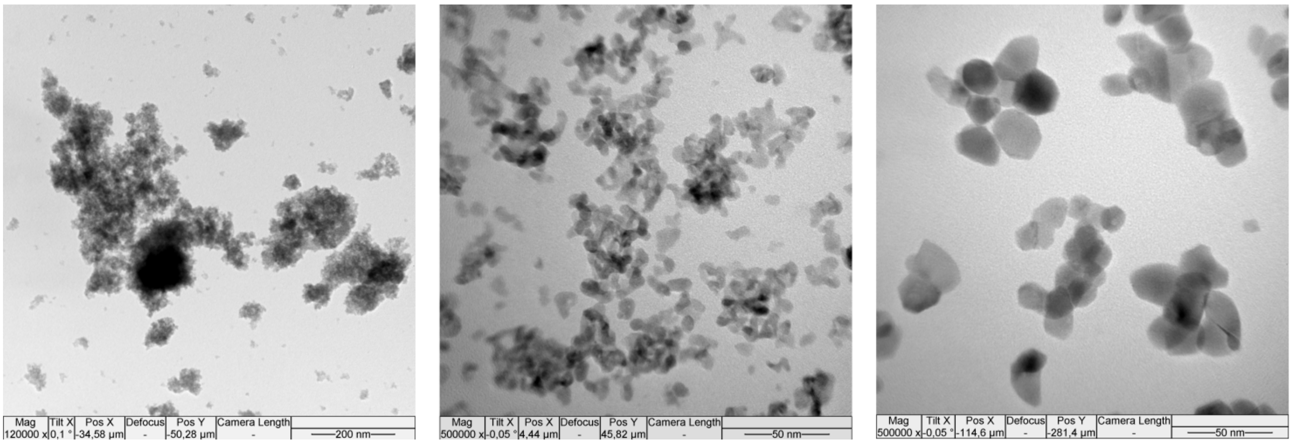

a b c

Figure 1. Electron microscopy of powders (a, b, c are P1, P2, P3 respectively)

In the P2 and P3 powders (Fig. 1b, Figure 1c) separate crystalline particles the size of which increases as the annealing temperature increases are isolated. At the same time, agglomerates of individual particles are also observed in the structure of the powder. Thus, the previously established inheritance of the structure of the initial amorphous xerogels of hydrated zirconium dioxide by nanocrystalline zirconium dioxide is confirmed [30]. At the same time, the heat treatment temperature is sufficient for the initial stage of sintering, which leads to the acquisition of strength by the aggregates and the consolidation of the structure [29].

The diffractograms of the studied powders are shown in Figure 2. As follows from the results obtained, the P1 powder is X-ray amorphous, while the P2 and P3 powders have a crystal structure characteristic of the tetragonal modification of zirconium dioxide. With an increase in the annealing temperature, the peaks narrow, which indicates an increase in the size of the crystallites.

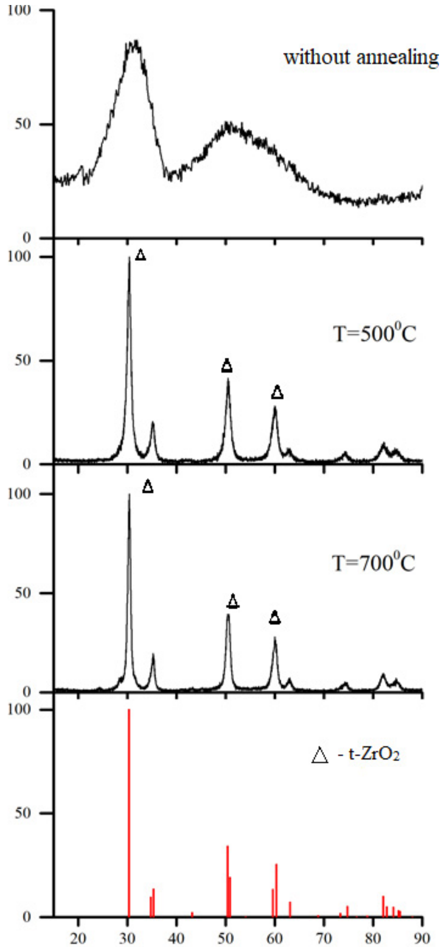

Figure 2. Diffractograms of the studied powders

The results of the thermal analysis of the P1 powder are shown in Figure 3.

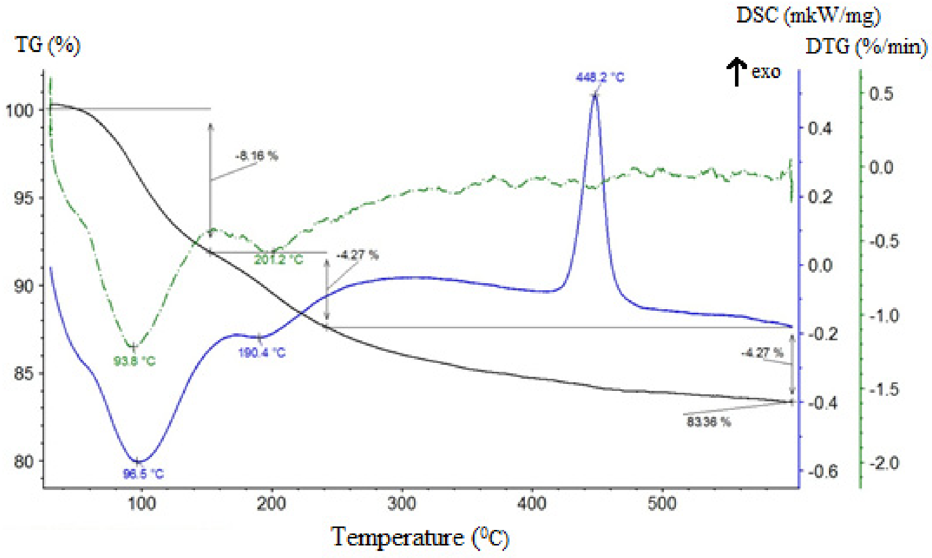

Figure 3. TG, DTG, and DSC curves for P1 powder

When the powder P1 is heated, its dehydration occurs, accompanied by the absorption of heat. The DSC curve shows two endothermic peaks caused by the removal of water present in the test substance in different states. The first and more pronounced peak (96.5 °C) is associated with the removal of physically adsorbed

[31], and the second (190.4 °C) is due to the removal of chemically bound water. Both peaks of the DSC curve are accompanied by a significant decrease in the sample mass (extremes at 93.8 and 201.2 °C on the DTG curve). The total weight reduction when heated to a temperature of 600 °C was 16.6 %. At a temperature of 448.2 °C, a sharp exothermic peak is observed on the DSC curve. This thermal effect is not accompanied by a noticeable change in the mass of the sample, which allows it to be associated with the crystallization process of partially stabilized zirconium dioxide. This conclusion is confirmed by the previously presented results of the XRD.

From the consideration of Figure 4 it follows that that the nature of the compaction depends on the type of powder (P1, P2, P3). For a sample obtained from powder P1 already at the initial stage of heating there is a noticeable shrinkage of the sample, accompanied by a peak at temperature approximately equal to the crystallization temperature of the tetragonal phase of zirconium dioxide, obtained from the results of thermal analysis. Also, at the final stage of the process, there is an expansion of the sample, apparently a consequence of the transition part of the tetragonal phase into monoclinic. For samples obtained from powders P2 and P3 there are practically no differences in the nature of the shrinkage process.

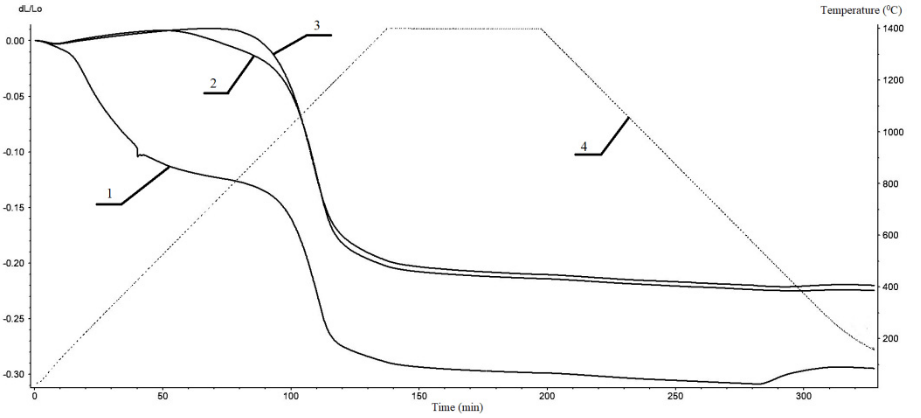

Figure 4. Dilatometric curves of powder compacts P1,
P2 and P3 (curves 1–3, respectively), 4 is thermal annealing mode.

Table 1 presents the results determining the density of compacts ρ_{pr}, density of ceramics sintered from them $\rho_{hydrost}$, porosity Θ and microhardness H_y for different types of samples.

Table 1

Physical properties of compacts and sintered ceramics

Sample type	ρ_{pr}, g/cm^3	$\rho_{hydrost}$, g/cm^3	Θ, %.	H_v, GPa
P1	2,44	4,98	16,0	9,1
P2	2,53	5,21	10,8	9,4
P3	2,62	5,18	12,3	8,2

Table 1 shows that when using powders P2 and P3 the characteristics of the sintered ceramics are significantly higher than when using P1 powder. Highest density and lowest density of sintered ceramics is achieved by using P2 powder.

Conclusion

Thermal analysis methods were used to study the processes occurring when the powder P1 is heated in an air atmosphere, obtained by coprecipitation from chloride starting components. The processes of compaction and sintering of powder compacts, made from initial powders P1 and after their annealing at temperatures of 500 and 700 °C (powders P2 and P3, respectively). At the same time, the following was established.

The heating of the P1 powder was accompanied by dehydration, the main part of which ends at a temperature of about 200^0C. Total mass yield when heated to 600 °C is 16.6 %. P3 powders obtained by annealing the initial P1 powder at a temperature of 700^0C are characterized by a nanoscale crystal structure. The average crystallite size according to the results of XRD and microscopy was 25 nm.

The highest density of ceramics obtained when sintering a sample of powder P2, which is most likely due to a lower density of agglomerates than in P3 powder.

References

1 Arsent'ev M. Yu. Investigation of some physicochemical properties of ceramics, single crystals, and nanofilms based on zirconia, hafnia, and rare-earth oxides / M. Yu. Arsent'ev, P.A. Tikhonov, M.V. Kalinina, N.S. Andreeva // Glass Physics and Chemistry. — 2010. — Vol. 36, No. 4. — P. 478–483.

2 Dimitrov D.T. Oxygen detection using junctions based on thin films of yttria-stabilized zirconia doped with platinum nanoparticles and pure yttria-stabilized zirconia / Dimitrov D.T., Dushkin C.D., Petrova N.L., Todorovska R.V., Todorovsky D.S., Anastasova S.Y., Oliver D.H. // Sensors and Actuators A: Physical. — 2007. — Vol. 137(1). — P. 86–95.

3 Грязнов Р.В. Технология и свойства тонкопленочных материалов ZrO_2–SiO_2 : автореф. дис. / В. Грязнов. — Томск, 2003. — 21 с.

4 Crisan M. Sol–gel ZrO_2-SiO_2 coatings for optical application / Crisan M., Gartner M., Predoana L., Scurtu R., Zaharescu M., Gaurila R. // Journal of Sol–Gel Science and Technology. — 2004. — Vol. 32(1–3). — P. 167–172.

5 Zhang Q.H. Preparation and characterization of zirconia-silica and zirconia-magnesia supports for normal-phase liquid chromatography / Q.H. Zhang, Y.Q. Feng, S.L. Da // Analytical Sciences. — 1999. Vol. 15(8). — P. 767–772.

6 Shalliker R.A. The measurement of pore size distribution, surface areas and pore volumes of zirconia, and zirconia-silica mixed oxide stationary phases using size exclusion chromatography/ Shalliker R.A., Douglas G.K., Rintoul L., Comino P.R., Kavanagh P.E. // Journal of Liquid Chromatography and Related Technologies. — 1997. — Vol. 20(10). — P. 1471–1488.

7 Shalliker R.A. Retention behavior of basica solutes on zirconia-silica composite stationary phase supports in normal phase liquid chromatography/ Shalliker R.A., Rizk M., Stocksiek C., Sweeney A.P. // Journal of Liquid Chromatography and Related Technologies. — 2002. — Vol. 25(4). — P. 561–572.

8 Подденежный Е.Н. Классификация способов получения ультрадисперсных оксидных порошков (обзор) / Е.Н. Подденежный, А.А. Бойко. // Вестн. Гомел. гос. техн. ун-та им. П.О. Сухого. — 2003. — № 1. — С. 21–27.

9 Матренин С.В. Наноструктурные материалы в машиностроении: учеб. пос. / С.В. Матренин, Б.Б. Овечкин. — Томск: ТПУ, 2009. — 185 с.

10 Хасанов О.Л. Метод коллекторного компактирования нано- и полидисперсных порошков: учеб. пос. / О.Л. Хасанов. — ТПУ, 2009. — 102 с.

11 Шевченко А.В. Микроструктурное проектирование материалов в системе ZrO_2 -Y_2O_3 - CeO_2 - Al_2O_3 / А.В. Шевченко, Е.В. Дудник, В.В. Цукренко, А.К.Рубан // Порошковая металлургия. — 2010. — № 9/10. — С. 43–51.

12 Menvie Bekale V. Processing and microstructure characterization of ceria-doped yttria-stabilized zirconia powder and ceramics / Menvie Bekale V., Legros C., Haut C., Sattonnay G., Huntz A.M. // Solid state Ionics. — 2006. — Vol.177. — P. 3339–3347.

13 Lee W.S. Synthesis and microstructure of Y_2O_3-doped ZrO_2-CeO_2 composite nanoparticles by hydrothermal process / Lee W. S., Kim S. W., Koo B. H., Bae D. S. // Colloids and Surfaces A: Physicochem. Eng. Aspects. — 2008. — Vol. 313–314. — P. 100–104.

14 Lange F.F. Transformation toughening Part 4. Fabrication, fracture toughness and strength of Al_2O_3 -ZrO_2 composites / F.F. Lange // J. Mater. Sci. — 1982. — Vol. 17. — P. 247–254.

15 Буякова С.П. Формирование структуры пористой керамики, спеченной из нанокристаллических порошков / С.П. Буякова, С.Н. Кульков // Огнеупоры и техническая керамика. — 2005. — № 11. — С. 6–11.

16 Лукин Е.С. Оксидная керамика нового поколения и области ее применения / Е.С. Лукин, Н.А. Макаров, А.И. Козлов, Н.А. Попова, Е.В. Ануфриева, М.А. Вартанян, И.А. Козлов, М.Н. Сафина, Д.О. Лемешев, Е.И. Горелик // Стекло и керамика. — 2008. — № 10. — С. 27–31.

17 Бакунов В.С. Особенности технологии высокоплотной технической керамики / В.С. Бакунов, Е.С. Лукин // Стекло и керамика. — 2008. — № 2. — С. 3–7.

18 Бакунов В.С. Оксидная керамика: Спекание и ползучесть: учеб. пос. / В.С. Бакунов, А.В. Беляков, Е.С. Лукин, У.Ш. Шаяхметов // Министерство образования и науки Российской Федерации. — М.: Росс. хим.-техн. ун-т им. Д.И. Менделеева, 2007. — 584 с.

19 Валиев Р.З. Наноструктурные материалы, полученные интенсивной пластической деформацией / Р.З. Валиев, И.В. Александров. — М.: Логос, 2000. — 272 с.

20 Морозова Л.В. Получение нанокекрамики на основе диоксида циркония с высокой степенью тетрагональности / Л.В. Морозова, М.В. Калинина, Н.Ю. Ковалько, М.Ю. Арсентьев, О.А. Шилова // Физика и химия стекла. — 2014. — № 3. — С. 462–468.

21 Морозова Л.В. Получение нанокерамики на основе диоксида циркония для реставрационной стоматологии / Л.В. Морозова, М.В. Калинина, И.А. Дроздова, И.Г. Полякова, О.А. Шилова // Институт стоматологии. — 2014. — № 3 (64). — С. 98, 99.

22 Тайыбов А.Ф. Дилатометрия керамик на основе оксидов алюминия и циркония, полученных методом распылительной сушки / А.Ф. Тайыбов, А.Э. Илела, Г.В. Лямина // Междунар. науч.-исслед. журн. — 2013. — № 10–1 (17). — С. 49–51.

23 Ворожцов А.Б. Синтез дисперсных металлооксидных материалов. Кн. 2. Плазмохимический метод получения оксидов титана и циркония / А.Б. Ворожцов, А.С. Жуков, Т.Д. Малиновская, В.И. Сачков / отв. ред. Т.Д. Малиновская. — Томск: Изд-во НТЛ, 2014. — 168 с.

24 Andrievski R.A. Nanostructured titanium, zirconium and hafnium diborides: the synthesis, properties, size effects and stability / R.A. Andrievski // Russian Chemical Reviews. — 2015. — Vol. 84 (5). — P. 540–554.

25 Ремпель А.А. Физика твердого тела / А.А. Ремпель. — Екатеринбург: УГТУ-УПИ, 2007. — 174 с.

26 Петрова Е.В. Физико-химические основы получения и структурно-чувствительные свойства наноразмерных оксидов p, d - металлов как прекурсоров композиционных материалов: дисс. д-ра хим. наук: 02.00.04 / Е.В. Петрова. — Казань, 2018. — 344 с.

27 Вассерман И.М. Химическое осаждение из растворов / И.М. Вассерман. — Л.: Химия, 1980. — 207 с.

28 Константинова Т.Е. Производство нанодисперсных порошков диоксида циркония: от новации к инновациям / Т.Е. Константинова, И.А. Даниленко, В.В. Тонкий, В.А. Глазунова // Наука инновации. — 2005. — № 1. — С. 78–87.

29 Галахов А.В. Структура порошкового компакта. — Ч. 1. / А.В. Галахов // Новые огнеупоры. — 2014. — № 5. — С. 22–32.

30 Иванов В.К. Исследование эволюции мезоструктуры гидратированного диоксида циркония на разных стадиях термической обработки / В.К. Иванов, Г.П. Копица, С.В. Григорьев, О.С. Полежаева, В.М. Гарамус // Физика твердого тела. — 2010. — Т.52. –№ 5. — С. 898–904.

31 Кульметьева В.Б. Синтез нанокристаллического диоксида циркония, стабилизированного оксидом иттрия, для низкотемпературного спекания / В.Б. Кульметьева, С.Е. Порозова, Е.С. Гнедина // Изв. вузов. Порошковая металлургия и функциональные покрытия. — 2011. — № 2. — С. 3–9.

С. Шевелев, Е. Шевелева, О. Старый

Бастапқы ұнтақты термиялық өңдеу режимінің циркония керамикасын дилатометрия әдісімен біріктіру тиімділігіне әсерін зерттеу

Химиялық тұндыру әдісімен алынған иттриймен жартылай тұрақтандырылған циркония ұнтақтарына қатысты синхронды термиялық және рентгендік құрылымдық талдау әдістерін қолдана отырып, ауада өңдеу кезінде осы ұнтақтардың дегидратация процестері зерттелді. Дилатометрия әдісін қолдана отырып, термиялық күйдіру кезінде ұнтақты компактілердің тығыздау заңдылықтары тексерілген. Алынған ұнтақтар негізінен цирконийдің тетрагональді модификациясынан тұрады және наноөлшемдері бар екендігі анықталды. Бөлшектердің орташа мөлшері — 25 нм. Бұл ретте алынған ұнтақтар агломерацияның жоғары дәрежесімен сипатталады. Термиялық күйдіру температурасының 500-ден 700 ℃-қа дейін жоғарылауы агломерат ішіндегі жеке бөлшектердің ішінара пісірілуіне әкеліп соғатындығы көрсетілген және қатаң агломераттардың пайда болуына әкеледі, олардың болуы ықшамдау және кейінгі синтездеу процестерін қиындатады. Мұндай агломераттардың пайда болуы тығыздығы мен кеуектілігі жоғары механикалық сипаттамалары бар керамиканы алуға кедергі келтіреді. Термиялық күйдіру температурасының жоғарылауы күйдірілген керамиканың тығыздығының төмендеуіне және оның қаттылығының төмендеуіне әкеледі.

Кілт сөздер: цирконий диоксиді, дилатометрия, тұнба түзу, хлоридтер, микроскопия, агломерация.

С. Шевелев, Е. Шевелева, О. Старый

Исследование влияния режима термической обработки исходного порошка на эффективность спекания циркониевой керамики методом дилатометрии

С использованием методов синхронного термического и рентгеноструктурного анализа применительно к порошкам диоксида циркония, частично стабилизированного иттрием, полученных методом химического соосаждения, исследованы процессы дегидратации этих порошков при отжиге на воздухе. При помощи метода дилатометрии изучены закономерности уплотнения порошковых компактов при термическом спекании. Установлено, что полученные порошки состоят преимущественно из тетрагональной модификации диоксида циркония и имеют наноразмеры. Средний размер частиц – 25 нм. При этом полученные порошки характеризуются высокой степенью агломерации. Показано, что увеличение температуры термического отжига с 500 до 700 ℃ приводит к частичному припеканию отдельных частиц внутри агломерата, и вызывает формирование жестких агломератов, наличие которых затрудняет процессы компактирования и последующего спекания. Наличие подобных агломератов препятствует получению керамики с высокими механическими характеристиками: плотностью и пористостью. Повышение температуры термического отжига приводит к снижению плотности спеченной керамики и снижению ее твердости.

Ключевые слова: диоксид циркония, дилатометрия, соосажение, хлориды, микроскопия, агломерация.

References

1 Arsent’ev, M. Yu. (2010). Investigation of some physicochemical properties of ceramics, single crystals, and nanofilms based on zirconia, hafnia, and rare-earth oxides. *Glass Physics and Chemistry*. 36(4), 478–483.

2 Dimitrov, D.T. (2007). Oxygen detection using junctions based on thin films of yttria-stabilized zirconia doped with platinum nanoparticles and pure yttria-stabilized zirconia. *Sensors and Actuators A: Physical*. 137(1), 86–95.

3 Gryaznov, R.V. (2003). Tekhnologiia i svoistva tonkoplenochnykh materialov ZrO_2–SiO_2 [Technology and properties of thin-film materials ZrO_2–SiO_2]. *Dissertation abstract*. Tomsk [in Russian].

4 Crisan, M. (2004) Sol–gel ZrO_2-SiO_2 coatings for optical application. *Journal of Sol–Gel Science and Technology*. 32(1–3), 167–172.

5 Zhang, Q.H. (1999). Preparation and characterization of zirconia-silica and zirconia-magnesia supports for normal-phase liquid chromatography. *Analytical Sciences*. 15(8), 767–772.

6 Shalliker, R.A. (1997). The measurement of pore size distribution, surface areas and pore volumes of zirconia, and zirconia-silica mixed oxide stationary phases using size exclusion chromatography. *Journal of Liquid Chromatography and Related Technologies*. 20(10), 1471–1488.

7 Shalliker, R.A. (2002). Retention behavior of basica solutes on zirconia-silica composite stationary phase supports in normal phase liquid chromatography. *Journal of Liquid Chromatography and Related Technologies*. 25(4), 561–572.

8 Poddenezhny, E.N., & Boyko, A.A. (2003). Classification of methods for producing ultrafine oxide powders. *Vestnik Gomelskogo gosudarstvennogo tekhnicheskogo universiteta imeni P.O. Sukhogo — Bulletin of the Gomel State Technical University named after P.O. Sukhoi,* 1, 21–27 [in Russian].

9 Matrenin, S.V., & Ovechkin, B.B. (2009). *Nanostrukturnye materialy v mashinostroenii [Nanostructured materials in mechanical engineering]*. Tomsk: TPU [in Russian].

10 Khasanov, O.L. (2009). *Metod kollektornogo kompaktirovaniia nano- i polidispersnykh poroshkov [Method of collector compaction of nano- and polydisperse powders]*. Tomsk: TPU [in Russian].

11 Shevchenko, A.V., Dudnik, E.V., Tsukrenko, V.V., & Ruban, A.K. (2010). Mikrostrukturnoe proektirovanie materialov v sisteme ZrO_2–Y_2O_3–CeO_2–Al_2O_3 [Microstructural design of materials in the system ZrO_2–Y_2O_3–CeO_2–Al_2O_3]. *Poroshkovaia metallurgiia — Powder metallurgy*. 9/10, 43–51 [in Russian].

12 Menvie Bekale, V. (2006). Processing and microstructure characterization of ceria-doped yttria-stabilized zirconia powder and ceramics. *Solid state Ionics*. 177, 3339–3347.

13 Lee, W. S. (2008). Synthesis and microstructure of Y_2O_3-doped ZrO_2-CeO_2 composite nanoparticles by hydrothermal process. *Colloids and Surfaces A: Physicochem. Eng. Aspects*. 313–314, 100–104.

14 Lange, F.F. (1982). Transformation toughening Part 4. Fabrication, fracture toughness and strength of Al_2O_3 -ZrO_2 composites *J. Mater. Sci.* 17, 247–254.

15 Buyakova, S.P., & Kulkov, S.N. (2005). Formirovanie struktury poristoi keramiki, spechennoi iz nanokristallicheskikh poroshkov [Formation of the structure of porous ceramics sintered from nanocrystalline powders]. *Ogneupory i tekhnicheskaia keramika — Refractories and technical ceramics*, 11, 6–11 [in Russian].

16 Lukin, Ye.S., Makarov, N.A., Kozlov, A.I., Popova, N.A., Anufriyeva, Ye.V., & Vartanyan, M.A., et al. (2008). Oksidnaia keramika novogo pokoleniia i oblasti ee primeneniia [New generation oxide ceramics and their fields of application]. *Steklo i keramika — Glass and ceramics*. 10, 27–31 [in Russian].

17 Bakunov, B.C., & Lukin, Ye.S. (2008). Osobennosti tekhnologii vysokoplotnoi tekhnicheskoi keramiki [Features of the technology of high-density technical ceramics]. *Steklo i keramika — Glass and ceramics*. 2, 3–7 [in Russian].

18 Bakunov, B.C., Belyakov, A.V., Lukin, Ye.S., & Shayakhmetov, U.Sh. (2007). Oksidnaia keramika: Spekanie i polzuchest [Oxide ceramics: Sintering and creep]. *Ministerstvo obrazovaniia i nauki Rossiiskoi Federatsii — Rossiiskii khimiko-tekhnologicheskii universitet imeni D.I. Mendeleeva*. Moscow [in Russian].

19 Valiyev, P.З., Aleksandrov, I.V. (2000). *Nanostrukturnye materialy, poluchennye intensivnoi plasticheskoi deformatsiei [Nanostructured materials obtained by severe plastic deformation]*. Moscow*:* Logos [in Russian].

20 Morozova, L.V., Kalinina, M.V., Koval'ko, N.Yu., Arsentyev, M.Yu., & Shilova, O.A. (2014). Poluchenie nanokeramiki na osnove dioksida tsirkoniia s vysokoi stepeniu tetragonalnosti [Production of nanoceramics based on zirconium dioxide with a high degree of tetragonality]. *Fizika i khimiia stekla — Physics and chemistry of glass,* 3, 462–468 [in Russian].

21 Morozova, L.V., Kalinina, M.V., Drozdova, I.A., Polyakova, I.G., Shilova, O.A. (2014). Poluchenie nanokeramiki na osnove dioksida tsirkoniia dlia restavratsionnoi stomatologii [Obtaining a nanoceramic based on zirconium dioxide with a high degree of tetragonality]. *Institut stomatologii — Institute of Dentistry*. 3 (64), 98, 99 [in Russian].

22 Tayybov, A.F., Ilela, A.E., & Lyamina, G.V. (2013). Dilatometriia keramik na osnove oksidov aliuminiia i tsirkoniia, poluchennykh metodom raspylitelnoi sushki [Dilatometry of ceramics based on alumina and zirconium oxides obtained by spray drying]. *Mezhdunarodnyi nauchno-issledovatelskii zhurnal — International research journal,* 10–1 (17), 49–51[in Russian].

23 Vorozhtsov, A.B., Zhukov, A.S., Malinovskaia, T.D., & Sachkov, V.I. (2014). *Sintez dispersnykh metallooksidnykh materialov. Kniga 2. Plazmokhimicheskii metod polucheniia oksidov titana i tsirkoniia [Synthesis of dispersed metal oxide materials. Book 2. Plasma-chemical method for obtaining titanium and zirconium oxides]*. Tomsk: NTL [in Russian].

24 Andrievski, R.A. (2015). Nanostructured titanium, zirconium and hafnium diborides: the synthesis, properties, size effects and stability. *Russian Chemical Reviews*. 84 (5), 540–554.

25 Rempel, A.A. (2007). Fizika tverdogo tela [Solid state physics]. Ekaterinburg: UGTU-UPI [in Russian].

26 Petrova, E.V. (2018). Fiziko-khimicheskie osnovy polucheniia i strukturno-chuvstvitelnye svoistva nanorazmernykh oksidov p, d – metallov kak prekursorov kompozitsionnykh materialov [Physicochemical foundations of preparation and structure-sensitive properties of nanosized oxides of p, d — metals as precursors of composite materials]. *Doctor's thesis*. Kazan [in Russian].

27 Vasserman, I.M. (1980). Khimicheskoe osazhdenie iz rastvorov [Chemical precipitation from solutions]. Leningrad: Khimiia [in Russian].

28 Konstantinova, T.E., Danilenko, I.A., Tonkiy, V.V., & Glazunova, V.A. (2005). Proizvodstvo nanodispersnykh poroshkov dioksida tsirkoniia: ot novatsii k innovatsiiam [Production of nanodispersed zirconium dioxide powders: from innovation to innovation]. *Nauka innovatsii — Science of Innovation*. 1, 78–87 [in Russian].

29 Galakhov, A.V. (2014). Struktura poroshkovogo kompakta. Chast 1. [Powder compact structure. Part 1]. *Novye ogneupory — New refractories*, 5, 22–32 [in Russian].

30 Ivanov, V.K., Kopitsa, G.P., Grigorev, S.V., Polezhaeva, O.S., & Garamus, V.M. (2010). Issledovanie evoliutsii mezostruktury gidratirovannogo dioksida tsirkoniia na raznykh stadiiakh termicheskoi obrabotki [Investigation of the evolution of the mesostructure of hydrated zirconium dioxide at different stages of heat treatment]. *Fizika tverdogo tela — Solid State Physics,* 52 (5), 898–904 [in Russian].

31 Kulmeteva, V.B., Porozova, S.E., & Gnedina, E.S. (2011). Sintez nanokristallicheskogo dioksida tsirkoniia, stabilizirovannogo oksidom ittriia, dlia nizkotemperaturnogo spekaniia [Synthesis of Yttria-Stabilized Nanocrystalline Zirconia for Low-Temperature Sintering]. *Izvestiia vuzov. Poroshkovaia metallurgiia i funktsionalnye pokrytiia — Izvestiya vuzov. Powder metallurgy and functional coatings,* 2, 3–9 [in Russian].

DOI 10.31489/2021Ph3/25-34
UDC 532.529

N.Zh. Jaichibekov[1], B.S. Shalabayeva[1*], V.N. Kireev[2]

[1]*Gumilyov Eurasian National University, Nur-Sultan, Kazakhstan;*
[2]*Bashkir State University, Ufa, Russia*
(**E-mail: shalabaeva.b.s@mail.ru*)

Modeling the dynamics of charged drop of one liquid in another under the action of an electric field

The work is devoted to the study of the features of the behavior of a group of droplets of one viscous liquid in another under the influence of various physical fields. When considering the dynamics of two drops under the action of an electric field it is assumed that a drop in the form of a sphere with radius a will be placed in an electric field with an intensity $\vec{E}$, investigates how droplets will react to each other under the influence of an electric field. A mathematical model has been built and a computer program has been developed for the numerical solution of this problem. The behavior of several drops in an electric field is studied for different physical parameters of the material of the drops and the environment, as well as for different initial distributions of drops and the strength of the electric field. It is shown for the first time that emulsion droplets distributed in space, under the action of an electric field, begin to move and after a certain time a new stationary structure of droplets is formed. It was found that the relaxation time depends on the electric field strength, the size of the droplets and their initial distribution.

Keywords: droplet dynamics, electromagnetic field, dispersed system, mathematical model, computer model, computational domain, dynamics of an emulsion system.

Introduction

The theoretical and experimental study of the behavior of individual drops of one viscous liquid in another under the influence of various physical fields (thermal, acoustic, electromagnetic) is of great importance in solving technological problems in various industries. A huge number of scientists from all over the world have been and are engaged in research on various aspects of this problem and have contributed to solving the problem [1–3]. In the case of one drop, the results obtained by the authors of this work are given in [4].

An emulsion is considered, consisting of spherical drops of one viscous incompressible fluid, distributed in the volume of another viscous incompressible fluid, immiscible with the first. Both liquids are considered to be dielectric. When considering the dynamics of two drops under the action of an electric field, it is assumed that a drop in the form of a sphere with radius a will be placed in an electric field with an intensity $\vec{E}$, investigates how droplets will react to each other under the influence of an electric field.

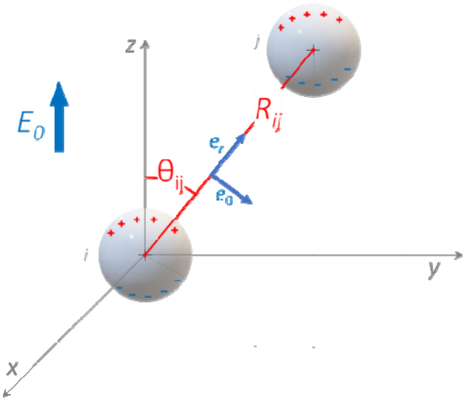

Figure 1. Interaction of two emulsion droplets in an electric field.

Mathematical model of the dynamics of two drops

Consider two spherical emulsion droplets i and j of the same diameter $d = 2a$, the distance between which R_{ij} (Fig. 1). It is assumed that the drops do not have a significant effect on the distribution of polarization charges in them and, using the point-dipole approximation, the electrostatic force acting on i-th drop from the j-th drop can be determined by the formula:

$$\vec{F}_{ij}^{e} = \left[(\vec{p}_i \cdot \nabla)\vec{E}_j\right]_{x=0}, \tag{1}$$

where $\vec{p}_i$ is the equivalent dipolet moment of the i-th drop (determined by the formula $\vec{p} = 4\pi\varepsilon_0\varepsilon_c\beta a^3 E_0\vec{e}_z$, and $\vec{E}_0, \vec{E}_j$ of the strengths of the electric field of the external environment and the electric field of the j-th drop, which are calculated, respectively, through the electrostatic potentials of the external environment, i.e.: $\varphi_c = -E_0 r\left[1-\beta\left(\frac{a}{r}\right)^3\right]\cos\theta$ and drop $\varphi_d = -E_0 r\frac{3}{\alpha+2}\cos\theta$. Substituting into formula (1) the expressions $\vec{p}, \varphi_c, \varphi_d$ and $\alpha = \frac{\varepsilon_d}{e_c}$, $\beta = \frac{\alpha-1}{\alpha+2}$ we get:

$$\begin{gathered}\vec{F}_{ij}^{e} = F_0\left(\frac{d}{R_{ij}}\right)^4\left[(3cos^2\theta_{ij}-1)\vec{e}_r + \sin 2\theta_{ij}\vec{e}_\theta\right],\\ F_0 = \frac{3}{16}\pi\varepsilon_0\varepsilon_c d^2\beta^2 E_0^2.\end{gathered} \tag{2}$$

When deriving formula (2) it was assumed that the origin of the spherical coordinate system is at the center of the i-th drop. Strictly speaking, formula (2) is exact only under the following conditions: the dielectric constants of the environment and droplets differ insignificantly, i.e., $\beta \longrightarrow 0$; the diameter of the droplets is much less than the distance between them, i.e., $R_{ij}/d \to \infty$.

A qualitative analysis of formula (2) makes it possible to predict the nature of the motion of two drops under the action of an external electric field.

a) If the drops are located along the electric field strength vector coinciding with the direction of the axis z $(\theta_{ij} = 0)$, then the vector $\vec{F}_{ij}^{e}$ will be directed along the vector $\vec{e}_r$ and the drops will attract.

b) If the line connecting the centers of the drops is perpendicular to the intensity vector $(\theta_{ij} = \pi/2)$, then the direction of the vector $\vec{F}_{ij}^{e}$ will be opposite to the direction of the vector $\vec{e}_r$ and drops will repel.

c) In case of an arbitrary arrangement of drops the force $\vec{F}_{ij}^{e}$ will rotate them, trying to arrange them in the direction of the intensity vector.

If the distance R_{ij} between the emulsion drops, it becomes enough, a short-acting repulsive force appears small (Fig. 2a)

$$\vec{F}_i^{r}(\vec{R}_i) = -F_0\exp\left(-\kappa\frac{R_{ij}-d}{d}\right)\vec{e}_r, \tag{3}$$

where κ is characteristic distance at which repulsive forces act.

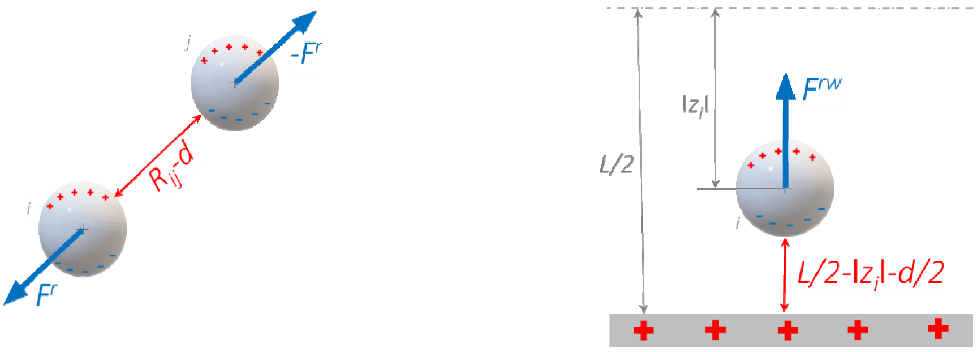

a) between drops; b) between a drop and an electrode

Figure 2. To the definition of repulsive forces

The repulsive force between the drop and the electrode is described similarly (Fig. 2b):

$$\vec{F}_i^{rw}(\vec{R}_i) = -F_0 \exp\left(-\kappa \frac{L/2 - |z_i| - d/2}{d} \right) \vec{n}\,, \tag{4}$$

where $\vec{n}$ is normal vector to the electrode surface directed inward of the emulsion, z_i is axis coordinate of the drop center *Z*.

A mathematical model of the dynamics of an emulsion system in an electric field, taking into account the considered forces, can be written by the following equation [5]:

$$m \frac{d^2 \vec{R}_i}{dt^2} = \sum_{\substack{j=1 \\ j \neq i}}^{n} \left[\vec{F}_{ij}^{e}(R_{ij}, \theta_{ij}) + \vec{F}_{ij}^{r}(R_{ij}, \theta_{ij}) \right] + \sum_{j=1}^{n} \vec{F}_{ij}^{\prime e}(R'_{ij}, \theta'_{ij}) + \vec{F}_i^{h}(\vec{R}_i) + \vec{F}_i^{rw}(\vec{R}_i) \tag{5}$$

where $\vec{R}_i$ is the radius vector of the center of the *i,* th drop, $m = \frac{1}{6}\pi d^3$ is the drop weight, $\vec{F}_i^{h}(\vec{R}_i)$ is the force of hydrodynamic resistance, according to the Hadamard-Rybchinsky formula. $\sum_{j=1}^{n} \vec{F}_{ij}^{\prime e}(R'_{ij}, \theta'_{ij})$ is the force of the electrical interaction between the *i*-th drop and the electrodes.

The solution of the ordinary differential equation (5) with closing relations (2)-(4) and a given initial distribution of drops will allow us to determine the dynamics of each drop in the emulsion and, thus, to simulate the dynamics of the emulsion as a whole under the action of an electric field.

Computer model of the dynamics of two drops

To build a computer model and carry out numerical modeling of the dynamics of emulsion drops in an electric field, we first write expressions for the forces entering the equations of the mathematical model in the two-dimensional case, using the global Cartesian coordinate system.

The strength of the electrical interaction between the *i*-th and *j*-th drops $\vec{F}_{ij}^{e}$ depends on distance R_{ij} between drops and angle θ_{ij} between the vector of the electric field strength and the vector connecting the centers of the drops. Suppose that all emulsion droplets are in the plane (*y*, *z*), the coordinates of the center of the *i*-th drop in the global Cartesian coordinate system we denote (y_i, z_i). Then we can write that:

$$R_{ij} = \sqrt{(y_i - y_j)^2 + (z_i - z_j)^2}\,,\ \cos\theta_{ij} = \frac{z_j - z_i}{R_{ij}},\ \sin\theta_{ij} = \frac{y_j - y_i}{R_{ij}}.$$

Vector $\vec{F}_{ij}^{e}$ in the local polar coordinate system associated with the *i*-th drop, it is decomposed in the vectors of the local basis $\vec{e}_r$ and $\vec{e}_\theta$: $\vec{F}_{ij}^{e} = (\vec{F}_{ij}^{e})_r \cdot \vec{e}_r + (\vec{F}_{ij}^{e})_\theta \cdot \vec{e}_\theta$, where

$$\left(\vec{F}_{ij}^{e}\right)_r = F_0 \left(\frac{d}{R_{ij}} \right)^4 (3\cos^2\theta_{ij} - 1)\,,\ \left(\vec{F}_{ij}^{e}\right)_\theta = 2F_0 \left(\frac{d}{R_{ij}} \right)^4 \sin\theta_{ij} \cos\theta_{ij}\,.$$

Because the relationship between the reference vectors of the local and global coordinate systems are given by $\vec{e}_r = \sin\theta \cdot \vec{e}_y + \cos\theta \cdot \vec{e}_z$, $\vec{e}_\theta = \cos\theta \cdot \vec{e}_y - \sin\theta \cdot \vec{e}_z$, then the projections of the vector $\vec{F}_{ij}^{e}$ on the axis of the global cartesian coordinate system (*y*, *z*) will be written in the following form:

$$\left(\vec{F}_{ij}^{e}\right)_y = \left(\vec{F}_{ij}^{e}\right)_r \sin\theta_{ij} + \left(\vec{F}_{ij}^{e}\right)_\theta \cos\theta_{ij} = F_0 \left(\frac{d}{R_{ij}} \right)^4 \sin\theta_{ij} \left(5\cos^2\theta_{ij} - 1 \right),$$

$$\left(\vec{F}_{ij}^{e}\right)_z = \left(\vec{F}_{ij}^{e}\right)_r \cos\theta_{ij} - \left(\vec{F}_{ij}^{e}\right)_\theta \sin\theta_{ij} = F_0 \left(\frac{d}{R_{ij}} \right)^4 \cos\theta_{ij} \left(5\cos^2\theta_{ij} - 3 \right).$$

The components of the vector of the repulsive force and the force of hydrodynamic resistance are written in a similar way in the global Cartesian coordinate system:

$$\left(\vec{F}_{ij}^{r}\right)_y = -F_0 \exp\left(-\kappa \frac{R_{ij}-d}{d}\right)\sin\theta_{ij}, \quad \left(\vec{F}_{ij}^{r}\right)_z = -F_0 \exp\left(-\kappa \frac{R_{ij}-d}{d}\right)\cos\theta_{ij},$$

$$\left(\vec{F}_{i}^{h}\right)_y = -\pi\mu_c d \frac{2\mu_c + 3\mu_d}{\mu_c+\mu_d}\frac{dy_i}{dt}, \quad \left(\vec{F}_{i}^{h}\right)_z = -\pi\mu_c d \frac{2\mu_c + 3\mu_d}{\mu_c+\mu_d}\frac{dz_i}{dt}.$$

Thus, we finally write the second-order differential equation (5) describing the dynamics of drops in an electric field in the form of a system of first-order differential equations (6):

$$\begin{cases} \dfrac{dy_i}{dt} = u_i, \\ \dfrac{dz_i}{dt} = v_i, \\ \dfrac{du_i}{dt} = \sum\limits_{\substack{j=1 \\ j\neq i}}^{N}\left(\vec{F}_{ij}^{e}\right)_y + \sum\limits_{\substack{j=1 \\ j\neq i}}^{N}\left(\vec{F}_{ij}^{r}\right)_y + \left(\vec{F}_{i}^{h}\right)_y, \\ \dfrac{dv_i}{dt} = \sum\limits_{\substack{j=1 \\ j\neq i}}^{N}\left(\vec{F}_{ij}^{e}\right)_z + \sum\limits_{\substack{j=1 \\ j\neq i}}^{N}\left(\vec{F}_{ij}^{r}\right)_z + \left(\vec{F}_{i}^{h}\right)_z. \end{cases} \tag{6}$$

The initial conditions are the coordinates of the initial position of the drops in space and their initial velocities (in all the results below, it is assumed that the drops at the initial moment of time are at rest).

For numerical simulation, consider water droplets in oil. Basic parameters for numerical simulation are given in the Table 1.

Table 1

Basic parameters for numerical simulation

Parameter	Symbol	Unit of Measurement	Value
Drop diameter	d	m	10^{-3}
Electric field strength	E_0	V/m	10^{6}
Parameter characterizing the repelling force of drops	κ	–	10^{2}
Environment			
Relative dielectric constant	ε_c	–	7.3
Dynamic viscosity	μ_c	Pa·s	10^{-1}
Drops			
Relative dielectric constant	ε_d	–	23.6
Dynamic viscosity	μ_d	Pa·s	10^{-3}

We begin numerical modeling by considering a system consisting of two drops in view of the possibility of carrying out a relatively simple qualitative analysis.

Results

Figure 3 shows the time dependences of the coordinates of the centers of drops of the same diameter for the cases when the centers of the drops at the initial moment of time are located on one of the coordinate axes symmetrically about the origin. The droplet diameters are the same, and the initial distance between them is 1 cm, i.e., ten times the diameter of the droplets. Curves of different colors correspond to different drops. If at the initial moment of time the centers of the drops are located on the y-axis (i.e., the vector connecting the centers of the drops is perpendicular to the z-axis and accordingly to the vector of the electric field strength), then the drops begin to move along the y-axis in opposite directions (Fig. 3 a).

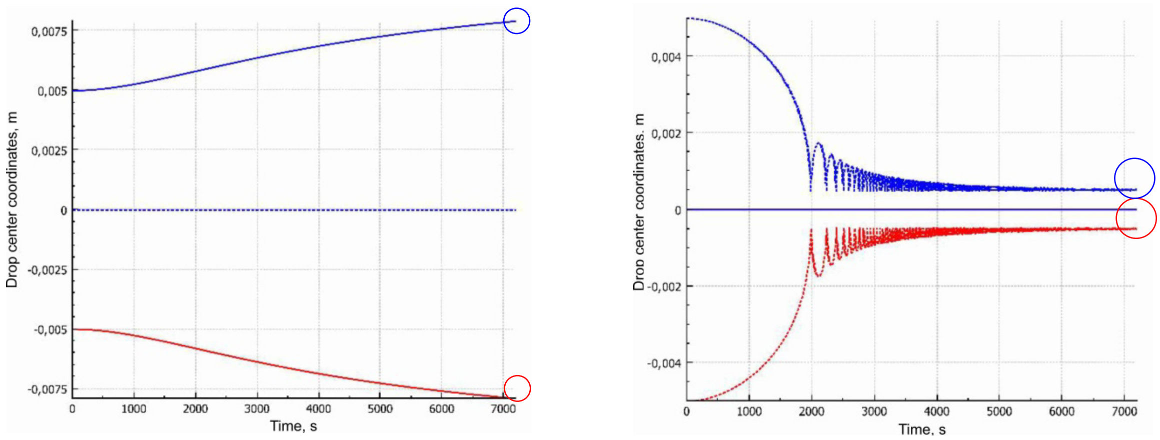

a) b)

a) the initial position of the drops on the *y*-axis b) the initial position of the drops on the *z* axis

Figure 3. Dependence of the coordinates of the centers of drops of the same diameter on time

A similar result was described in [5]: the existence of a critical value of the electric field strength was experimentally established, above which oppositely charged droplets began to repel. It can be seen from the Figure 3a that in two hours the distance between the drops increased by 1.5 times. At large times, the distance between drops will continue to increase slightly, and then the drops will stop at a certain distance determined by the force of hydrodynamic resistance.

A qualitatively different behavior of drops is observed in the case when the centers of the drops are located along the vector of the electric field strength (Fig. 3 b). In this case, the motion of the drops has an oscillatory character: first, the drops come closer to each other until the repulsive force becomes greater than the force of electrical interaction, after which the drops change the direction of movement to the opposite. Then the strength of the electrical interaction increases, the drops approach again, etc. After some time, the position of the drops stabilizes, and they are located in the direction of the electric field strength vector in close proximity to each other (the final positions of the drops are schematically shown in Figure 3 and on all the following red and blue circles).

Figure 4 shows the time dependences of the coordinates of the centers of drops of different diameters for the cases when the centers of drops at the initial moment of time are located on one of the coordinate axes symmetrically about the origin. The diameter of the red drop is five times the diameter of the blue drop. The initial distance between the centers of the droplets is still 1 cm.

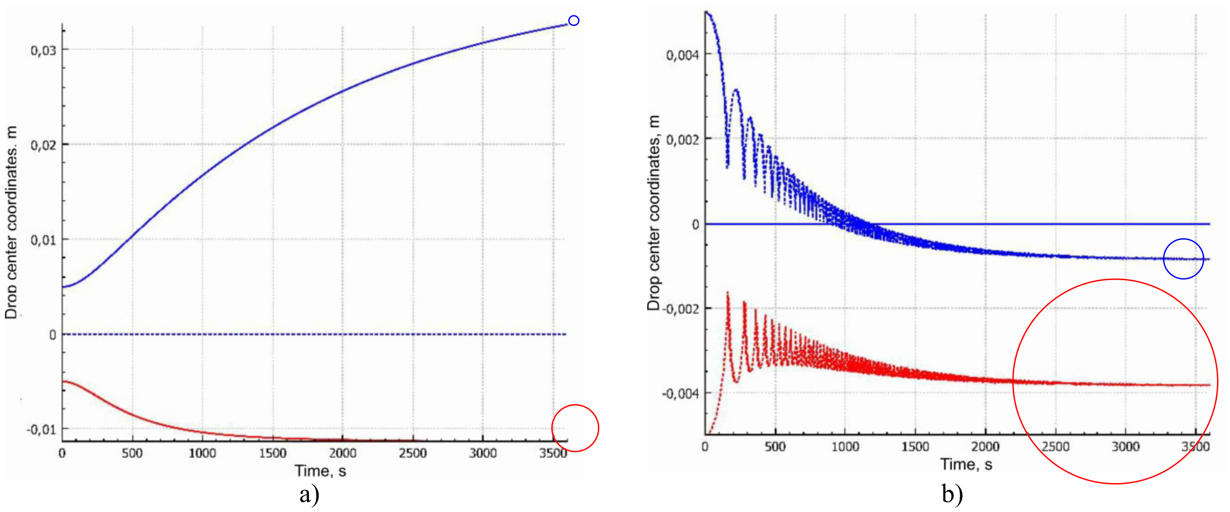

a) b)

a) the initial position of the drops on the *y*-axis; b) the initial position of drops on the *z* axis

Figure 4. Dependence of the coordinates of the centers of drops of different diameters on time

In principle, the nature of the droplet motion remains the same as for droplets of the same radius: droplets located perpendicular to the electric field strength vector are repelled, and droplets located along the strength vector are attracted, making oscillations. A drop with a smaller diameter (blue in Figure 4) is more affected. Figure 4 b shows that the small drop moves 6 mm, while the large drop moves a little more than 1 mm. An important parameter that determines the nature of the interaction between drops is the dimensionless parameter κ, characterizing the repulsive force between the drops (see formula (4)). This parameter depends on the physical properties of the drop material and the environment, as well as on the properties of the envelope surrounding the drop. Specific parameter value κ should be determined from appropriate experiments. Figure 5 shows the dependences of the coordinates of the centers of drops of the same diameter for different values of the parameter κ.

For small values of the parameter κ the value of the repulsive force is too small and non-physical interpenetration of drops into each other is observed (Fig. 5 a). The interpenetration of drops stops when the parameter is κ close to 100 (Fig. 5 b). A further increase in the parameter leads to a slight increase in the amplitude of oscillations, which does not affect the steady state of the drops (Fig. 5 c). Therefore, in further calculations the value of the parameter will be used $\kappa = 100$.

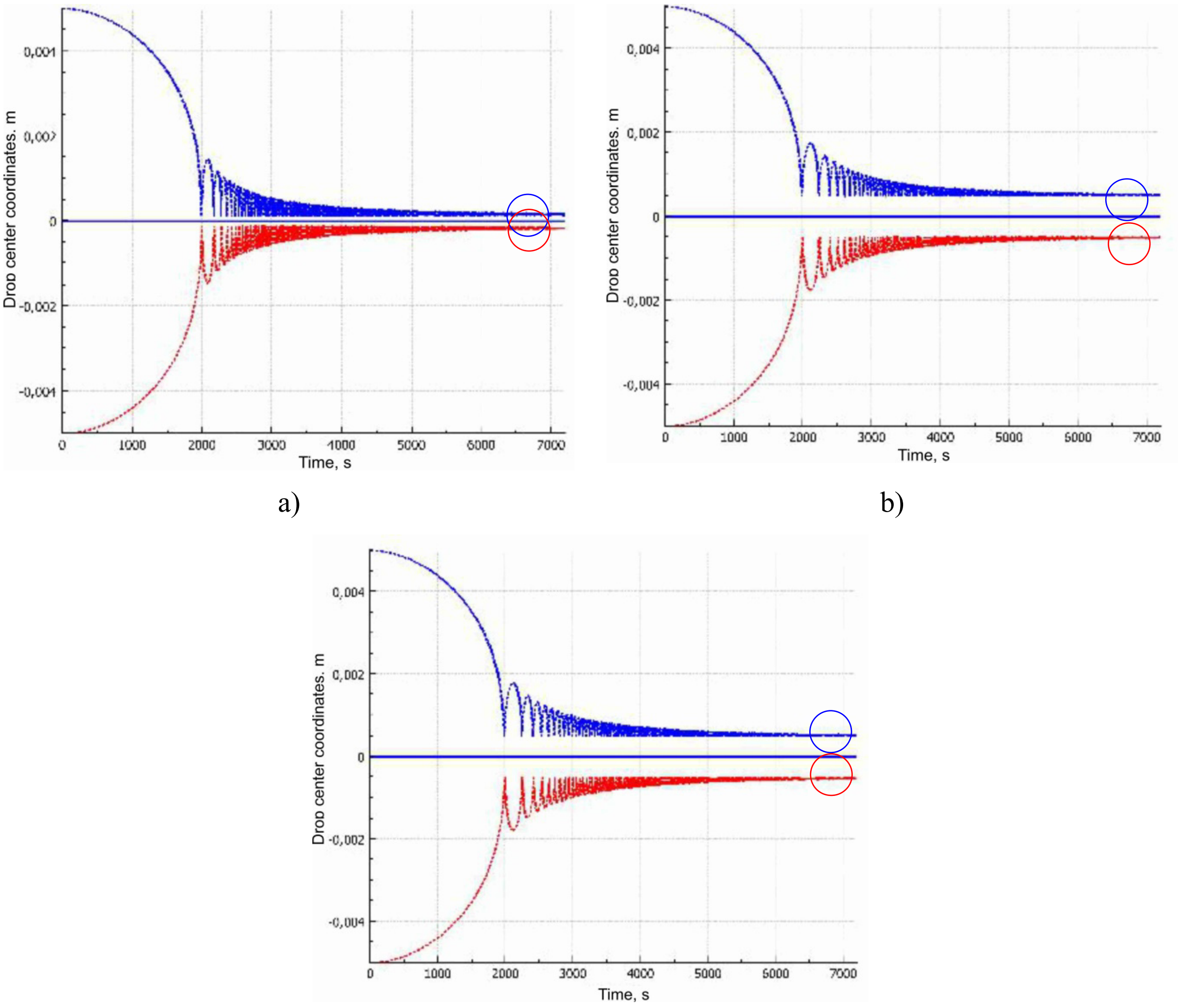

a)

b)

c)

a) $\kappa = 1$; b) $\kappa = 100$; c) $\kappa = 1000$

Figure 5. Dependence of the coordinates of the centers of drops of the same diameter on time

Consider the situation where the vector is connecting the centers of drops at an angle α to the vector of the electric field strength. Figures 6 and 7 show the dependences of the coordinates of the centers of droplets of the same diameter on time and the trajectory of the droplets at angles $\alpha = +45^o$ and $\alpha = -45^o$ accordingly.

As expected, the movement patterns in Figures 6 and 7 turned out to be symmetrical, therefore we will only analyze in detail the results in Figure 6. In contrast to the previous results, Figure 6 a shows four curves. Curves of different colors correspond to different droplets, the solid curve shows the change in the y coordinate, and the dashed curve shows the change in the z coordinate. It can be seen that under the action of an external electric field the droplets are subjected to a rotational moment and move to a stationary position along a curved trajectory (Fig. 6 b) simultaneously experiencing damped oscillations. In a stationary position, the drops are located on the z axis (i.e., in the direction of the electric field strength vector) symmetrically relative to the origin.

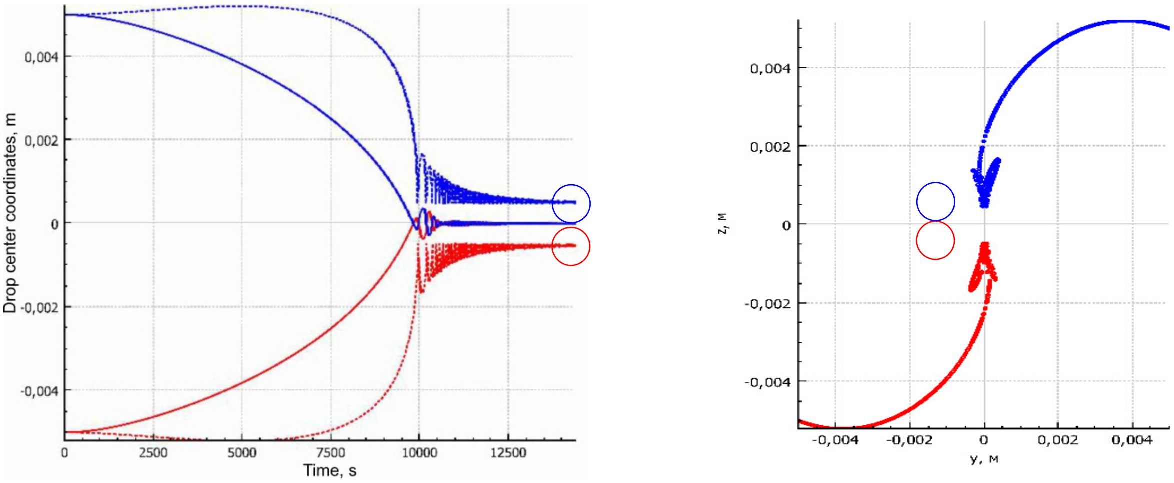

a) b)

a) time dependence of the coordinates of the centers of drops; b) droplet trajectories

Figure 6. Dynamics of drops of the same diameter at an angle $\alpha = +45^o$

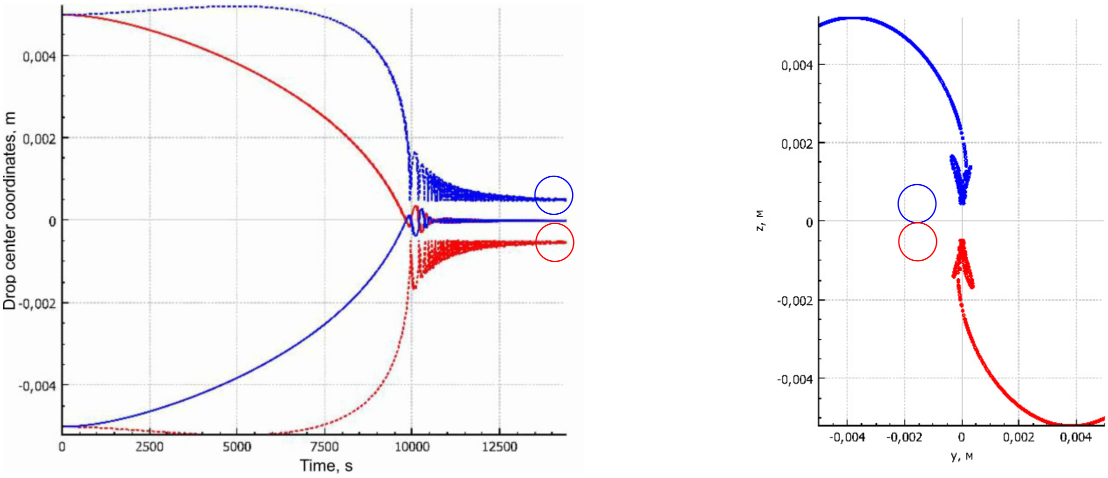

a) b)

a) time dependence of the coordinates of the centers of drops; b) droplet trajectories

Figure 7. Dynamics of drops of the same diameter at an angle $\alpha = -45^o$

As shown earlier (see Figure 3 a), if the angle α between the vector of the electric field strength and the vector connecting the centers of the drops is equal, then at the selected value of the strength the drops move in opposite directions. For it angle values is α close, but smaller, drops also begin to move in opposite directions, however, the radial component of the electric interaction force increases, the trajectory is curved, the direction of movement of the drops changes to and the drops begin to approach (Fig. 7, a, b). If the angle α is less than 45°, then the opposite motion of drops is not observed (Fig. 8).

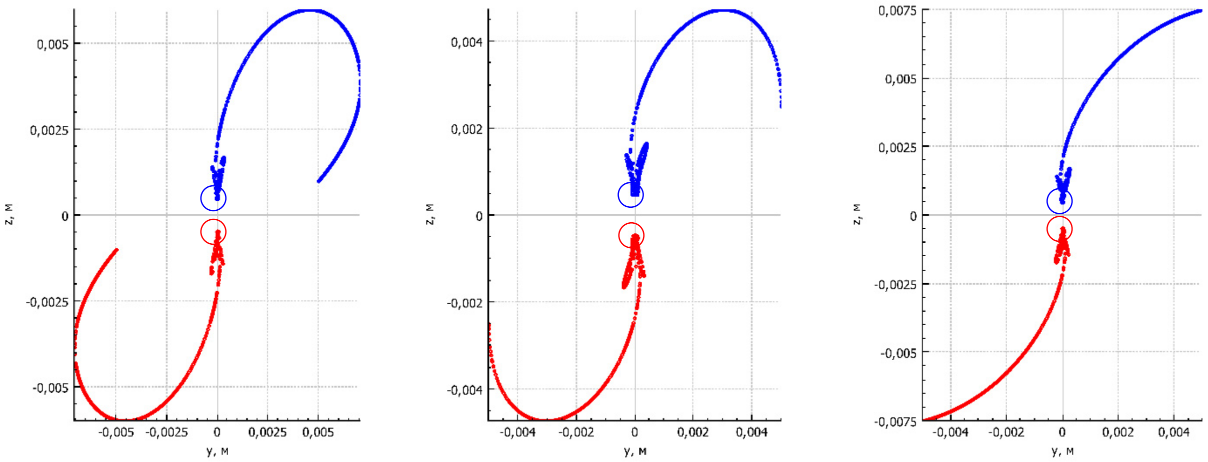

a) b) c)

a) $\alpha = 78,7^o$; b) $\alpha = 63,4^o$; c) $\alpha = 11,7^o$

Figure 8. Trajectories of droplets at different angles α

The magnitude of the electric field strength has a significant effect on the time to reach a steady state (Fig. 9). If with strength $2\cdot 10^6$ V/m drops come to a stationary position in about two hours (Fig. 9, c), then with a four times lower intensity B/m, this takes more than ten hours (Fig. 9, a).

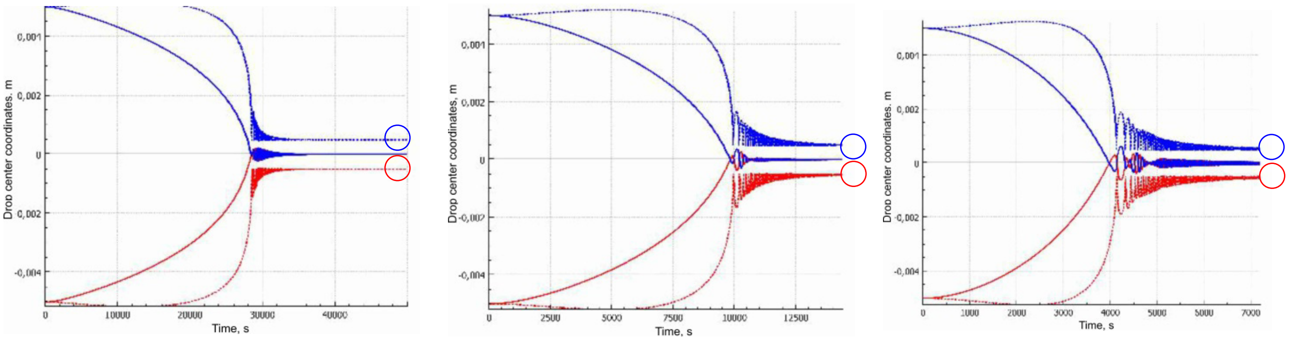

a) b) c)

a) $E_0 = 0,5\cdot 10^6$ B/m; b) $E_0 = 1\cdot 10^6$ B/м; c) $E_0 = 2\cdot 10^6$ B/m

Figure 9. Dependence of the coordinates of the centers of drops
of the same diameter on time at different strengths of the electric field

When simulating a system of three or more drops, all of the above regularities are observed, however, the dynamics of interaction is much more complex.

Conclusion

The mathematical model has been constructed and an algorithm has been developed for the numerical solution of the problem of the motion of two or more drops in an electric field, and a computer program has been created that implements this algorithm. The behavior of several drops in an electric field is studied for different physical parameters of the material of the drops and the environment, as well as for different initial distributions of drops and the strength of the electric field. It is shown that emulsion droplets distributed in space, which are initially at rest, begin to move under the action of an electric field, and after a certain time (relaxation time) a new stationary droplet structure is formed. It was found that the relaxation time depends on the electric field strength, the size of the drops and on their initial distribution. The resulting structures, depending on the parameters of the medium and the field, are either threadlike formations of drops oriented in the direction of the electric field, or separate chains of drops. In addition, the type of the structures formed also depends on the type of the selected dependence, which expresses the repulsive force between the drops. The obtained numerical results are in qualitative agreement with the known experimental data.

The work was carried out within the framework of the grant financing project of the Ministry of Education and Science of the Republic of Kazakhstan AP09562291 "Study of gas thermodynamics after an electric discharge in a supersonic flow".

References

1 Ковалева Л.А. Исследование устойчивости водонефтяной эмульсии в электромагнитном поле в зависимости от её диэлектрических свойств / Л.А. Ковалева, Р.З. Миннигалимов, Р.Р. Зиннатуллин // Изв. высш. учеб. зав. Нефть и газ. — 2010. — № 2. — С. 59–62.

2 Mandal, S. Effect of uniform electric field on the drop deformation in simple shear flow and emulsion shear rheology / S. Mandal, S. Chakraborty // Physics of Fluids. — 2017. — Vol. 29, 072109. DOI:10.1063/1.4995473

3 Шаймарданов В.Х. Процессы и аппараты технологии сбора и подготовки нефти и газа на промыслах / В.Х. Шаймарданов. — М.: Ижевск; НИЦ «Регулярная и хаотическая динамика»; Институт компьютерных исследований, 2013. — 508 с.

4 Джайчибеков Н.Ж. Моделирование динамики заряженной капли жидкости / Н.Ж. Джайчибеков, В.Н. Киреев, Б.С. Шалабаева, Ж.Ж. Омарова, З.А. Кутпанова // Вестн. Башкир. гос. ун-та. — 2018. — Т. 23. — № 3. — С. 645–649.

5 Ahn, K.H. Relaxation of polydisperse electrorheological suspensions / K.H. Ahn, D.J. Klingenberg // Journal of Rheology. — 1994. — Vol. 38(3). — P.713–741. DOI: 10.1122/1.550482.

Н.Ж. Джайчибеков, Б.С. Шалабаева, В.Н. Киреев

Электр өрісінің әсерінен бір сұйықтың зарядталған тамшыларының басқа сұйықтағы динамикасын моделдеу

Мақала әртүрлі физикалық өрістердің (электромагниттік күштердің) әсерінен бір тұтқыр сұйықтың тамшылар тобының басқа сұйықтағы қозғалысының ерекшеліктерін зерттеуге арналған. Бір тұтқыр сығылмайтын сұйықтан тұратын және де онымен араласпайтын, екінші тұтқыр сығылмайтын сұйықтың көлемінде таралған, сфералық тамшылардың эмульсиясы қарастырылған. Екі сұйық диэлектрик болып саналады. Электр өрісінің әсерінен екі тамшының динамикасын қарастырғанда, a радиусы бар шар тәрізді тамшылар кернеулігі $\vec{E}$ болатын электр өрісіне орналастырылады және электр өрісінің әсерінен тамшылардың бір-біріне қалай әсер ететіні зерттелген. Осы есептің сандық шешімін табу үшін математикалық модель құрылып, компьютерлік программа жасалды. Электр өрісіндегі бірнеше тамшылардың қозғалысы тамшылардың материалы мен қоршаған ортаның әртүрлі физикалық параметрлеріне, сонымен қатар тамшылардың әртүрлі бастапқы үлестірімдері мен электр өрісінің кернеулігіне байланысты зерттелді. Электр өрісінің әсерінен кеңістікте таралған эмульсия тамшылары қозғала бастайтындығы және белгілі бір уақыттан (релаксация уақытынан) кейін тамшылардың жаңа стационарлық құрылымы пайда болатыны бірінші рет көрсетілген. Релаксация уақыты электр өрісінің кернеулігіне, тамшылардың мөлшеріне және олардың алғашқы таралуына байланысты екендігі анықталды. Түрі тамшылар арасындағы $\vec{F}_i^r$ итергіш күшіне тәуелді болып келетін, пайда болған құрылымдар, сол орта мен өрістің параметрлеріне байланысты немесе электр өрісі бағытымен бағытталған жіп тәріздес тамшылардың түзілімдері немесе тамшылардың бөлек тізбектері болып келеді.

Кілт сөздер: тамшылардың динамикасы, электромагниттік өріс, дисперсті жүйе, математикалық модель, компьютерлік модель, есептеу аймағы, эмульсия жүйесінің динамикасы.

Н.Ж. Джайчибеков, Б.С. Шалабаева, В.Н. Киреев

Моделирование динамики заряженных капель одной жидкости в другой под действием электрического поля

Статья посвящена исследованию особенностей поведения группы капель одной вязкой жидкости в другой под действием различных физических полей (электромагнитных сил). Рассмотрен состав эмульсии, состоящей из сферических капель одной вязкой несжимаемой жидкости, распределенных в объеме другой вязкой несжимаемой жидкости, несмешивающейся с первой. Обе жидкости считаются диэлектрическими. При рассмотрении динамики двух капель под действием электрического поля капли в форме шара с радиусом a будут помещены в электрическое поле с напряженностью $\vec{E}$, и исследована реакция друг на друга под действием электрического поля. Построена математическая модель, и разработана компьютерная программа для численного решения данной задачи. Изучено поведение нескольких капель в электрическом поле при различных физических параметрах материала капель и окружающей среды, а также при различных начальных распределениях капель и напряженности электрического поля. Впервые показано, что распределенные в пространстве эмульсионные капли под действием электрического поля начинают движение и через определенное время (время релаксации) образуется новая стационарная структура капель. Установлено, что время релаксации зависит от напряженности электрического поля, размеров капель и от их начального распределения. Образующиеся структуры, вид которых зависит от силы отталкивания между каплями $\vec{F}_i^r$, в зависимости от параметров среды и поля, представляют собой либо нитевидные образования из капель, ориентированные по направлению электрического поля, либо отдельные цепочки капель.

Ключевые слова: динамика капель, электромагнитное поле, дисперсная система, математическая модель, компьютерная модель, расчетная область, динамика эмульсионной системы.

References

1 Kovaleva, L.A., Minnigalimov, R.Z., & Zinnatullin, R.R. (2010). Issledovanie ustoichivosti vodoneftianoi emulsii v elektromagnitnom pole v zavisimosti ot ee dielektricheskikh svoistv [Investigation of Water-in-Oil Emulsions in RadioFrequency and Microwave Electromagnetic Fields of Water-in-Oil Emulsions in RadioFrequency and Microwave Electromagnetic Fields]. *Izvestiia vysshikh uchebnykh zavedenii. Neft i gaz — Proceedings of higher educational institutions. Oil and gas*, 2, 59–62 [in Russian].

2 Mandal, S., & Chakraborty, S. (2017). Effect of uniform electric field on the drop deformation in simple shear flow and emulsion shear rheology. *Physics of Fluids, 29,* 072109

3 Shaymardanov, V.H. (2013). *Protsessy i apparaty tekhnologii sbora i podgotovki nefti i gaza na promyslakh [Processes and devices of technologies for gathering and treating oil and gas in the fields].* Moscow: Izhevsk Research Center «Regular and Chaotic Dynamics», Institute for Computer Research [in Russian].

4 Jaichibekov, N.Zh., Kireev, V.N., Shalabayeva, B.S., Omarova, Zh.Zh., & Kutpanova, Z.A. (2018). Modelirovanie dinamiki zariazhennoi kapli zhidkosti [Simulation of the dynamics of a charged liquid drop]. *Bulletin of Bashkir State Universitet — Vestnik Bashkirskogo gosudarstvennogo universiteta,* 3, 645–649 [in Russian].

5 Ahn, K.H., & Klingenberg, D.J. (1994). Relaxation of polydisperse electrorheological suspensions. *Journal of Rheology, 38(3),* 713–741.

DOI 10.31489/2021Ph3/35-44
UDC 533.9.082

A.A. Mutalip[1,2*], Y.A. Ussenov[1,2], A.K. Akildinova[1,2],
M.K. Dosbolayev[3], M.T. Gabdullin[1,4], T.S.Ramazanov[3]

[1]*NNLOT, Faculty of Physics and Technology, Al-Farabi Kazakh National University, Almaty, Kazakhstan;*
[2]*Institute of Applied Science and Information Technologies, Almaty, Kazakhstan;*
[3]*IETP, Faculty of Physics and Technology, Al-Farabi Kazakh National University, Almaty, Kazakhstan;*
[4]*Kazakhstan-British Technical University, Almaty, Kazakhstan*
([*]E-mail: mutalip.abdurashid@gmail.com)

Determination of the reduced electric field in surface dielectric barrier discharge plasmas

In this paper the experimental determination of the reduced electric field (E/n) in plasma of dielectric coplanar surface barrier discharge (DCSBD) at atmospheric pressure was demonstrated. The plasma characteristics and the experimental setup properties were described, and the optical emission spectrum of the plasma was also measured. The results of optical emission spectroscopy showed the presence of nitrogen molecular bands in the emission spectrum of DCSBD. In particular, the second positive and the first negative systems, as well as low intensity OH and NO lines were identified. The main transport properties of electrons, such as mobility, mean average energy, and diffusion coefficients were calculated using the BOLSIG+ open source software. The dependence of the ratio of intensities of the nitrogen spectral lines on the reduced electric field, the dependence of the E/n on plasma power, and the dependence of the electron energy distribution function (EEDF) on E/n were obtained. An algorithm in the form of a block diagram for determining the reduced electric field by the BOLSIG + program and experimentally measured spectral line intensities are presented. The utilized method are quite simple, accessible and versatile.

Keywords: plasma, dielectric barrier discharge, spectroscopy, reduced electric field, lines intensity, nitrogen spectrum, Boltzmann equation.

Introduction

Dielectric barrier discharge (DBD) is a discharge ignited between electrodes, one or both of which are covered with a dielectric [1, 2]. The DBD can generate high-density atmospheric pressure plasma jets using an air flow as a source gas [3]. At the same time, the generation of DBD does not require large vacuum installations, which favorably distinguishes its operation in comparison with other types of discharges [4]. Another distinctive feature of the dielectric barrier discharge is the ability to generate low-temperature, “cold” plasma at atmospheric pressure, which is a key point in the processing of crops, biological samples, and various polymeric and heat sensitive materials. Also, atmospheric pressure plasma (APP), obtained on the basis of a dielectric barrier discharge, is widely used in plasma medicine, water disinfection, nanotechnology and thin film coating [5, 6].

There are two types of dielectric barrier discharge: volume dielectric barrier discharge and surface dielectric barrier discharge. A bulk DBD consists of two parallel electrodes covered with a dielectric layer, or two electrodes located on a dielectric plate. Plasma is generated in the volume of the gap between the electrodes. The configuration of the surface dielectric barrier discharge is as follows: one electrode is located on the surface of the dielectric plate, the other electrode is embedded on the other side of this plate and the discharge is ignited directly on the surface of the dielectric [7]. There is also a surface coplanar dielectric barrier discharge, which occupies an intermediate position between volume and surface discharges. The difference between this discharge is that both electrodes are built in into the dielectric, and the discharge is ignited on the surface of the dielectric.

The wide range of applications of atmospheric pressure plasmas requires a detailed study of the optical properties. The electric field plays a key role in the motion and spatial distribution of charged particles in low-temperature plasmas. The advantage of optical diagnostic methods is that they are non-contact and do not affect the object under the test. Methods based on optical radiation or absorption are characterized by relatively simple measurement equipments.

Several spectroscopic methods can be used to determine the values of the electric field. One of the optical methods is Thomson scattering. However, in such case the scattered laser signal is very weak and several orders of magnitude lower than the incident laser beam, and therefore requires an accurate and expensive installation to evaluate it. Also, there are special requirements for the laser: the laser power must be high enough to obtain an intense scattered signal, and at the same time laser radiation should not introduce perturbations on the diagnosed plasma itself [8].

The Stark shifting is also used to measure the electric field of atmospheric pressure plasmas. Stark polarization spectroscopy uses the Stark effect, which affects the emission spectra depending on the local electric field. Electric fields cause a splitting of energy levels, and a shift of these levels, depending on the electric field. In general, the Stark shift is widely used for dense plasma with electron density above 10^{16} cm^{-3}, and for these plasma conditions, the theoretical data that can be taken for evaluation are well studied. However, this method requires a monochromator with very high resolution, which is usually not easily available [9].

The method of fluorescence spectroscopy includes exposure of the object under study and collection of scattered radiation. Next, a spectrum is generated with different intensities in a given wavelength range. The disadvantage of this method is the necessity to use additional CCD (charge-coupled device) cameras, for visualization of laser-induced fluorescence, which complicates the measurement process [10].

This article demonstrates the determination of the reduced electric field (E/n) of a coplanar surface barrier discharge by measuring optical emission spectroscopy and solving the Boltzmann equation [11]. The described method is quite simple, accessible and versatile.

Experimental setup

The experiments were carried out on an RPS400 setup. The RPS400 is an atmospheric pressure plasma generator which provides an uniform plasma area of approximately 8 cm x 20 cm. The RPS400 system uses a diffuse coplanar surface barrier discharge cell to generate plasma at ambient air, which enables the processing of plastics, metal, wood and glass based products. A schematic diagram of the DCSBD setup is shown in Figure 1 [12]. The conductive electrodes are parallel to each other and embedded in a ceramic dielectric. Plasma is formed on the ceramic surface over an area of 80 mm * 200 mm and reaches a height of about 0.3 mm. The electrodes are made of silver with width of 1.8 mm, thickness of 0.1 mm, length of 230 mm and are located at a distance of 1 mm from each other. The thickness of the ceramic layer between the electrodes and the plasma is 0.4 mm. The discharge was activated by a sinusoidal high voltage (17 kHz, approximately 3 kV peak-to-peak) supplied with an HV plasma power supply. The power of the supplied discharge can be manually adjusted from 80 W to 400 W.

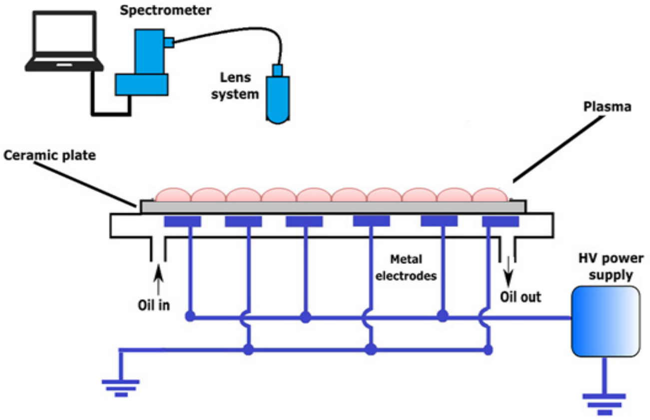

Figure 1. The schematic diagram of electrodes and optical measurement system of DCSBD

Method for determining the reduced electric field

To study the chemical composition and kinetic reactions of the discharge the optical properties of the DCSBD were studied. To achieve this goal the SolarSystems optical emission spectrometer was used. The spectrometer consists of an optical lens system that records a signal collected in a single unit, an optical fiber and the spectrometer itself. Signal registration is performed by a linear Toshiba TDC1304CCD detector. A personal computer was used to digitize and process the signal.

The ratio of the intensities of the spectral lines of nitrogen can be represented in the form of equation (1) [13]. The left side of the equation is the ratio of the intensities of the nitrogen lines, is found experimentally through the obtained spectrum, and the right side, in particular the reaction rate constant (*k*), is found numerically through the BOLSIG + program [14]. The rest of the values are constant for certain experimental conditions (Table 1):

$$R = \frac{I_B\left(\frac{E}{n}\right)}{I_C\left(\frac{E}{n}\right)} = \frac{k_B\left(\frac{E}{n}\right)\tau_0^C\, T_B\, \tau_{air}^B}{k_C\left(\frac{E}{n}\right)\tau_0^B\, T_C\, \tau_{air}^C}, \tag{1}$$

where R is the intensity ratio of the nitrogen lines, I is the intensity of the certain line, k is the reaction rate constant, τ_0 is the lifetime of excited or ionized states of nitrogen molecules, T is a parameter that depends on the sensitivity of the photo detector, τ_{air} is the lifetime in air, indices B and C indicate the following reactions (ionization and excitation) of the nitrogen molecule [15]:

$$N_2^+\left(B^2\Sigma_u^+, \vartheta = 0 \rightarrow X^2\Sigma_g^+, \vartheta = 0\right),\ 391{,}4\ \text{nm},$$

$$N_2\left(C^3\Pi_u, \vartheta = 0 \rightarrow B^3\Pi_g, \vartheta = 0\right),\ \ 337{,}1\ \text{nm}.$$

Table 1

Lifetimes of radiative and of excitation states of some excited states of a nitrogen molecule and ion

Reaction of a nitrogen molecule	*Radiation lifetime*τ_0 *(ns)*	*lifetime of excitation states* τ_{air} *(ns)*
$\left(C^3\Pi_u, \vartheta = 0 \rightarrow B^3\Pi_g, \vartheta = 0\right)$	40	0,62
$\left(B^2\Sigma_u^+, \vartheta = 0 \rightarrow X^2\Sigma_g^+, \vartheta = 0\right)$	60	0,134

From the obtained spectrum we could find the ratio of the intensities of the first negative system of the nitrogen molecule $N_2^+\left(B^2\Sigma_u^+, \vartheta = 0 \rightarrow X^2\Sigma_g^+, \vartheta = 0\right)$ to the second positive system of the nitrogen molecule $N_2\left(C^3\Pi_u, \vartheta = 0 \rightarrow B^3\Pi_g, \vartheta = 0\right)$, which appear at wavelengths of 391.4 and 337.1 nm, respectively.

At the same time, in the BOLSIG + program we can calculate the reaction rate constant, choosing different values of E/n and appropriate database for cross sections. BOLSIG+ is a free and user-friendly computer program for the numerical solution of the Boltzmann equation for electrons in weakly ionized gases in uniform electric fields, conditions which occur in swarm experiments and in various types of gas discharges and collisional low-temperature plasmas. The principle of the program and the formulas used are described in detail by the authors of this program [11].

When the experimental data coincide with the numerical result (BOLSIG +), we extract the electron energy distribution function (EEDF), which is the main quantity for studying kinetic processes in plasma and other transport properties for their further use in calculations and numerical simulations. If the results do not coincide, we return to the selection of E/n in the BOLSIG + program until they coincide with our experimental results. This algorithm is graphically displayed in Figure 2.

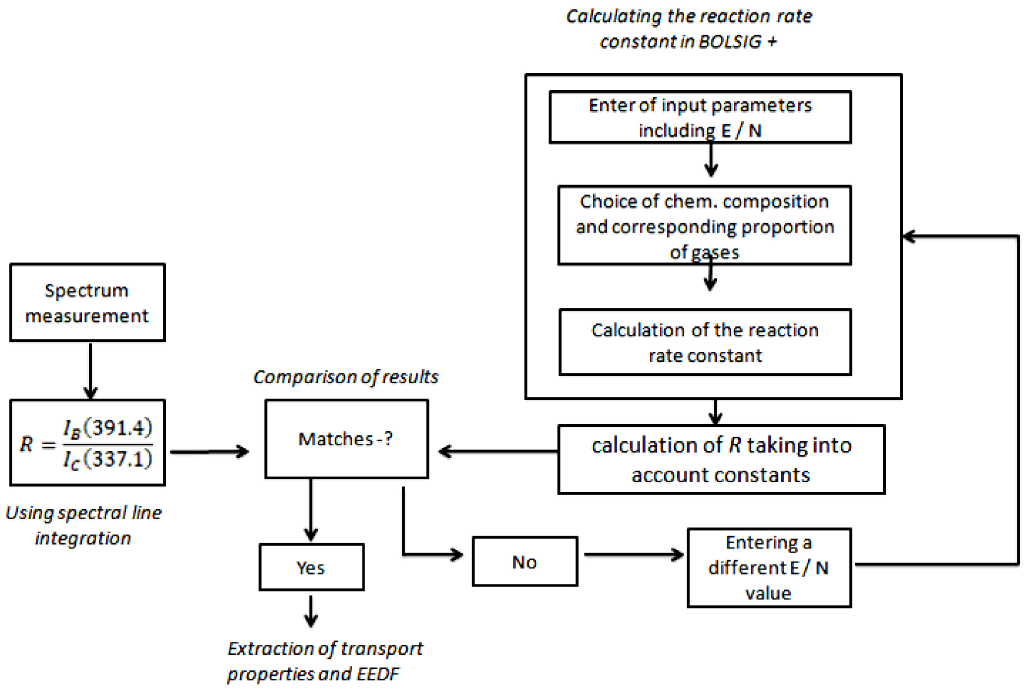

Figure 2. Algorithm for determining the reduced electric field by calculating transport properties in the BOLSIG + program and experimental measurement of the intensities of nitrogen spectral lines

Results and discussion

The experiments were carried out in the plasma power range from 200 W to 400 W with a step of 50 W. It can be seen from the results of the experiment that with an increase in power the surface of the DCSBD discharge cell is gradually filled with multiple microdischarge channels (Fig. 3). Complete filling of the surface is observed at a power of 220 W. At a power of 400 W the surface of the discharge cell is uniformly and closely filled with dense plasma. Below discharge cell surface images are shown at 220 W applied power (the surface is completely filled with micro-discharges) and at a power of 400 W (maximum power) (Fig. 3).

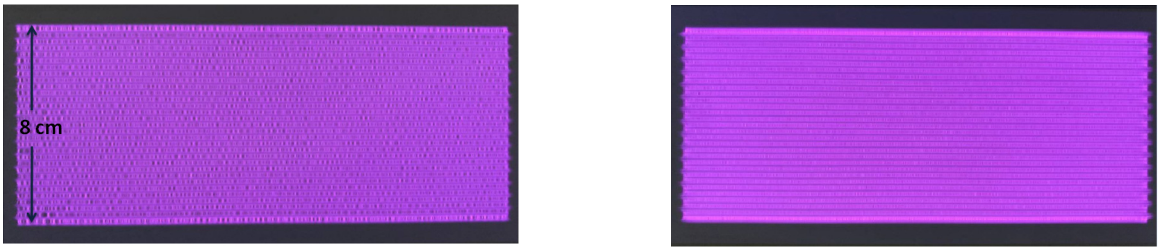

a) b)

Figure 3. Images of the surface of the discharge cell at powers of 220 W (a) and 400 W (b)

Using optical emission spectroscopy, the chemical composition of the DCSBD was determined. Molecular nitrogen bands, namely the second positive (N_2 (C-B)) and the first negative (N_2 + (B-X)) systems were observed in the emission spectrum. In Figure 4 the observed peaks from 300 nm to 470 nm are composed of OH (308 nm) radicals, N_2 (337 nm and 357 nm) and N_2^+ (380 nm, 390 nm, 427 nm and 470 nm). Due to the large number of nitrogen molecules in the atmosphere, nitrogen bands are naturally dominant. OH radicals are also visible due to the presence of water vapor in the air [16]. The line intensities of other radicals and chemically active molecules, such as NO, which are common for air plasma under room conditions, were negligibly low due to the low density and effective collisional quenching of the corresponding excited states.

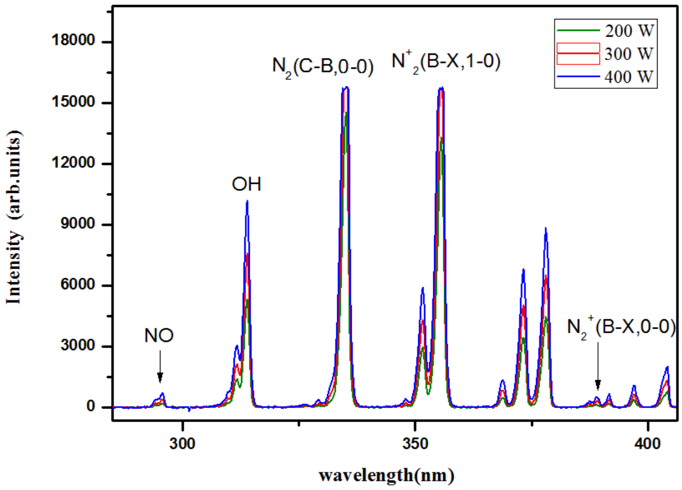

Figure 4. DCSBD spectrum different applied powers

The values $T_B(391{,}4\text{ nm})$ and $T_C(337{,}1\text{ nm})$ show the sensitivity of the photodetector at the respective wavelengths. Information on the sensitivity of the photodetector is indicated in the technical documentation. In the technical documentation of our Toshiba TDC1304 optical device the wavelength starts from 400 nm, but we are interested in the wavelength from 300 to 400 nm, namely 337.1 nm and 391.4 nm, where the rotational structures of the nitrogen molecule are recorded. To find the sensitivity of the wavelengths of interest to us, we extrapolated the graphical data (Fig. 5). As a result, the sensitivity ratio of the photodetector at these wavelengths was Tb/Tc = 1.19.

To calculate the total intensity of the nitrogen spectral lines, the molecular spectrum was integrated over the wavelength taking into account the rotational structure of the molecule. After calculating the total intensity of the lines of interest to us, their ratio was calculated for further comparison with the results obtained by solving the Boltzmann equation.

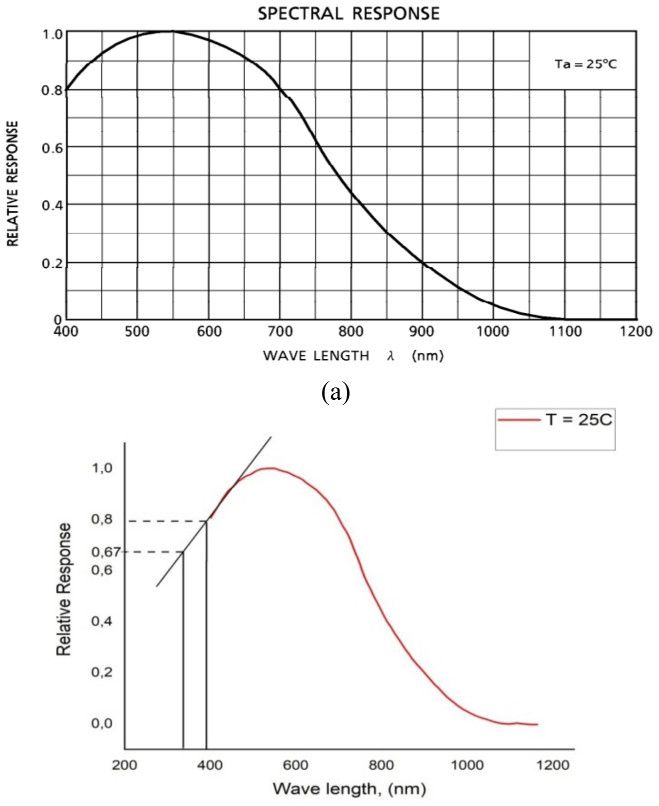

(a)

(б)

Figure 5. (a) the sensitivity of the photodetector from 400 to 1200 nm, (b) estimation of the sensitivity in the range of 300–400 nm using the extrapolation of the graph

As mentioned above, the BOLSIG + program was used to solve the Boltzmann equation for electrons. The input parameters are the E/n value, the composition of the plasma-forming gas in a percentage, the degree of ionization, the gas temperature, and the overall density of particles. As a result, the solution of the equation gives transport properties, including the reaction rate constants k, which was subsequently used to numerically calculate the ratio of spectral lines. The rate constants for different values of E/n are shown in Table 2. The results of determining the ratios of spectral lines and their dependence on the values of the reduced electric field are shown in Figure 6. Figure 6 shows that the dependence in the range from 400 to 600 Td is linear. This graph can be used as a gradient-level curve and is convenient in that it allows to quickly and visually evaluate the reduced electric field, comparing it with the obtained experimental ratios of spectral lines.

Table 2

Reaction rate constants for different values of reduced electric field

Reduced electric field E/n (Td)	Reaction rate constants(m^3/s)	
	$N_2\left(C^3\Pi_u, \vartheta = 0 \rightarrow B^3\Pi_g, \vartheta = 0\right)$ 11 eV (λ= 337.1 nm)	$N_2^+\left(B^2\sum_u^+, \vartheta = 0 \rightarrow X^2\sum_g^+, \vartheta = 0\right)$ 18,7 eV(λ= 391,4nm)
420	0.2032E-14	0.9336E-16
430	0.2085E-14	0.1014E-15
480	0.2330E-14	0.1465E-15
520	0.2503E-14	0.1886E-15
560	0.2658E-14	0.2658E-14

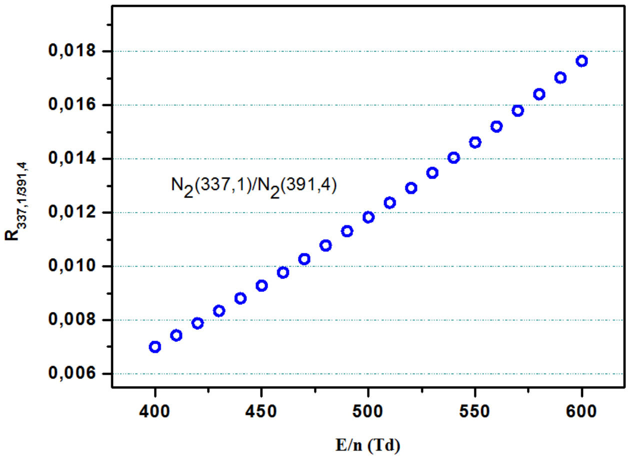

Figure 6. Dependence of the intensity ratio of the spectral lines $N_2^+(391,4)$ and $N_2(337,1)$ on the reduced electric field (E/n)

Further, the above procedure was repeated for different E/n. Figure 7 demonstrates the dependence of the reduced electric field on the discharge power. It is expected that an increase in power leads to an increase in E/n as an increase in power is accompanied by an increase in high-voltage applied to the electrodes of the discharge cell. The obtained values of E/n for air plasma in a surface barrier discharge are in agreement with the results of other related works [17,18] where the investigated plasma and discharge geometry, conditions are quite similar.

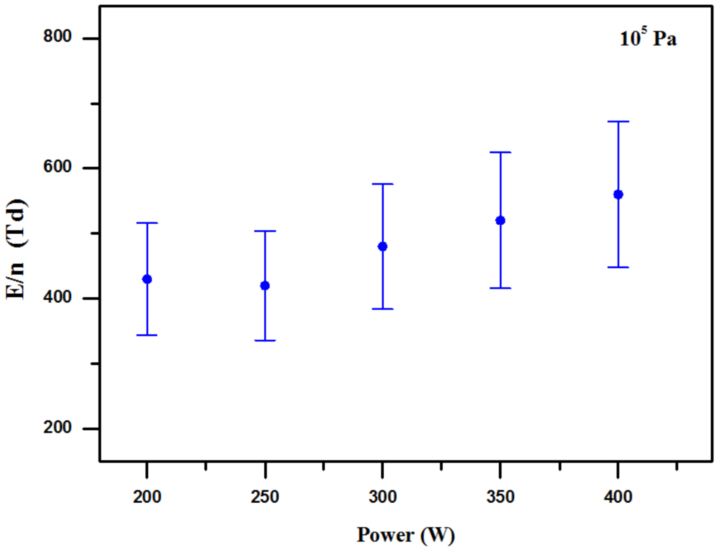

Figure 7. Dependence of the reduced electric field on the discharge power

EEDF is important for studying the various properties of the plasma, since it is necessary for characterization of kinetic processes with the participation of electrons [19]. The EEDF obtained for different values of the reduced electric field shows an increase in the energy and also in the number of fast electrons at the tail of the distribution (Fig. 8). At the same time, the number of low-energy electrons decreases slightly. The increase in the electron energy can be explained by the fact that the increase in E/n makes an additional contribution to the kinetic energy of the electrons, since the electrons mainly gain the energy due to the electric field, accelerating by the Coulomb forces in the gaseous medium. In our case, an increase in E/n means a direct increase in the electric field, since the pressure of the plasma-forming gas remains constant at room conditions. A slight decrease in the number of low-energy electrons is due to the fact that their energy also increases and they contribute to the number of high energy electrons on the tail of the EEDF.

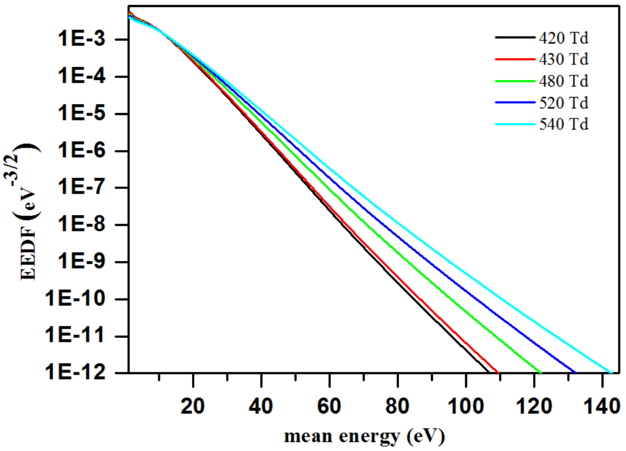

Figure 8. The electron energy distribution function at different values of the reduced electric field

In addition to the EEDF, solving the Boltzmann equation using the BOLSIG + program makes it possible to determine the transport properties of electrons, such as average energy, mobility, diffusion coefficient, and Townsend coefficient, the results of which are shown in Table 3.

Table 3

Transport coefficients for different values of the power

Power (W)	Mean energy (eV)	Mobility*N $((m*V*s)^{-1})$	Diffusion coefficient $((m*s)^{-1})$	Townsend coefficient α (m^{-1})
200	8.962	0.8318E+24	0.5339E+25	0.4318E-20
250	9.098	0.8264E+24	0.8264E+241	0.4535E-20
300	9.643	0.8067E+24	0.5562E+25	0.5427E-20
350	10.18	0.7888E+24	0.5732E+25	0.6345E-20
400	10.71	0.7722E+24	0.5894E+25	0.7279E-20

The quantitative values of these parameters allows to correctly model and calculate various kinetic properties of a gas-discharge plasma at atmospheric pressure by different numerical simulation methods.

Conclusion

A method for the determination of the reduced electric field (E/n) of diffuse surface dielectric barrier discharge plasma by emission spectra was demonstrated. The method is based on the experimental measurement of the intensity ratio of nitrogen spectral lines and the solution of the Boltzmann equation. The experiments were carried out at different applied powers from 200 W to 400 W with a step of 50 W. The dependence of the line intensity ratio on E/n was obtained, and the main transport properties of electrons and EEDF, which are necessary for numerical simulation of plasma properties, were calculated. The dependence of E/n on the applied discharge power was plotted. The obtained experimental data might be useful for the study of kinetic processes of DCSBD plasma.

Acknowledgment: This work was supported by a grant AP08052056 from the Science Committee of the Ministry of Education and Science of the Republic of Kazakhstan.

References

1 Brandenburg R. Dielectric barrier discharges: Progress on plasma sources and on the understanding of regimes and single filaments / R.Brandenburg // Plasma Sources Sci. Technol. — 2017. — Vol. 26(5). — P. 3001. DOI: 10.1088/1361–6595/AA6426

2 Akishev Y.S. Role of the volume and surface breakdown in a formation of microdischarges in a steady-state DBD / Y.S. Akishev, G. Aponin, A. Balakirev, M. Grushin, V. Karalnik, N. Trushkin // Eur. Phys. J. D. — 2011. –Vol. 61(2). — P. 421–429. DOI: 10.1140/epjd/e2010–10219–7

3 Usenov E.A. The Memory Effect of Microdischarges in the Barrier Discharge in Airflow / E.A. Usenov, Yu.S. Akishev, A.V. Petryakov, T.S. Ramazanov, M.T. Gabdullin & A. Ashirbek // Plasma Phys. Reports. — 2020. — Vol. 46(4). — P. 459–464. DOI: 10.1134/S1063780X20040145

4 Penkov O. A review of recent applications of atmospheric pressure plasma jets for materials processing / O. Penkov, M. Khadem, Won Suk Lim, Dae-Eun Kim // Journal of Coatings Technology and Research. — 2015. — Vol. 12(1). — P. 225–235. DOI: 10.1007/s11998–014–9638-z

5 Ussenov Y.A. Dust Particle Synthesis by the Combined Plasma Source at Atmospheric Pressure / Y.A. Ussenov, A.S. Pazyl, M.K. Dosbolayev, M.T. Gabdullin, T.T. Daniyarov, T.S. Ramazanov // Plasma Sci. Institute of Electrical and Electronics Engineers Inc. — 2019. — Vol. 47(8). — P. 4159–4164. DOI: 10.1109/TPS.2019.2927843

6 Ussenov Y.A. Particle formation during deposition of SiOx nanostructured thin films by atmospheric pressure plasma jet / Y.A. Ussenov, L. Hansen, T. Krueger, T.S. Ramazanov, H. Kersten // Jpn. J. Appl. Phys.– 2020. –Vol. 59(3). — P. 14–23. DOI: 10.35848/1347–4065/ab72ca

7 Xu X. Dielectric Barrier Discharge-Properties and Applications / X. Xu // Thin Solid Films. — 2001. — Vol. 390(1–2). — P. 237–242. DOI: 10.1016/S0040–6090(01)00956–7

8 Carbone E. Thomson scattering on non-equilibrium low density plasmas: Principles, practice and challenges / E. Carbone, S. Nijdam // Plasma Phys. Control. Fusion. IOP Publishing. — 2015. — Vol. 57(1). — P. 014–026. DOI: 1088/0741–3335/57/1/014026

9 Sretenovic' G.B. Thomson scattering on non-equilibrium low density plasmas: Principles, practice and challengesc / G.B. Sretenovic', I.B. Krstic', V.V. Kovacˇevic´, B.M. Obradovic´, M.M. Kuraica // Appl. Phys. Lett. — 2011. — Vol. 99(1). — P. 161502–1. DOI: 10.1063/1.3653474

10 Ramanujam N. Fluorescence spectroscopy of neoplastic and non-neoplastic tissues / N. Ramanujam // Neoplasia. Neoplasia Press, Inc. — 2000. — Vol. 2(1–2). — P. 89–117. DOI: 10.1038/sj.neo.7900077

11 Hagelaar G.J.M. Solving the Boltzmann equation to obtain electron transport coefficients and rate coefficients for fluid models / G.J.M. Hagelaar, L.C. Pitchford // Plasma Sources Sci. Technol. — 2005. — Vol. 14(4). — P. 722–733. DOI: 10.1088/0963–0252/14/4/011

12 Акильдинова А.К. Электрические и оптические свойства диэлектрического копланарного поверхностного разряда / А.К. Акильдинова, Е.А. Усенов, А.С. Пазыл, М.Т. Габдуллин, М.К. Досболаев, Т.С. Рамазанов, Т.Т. Данияров // Вестн. Казах. нац. ун-та. Сер. физ. — 2018. — № 2 (65). — С. 58–65.

13 Kozlov K.V. Spatio-temporally resolved spectroscopic diagnostics of the barrier discharge in air at atmospheric pressure / K.V. Kozlov, H-E. Wagner, R. Brandenburg, P.Michel // J. Phys. D. Appl. Phys. — 2001. — Vol. 34(21). — P. 3164–3176. DOI: 10.1088/0022–3727/34/21/309

14 Hagelaar G.J.M. Brief documentation of BOLSIG + version 03 [Electronic resource] / G.J.M. Hagelaar. — Access mode: http://www.bolsig.laplace.univ-tlse.fr/wp-content/uploads/2016/03/bolsigdoc0316.pdf– 2016.

15 Korbut A.N. Emission properties of an atmospheric-pressure helium plasma jet generated by a barrier discharge / A.N. Korbut, V.A. Kelman, Yu.V.Zhmenyak, M.S. Klenovskii // Opt. Spectrosc. — 2014. — Vol. 116(6). — P. 919–925. DOI: 10.1134/S0030400X14040146

16 Berlich R. Spatially resolved measurement of femtosecond laser induced refractive index changes in transparent materials / R.Berlich, J.Choi, C.Mazuir, W.V. Schoenfeld, S.Nolte, M. Richardson // Opt. Lett. — 2012. — Vol. 37(14). — P. 3003–3005. DOI: 10.1364/OL.37.003003

17 Starikovskaia S.M. On electric field measurements in surface dielectric barrier discharge / S.M. Starikovskaia, K. Allegraud, O. Guaitella, A. Rousseau // J. Phys. D. Appl. Phys. — 2010. — Vol. 43(12). — P. 124007–1. DOI: 10.1088/0022–3727/43/12/124007

18 Roupassov D.V. Flow separation control by plasma actuator with nanosecond pulsed-periodic discharge / D.V. Roupassov, A.A. Nikipelov, M.M. Nudnova, A.Yu. Starikovskii // AIAA J. — 2009. — Vol. 47(1). — P. 168–185. DOI: 10.2514/1.38113

19 Takahashi K. Electron energy distribution of a current-free double layer: Druyvesteyn theory and experiments / K. Takahashi, C. Charles, R.W. Boswell, T. Fujiwara // Phys. Rev. Lett. — 2011. — Vol. 107(3). — P. 1–4. DOI: 10.1103/PhysRevLett.107.035002

А.А. Муталип, Е.А. Усенов, А.К. Акильдинова,
М.Қ. Досболаев, М.Т. Габдуллин, Т.С. Рамазанов

Диэлектрлік беттік тосқауылдық разрядтағы плазманың меншікті электр өрісін анықтау

Мақалада атмосфералық қысымдағы диэлектрлік копланарлық беттік тосқауылдық разрядтағы (ДКБТР) меншікті электр өрісін (E/n) эксперименттік түрде анықтау көрсетілген. Плазма мен экспериментaлдық қондырғының параметрлері сипатталған және плазманың оптикалық эмиссиялық спектрі алынды. Оптикалық эмиссиялық спектроскопияның нәтижелері ДКБТР сәулелену спектрінде молекулалық азот жолақтарының болуын көрсетті, атап айтқанда, екінші оң және бірінші теріс жүйелері, сонымен қатар интенсивтілігі төмен OH және NO спектрлік сызықтар жүйесі. Электрондардың негізгі тасымалдық қасиеттері ретінде қозғалғыштық, орташа энергия, диффузия коэффициенті BOLSIG+ ашық бағдарламалық жасақтамасын қолдана отырып есептелді. Меншікті электр өрісінің азоттың спектрлік сызықтарының интенсивтілігінің арақатынасына тәуелділігі, қуаттың және электрондар энергиясының таралу функциясының (ЭЭТФ) E/n-ге тәуелділігі анықталды. BOLSIG+ бағдарламасында меншікті электр өрісін анықтау және спектрлік сызықтардың интенсивтілігін өлшеу алгоритмі блок-схема түрінде көрсетілген. Пайдаланылған әдіс оңайлығымен, қолжетімділігімен және әмбебаптығымен ерекшеленген.

Кілт сөздер: плазма, диэлектрлік барьерлік разряд, спектроскопия, меншікті электр өрісі, сызықтар интенсивтілігі, азот спектрі, Больцман теңдеуі.

А.А. Муталип, Е.А. Усенов, А.К. Акильдинова,
М.Қ. Досболаев, М.Т. Габдуллин, Т.С. Рамазанов

Определение приведенного электрического поля в плазме диэлектрического поверхностного барьерного разряда

В статье продемонстрировано экспериментальное определение приведенного электрического поля (E/n) диэлектрического копланарного поверхностного барьерного разряда (ДКПБР) при атмосферном давлении. Описаны характеристики плазмы и экспериментальной установки, был получен оптический эмиссионный спектр плазмы. Результаты оптико-эмиссионной спектроскопии показали наличие в спектре излучения ДКПБР молекулярных полос азота, а именно второй положительной и первой отрицательной систем, а также линии OH и NO с низкой интенсивностью. Были рассчитаны основные транспортные свойства электронов, такие как подвижность, средняя энергия, коэффициент диффузии, с помощью открытого программного пакета BOLSIG+. Были получены зависимости соотношения интенсивностей спектральных линий азота от приведенного электрического поля от мощности, функции распределения энергии электронов (ФРЭЭ) от приведенного электрического поля. Представлен алгоритм действий для определения приведенного электрического поля в программе BOLSIG+ и экспериментального измерения интенсивности спектральных линий в виде блок-схемы. Использованный метод отличался достаточной простотой, доступностью и универсальностью.

Ключевые слова: плазма, диэлектрический барьерный разряд, спектроскопия, приведенное электрическое поле, интенсивность линий, спектр азота, уравнение Больцмана.

References

1 Brandenburg, R. (2017). Dielectric barrier discharges: Progress on plasma sources and on the understanding of regimes and single filaments. *Plasma Sources Sci. Technol., 26(5),* P. 3001–1.

2 Akishev, Y.S., Aponin, G., Balakirev, A., Grushin, M., Karalnik, V., & Trushkin, N. (2011). Role of the volume and surface breakdown in a formation of microdischarges in a steady-state DBD. *Eur. Phys. J. D., 61(2),* 421–429.

3 Usenov, E.A., Akishev, Yu. S., Petryakov, A.V., Ramazanov, T.S., Gabdullin, M.T., & Ashirbek A. (2020). The Memory Effect of Microdischarges in the Barrier Discharge in Airflow. *Plasma Phys. Reports, 46(4),* 459–464.

4 Penkov, O., Khadem, M., Won Suk Lim & Dae-Eun Kim (2015). A review of recent applications of atmospheric pressure plasma jets for materials processing. *Journal of Coatings Technology and Research, 12(1),* 225–235.

5 Ussenov, Y.A., Pazyl, A.S., Dosbolayev, M.K., Gabdullin, M.T., Daniyarov, T.T., & Ramazanov, T.S. (2019). Dust Particle Synthesis by the Combined Plasma Source at Atmospheric Pressure. *Plasma Sci. Institute of Electrical and Electronics Engineers Inc.,* 47(8), 4159–4164.

6 Ussenov, Y.A., Hansen, L., Krueger, T., Ramazanov, T.S., & Kersten, H. (2020). Particle formation during deposition of SiOx nanostructured thin films by atmospheric pressure plasma jet. *Jpn. J. Appl. Phys.,* 59(3), 14–23.

7 Xu, X. (2001). Dielectric Barrier Discharge-Properties and Applications. *Thin Solid Films,* 390(1–2), 237–242.

8 CarboneE.&NijdamS. (2015). Thomson scattering on non-equilibrium low density plasmas: Principles, practice and challenges. *Plasma Phys. Control. Fusion. IOP Publishing,* 57(1), 014–026.

9 Sretenovic', G.B., Krstic', I.B., Kovacˇevic´, V.V., Obradovic, B.M. & Kuraica, M.M. (2011). Spectroscopic measurement of electric field in atmospheric-pressure plasma jet operating in bullet mode. *Appl. Phys. Lett.,* 99(1), 161502–1.

10 Ramanujam, N. (2000). Fluorescence spectroscopy of neoplastic and non-neoplastic tissues. *Neoplasia. Neoplasia Press, Inc.,* 2(1–2), 89–117.

11 Hagelaar, G.J.M. & Pitchford, L.C. (2005). Solving the Boltzmann equation to obtain electron transport coefficients and rate coefficients for fluid models. *Plasma Sources Sci. Technol.,* 14(4), 722–733.

12 Akildinova, A.K., Ussenov, Y.A., Pazyl, A.S., Gabdullin, M.T., Dosbolayev, M.K., Ramazanov, T.S., & Daniyarov, T.T. (2018). Electricheskie i opticheskie svoistva dielektricheskogo koplanarnogo poverkhnostnogo razriada [Electrical and optical properties of diffuse coplanar surface barrier discharge]. *Vestnik Kazakhskoho natsionalnogo universiteta. Seriia fizicheskaia, 2(65),* 58–65 [in Russian].

13 Kozlov, K.V., Wagner, H-E., Brandenburg, R. & Michel, P. (2001). Spatio-temporally resolved spectroscopic diagnostics of the barrier discharge in air at atmospheric pressure. *J. Phys. D. Appl. Phys.,* 34(21), 3164–3176.

14 Hagelaar, G.J.M. (2016). Brief documentation of BOLSIG + version 03. *bolsig.laplace.univ-tlse.fr.* Retrived from http://www.bolsig.laplace.univ-tlse.fr/wp-content/uploads/2016/03/bolsigdoc0316.pdf

15 Korbut, A.N., Kelman, V.A.,.Zhmenyak, Yu.V., & Klenovskii, M.S. (2014). Emission properties of an atmospheric-pressure helium plasma jet generated by a barrier discharge. *Opt. Spectrosc.,* 116(6), 919–925.

16 Berlich, R., Choi, J., Mazuir, C., Schoenfeld, W.V., Nolte, S., & Richardson, M. (2012). Spatially resolved measurement of femtosecond laser induced refractive index changes in transparent materials. *Opt. Lett.,* 37(14), 3003–3005.

17 Starikovskaia, S.M., Allegraud, K., Guaitella, O. & Rousseau, A. (2010). On electric field measurements in surface dielectric barrier discharge. *J. Phys. D. Appl. Phys.,*43(12), 124007–1.

18 Roupassov, D.V., NikipelovA.A., Nudnova, M.M. &Starikovskii, A.Yu. (2009). Flow separation control by plasma actuator with nanosecond pulsed-periodic discharge. *AIAA J.,* 47(1), 168–185.

19 Takahashi, K., Charles, C., Boswell, R.W. & Fujiwara, T. (2011). Electron energy distribution of a current-free double layer: Druyvesteyn theory and experiments. *Phys. Rev. Lett.,* 107(3), 1–4.

DOI 10.31489/2021Ph3/45-51
UDC 66.088

M.K. Kylyshkanov[1,2], K.A. Shestakov[1], Zh.B. Sagdoldina[2],
B.K. Rakhadilov[2], A.B. Kengesbekov[2,3*]

[1]JSC "Ulba Metallurgical Plant", Ust-Kamenogorsk, Kazakhstan;
[2]Sarsen Amanzholov EKU, Ust-Kamenogorsk, Kazakhstan;
3Institute of Composite Materials, Ust-Kamenogorsk, Kazakhstan
*(*e-mail: aidar.94.01@mail.ru)*

Processing of industrial waste by plasma-chemical method

In this paper the results of the processing of magnesium fluoride by plasma-chemical method to obtain periclase and a solution of hydrogen fluoride (hydrofluoric acid) were presented. For the industrial implementation of plasma technologies it is necessary to study the main parameters of plasma processes for obtaining reducing gases and processing metal oxides with them, to solve the issues of their hardware design, to increase the service life of plasma torches for their use in continuous metallurgical processes. The purpose of this work was to determine the conditions for the plasma-chemical process of processing magnesium fluoride. Thermal analysis of magnesium fluoride on a TGA/DSC2 thermogravimetric analyzer was performed. Thermogravimetric analysis showed that in the temperature range under consideration the process is endothermic, and at a temperature of ~1280 °C a phase transition of the 1st kind is observed due to the melting of magnesium fluoride. The fractional composition of MgF_2 and MgO powders was studied using the Analysette-22 Nanotech laser diffraction analyzer. The results of the evaluation of the fractional composition of powders have a significant difference. At the same time, the convergence of the data obtained using laser diffraction and electron microscopy methods was found.

Keywords: industrial waste processing, plasma chemistry, magnesium fluoride, magnesium oxide, thermogravimetric analysis, granulometric composition.

Introduction

In plasma metallurgy the processing of ores (oxides, etc.) is carried out by their thermal decomposition in plasma. A reducing agent (carbon, hydrogen, methane, etc.) or a sharp cooling of the plasma flow that violates the thermodynamic equilibrium is used to prevent reverse reactions. Plasma metallurgy allows for direct reduction of metal from ore, significantly accelerate metallurgical processes, obtain clean materials, and reduce fuel consumption (reducing agent) [1, 2]. The disadvantage of plasma metallurgy is the high consumption of electricity used to generate plasma. However, the use of low-temperature plasma makes it possible to comprehensively solve the problems of metallurgy and energy and significantly improve the environmental situation in industrial areas through the use of gaseous energy fuels and reducing agents used in blast furnace smelting and metallurgy processes. In the future the role of plasma chemical technologies will increase and will be quite profitable in industrial applications. Having a high reduction potential, plasma gases can provide elective processing of slurries of the main metallurgical processing processes, containing, in particular, non-ferrous and rare metals. Thus, the use of plasma can solve the problems of creating waste-free technologies and the shortage of raw materials in non-ferrous metallurgy [3, 4].

Beryllium is obtained by reducing beryllium fluoride with magnesium according to the technological scheme in JSC "Ulba Metallurgical Plant". In this case, the follaving reaction is carried out: $BeF_2+Mg\rightarrow MgF_2+Be$. The requirements for beryllium for use in the nuclear industry in terms of the content of impurities are of fundamental importance [5]. Beryllium fluoride BeF_2 must be of high purity, since the impurities are practically not removed during the reduction process. When conducting a reaction with a stoichiometric component ratio it is not possible to obtain a good separation of the reaction products, so a significant excess of BeF_2 is usually introduced into the charge. Good results are achieved when administered in a mixture of magnesium in an amount of only 75 % stoichiometric. Excess BeF_2 makes the slag more fusible and fluid, dissolves BeO, reduces the equilibrium amount of magnesium in the reaction mixture, and partially binds MgF_2 with magnesium fluoride. To remove slag, magnesium and intermetallic impurities from magnesium-thermal beryllium, it is subjected to vacuum melting in induction furnaces in crucibles made of beryllium oxide at a rarefaction of 133–267 Pa and a temperature of 1500–550 °C. In this case, free magnesium and beryllium fluoride evaporate, and non-volatile impurities MgF_2, VeO, Ve_2C, etc. in the form of slag float to the surface of the melt or settle to the bottom of the crucible. After this operation, the MgF_2 is filtered, washed, and sent to the dump. Thus, there is an urgent task of processing the waste of magnesium fluoride formed at beryllium production in the process of magnesium thermal reduction of beryllium fluoride and the sale of magnesium fluoride as a commercial product.

The authors of the work carry out experimental work on the processing of magnesium fluoride by a plasma-chemical method, by exposure to steam plasma to produce periclase (MgO) and capture gaseous products and to obtain a solution of hydrogen fluoride (hydrofluoric acid). For the industrial implementation of plasma technologies, it is necessary to study the main parameters of plasma processes for producing reducing gases and treating metal oxides with them, to evaluate the economic efficiency of plasma-metallurgical processes, to solve the issues of their hardware design, to increase the service life of plasma torches for their use in continuous metallurgical processes.

Experimental part

Experimental-industrial plasma-chemical plant for processing industrial waste was created on the basis of JSC “Ulba Metallurgical Plant”. In the process of plasma-chemical decomposition of magnesium fluoride by ionized water vapor with the formation of solid magnesium oxide, a large amount of hydrogen fluoride gas is released, the workplace must be equipped with exhaust ventilation. Effective protection of personnel requires a set of sanitary measures: from personal respiratory protection to extensive measures to prevent air pollution. In addition, the operation of the plasma torch is accompanied by a strong whistling sound and a very bright flame of the torch. Therefore, when working a gas mask, a welding light filter and anti-noise headphones are used. Prevention of environmental air pollution involves the prevention of unorganized air escape from rooms with high pollution, as well as the cleaning of industrial and ventilation emissions.

The installation for studying the process of plasma-chemical decomposition of magnesium fluoride to produce its oxide and hydrogen fluoride consists of a plasma torch, a steam generator, a power source and a reaction chamber. For the operation of the plant, a power source of the DV-1 ore-thermal furnace with an operating voltage of 600 V was used. A plasmatron was developed and created for the plasma chemical process (Fig. 1).

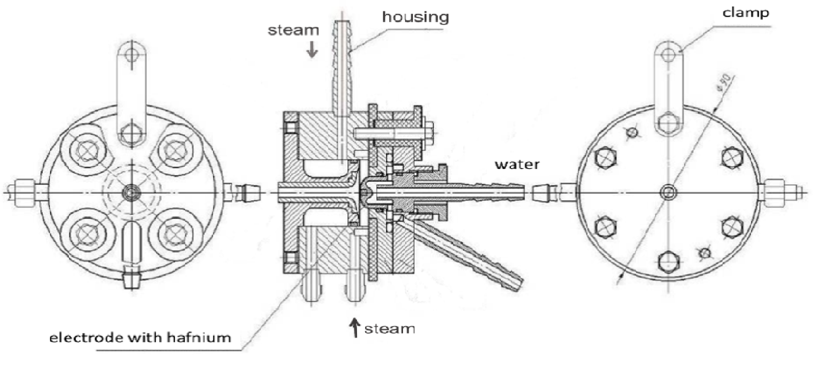

Figure 1. Assembly drawing of the plasma torch

A low-pressure steam generator (up to 2 kgf/cm^2) is manufactured to supply the plasma torch with water vapor, which provides the plasma torch with steam at a temperature of up to 130 °C. During the tests, a coil for superheating steam to temperatures of about 300 °C was additionally included in the design of the installation, which excludes steam condensation in the cooled areas of the plasma torch.

The dimensional characteristics of MgF_2 and MgO powders were studied using the Analysette-22 Nanotech laser diffraction analyzer (Fritsch, Germany). The device allows to determine the particle size distribution in the range of 0.01–2000 microns. The principle of operation is the diffraction of coherent laser radiation on small particles. The samples are dispersed in a liquid medium (in this case, water), and the stability of the colloid is maintained by ultrasonic treatment. Micrographs of the powders were obtained using a scanning electron microscope JSM-5610 (Jeol, Japan).

Thermal analyses were performed on a TGA/DSC2 thermogravimetric analyzer (METTLER TOLEDO, Switzerland) [6]. The sensitivity of the balance is 0.1 micrograms over the entire measurement range. The sample weight was 88.366 mg. The sensitivity of the scales is 0.1 micrograms. The experiments were carried out in the temperature range of 20-1300 °C, in the atmospheric air current, at a heating rate of 10 ° per min in corundum and platinum crucibles. The phase transition heats were calculated as the area under the measured peak according to ISO 11357–1 DIN 51007.

Research results

The research resultsof the dimensional characteristics of MgF_2 and MgO powders are shown in Figures 2 and 3: each point of the integral curve Q3(x) shows how many percent of the particles have a size less than or equal to this one; each point of the histogram dQ3 (x) shows the number of particles in percent with this size. Table 1 shows the results of the study of the size distribution of microparticles.

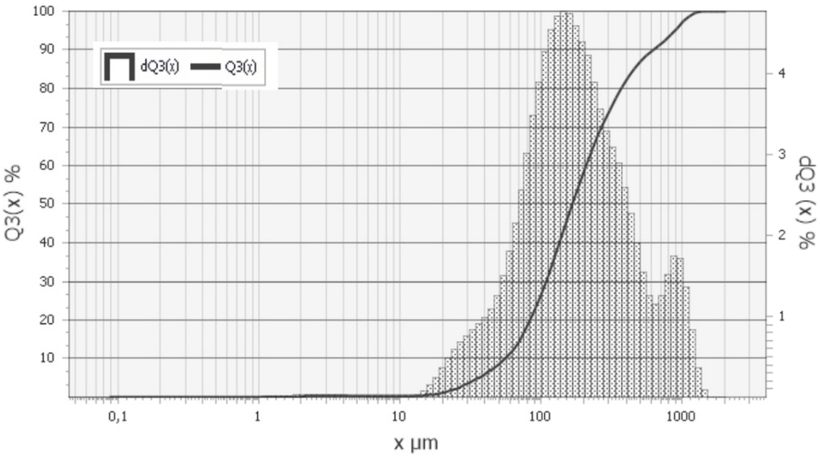

Figure 2. Size distribution of MgF_2 powder microparticles

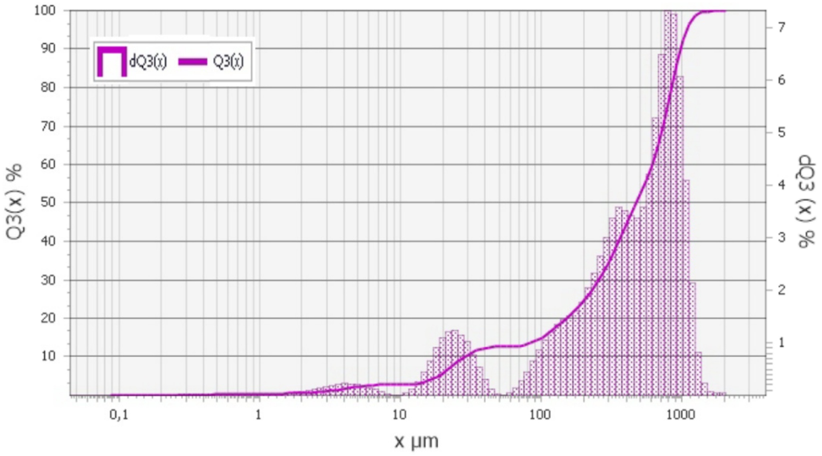

Figure 3. Size distribution of MgO powder microparticles

Table 1

Results of the particle size study

MgF_2		MgO	
Q3(x), %	X, µm	Q3(x), %	X, µm
10	55,1	10	28,5
20	84,2	20	151,4
30	109,2	30	256,8
40	135,7	40	353,6
50	167,2	50	470,6
60	208,7	60	612,1
70	269,1	70	727,8
80	368,8	80	835,9
90	617	90	968,3

As can be seen from Table 1 and Figure 3, the size distribution of MgO particles has a polymodal distribution and contains large agglomerates (Fig. 4 b, d). The obtained data coincide with the results obtained using electron microscopy (Fig. 4). It is worth noting that in the method of processing solid waste particles suspended in the plasma stream, an important parameter is the particle size of the initial substance (in our case, MgF_2), which is fed to the plasma in the form of a powder. The following processes take place in the plasma flow: heating of raw material particles to a high temperature, their melting, evaporation, chemical reactions, formation of product particles, cooling. However, there is a possibility of heterogeneous interaction of solid and liquid particles of the feedstock with the plasma, leading to the appearance of larger particles. The product may contain impurities of the starting metals and the reducing agent. This is the main disadvantage of the plasma-chemical method — a wide particle size distribution and low selectivity of the process [7]. As can be seen from Figure 2, the size distribution of MgF_2 particles is monomodal. This particle distribution does not contribute to the dense packing of the particles in the process of making MgF_2 briquettes, since the voids between the particles are filled with a binder. To solve this problem a method for manufacturing MgF_2 briquettes is being developed to improve the homogeneity of the chemical process in the plasma in the future.

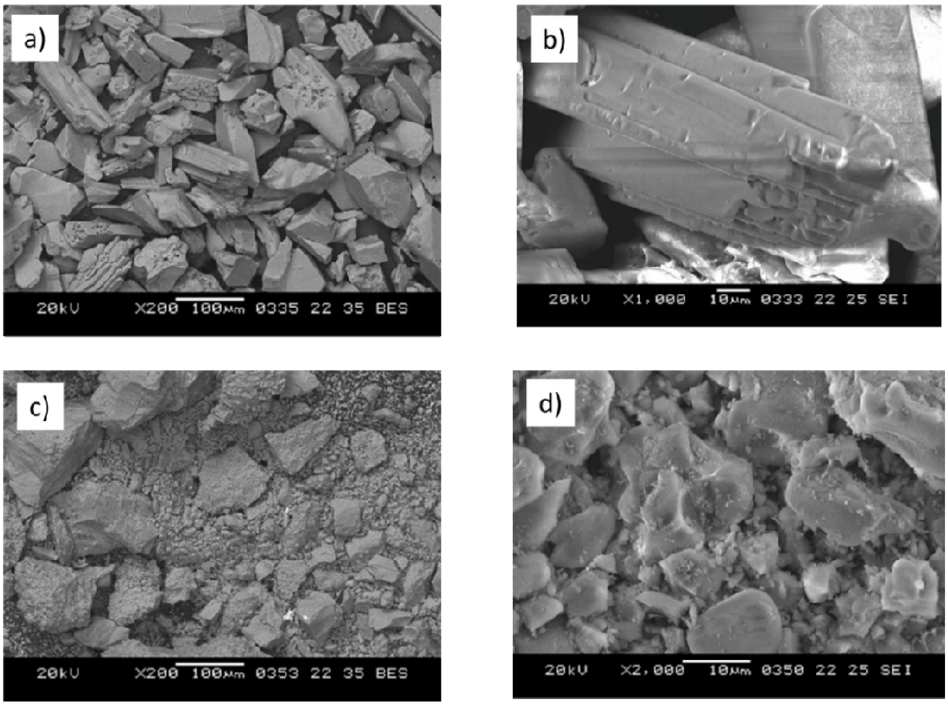

Figure 4. SEM image of powders and detailed analysis: a) and b) MgF_2; c) and d) MgO

The vapor-water plasma, depending on the temperature, consists of hydrogen, oxygen and their derivatives H, O, OH, H+, O+, O++, and electrons. This composition of steam-water plasma determines its redox character and high environmental friendliness during various plasma chemical processes. Strong intraatomic bonds, due to the small size of the hydrogen atom, determine the highest values of the enthalpy in the steam-water plasma. For example, its enthalpy at 5000 K is 7.25 times greater than the enthalpy of air with the same temperature. This determines the high rate of thermal interaction with other technological components involved in the plasma chemical process, compared to other plasmas. In addition, the steam-water plasma does not contain in its composition ballast components such as nitrogen in the air plasma, which means that the plasma chemical reactions are carried out with the highest possible thermal efficiency. The operating temperature in the low-temperature plasma jet is 5000 °C or more, which makes it possible to implement a large number of high-temperature metallurgical processes. To assess the possibility of their implementation, first of all, it is necessary to perform a thermogravimetric analysis of magnesium fluoride (Fig. 5).

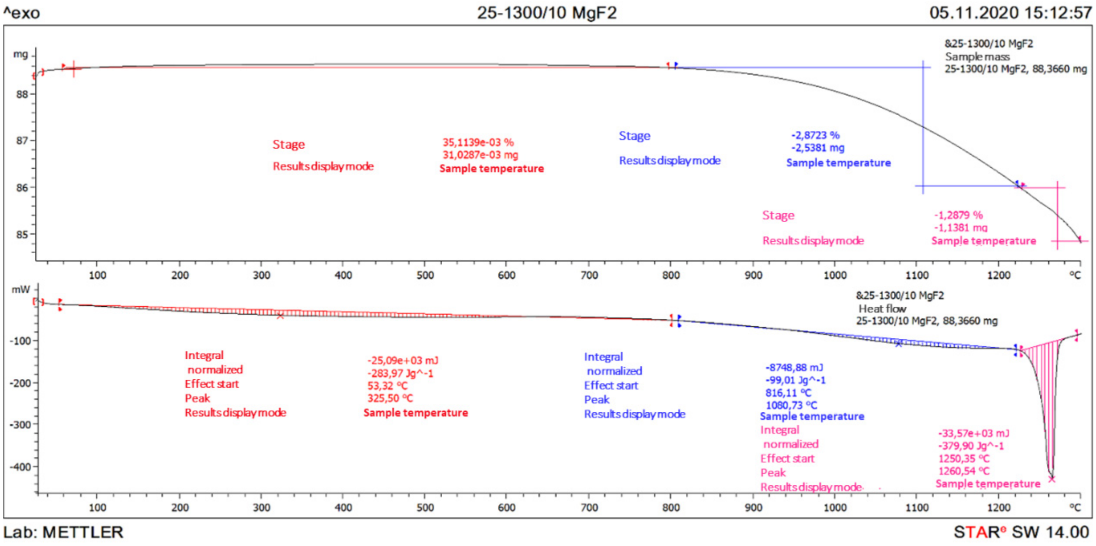

Figure 5. Results of thermogravimetric analysis of magnesium fluoride MgF_2

The thermogravimetric analysis of magnesium fluoride showed that the sample is practically stable when heated to 1080.73 °C. A small gain of 0.035 % can be attributed to the oxidation of magnesium fluoride when heated to 325.5 °C. The sample combustion process starts at 1080.73 °C and ends at 1260 °C. The endothermic effect at 1260.54 °C and the mass loss are associated with the melting of magnesium fluoride.

Conclusion

A pilot plasma chemical plant for processing industrial waste has been created. The installation for studying the process of plasma-chemical decomposition of magnesium fluoride to produce its oxide and hydrogen fluoride consists of a plasma torch, a steam generator, a power source and a reaction chamber. Aplasmatron was developed and created for the plasma chemical process. The condition of the plasma-chemical process of processing magnesium fluoride is determined. Thermogravimetric analysis has shown that the process temperature range under consideration is endothermic, i.e., its implementation requires an external heat supply, and the combustion process of magnesium fluoride begins at 1080.73 °C and ends at 1260 °C. On the basis of the conducted experimental studies aimed at studying the granulometric composition of the initial MgF_2 powder, it was found that the particle size distribution has a monomodal character and contains large agglomerates. This can lead to incomplete recycling of magnesium fluoride waste into magnesium oxide of low-temperature and high-temperature modifications.

Acknowledgments

This paper was performed within the grant financing of scientific research of the Committee of Science of the Ministry of Education and Science of the Republic of Kazakhstan. Grant AP08857800.

References

1 Ларин В.К. Плазмохимический способ получения ультрадисперсных (нано-) порошков оксидов металлов и перспективные направления их применения / В.К. Ларин, В.М. Кондаков, Е.Н. Малый, В.А. Матюха, Н.В. Дедов, Э.М. Кутявин, Ю.Н. Сенников, И.А. Степанов, Ю.Ф. Иванов // Изв. вузов. Цветная металлургия. — 2003. — № 8. — С. 59–64.

2 Пархоменко В.Д. Плазмохимическая технология / В.Д. Пархоменко, П.И. Сорока, Ю.И. Краснокутский, П.Н. Цыбулев, В.Г. Верещак, А.И. Максимов, А.Л. Моссэ, А.Б. Амбразявичус. — Новосибирск: Наука. Сибир. отд., 1991. — Т. 4.– 392 с.

3 Rakhadilov B.K. Development of air-plasma technology for hardening cutting tools by applying wear-resistant coatings / B.K. Rakhadilov, A.B. Kenesbekov, P. Kowalevski, Y.A. Ocheredko, Zh.B. Sagdoldina // News of the National Academy of Sciences of the Republic of Kazakhstan, Series of Geology and Technical Sciences. — 2020. — Vol. 3(441). — P. 54–62.

4 Rakhadilov B. K.Preparation of powder coatings on the surface of steel balls by mechanochemical synthesis / B.K. Rakhadilov, D.B. Buitkenov, Zh.B.Sagdoldina, L.G. Zhurerova, W.Wieleba // Bulletin of the university of Karaganda-Physics. — 2020. — Vol. 4(100). — P. 8–13.

5 Тихинский Г.Ф. Получение редких и тугоплавких материалов особой чистоты / Г.Ф. Тихинский, В.М. Ажажа, Г.П. Ковтун, В.А. Еленский // Вопросы атомной науки и техники. Сер. Вакуум, чистые материалы, сверхпроводники. — 1998. — Вып. 1(2). — С. 49.

6 Gallagher P.K. Thermomagnetometry / P.K. Gallagher // J. Therm. Anal. Calorim. — 1997. — Vol. 49(1). — P. 33–44.

7 Крапивина С.А. Плазмохимические технологические процессы / С.А. Крапивина. — Л.: Химия, 1981. — 247 с.

М.К. Кылышканов, К.А. Шестаков, Ж.Б. Сагдолдина, Б.К. Рахадилов, А.Б. Кенесбеков

Өндірістік қалдықтарды плазмохимиялық әдіспен өңдеу

Мақалада периклаз және фторлы сутегі (плавик қышқылы) ерітіндісін алу мақсатында магний фторидін плазмохимиялық тәсілмен қайта өңдеу бойынша нәтижелер ұсынылды. Плазмалық технологияларды өнеркәсіптік іске асыру үшін қалпына келтіру газдарын алудың және олармен металл оксидтерін өңдеудің плазмалық процестерінің негізгі параметрлерін зерттеу, оларды аппаратуралық ресімдеу, үздіксіз металлургиялық процестерде қолдану үшін плазмотрондардың жұмыс ресурсын арттыру мәселелерін шешу қажет. Бұл жұмыстың мақсаты магний фторидін өңдеудің плазмохимиялық процесінің шарттарын анықтау. Магний фторидіне термиялық талдау TGA/DSC2 термогравиметриялық анализаторында жүргізілді. Термогравиметриялық талдау қарастырылып отырған температура диапазонында процесс эндотермиялық және ~1280 С температурада магний фторидінің еруіне байланысты 1-ші типтегі фазалық ауысу бар екенін көрсетті. MgF_2 және MgO ұнтақтарының фракциялық құрамы Analysette-22 Nanotech лазерлік дифракциялық анализаторында зерттелген. Ұнтақтардың фракциялық құрамын бағалау нәтижелері айтарлықтай айырмашылыққа ие. Бұл жағдайда лазерлік дифракция және электронды микроскопия әдістерін қолдану арқылы алынған мәліметтердің ұқсастығы анықталды.

Кілт сөздер: өнеркәсіптік қалдықтарды қайта өңдеу, плазмохимия, магний фториді, магний оксиді, термогравиметриялық талдау, гранулометриялық құрам.

М.К. Кылышканов, К.А. Шестаков, Ж.Б. Сагдолдина, Б.К. Рахадилов, А.Б. Кенесбеков

Переработка промышленных отходов плазмохимическим способом

В статье были представлены результаты по переработке фторида магния плазмохимическим способом с целью получения периклаза и раствора фтористого водорода (плавиковой кислоты). Для промышленной реализации плазменных технологий необходимо исследовать основные параметры плазменных процессов получения восстановительных газов и обработки ими оксидов металлов, решить вопросы их аппаратурного оформления, повышения ресурса работы плазмотронов для применения их в непрерывных металлургических процессах. Целью данной работы являлось определение условия проведения плазмохимического процесса переработки фторида магния. Проведен термический анализ фторида магния на термогравиметрическом анализаторе TGA/DSC2, который показал, что в рассматриваемом диапазоне температур процесс является эндотермическим, и при температуре ~1280 ˚С наблюдается фазовый переход 1-го рода, обусловленный плавлением фторида магния. Фракционный состав порошков MgF_2 и MgO исследован на лазерном дифракционном анализаторе Analysette-22 Nanotech. Результаты оценки фракционного состава порошков имеют существенное различие. При этом обнаружена сходимость данных, полученных с использованием методов лазерной дифракции и электронной микроскопии.

Ключевые слова: переработка промышленных отходов, плазмохимия, фторид магния, оксид магния, термогравиметрический анализ, гранулометрический состав.

References

1 Larin, V.K., Kondakov, V.M., Malyy, Ye.N., Matyukha, V.A., Dedov, N.V., Kutyavin, E.M., Sennikov, Yu.N., Stepanov, I.A., & Ivanov, Yu.F. (2003). Plazmokhimicheskii sposob polucheniia ultradispersnykh (nano-) poroshkov oksidov metallov i perspektivnye napravleniia ikh primeneniia [Plasma-chemical method for producing ultrafine (nano-) metal oxide powders and promising areas of their application]. *Izvestiia vuzov. Tsvetnaia metallurgiia — News universities. Non-ferrous metallurgy*, 8, 59–64 [in Russian].

2 Parkhomenko, V.D., Soroka, P.I., Krasnokutski, Yu.I., Tsybulev, P.N., Vereshchak, V.G., Maksimov, A.I., Mosse, A.L., & Ambrazevichus, A.B. (1991). *Plazmokhimicheskaia tekhnologiia [Plasma-chemical technology]*. Novosibirsk: Nauka. Sibirskoe otdelenie [in Russian].

3 Rakhadilov, B.K., Kenesbekov, A.B., Kowalevski, P., Ocheredko, Y.A., & Sagdoldina, Z.B. (2020). Development of air-plasma technology for hardening cutting tools by applying wear-resistant coatings, *News of the National Academy of Sciences of the Republic of Kazakhstan, Series of Geology and Technical Sciences*, 3(441), 54–62.

4 Rakhadilov, B.K., Buitkenov, D.B., Sagdoldina, Zh.B., Zhurerova, L.G., & Wieleba, W. (2020). Preparation of powder coatings on the surface of steel balls by mechanochemical synthesis, *Bulletin of the university of Karaganda-Physics*, 4 (100), 8–13.

5 Tikhinskiy, G.F., Azhazha, V.M., Kovtun, G.P., & Yelenskiy, V.A. (1998). Poluchenie redkikh i tugoplavkikh materialov osoboi chistoty [Production of rare and refractory materials of high purity]. *Voprosy atomnoi nauki i tekhniki. Seriia Vakuum, chistye materialy, sverkhprovodniki — Questions of atomic science and technology. Series Vacuum, pure materials, superconductors,* 1(2), 49 [in Russian].

6 Gallagher, P.K. (1997). Thermomagnetometry. *J. Therm. Anal. Calorim*, 49(1), 33–44.

7 Krapivina, S.A. (1981). *Plazmokhimicheskie tekhnologicheskie protsessy [Plasma chemical technological processes]*. Moscow: Khimiia [in Russian].

DOI 10.31489/2021Ph3/52-59
UDC 533.682

N.K. Tanasheva[1*], A.R. Bakhtybekova[1], L.L. Minkov[2], S.A. Bolegenova[3],
N.N. Shuyushbaeva[4], A.Zh. Tleubergenova[1], B.A. Toktarbaev[4]

[1]Karagandy University of the name of academician E.A. Buketov, Kazakhstan;
[2]National Research Tomsk State University, Russia;
[3]Al Farabi Kazakh National University, Almaty, Kazakhstan;
[4]Sh.Ualikhanov Kokshetau University, Kazakhstan
(E-mail: nazgulya_tans@mail.ru)

Influence of a rough surface on the aerodynamic characteristics of a rotating cylinder

The article considers the influence of the relative roughness of a cylindrical blade on aerodynamic characteristics. It is known that the operation basis of blades under consideration is the Magnus effect, which is characterized by appearance of a lifting force (Magnus force), when the cylinders rotate in a transverse flow. This force is used to rotate the wind wheel, similar to lifting force, but can have a much larger value when selecting optimal conditions, both geometric and aerodynamic. The authors conducted a comparative analysis of cylinder layout with a relative roughness (0.005 ÷ 0.02). Experimental studies of aerodynamics process of rotating cylinders were carried out in the aerodynamic laboratory using the T-1-M wind tunnel at an air flow value of 5 to 15 m/s. Graphs of dependences of rotating cylinder's lifting force and drag force on the changing air flow velocity and on relative roughness, k/d, are obtained. For further study experimental cylinder layout's aerodynamic parameters, the most optimal is the variant with a relative roughness value of 0.02, which had high indicators, was selected. In the course of experimental studies, graphs of the dependence of the values of lift and drag force on the angles of attack of a single rotating cylinder with a rough surface on the speed and angle of attack of the wind flow (0°, 30° and 60°) were obtained. It is established that the effective angle of attack is 0°, at which aerodynamic characteristics's maximum values were obtained.

Keywords: cylinder, aerodynamics, Magnus effect, wind tunnel, relative roughness, angle of attack, lifting force, drag force, air flow.

Introduction

The cylindrical body is classically an integral element of almost all aerohydrodynamic apparatuses and heat exchange devices. In the process of developing a multi-blade wind turbine with power elements in the form of rotating cylinders of variable cross-section at the initial stage, it was necessary to study the aerodynamics of cylinders of constant cross-section [1–3]. In particular, the aerodynamic phenomena and processes that are of interest arise when the cylinder flows transversely and the cylinder rotates simultaneously around its axis [4–9].

The Magnus effect, which was first described in 1853 by the German physicist Heinrich Magnus [10–13], occurs when the air flows around the rotating cylinders. The aerodynamics of a cylindrical blade operating on the basis of the Magnus effect was studied. The influence of the cylindrical blade shape on the Magnus force value is estimated using particle image velocimetry [8].

The two-dimensional transverse flow of a rarefied gas flow around a rotating circular cylinder was studied by means of calculations using the test particle method. A distinctive feature of the work is the identification of mechanisms for changing the sign in the values of the lifting force. The influence of the angular velocity of rotation on the pressure distribution in the cylinder is considered [9].

According to the results of another work, the main parameters of the rotating cylinders influencing the efficiency of the propeller are its speed of rotation and elongation, while at low settings it is the relative speed of rotation of the cylinder, such parameters are the Reynolds number, relative roughness of the cylinder surface and the degree of turbulence [10].

Comparative studies on the torque generated by improving the surface roughness of wind turbine blades based on the Magnus effect were conducted [14, 15]. The results showed that the torque coefficient generated by the sandpaper is 0.079–0.016, which is almost five times the value of the torque coefficient of a cylinder with a smooth surface. An additional advantage is that the roughness of the ground surface significantly increases the performance of the wind turbine up to four times based on the torque, compared to smooth surfaces.

These important data indicates that when using a rough surface it is possible to optimize the aerodynamic parameters of the cylinders as much as possible.

The purpose of this work is to analyze the dependence of the aerodynamic parameters of a cylinder with a rough surface, as well as to determine the optimal value of the angle of attack of the air flow.

Experimental part

The study of the aerodynamic characteristics of the cylinder was carried out on a laboratory stand, which allows to measure the lift and drag force at different values of the cylinder rotation speed [13, 16].

Special nets and devices installed in the channels of the wind tunnel made it possible to ensure a sufficiently uniform air flow in the working part over the entire cross-section. The flow rate varies in the range (5÷15) m/s.

Figure 1 (a, b) shows a sample of a cylinder with a rough surface, as well as a diagram of an experimental setup for studying the aerodynamics of a rotating cylinder in a flow. To conduct experimental studies on the aerodynamics of a rotating cylinder when flowing around the air flow, a model with a rough surface was made. The ram air velocity was measured with a Skywatch Atmos cup anemometer. The drag force and the lift force of the cylinder were measured using an aerodynamic balance. The angle of attack of the cylindrical blades was measured by comparison with rigid control (reference) instruments.

a) Sample of a cylinder with a rough surface

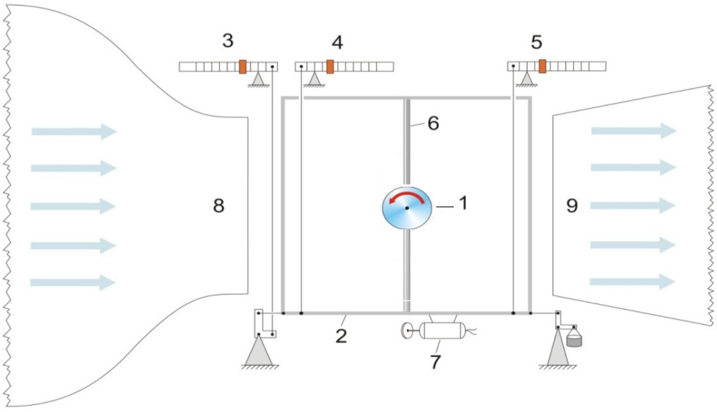

b) Scheme

1 is the study cylinder; 2 is the mounting frame layout with aerodynamics and weights; 3 is the scales that measure the force of drag; 4, 5 is the scales measuring the lift force; 6 is the rack mounting of cylinders; 7 is the motor for rotation of the cylinder; 8, 9 is the confuser and diffuser wind tunnel

Figure 1. Working part of the T-1-M wind tunnel

The diameter of the cylinder layout is 0.15 m, the length is 0.3 m. The manufactured cylinder with a rough surface is driven by a belt drive powered by an autotransformer of a variable-speed electric motor. The cylinder is easy to start, friction is reduced as much as possible due to special lubrication and a high degree of grinding of the axis of rotation and the inner surface of the cylinder.

The geometric scheme and size of the sample of the cylinder under study with spherical ends is shown in Figure 2.

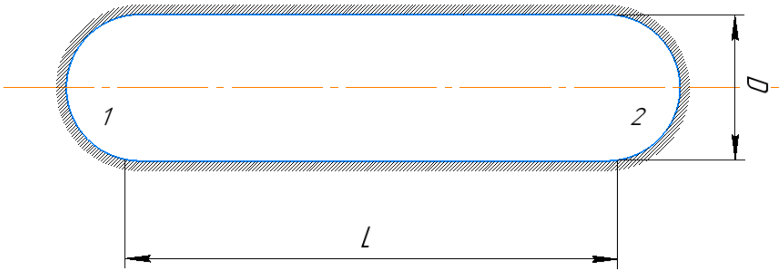

1 — left hemisphere, 2 — right hemisphere, L = 300 mm, D = 150 mm

Figure 2. Geometric diagram of the sample, a rotating cylinder with spherical ends

The value of the relative roughness of the cylinder layout varies from 0.005 to 0.02.

The formula for determining the relative roughness:

$$\bar{k} = \frac{k}{d},$$

where k is the average height of the protrusions of the roughness of the cylinder surface, microns; d is the diameter of the cylinder, m. The roughness distribution over the cylinder surface is uniform. The surface grain density of the rough medium is 100–120 pcs/cm^2.

Results and discussion

Experimental studies of the aerodynamic parameters of a single rotating cylinder with a rough surface under different wind flow regimes and relative roughness values are carried out.

Figure 3 shows a graph of the dependence of the lifting force of a single rotating cylinder on the air flow velocity with relative roughness values of 0.005–0.02.

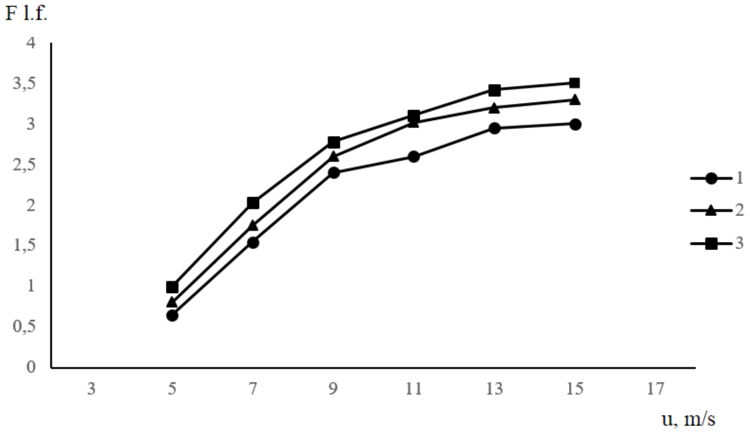

Figure 3. Graph of the dependence of the lifting force of the rotating cylinder on the change in the air flow velocity and on k/d: 1) 0.005, 2) 0.01, 3) 0.02.

As can be seen from Figure 3, with an increase in the value of the relative roughness (surface roughness), the lifting force of the cylinder increases. This is due to the fact that during the rotation of the cylinder with an increase in the relative surface roughness the resulting boundary layer expands.

It is known [17] that the roughness provides a continuous flow around the cylinder, compared to the smooth surface of the cylinder. This is due to the stronger “grip” of the boundary layer with a rough surface than with a smooth one. The rough surface, most effectively captures the air particles moving around the wall area when the cylinder rotates, which in turn creates a rotational air flow, thereby increasing the efficiency of the work.

Figure 4 shows a graph of the dependence of the drag force of a rotating cylinder on changes in the air flow velocity and relative roughness. Hence, it can be concluded that the roughness also has a significant effect on the drag force by forming micro-roughness when flowing around the air flow. In the case of a turbulent boundary layer, the effect of roughness becomes stronger and earlier, the greater the relative roughness of the surface. The drag force of the rough surface will mainly consist of the resistance of the roughness bumps streamlined by the air flow.

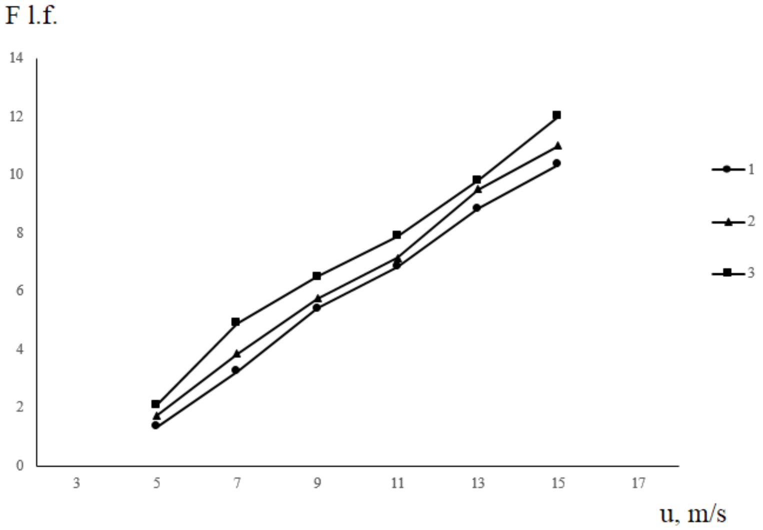

Figure 4. Graph of the dependence of the drag force of a rotating cylinder
on the change in the air flow velocity and on k/d: 1) 0.005, 2) 0.01, 3) 0.02

To further study the aerodynamic parameters of the experimental cylinder layout the most optimal variant with a relative roughness value of 0.02 was selected, which had high indicators.

In the course of research the dependences of the lifting force and drag force of a single rotating cylinder with a rough surface on the speed and angle of attack of the wind flow (0°, 30° and 60°) were obtained, and shown in Figure 5 (a, b, c).

As can be seen from the figure 5 (a, b, c)... the amount of lifting force increases to a certain value of the cylinder rotation speed (in our case, u=11 m/s), with a further increase in speed a sharp increase in lifting force is not observed. When conducting a comparative assessment of these dependencies, it was found that with the direct transverse direction of the wind air flow (angle of attack of the flow α=0°) the maximum lifting force of 3.5 N is achieved with a flow speed of 15 m/s, almost 4 times more than with a similar speed value with an angle of attack α=60°. This is explained by the fact that at small values of the angle of attack up to 10° the flow pattern is attached, at angles of attack from 10° to 30° the character of the detached flow is symmetrical vortices, and at average values of the angles of attack 30° to 60° an invariable asymmetric vortex pattern occurs, in which transverse forces are formed, pressure on the cylinder is exerted [18].

The measurement of the horizontal component of the aerodynamic force generated by the flow around the rotating cylinder makes it possible to determine the dependence of the drag force on the speed and direction of the air flow.

As can be seen from the figures, the qualitative nature of the presented dependencies at different angles of attack of the air flow practically repeat each other.

An increase in the values of the air flow velocity leads to an increase in the drag force of the rotating cylinder. As a result of the conducted studies the comparative efficiency of the rotating cylinder with a rough surface is shown, at the angle of attack of the air flow α=0°, with the direct transverse direction of the wind air flow, the flow velocity of 15 m/s-the maximum value of the drag force of the rotating cylinder is equal to 12 N.

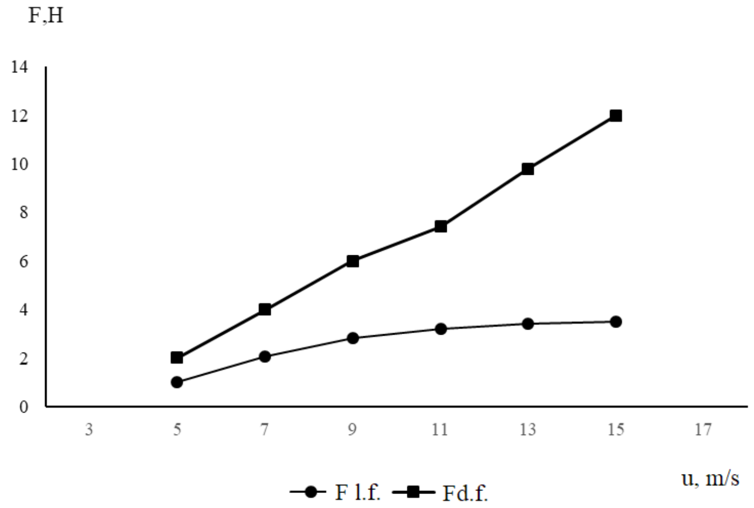

a) at an angle of attack of 0 degrees

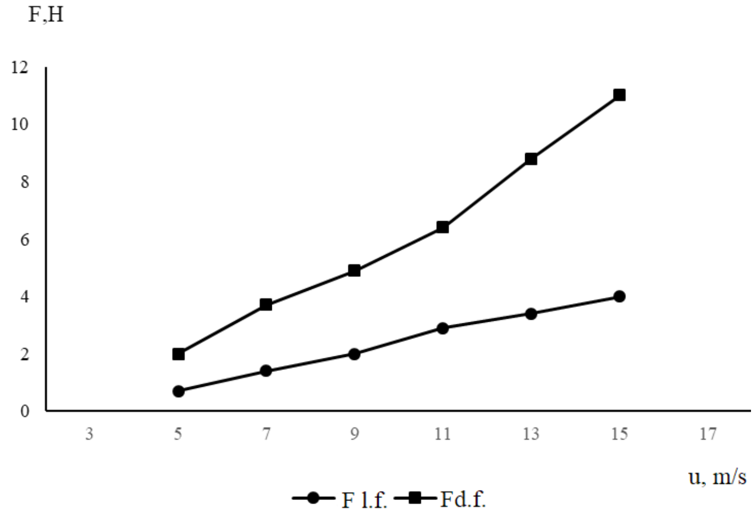

b) at an angle of attack of 30 degrees

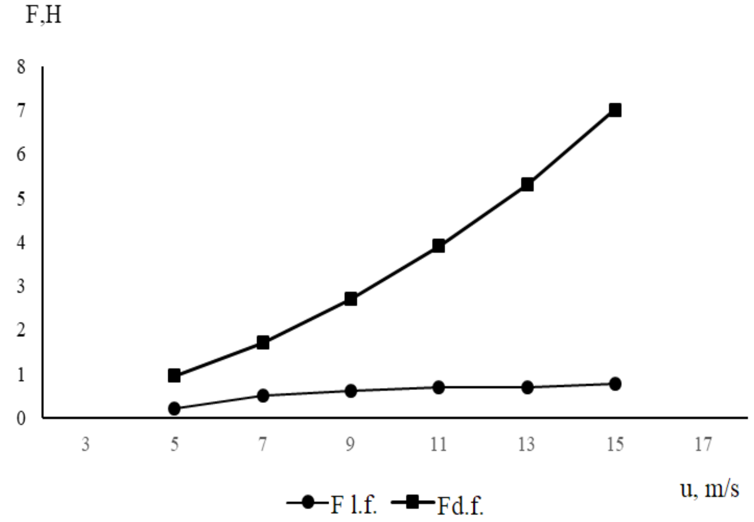

c) at an angle of attack of 60 degrees

Figure 5. The dependence of the lifting force and the drag force of a rotating cylinder with a rough surface on the air flow velocity at an angle of attack of the wind flow (0°, 30° and 60°)

Conclusions

This paper presents the results of studies of the aerodynamic characteristics of cylindrical blades of a wind power plant. During the execution of the work:

– a comparative graph of the dependence of the lifting force and drag force on the change in the air flow velocity and the relative surface roughness is obtained. Based on the results of these studies, the optimal surface of the cylinder layout with a relative roughness ($\bar{k}$) of 0.02 was chosen, which gives a stronger adhesion of the boundary layer to the surface than other rough surfaces considered;

– the dependences of the lifting force and the drag force at the angles of attack of 0, 30, 60 degrees are obtained and analyzed. Comparing these dependencies it was found that at a flow rate of 15 m/s, the maximum value of the drag force and lift force, 12 H and 3.5 N respectively, is achieved, which entails an increase in the efficiency and efficiency of the wind power plant (the angle of attack was 0°).

References

1 Bychkov N.M. Magnus wind turbines as an alternative to the blade ones / N.M. Bychkov, A.V. Dovgal, V.V. Kozlov // Journal of Physics: Conference Series. — 2007. — No. 75.

2 Бычков Н.М. Ветродвигатель с эффектом Магнуса. 3. Расчетные характеристики ветроколеса / Н.М. Бычков // Теплофизика и аэромеханика. — 2008. — Т. 15, № 2. — С. 341–352.

3 Ishkhanyan M.V. Wind Turbine of the Savonius–Magnus Type with Conical Blades: Dynamics and Control / M.V. Ishkhanyan, L.A. Klimina // Journal of Computer and Systems Sciences International. — 2020. — Issue 4. DOI:10.1134/S1064230720040085

4 Tanasheva N.K. Investigation of aerodynamic characteristics from the airflow angle of the rotating cylinder / N.K. Tanasheva, A.N., Dyusembaeva, L.L. Min’kov // Bulletin of the University of Karaganda-Physics. — 2018. — No. 1(89). — P. 88–92.

5 Richmond-Navarro G. Magnus wind turbine power model based on direct solutions using the blade element momentum theory and symbolic regression/ G. Richmond-Navarro, W.R. Calderon-Munoz, R. LeBoeuf, P.A. Castillo // IEEE Transactions on sustainable energy. — 2017. —Vol. 8., No. 1. — P. 425–430.

6 Sedaghat A. Magnus type wind turbines: Prospectus and challenges in design and modelling / A. Sedaghat // Renewable Energy. — 2014. — Vol. 62. — P. 619–628.

7 Luo D. Analytical solution on Magnus wind turbine power performance based on the blade element momentum theory / D. Luo, D. Huang, G. Wu // Journal of Renewable and Sustainable Energy. — 2011. — 3 (033104). DOI: 10.1063/1.3588039.

8 Massaguer A. Blade shape influence on aerodynamic efficiency of a Magnus wind turbine using particle image velocimetry / A. Massaguer, E. Massaguer, T. Pujol, M. Comamala, J. Velayos. International Conference on Renewable Energies and Power Quality (ICREPQ’14), (8–10 april 2014). Cordoba (Spain): Renewable Energy and Power Quality Journal. —2014. — No.1 2. — P.419–424. DOI: org/10.24084/repqj12.354

9 Басс В.П. Зависимость силы Магнуса от числа Кнудсена при поперечном стационарном обтекании вращающегося цилиндра / В.П. Басс, Л.Л. Печерица // Техн. механика. — 2009. — № 3. — С. 62–76.

10 Бычков Н.М. Ветродвигатель с эффектом Магнуса 2. Характеристики вращающегося цилиндра / Н.М. Бычков // Теплофизика и аэромеханика. — 2005. — Т. 12, № 1. — С. 159–175.

11 Kussaiynov K. The effect of porosity on the aerodynamic characteristics of a rotating cylinder / K. Kussaiynov, N.K. Tanasheva, M.M. Turgunov, G.M. Shaimerdenova, A.R. Alibekova // Modern applied science. — 2015. — Vol. 9, No. 2. — P. 42–48. DOI:10.5539/mas.v9n2p215

12 Hansen K.S. The impact of turbulence intensity and atmospheric stability on power deficits due to wind turbine wakes at Horns Rev wind farm / K.S. Hansen, R.J. Barthelmie, L.E. Jensen, A. Sommer // Wind Energy. — 2012. — 15(1). — P. 183–196. DOI: 10.1002/we.512

13 Tanasheva N.K. The study of the aerodynamic coefficients of rotating / N.K. Tanasheva, A.N. Dyusembaeva, B.R. Nussupbekov, L.L. Min’kov, Zh.G. Nurgalieva, K.K. Sadenova // Bulletin of the University of Karaganda-Physics. — 2019. — No 2 (94). — P. 108–113.

14 Marzuki O.F. Magnus wind turbine: the effect of sandpaper surface roughness on cylinder blades / O.F. Marzuki, A.Sh. Mohd Rafie, F.I. Romli, K.A. Ahmad // Acta Mechanica. — 2018. — Vol. 229. — P. 71–85. DOI:10.1007/s00707-017-1957-6

15 Marzuki O.F. An experimental investigation on the effect of surface roughness on the performance of Magnus wind turbine / O.F. Marzuki, A. Sh. Mohd Rafie, F.I. Romli, K.A. Ahmad // Journal of Engineering and Applied Sciences. — 2015. — Vol. 10, No. 20. — P.9725–9729.

16 Tanasheva N.K. Studying the dependence of the aerodynamic characteristics of rotating cylinders on the rake angle of air / N.K. Tanasheva, N.N. Shuyushbayeva, E.K. Mussenova // Technical Physics Letters. — 2018. — Vol. 44, Issue 9. — P. 787–789.

17 Шлихтинг Г. Теория пограничного слоя / Г. Шлихтинг. — М.: Наука, 1974. — 712 с.

18 Гумеров А.В. Исследование поперечной силы при обтекании тел вращения под большими углами атаки / А.В. Гумеров, Л.В. Гумерова, Е.М. Бальзанникова // Вестн. Самар. гос. аэрокосм. ун-та. — 2009. — № 1. — С. 14–23.

Н.К. Танашева, А.Р. Бахтыбекова, Л.Л. Миньков, С.А. Болегенова,
Н.Н. Шуюшбаева, А.Ж. Тлеубергенова, Б.А. Токтарбаев

Айналмалы цилиндрдің аэродинамикалық сипаттамасына кедір-бұдыр бетінің әсері

Мақалада цилиндрлік қалақшаның тиісті кедір-бұдырлығының аэродинамикалық сипаттамаларға әсері қарастырылған. Қарастырылатын қалақшалардың жұмысының негізі Магнус эффектісі екендігі белгілі, ол цилиндрлерді көлденең ағынмен айналдыру кезінде көтеру күшінің (Магнус күшінің) пайда болуымен сипатталады. Бұл күш жел доңғалағын айналдыру үшін қолданылады, көтергіш күшке ұқсас, бірақ геометриялық сияқты және аэродинамикалық оңтайлы жағдайларды таңдаған кезде әлдеқайда үлкен мәнге ие болуы мүмкін. Жұмыстың авторлары 0,005-тен 0,02-ге дейін өзгеретін салыстырмалы кедір-бұдырлы бетті цилиндрлердің макетіне талдаулар жүргізді. Айналмалы цилиндрлердің аэродинамика үдерісін зерттеу бойынша тәжірибелік зерттеулер ауа ағынының мәні 5-тен 15 м/с кезінде Т-1-М аэродинамикалық құбырын пайдалана отырып, аэродинамикалық зертханада жүргізілді. Айналмалы цилиндрдің көтеру күші мен кедергі күшінің ауа ағынының жылдамдығының өзгеруінен және тиісті кедір-бұдырлығынан тәуелділігінің графигі алынды, *k/d*. Цилиндрдің тәжірибелік макетінің аэродинамикалық көрсеткіштерін одан әрі зерттеу үшін, жоғары көрсеткіштерге ие болған, тиісті кедір-бұдырлығының 0.02 мәнімен ең оңтайлы нұсқа таңдалды. Тәжірибелік зерттеулер барысында жел ағынының жылдамдығы мен шабуыл бұрышынан (0°, 30° және 60°) беті кедір-бұдыр бір айналмалы цилиндрдің шабуыл бұрыштарынан көтеру күші мен кедергі күші мәндерінің тәуелділік графиктері алынды. Тиімді шабуыл бұрышы 0° екендігі анықталды және жұмыстың авторлары аэродинамикалық сипаттамалардың максималды мәндерін алды.

Кілт сөздер: цилиндр, аэродинамика, Магнус эффектісі, аэродинамикалық құбыр, тиісті кедір-бұдыр, шабуыл бұрышы, көтеру күші, кедергі күші, ауа ағыны.

Н.К. Танашева, А.Р. Бахтыбекова, Л.Л. Миньков, С.А. Болегенова,
Н.Н. Шуюшбаева, А.Ж. Тлеубергенова, Б.А. Токтарбаев

Влияние шероховатой поверхности на аэродинамические характеристики вращающегося цилиндра

В статье рассмотрено влияние относительной шероховатости цилиндрической лопасти на аэродинамические характеристики. Известно, что основой работы рассматриваемых лопастей является эффект Магнуса, который характеризуется появлением подъемной силы (силы Магнуса) при вращении цилиндров в поперечном потоке. Эта сила используется для вращения ветроколеса, аналогично подъемной силе, но может иметь гораздо большую величину при подборе оптимальных условий, как геометрических, так и аэродинамических. Авторы работы провели сравнительный анализ макета цилиндров с относительной шероховатостью, которая варьировалась от 0,005 до 0,02. Экспериментальные исследования по изучению процесса аэродинамики вращающихся цилиндров были проведены в аэродинамической лаборатории с использованием аэродинамической трубе Т-1-М при значении воздушного потока от 5 до 15 м/с. Получены графики зависимостей подъемной силы и силы лобового сопротивления вращающегося цилиндра от изменения скорости воздушного потока и от относительной шероховатости, *k/d*. Для дальнейшего исследования аэродинамических показателей экспериментального макета цилиндра был выбран наиболее оптимальный вариант со значением относительной шероховатости 0,02, который имел высокие показатели. В ходе экспериментальных исследований получены графики зависимостей значений подъемной силы и силы лобового сопротивления от углов атаки одиночного вращающегося цилиндра с шероховатой поверхностью от скорости и угла атаки потока ветра (0°, 30 и 60°). Установлено, что эффективным углом атаки является 0°, при котором авторы работы получили максимальные значения аэродинамических характеристик.

Ключевые слова: цилиндр, аэродинамика, эффект Магнуса, аэродинамическая труба, относительная шероховатость, угол атаки, подъемная сила, сила сопротивления, воздушный поток.

References

1 Bychkov, N.M. (2007). Magnus wind turbines as an alternative to the blade. *Journal of Physics: Conference Series*, 75.

2 Bychkov, N.M. (2008). Vetrodvigatel s effektom Magnusa. 3. Raschetnye kharakteristiki vetrokolesa [The wind turbine with the Magnus effect. 3. Design characteristics of the wind wheel]. *Teplofizika i aeromekhanika — Thermophysics and Aeromechanics*, 15(2), 341–352 [in Russian].

3 Ishkhanyan, M.V. & Klimina, L.A. (2020). Wind Turbine of the Savonius–Magnus Type with Conical Blades: Dynamics and Control. *Journal of Computer and Systems Sciences International*, 4. DOI:10.1134/S1064230720040085

4 Tanasheva, N.K., Dyusembaeva, A.N., & Min'kov, L.L. (2018). Investigation of aerodynamic characteristics from the airflow angle of the rotating cylinder. *Bulletin of the University of Karaganda-Physics*, 1(89), 88–92.

5 Richmond-Navarro, G., Calderon-Munoz, W.R., LeBoeuf, R., & Castillo P. (2017). A Magnus wind turbine power model based on direct solutions using the blade element momentum theory and symbolic regression. *IEEE Transactions on sustainable energy*, 8(1), 425–430.

6 Sedaghat, A. (2014). Magnus type wind turbines: Prospectus and challenges in design and modelling. *Renewable Energy*, 62, 619–628.

7 Luo, D., Huang, D., & Wu, G. (2011). Analytical solution on Magnus wind turbine power performance based on the blade element momentum theory. *Journal of Renewable and Sustainable Energy,* 3, 033104. DOI: 10.1063/1.3588039.

8 Massaguer, A., Massaguer, E., Pujol, T., Comamala, M., & Velayos, J. (2014). Blade shape influence on aerodynamic efficiency of a Magnus wind turbine using particle image velocimetry, International Conference on Renewable Energies and Power Quality (ICREPQ'14), 8–10 april 2014. Cordoba (Spain): *Renewable Energy and Power Quality Journal*, 12, 419–424. DOI: org/10.24084/repqj12.354

9 Bass, V.P., & Pecheritsa, L.L. (2009). Zavisimost sily Magnusa ot chisla Knudsena pri poperechnom statsionarnom obtekanii vrashchaiushchegosia tsilindra [Dependence of the Magnus force on the Knudsen number in the transverse stationary flow around a rotating cylinder]. *Tekhnicheskii mekhanika — Tech. Mechanics*, 3, 62–76 [in Russian].

10 Bychkov N.M. (2005). Vetrodvigatel s effektom Magnusa. 2. Kharakteristiki vrashchaiushchegosia tsilindra [Wind turbine with Magnus effect. 2. Characteristics of the rotating cylinder]. *Teplofizika i aeromekhanika — Thermophysics and Aeromechanics*, 12 (1), 159–175 [in Russian].

11 Kussaiynov, K., Tanasheva, N.K., Turgunov, M.M., Shaimerdenova, G.M., & Alibekova A.R. (2015) The effect of porosity on the aerodynamic characteristics of a rotating cylinder. *Modern applied science*, 9 (2), 42–48. DOI:10.5539/mas.v9n2p215

12 Hansen, K.S., Barthelmie, R. J., Jensen, L.E., & Sommer, A. (2012). The impact of turbulence intensity and atmospheric stability on power deficits due to wind turbine wakes at Horns Rev wind farm. *Wind Energy*,15(1), 183–196. DOI: 10.1002/we.512

13 Tanasheva, N.K., Dyusembaeva, A.N., Nussupbekov, B.R., Min'kov, L.L., Nurgalieva, Zh.G., & Sadenova, K.K. (2019). The study of the aerodynamic coefficients of rotating. *Bulletin of the University of Karaganda-Physics*, 2 (94), 108–113.

14 Marzuki, O.F., Mohd Rafie, A.Sh., Romli, F.I., & Ahmad K.A. (2018). Magnus wind turbine: the effect of sandpaper surface roughness on cylinder blades. *Acta Mechanica*, 229, 71–85. DOI:10.1007/s00707-017-1957-6

15 Marzuki, O.F. Mohd Rafie, A.Sh., Romli, F.I., & Ahmad, K.A. (2015). An experimental investigation on the effect of surface roughness on the performance of Magnus wind turbine. *Journal of Engineering and Applied Sciences*., 10 (20), 9725–9729.

16 Tanasheva, N.K., Shuyushbayeva, N.N., & Mussenova, E.K. (2018). Studying the dependence of the aerodynamic characteristics of rotating cylinders on the rake angle of air. *Technical Physics Letters*, 44(9), 787–789.

17 Schlichting, G. (1974). Teoriia pogranichnogo sloia [Theory of the Boundary layer]. Moscow: Nauka [in Russian].

18 Gumerov, A.V., Gumerova, L.V., & Balzannikov E.M. (2009). Issledovanie poperechnoi sily pri obtekanii tel vrashcheniia pod bolshimi uglami ataki [Study of the lateral force by the flow around bodies of revolution at high angles of attack]. *Vestnik Samarskogo gosudarstvennogo aerokosmicheskogo universiteta — Bulletin of the Samara State Aerospace University,* 1, 14–23 [in Russian].

DOI 10.31489/2021Ph3/60-70
UDC 624

Ye. Utepov[1,2], A. Tulebekova[1,2,]*, S. Akhazhanov[3], Sh. Zharassov[2], D. Bazarbayev[2]

[1]*CSI Research & Lab (LLP), Nur-Sultan, Kazakhstan;*
[2]*L.N. Gumilyov Eurasian National University, Nur-Sultan, Kazakhstan;*
[3]*Karagandy University of the name of academician E.A. Buketov, Kazakhstan*
*(*E-mail:krasavka5@mail.ru)*

Prototyping of a concrete maturity sensor with a hermetically sealed housing made of two-component plastic

The construction industry, traditionally considered quite conservative, is now going through a marked change. With competition intensifying, companies have begun to gradually adopt various digital technologies to reduce construction costs, such as the wireless concrete monitoring sensors, which implement a temperature-strength monitoring method for concrete. Each device has its technological features, which are taken into account in the development of the concepts. Enclosure design is the most important stage of product development. An enclosure made in-house has many advantages and disadvantages. The most important part of the design of an electronic device enclosure is the preliminary research stage. This article presents features of wireless monitoring sensor enclosure design. A data acquisition station (DAS), also referred to in the network topology as a "gateway", will be used to collect data from the wireless monitoring sensor over the selected protocol. The server application was created based on HTML, PHP, CSS, JavaScript. Testing of the wireless monitoring sensor, SDS, and the server application working together showed full functionality. A study is also given on the determination of concrete strength using the developed sensor according to the ASTM method and using the IPS MG 4.0 by GOST.

Keywords: enclosure design, strength, sensor, software, concrete curing temperature, requirement, non-destructive testing of concrete, monitoring.

Introduction

The concrete strength is the main characteristic that establishes the ability of concrete or reinforced concrete structure to bear the design loads. Standards specify that there are four steps in the use of the method of calculating the current strength of concrete by its maturity: establishing the maturity-strength relationship in the laboratory; embedding maturity sensors inside the formwork at the construction site; sensor reading of concrete maturity at the construction site; data analysis [1–3]. The first phase involves the development of a housing for a wireless concrete strength monitoring sensor.

All electronic devices are quite different in their functionality and set of tasks. Despite this, there is a common set of rules that can be applied to the design of a product enclosure. Enclosure development consists of several stages [4]:

– Creation of the product concept. At this stage the idea goes through a commercial success analysis. Competing products are identified and a technical level map is drawn up. The technical level map is a comparative table that identifies the unique combination of product functionality and business model to ensure the commercial success of the device being created. Specialists and experts in the required industry prepare a technical and commercial proposal and a product concept design describing the functional features and benefits. In parallel, business analysts create a business plan based on the selected business model and expert assessments. As a rule, the result of this stage is a finished product [4];

– Technical development of the product. At this stage, a conceptual design (PD) is created, terms of reference (TOR) are developed, specifications are created, and product use cases are analyzed. A device feasibility study is carried out, often culminating in the assembly and testing of a product prototype. The selected software, and hardware solutions are evaluated, and the problem areas from the point of view of further technical implementation, platform performance, and other important characteristics are studied. The result of the technical study of the product is a decision on the correctness of the chosen platform and the justification of technical solutions;

– Development of an electronic device, including the specification of the list of components to be used, the design of the circuit diagram, and the creation of a list of components. The interface is designed, the function tree is built and the control concept is created. Simultaneously with the development of the schematic diagram, the design of the device enclosure is completed. Based on the sketch, a model and design of the device are developed. The software architecture developed in the previous stage is implemented and the software is adapted and finalized. All kinds of tests are developed to check the correctness of both software and hardware;

– At this stage prototypes are created to test their performance and to eliminate possible errors made in the previous design stages. Prototypes have the advantage of solving marketing problems. At this stage, components are procured, and production is placed on the manufacture and assembly of printed circuit boards. After the assembly of the sample PCBs, the operating system and bootloader are ported, drivers, low-level procedures, and application software are finalized. All product components are assembled and integration testing is performed. The result of this stage is the production of working prototypes and changes to the design documentation based on the results of integration testing;

– At this stage, the device class and the need for testing are determined. Based on the preliminary results of the certification, the protocols with the results of the measurements are generated and, if necessary, changes are made to the design documentation;

– Preparation for production and release of a pilot batch. A pilot batch is the starting point for serial production and a check on the manufacturability of the device in real production. At this stage, product defects that were not detected on a small number of prototypes are identified and minor adjustments are made to the circuit, enclosure design, and printed circuit board;

– Full support by the developer for an industrial product that is ready for implementation.

The next step is to verify that the software works and to determine the “strength-maturity” relationship obtained in advance by laboratory testing of the concrete composition chosen, according to the ASTM C1074 maturity method.

Features of hull design

One important feature is the design of the enclosure after the stuffing has been completed [5]. In general, plastic parts are produced on special machines — injection moulding machines (IMMs), on which moulds corresponding to the parts are installed [6]. Molten plastic is injected under pressure into the mould cavity of the mould, after which it is cooled and opened to remove the part [7].

The faster and cheaper production of moulds has led to maximum standardization of the elements. As a result, mould making is essentially reduced to the creation of mould inserts. A high proportion of the cost of the moulds is made up of high-grade steel, which accounts for around 80 % of the cost of the moulds. The quality of the steel used in the molds determines the lifetime of the mold [8]. The leading mold maker is China. The price of moulds in China varies greatly from manufacturer to manufacturer, although it is several times cheaper than in Europe. On the mould production time, Europe is inferior to China. The main problems when dealing with Chinese manufacturers are the difficulty of controlling delivery times and quality [9].

The main material used for enclosures in the electrical industry is plastic. It is widely used because of its good appearance, shiny surface, sufficient plasticity, and ability to retain its properties over a wide temperature range. It should be noted that parts with special properties require more careful selection of material. In addition to ABS plastic, materials such as polystyrene, polycarbonate, glass-filled polyamide are often used [10]. The aforementioned materials are colored by adding a pigment of a certain color. This way any color can be obtained, but the coloring technology requires the use of specialized equipment. To avoid such problems, super concentrates (plastic granules dyed with excessive amounts of pigment) are used [11]. Plastic injection moulding may seem a simple enough process, and with the emergence of inexpensive Chinese and Taiwanese machines it has become even more affordable. However, the efficiency and reliability of such production will be very low, no better than casting the body in a polyurethane or silicone mould of your own making [8]. Polyurethane and silicone moulds are often used in the production of various products. Not only plastic but also plaster and even concrete can be poured into them. A silicone mould can also be made by hand. The base ingredient for the mould is a silicone ingredient. It is a set of liquid silicone and catalyst, i.e. hardener. The working principle is simple: the 2 components are mixed in certain proportions and the resulting mixture is poured over the object to be removed from the mould.

Development of the Reinforced Concrete PM enclosure

The development of the enclosure was carried out for a wireless sensor for monitoring reinforced concrete structures. Computer-aided design (CAD) software was used for visualization. There are many analogs of such programs on the market, the classification is presented in Table 1 [9].

Table 1

Classification of CAD programs

№	Program	The complexity of the task to be performed	User level	Not recommended for use
1	Google SketchUp	Simple enclosures	Newcomer	Projects for series production
2	Blender	All enclosures	Beginner and above	Projects with complex geometry or surfaces
3	COMPAS-3D	All enclosures	Beginner and upper	Projects with complex geometry
4	SolidWorks	All enclosures	Beginner and upper	Projects with a complex surface or design
5	Inventor	All enclosures	Specialist	-
6	NX	All enclosures	Specialist	-
7	CATIA	All enclosures	Beginner and upper	-

After selecting the computer visualization software, the board and the main components of the device are modeled in 3D. Around the resulting 3D model the enclosure is built. An important role at the stage of construction of the 3D model is played by dimensions of parts, which should be envisaged in 2D. Accuracy of measurement excludes possible alterations [12]. To check the dimensional accuracy at an early stage of the 2D sketch a ream is made on heavyweight paper (Fig. 1).

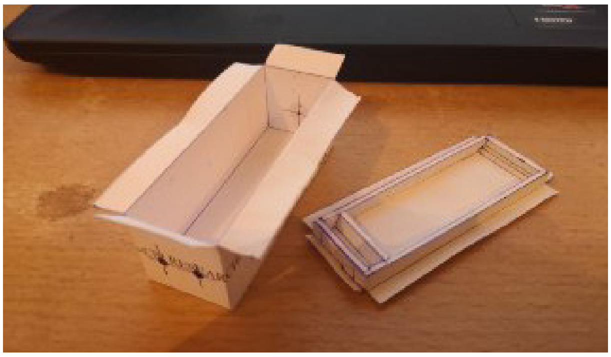

Figure 1. The reamer from the 2D drawings

Blender [13] is used to visualize the future model of the sensor housing in 3D. In Blender, the construction of the enclosure starts around the board from the largest dimensions and gradually progresses to smaller ones (Fig. 2) [12].

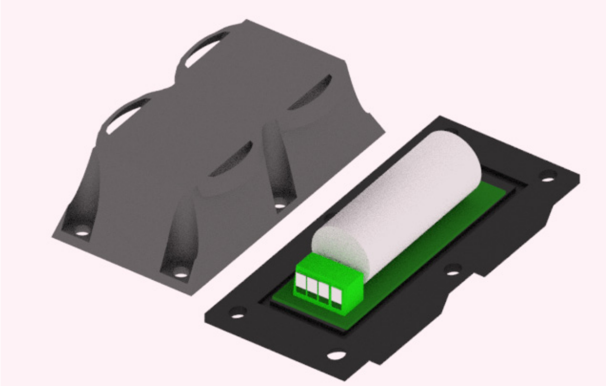

Figure 2. The 3D model of building a square enclosure around the board

According to the initial sketch, the activation mechanism and cable entry hole are provided on the top of the enclosure, with a rib through which a clamp will be passed to hold the transducer in a stationary position. Rubber gaskets (Fig. 3, a) and a gland for the hole through which the cable enters the sensor housing are used to seal the housing. The gland consists of the body, gasket, gasket nut, gasket, and fixation nut (Fig. 3, b). The gasket and gasket are made of neoprene. The body, packing nut, and retaining nut are made of nylon. The gland is installed using a pipe wrench (gas wrench).

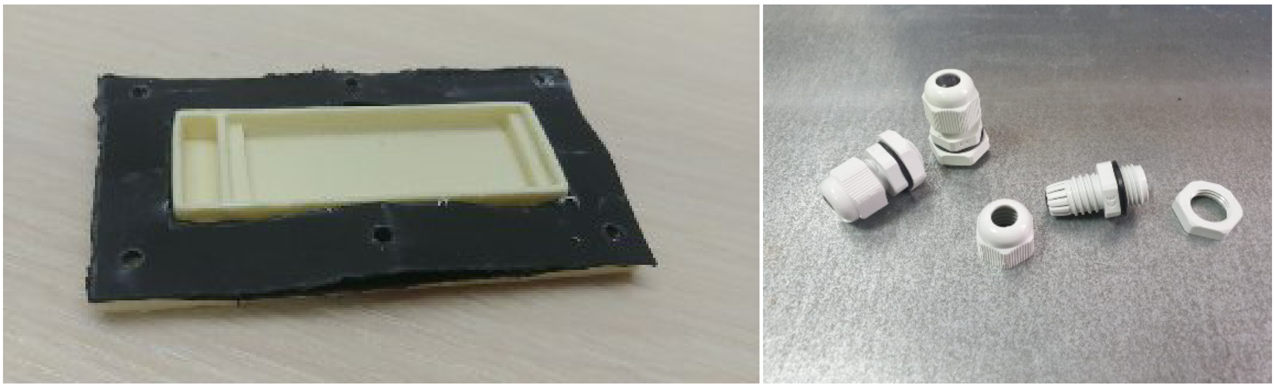
(a) (b)

Figure 3. Elements for sealing the enclosure: a) rubber gasket; b) gland for PG7 cable.

The 3D model in STL format is transferred to the 3D printer software. The software allows the model to be automatically or manually positioned in the virtual workspace [14]. All auxiliary elements are then generated and the amount of consumables, as well as the printing time, is calculated (Fig. 4).

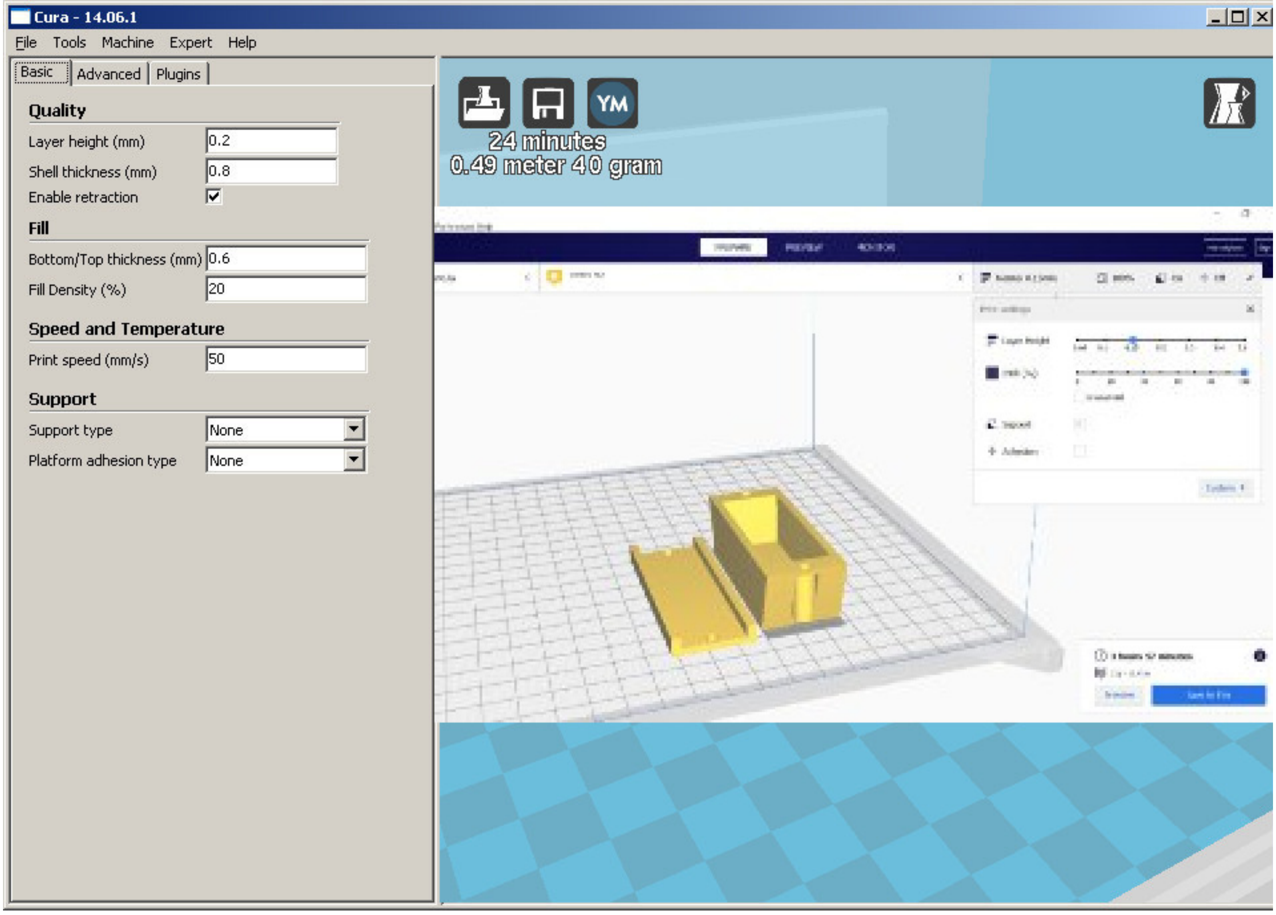

Quality
Layer height (mm) 0.2
Shell thickness (mm) 0.8
Enable retraction ☑
Fill
Bottom/Top thickness (mm) 0.6
Fill Density (%) 20
Speed and Temperature
Print speed (mm/s) 50
Support
Support type None
Platform adhesion type None

24 minutes
0.49 meter 4.0 gram

Figure 4. 3D printer software for calculating the number of consumables and time to print

Print auxiliaries are considered to be materials to support the parts as they are positioned over the printing area. Before the printing process begins, the model is automatically divided into horizontal layers and the paths of the printhead are calculated. The 3D printing process then starts: a heating head with spinnerets (extruder) melts thin plastic filament (fishing line) and layers it according to the data in the mathematical 3D model (Fig. 5) [15].

Figure 5. The process of printing on a 3D printer

Once the product has been printed, auxiliary structures are removed by hand or dissolved using a special solution. As a result of the printed model, it is possible to see flaws in the construction and design of the enclosure. When attempting to assemble the enclosure, insufficient rigidity of the enclosure walls was detected. Therefore, the next solution is to return to the previous stage and make corrections to the model. You can modify the finished model by using improvised materials, for example, using liquid plastic, plasticine, or cardboard to increase the thickness of the part or add a new element. The more prototypes produced, the more flaws will be identified and the final product will be as well thought out as possible (Fig. 6, a, b).

(a) (b)

Figure 6. Refinement of the printed model: a — refilling the plastic on the edges of the upper body, b — increasing the height of the bottom body rim with paper

When pouring the silicone, the moulds must be able to fit together smoothly. The first part of the mould must have holes and the second part must have protrusions.

The curing time of the plastic after printing is about 20 minutes. During the design and casting process the hull underwent no small amount of modification. At the time of the virtual model the edges of the hull were enlarged so that the joint between the top and the bottom was tight, and after 3D printing rigidity ribs were added (Fig. 7).

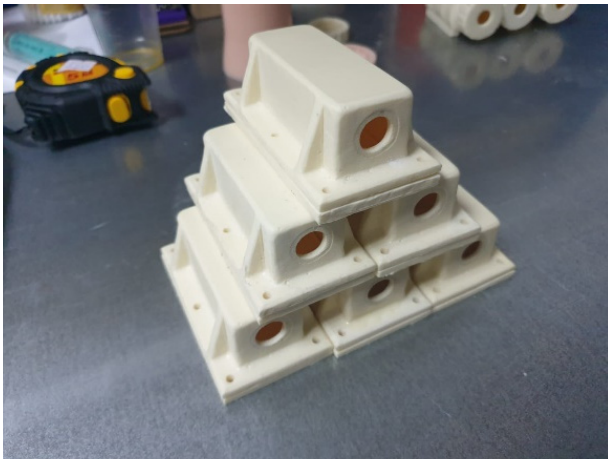

Figure 7. Prefabricated sensor housing

Once the enclosure is ready, testing should be carried out to check the performance.

User interaction with wireless sensor

User interaction with the wireless sensor measurement suite begins with the software (Fig. 8). The user accesses the software via the browser on a mobile device or personal computer. The user selects an existing project or creates a new one, where they specify its name, location, and, if necessary, additional information. Once the project has been fully created and the project data verified, the required number of temperature gauges is added. The concrete composition to be monitored on-site is then selected. It is to be noted that a concrete composition has a concrete strength-maturity curve obtained by performing concrete tests based on the ASTM C1074 maturity method. This dependency is entered into the database by the administrator of the wireless sensor's owner.

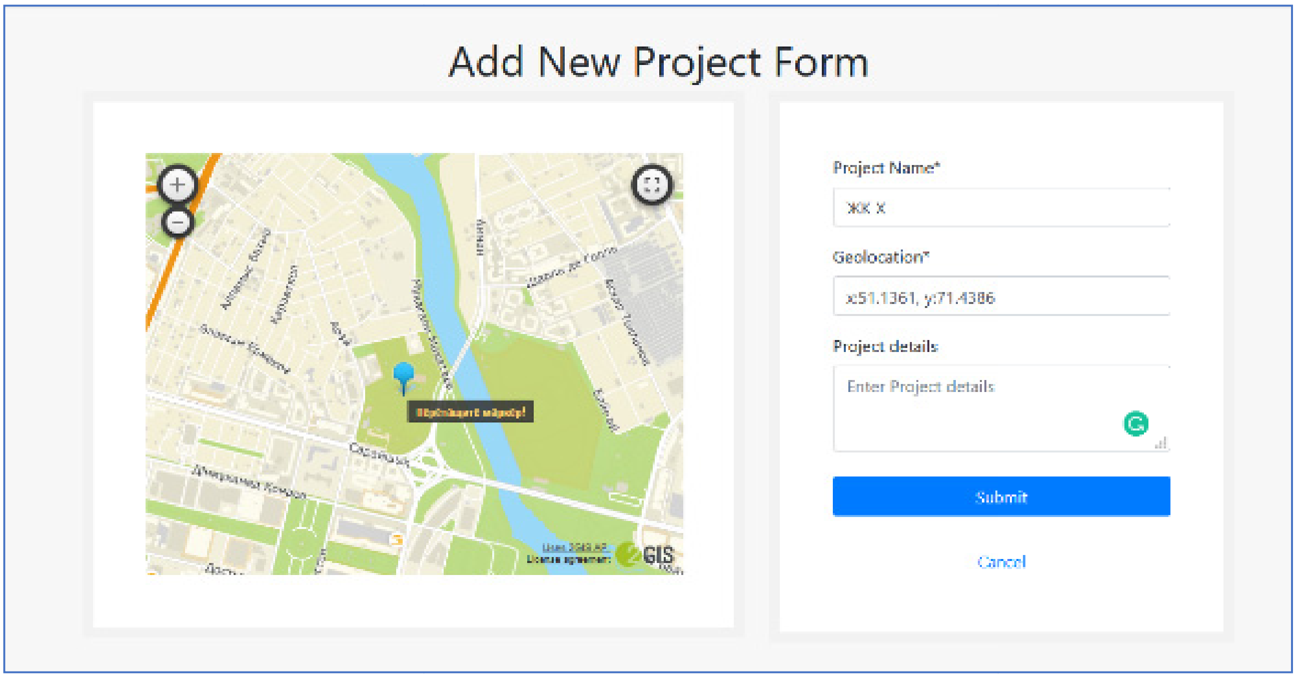

Add New Project Form

Project Name*

ЖК X

Geolocation*

x:51.1361, y:71.4386

Project details

Enter Project details

Figure 8. New project creation page

Experimental studies of the selected concrete composition

A series of tests was carried out to check the operation of the wireless sensor: two 50x50x50 cm cubes were prepared by ASTM C 1074, in which the sensors were immersed and the hardening temperature of the concrete was measured for 28 days at 0.5-hour intervals (Fig. 9).

Figure 9. Experimental studies

The strength tests of the specimens by the nondestructive control method were performed using a shock-pulse device IPS MG4 [16–17] (Fig. 10).

Figure 10.The strength tests by IPS MG4

The strength values were then calculated according to the standards [1, 16, 17].

Results and Discussion

The maturity function by ASTM C 1074 is a mathematical expression that uses the measured temperature history of the cement mix during the curing period to calculate an index indicating maturity at the end of that period. Using the calculated maturity index and the strength to maturity ratio, the strength of the concrete is estimated. So the results of concrete strength by ASTM are presented in Figure 11 a, b and by GOST in Figure 12.

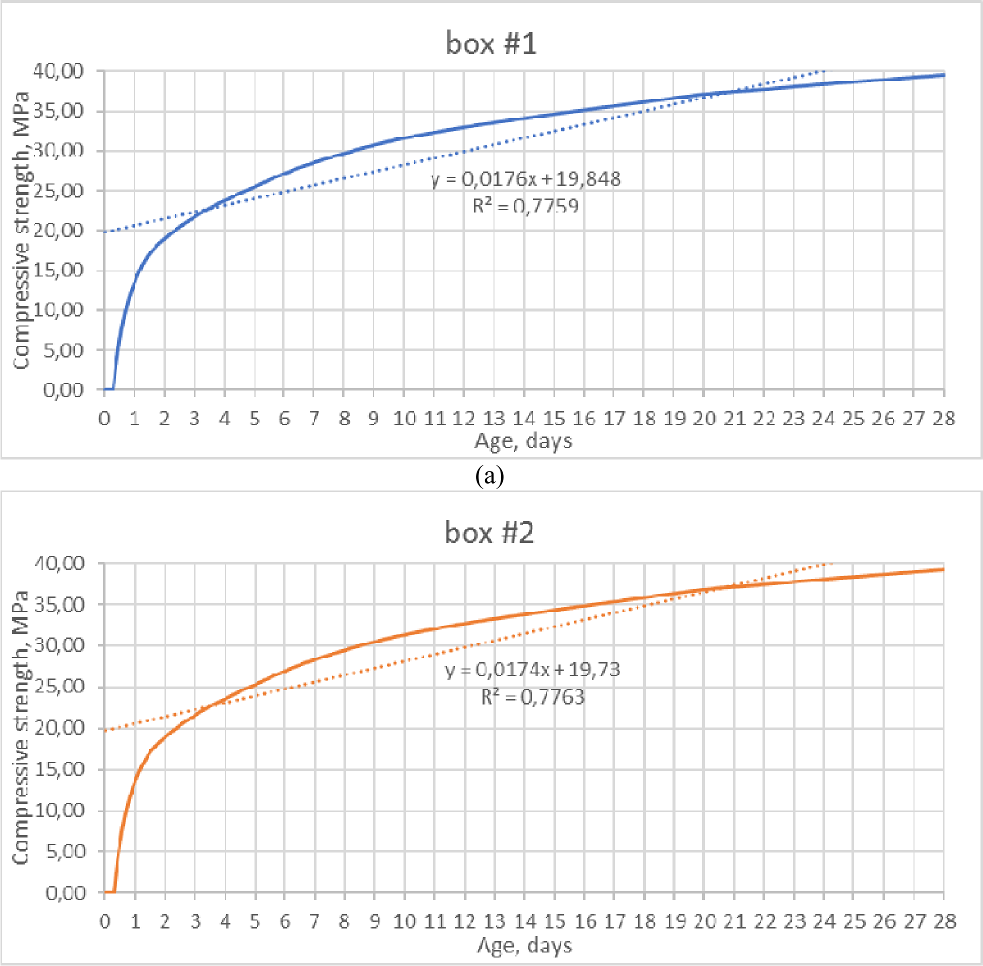

(a)

(b)

Figure 11. Results of determination of concrete strength by ASTM: a) box 1; b) box 2

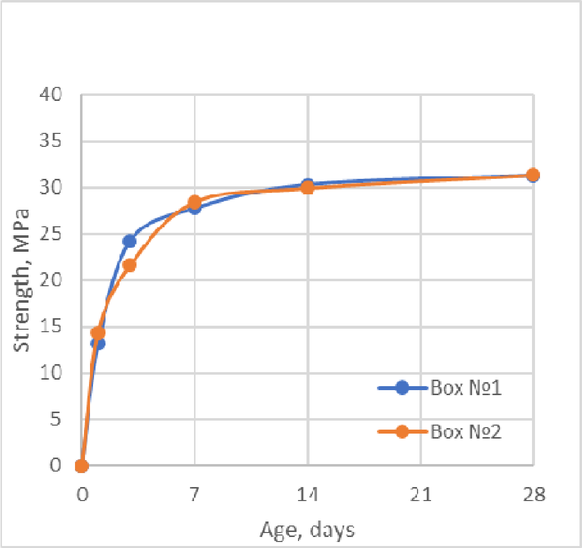

Figure 12. Concrete strength by GOST

To verify the operation of the wireless monitoring sensor two boxes with the sensor were tested by ASTM C 1074; the determination of strength using the IPS MG 4.0 by GOST [16–17] was performed as well. The results showed that the convergence of the values obtained in the tests with the wireless monitoring sensor and by IPS MG 4.0 was satisfactory.

The following conclusions can be made based on the results of the studies: the received data of strength by the sensor has a high degree of reliability, as evidenced by results that were received by the national standard. A slight difference is observed at the initial stage of concrete curing, on the second day the temperature regimes specimens are aligned.

Also based on the results of the work it has been revealed that the shape of the enclosure plays an important role in the design of an electronic device. The specifications and operational requirements of the device have a direct impact on the cost of the product, with the design, testing, and serial production of the enclosure accounting for a significant part of the cost. Each stage in the development of an enclosure is a critical moment, and one of these is the construction of the 3D model, where several basic rules must be observed: there must be no collisions and overlapping parts; all parts must assemble and fully match each other; use uniform dimensions for enclosure walls and repeating parts; and use symmetry and mirror placement of parts. Once the enclosure is ready, testing must be carried out to check the performance with software.

Conclusions

The development of new materials, equipment, and quality control techniques makes it possible to obtain products with high strength, durability, and resistance to wear and tear. In addition to high product quality in the form of building structures, construction companies are also aiming to make a profit. For example, by optimizing the removal cycles of the formwork, time can be saved and overhead costs and labor can be reduced. Timely detection of the point of maturity of a reinforced concrete structure and the decision to load it can generate additional profits by reducing the construction time. There are alternative methods of calculating and predicting the strength of concrete based on modern technology, such as embedded sensors and sensors. The presented embedded wireless sensor for monitoring reinforced concrete structures has no analogs in Kazakhstan. To further verify the performance of the solution, laboratory tests of concrete samples were conducted, the results of which will be used as an initial matrix to be loaded into the server application.

Acknowledgments

This research was funded by the Science Committee of the Ministry of Education and Science of the Republic of Kazakhstan (Grant № AP08956209).

References

1 ASTM C1074. Standard Practice for Estimating Concrete Strength by the Maturity Method. — P.: ASTM International, 2019.

2 NEN 5970. Determination of strength of fresh concrete with the method of weighted maturity. — D.: Netherlands Standardization Institute, 2001.

3 ST–NP SRO SSK–04–2013. Temperature and strength control of concrete during the construction of monolithic structures in winter. — Ch.: UCC, 2013. — P. 25.

4 Utepov Ye.Maturity sensors placement based on the temperature transitional boundaries / Ye. Utepov, A. Aniskin, A. Ibrashov, A.Tulebekova // Magazine of Civil Engineering. — 2019. — No. 90 (6). — P. 93–103.

5 Boothroyd G. Product design for manufacture and assembly / G. Boothroyd // Computer-Aided Design. — 1994. — No. 26(7). — P. 505–520.

6 Heckele M. Review on micro molding of thermoplastic polymers / M. Heckele, W.K. Schomburg // Journal of Micromechanics and Microengineering. — 2003. — No. 14(3). — P. R1–R14.

7 Taheri S. A review on five key sensors for monitoring of concrete structures / S. Taheri // Constr. Build. Mater. — 2019. – No. 204. — P.492–509.

8 Thiriez A. An environmental analysis of injection molding / A. Thiriez, T. Gutowski // Proceedings of the 2006 IEEE International Symposium on Electronics and the Environment. — 2006. — P. 195–200.

9 Hannan M. A review on sensors and systems in structural health monitoring / M. Hannan, K. Hassan, K. Jern // Smart Struct. Syst. — 2018. — No. 22 (5). — P. 509–525.

10 Sun J. Shape optimization using evolutionary techniques in product design / J. Sun, J.H. Frazer, T. Mingxi // Computers & Industrial Engineering. — 2007. — No. 53(2). — P. 200–205.

11 Rodrigues E. An approach to urban quarter design using building generative design and thermal performance optimization / E. Rodrigues, A.R. Amaral, A.R. Gaspar // Energy Procedia. — 2015. — No. 78. — P. 2899–2904.

12 Alcaide-Marzal J. A 3D shape generative method for aesthetic product design / J. Alcaide-Marzal, J.A. Diego-Mas, G.A. Acosta-Zazueta // Design Studies. — 2020. — No. 66. — P. 144–176.

13 Tovey M. Sketching, concept development and automotive design / M. Tovey, S. Porter, R. Newman // Design Studies. — 2003. — No. 24(2). — P. 135–153.

14 Szilvśi-Nagy M. Analysis of STL files / M. Szilvśi-Nagy, M. Mátyási // Mathematical and Computer Modelling. — 2003. — No. 38(7–9). — P. 945–960.

15 Utepov Y. Prototyping an embedded wireless sensor for monitoring reinforced concrete structures / Y. Utepov, O. Khudaibergenov, Y. Kabdush, A. Kazkeev // Computers and Concrete. — 2019. — No. 24. — P. 95–102.

16 ГОСТ 22690. Определение прочности механическими методами неразрушающего контроля. — М.: Стандартинформ, 2015.

17 ГОСТ 10180. Методы определения прочности по контрольным образцам. — М.: Стандартинформ, 2012.

Е. Утепов, А. Тулебекова, С. Ахажанов, Ш. Жарасов, Д. Базарбаев

Екікомпонентті пластиктен жасалған герметикалық корпусы бар бетонның жетілу сенсорының прототипін жасау

Дәстүрлі түрде консервативті деп саналатын құрылыс индустриясы қазір айтарлықтай өзгерістерден өтуде. Бәсекелестіктің күшеюі жағдайында компаниялар құрылысқа жұмсалатын шығындарды төмендету үшін әртүрлі цифрлық технологияларды біртіндеп қолдана бастады, бұл бетонның температуралық-беріктік бақылау әдісін іске асыратын темірбетон конструкцияларының (ТБК) мониторингтік сымсыз датчигі болып табылады. Әр құрылғының өзіндік технологиялық ерекшеліктері бар, олар тұжырымдамаларды әзірлеу кезінде ескеріледі. Корпустың дизайны — өнімді дамытудың маңызды кезеңі. Өз өндірісінің корпусы көптеген артықшылықтарға да, кемшіліктерге де ие. Электрондық құрылғы корпусын дамытудың маңызды бөлігі — алдын-ала зерттеу кезеңі. Мақалада ТБК корпусын дамытудың ерекшеліктері берілген.

Таңдалған хаттама Бойынша ТБК-дан деректерді жинау үшін желілік топологияда «шлюз» деп аталатын деректерді жинау станциясы (ДЖС) қолданылған. Серверлік қосымша HTML, PHP, CSS және JavaScript негізінде құрылды. ТБК, ДЖС және серверлік қосымшаның бірлескен жұмысын тетілеу толық функционалдылықты көрсетті. Сондай-ақ, ASTM C1074 стандартына сәйкес таңдалған қоспаның «беріктік жетілу» тәуелділігін анықтау бойынша зерттеулер келтірілген, оны пайдаланушы сенсордың бағдарламалық жасақтамасына енгізеді.

Кілт сөздер: корпустың дизайны, беріктігі, сенсоры, бағдарламалық жасақтамасы, талаптары, бетонның қатаю температурасы, бетонды бұзбай бақылау, мониторинг.

Е. Утепов, А. Тулебекова, С. Ахажанов, Ш. Жарасов, Д. Базарбаев

Разработка прототипа датчика зрелости бетона с герметическим корпусом из двухкомпонентного пластика

Строительная индустрия, традиционно считающаяся достаточно консервативной, сейчас проходит через заметные изменения. В условиях усиления конкуренции компании начали постепенно применять различные цифровые технологии для снижения затрат на строительство. Таким и является беспроводной датчик мониторинга железобетонных конструкций (БДМ), реализующий метод температурно-прочностного контроля бетона. У каждого устройства свои технологические особенности, что учитывается при разработке концептов. Дизайн корпуса — важнейший этап разработки изделия. Корпус собственного изготовления обладает как многими преимуществами, так и недостатками. Важнейшая часть разработки корпуса электронного устройства — этап предварительных исследований. В статье представлены особенности разработки корпуса БДМ. Для сбора данных с БДМ по выбранному протоколу будет использоваться Станция сбора данных (ССД), именуемая в топологии сети как «шлюз». Серверное приложение создавалось на основе HTML, PHP, CSS и JavaScript. Тестирование совместной работы БДМ, ССД и серверного приложения показало полную функциональность. Кроме того, приведены исследования по определению зависимости «прочность – зрелость» выбранного состава смеси согласно стандарту ASTM C1074, которые затем пользователь заносит в программное обеспечение датчика.

Ключевые слова: конструкция корпуса, прочность, датчик, программное обеспечение, температура твердения бетона, требование, неразрушающий контроль бетона, мониторинг.

References

1 ASTM C1074.Standard Practice for Estimating Concrete Strength by the Maturity Method (1998). Pennsylvania: ASTM International.

2 NEN 5970.Determination of strength of fresh concrete with the method of weighted maturity(2001). Delft: Netherlands Standardization Institute.

3 ST–NP SRO SSK–04–201.Temperature and strength control of concrete during the construction of monolithic structures in winter(2013). Chelyabinsk: UCC.

4 Utepov, Ye., Aniskin, A., Ibrashov, A., & Tulebekova, A. (2019). Maturity sensors placement based on the temperature transitional boundaries. *Magazine of Civil Engineering, 90 (6),* 93–103.

5 Boothroyd, G. (1994). Product design for manufacture and assembly. *Computer-Aided Design, 26(7),* 505–520.

6 Heckele, M. & Schomburg, W.K. (2003). Review on micro molding of thermoplastic polymers. *Journal of Micromechanics and Microengineering, 14(3),* R1–R14.

7 Taheri, S. (2019). A review on five key sensors for monitoring of concrete structures. *Constr. Build. Mater, 204,* 492–509.

8 Thiriez, A., & Gutowski, T. (2006). An Environmental Analysis of Injection Molding. *Proceedings of the 2006 IEEE International Symposium on Electronics and the Environment,* 195–200.

9 Hannan, M., Hassan, K. & Jern, K. (2018). A review on sensors and systems in structural health monitoring*. Smart Struct. Syst., 22 (5),* 509–525.

10 Sun, J., Frazer, J.H. & Mingxi, T. (2007). Shape optimization using evolutionary techniques in product design. *Computers & Industrial Engineering, 53(2),* 200–205.

11 Rodrigues, E., Amaral, A.R., Gaspar, A.R. & Gomes, A. (2015). An approach to urban quarter design using building generative design and thermal performance optimization. *Energy Procedia, 78,* 2899–2904.

12 Alcaide-Marzal, J., Diego-Mas, J.A. & Acosta-Zazueta, G. (2019). A 3D shape generative method for aesthetic product design. *Design Studies, 66,* 144–176.

13 Tovey, M., Porter, S. & Newman, R. (2003). Sketching, concept development and automotive design. *Design Studies, 24(2),* 135–153.

14 Szilvśi-Nagy, M. & Mátyási, G. (2003). Analysis of STL files. *Mathematical and Computer Modelling, 38(7–9),* 945–960.

15 Utepov, Y., Khudaibergenov, O., Kabdush, Y. & Kazkeev, A. (2019). Prototyping an embedded wireless sensor for monitoring reinforced concrete structures. *Computersand Concrete, 24,* 95–102.

16 HOST 22690. Opredelenie prochnosti mekhanicheskimi metodami nerazrushaiushchego kontrolia [Concretes. Determination of strength by mechanical methods of nondestructive testing]. (2015). Moscow: Standartinform [in Russian].

17 HOST 10180. Metody opredeleniia prochnosti po kontrolnym obraztsam [Concretes. Methods for strength determination using reference specimens] (2012). Moscow: Standartinform [in Russian].

DOI 10.31489/2021Ph3/71-82
UDC: 661.845:666.3

A.V.Pavlov[1,2], E.E. Aiymkhanov[2], Zh.B. Sagdoldina[1],
A.B. Kassymov[3], D.R. Baizhan[1*], M.S. Zhaparova[1]

[1]Sarsen Amanzholov East Kazakhstan University, Ust-Kamenogorsk, Kazakhstan;
[2]Ceramic plant, Ust-Kamenogorsk, Kazakhstan;
[3]Shakarim University of Semey, Kazakhstan
*(*E-mail: daryn.baizhan@mail.ru)*

Research of methods for introducing TiO_2 nanoparticles into a micron matrix of BeO and TiO_2 powders and their effect on the rheological properties of a casting slip

This article presents the research results of methods for introducing nanodispersed TiO_2 powders into a micron matrix of beryllium and titanium oxides. It is shown that the presence of nanoparticles over 5.0 wt.% negatively affects the rheological properties of the casting slip and vice versa, the addition of nanoparticles in the range of 0.1–2.0 wt.% contributes to reducing the viscosity and increasing the casting ability of the slipping mass. Macrostructural analysis of the sintered billet indicates the complete absence of structural elements in the form of conglomerates of nanoparticles, or nano- and micro-TiO_2 particles. The developed method of introducing nanoparticles makes it possible to obtain products with their uniform distribution over the entire volume of the workpiece by slip casting under pressure. Further, the authors of the scientific work planned to research the effect of nanoparticles on the thermophysical and impedance characteristics of the obtained ceramics. Research into the effect of nanopowders on the electrophysical properties of beryllium ceramics is not known in the scientific world. The most important properties that the BeO+TiO_2 ceramics should possess is the ability to absorb ultrahigh frequency radiation, while it should heat up a little, i.e., conduct heat well. It is necessary to introduce the TiO_2 phase into the composition of the BeO ceramics as much as possible to obtain a high coefficient.

Keywords: TiO_2 nanoparticles, charge, casting slip, rheological properties, beryllium oxide, ceramics, macrostructure.

Introduction

Currently metals and alloys are increasingly being replaced by ceramic materials that have not only heat resistance and high strength, but also special electrical properties, for example, the ability to absorb electromagnetic radiation, which contributes to their widespread use in electronic engineering [1–2].

It is known that when TiO_2 microparticles are added to the composition of ceramics based on BeO, its dielectric constant and electrical conductivity with appropriate heat treatment in a reducing atmosphere can change significantly [3–4]. The main advantages of absorption (BeO + TiO_2) ceramics include the absence of magnetic properties and decomposing compounds, and the thermodynamic stability of properties in a wide temperature range [5]. It has been established that the addition of TiO_2 impurities to BeO of at least 30 wt % leads to a significant increase in the dielectric constant, and an increase in the degree of TiO_2 reduction is accompanied by an increase in the dielectric loss tangent [6].

Currently the most effective material is the composition BeO+30wt.% TiO_2. Improvement of the performance characteristics of such ceramics can be achieved by introducing TiO_2 nanoparticles into its composition, which will contribute to the expansion of the operating frequency range, increasing the stability of parameters during operation and the impact of external factors, expansion of the nomenclature in the field of special applications [7].

Radiation is absorbed by the entire volume of the particle with a decrease in the size of TiO_2 particles, down to nanoscale values [8].

A smaller crystal size leads to a larger specific surface area and, consequently, to an increase in the number of active centers, bulk and surface defects available for reactions. Reducing reactions proceed more efficiently and changing the electrical and chemical properties. As a result of the quantum size effect, the energy structure changes significantly, leading to optical absorption, photoluminescence, optical nonlinearity and other properties [9].

Thus, the questions of the influence of TiO_2 nanoparticles on the mechanisms of billet formation and the rheological properties of the casting slip of (BeO+TiO_2)-ceramic have not been studied. There is no clear justification for the effect of TiO_2 nanoparticles on the phase composition and mechanisms of structure formation, structure of such ceramics during sintering [10].

Synthesis and research of nanophase high-temperature ceramics with increased density, thermal conductivity, special structural and electrophysical properties is useful for electronic engineering and instrument making in means of radar, navigation and long-distance communications. Interest in composite ceramics based on beryllium oxide with introduced impurities is caused by the needs of new areas of radio electronic engineering and special instrumentation, the development of modern long-distance communication systems, radar and navigation, and broadband systems for special purposes. Beryllium oxide in the process of sintering composite ceramics gives TiO_2 increased density, mechanical strength and thermal conductivity. Different ratios of TiO_2 components in ceramics and the degree of its reduction make it possible to control the amount of ultrahigh frequency absorption by such ceramics. In connection with the above, the development of a technology for obtaining a new material based on beryllium oxide modified with TiO_2 nanopowders is an important task. The aim of this work is to study the methods of introducing nanodispersed TiO_2 powders into the micron matrix of beryllium and titanium oxides.

Material and methods of research

The measurement of the specific surface area was determined on a device for dispersive analysis of the PSC series, the principle of operation of which is based on the method of gas permeability of Kozeny and Karman [11].

The determination of the bulk density of the researched powders was carried out according to the approved factory methodology based on the determination of the bulk density of a unit volume of free bulk powder. The bulk density of the powder with this measurement method is determined by the formula:

$$\gamma = \frac{P_2 - P_1}{V} \tag{1}$$

where, γ — bulk density of powder, g/cm^3; P_2 — powder cylinder weight, g; P_1 — empty cylinder weight, g; ν — calibrated cylinder volume (25 cm^3) [12].

The microstructure, granulometric structure, and phase analysis of powders and sintered samples were studied by using a scanning electron microscope with a JSM-6390LV, 2007 energy dispersive microanalysis, with a resolution in high vacuum up to 3 nm and the possibility of obtaining images in secondary and reflected electrons.

X-ray phase analysis of the powders and the obtained samples was carried out by using an X'PertPRO X-ray diffractometer of thr PANanalytical firm, 2005.

The main parameter of the slip mass «casting ability» was determined on a special factory-made installation PLC-1, which is designed to determine the casting ability of hot thermoplastic slips prepared from ceramic mixes under conditions close to the operation of injection molding machines [13].

Determination of viscosity η in the temperature range 55–80 °C was carried out by using a rotational viscometer RV-8.

The measurement sequence was in accordance with the recommendations of the factory instructions, where the viscosity value was calculated by the formula:

$$\eta = K\frac{P + m - F}{\omega} \tag{2}$$

where η — experiment of material viscosity, poise; P — the total weight of the load installed on two cups, g; m — weight of cups with hooks, g; F — friction loss in bearings, g; ω — inner cylinder rotation speed, sec^{-1}, which is calculated by the formula:

$$\omega = \frac{5}{\tau} \tag{3}$$

where τ — time of five revolutions of the inner cylinder; K — device constant, which depends on the dimensions of the working cylinders and the height of the material loading, cm^{-1}·s^{-2}, is calculated by the formula:

$$K = \frac{R \cdot g}{8\pi^2\left[r_1^2 \cdot r_2^2 \cdot h/(r_2^2 - r_1^2) + r_1^3 \cdot r_2^3/(r_2^3 - r_1^3)\right]} \tag{4}$$

where R — the radius of the pulley on which the thread is wound, cm; r_1- radius of the inner cylinder and hemisphere, cm; r_2 — radius of the outer cylinder, cm; h — immersion height of the inner cylinder into the material, cm; g — acceleration of gravity 981 cm/s^2 [14].

The value of apparent density was determined according to [15].

Results and discussions

It is necessary to carry out complex physicochemical and mechanical studies of the feedstock and sintered products obtained on its basis to predict and correctly interpret the mechanisms of structure formation in ceramics based on BeO with the addition of micro- and nanocrystalline TiO_2 powders, the formation of a structure with specified parametric characteristics and properties.

The highly sintered beryllium oxide powder used in this work was obtained by grinding sintered ceramic scrap in vibrating mills. The characteristics of the powder meet the requirements of TU 95–143–79, for grade «B2» (Table 1).

Table 1

The main characteristics of the used powder of beryllium oxide grade «B2»

Characteristic, № of batch		p 67
Bulk weight $\rho_o \times 10^3$ kg/m^3		0.77
Specific surface area S, cm^2/g		11 000
Moisture % weight		0.08
Average crystal size, μm		5
Elemental content of impurities,% wt	boron	$1.7\cdot10^{-5}$
	silicon	$7.3\cdot10^{-3}$
	manganese	$8.2\cdot10^{-4}$
	iron	$5.1\cdot10^{-2}$
	magnesium	$5.2\cdot10^{-3}$
	chrom	$1.0\cdot10^{-2}$
	nickel	$1.1\cdot10^{-2}$
	aluminum	$3.2\cdot10^{-2}$
	copper	$8.0\cdot10^{-4}$
	zinc	$7.5\cdot10^{-3}$
	calcium	$4.2\cdot10^{-3}$
	silver	$1.1\cdot10^{-5}$
	cadmium	$1.2\cdot10^{-5}$
	lithium	$6.7\cdot10^{-4}$
	sodium	$8.7\cdot10^{-3}$
The amount of impurities,% wt		0.14

The main characteristics of the used micron TiO_2 powder of the rutile modification in terms of quality and chemical composition, according to the passport data, are given in Table 2.

Table 2

Main characteristics of the used micron TiO_2 powder, RK grade, rutile modification

The name of indicators	TI requirements, %	Analysis results
Mass fraction of titanium dioxide,%, not less	99	99.5
Mass fraction of rutile form,%, not less	97	100
Mass fraction of iron compounds in terms of Fe_2O_3,%, no more	0.08	0.05
Mass fraction of phosphorus compounds in terms of P_2O_5,%, no more	0.03	0.03
Mass fraction of sulfur compounds in terms of SiO_3,%, no more	0.03	0.01
Mass fraction for silicon compounds in terms of SiO_2,%, no more	0.15	0.15
Mass fraction of «metallic iron»,%, no more	0.02	0.01
Specific surface, cm^2/g, within	3300–4600	4060

Micron titanium dioxide powder was additionally sieved with a vibrating sieve through a metal mesh № 0045. Powders with a specific surface area of at least 4500 cm^2/g were selected. The average particle size was 5–10 μm. Surface morphology and particle size distribution of micron TiO_2 powder after sieving is shown in Figure 1 (a, b).

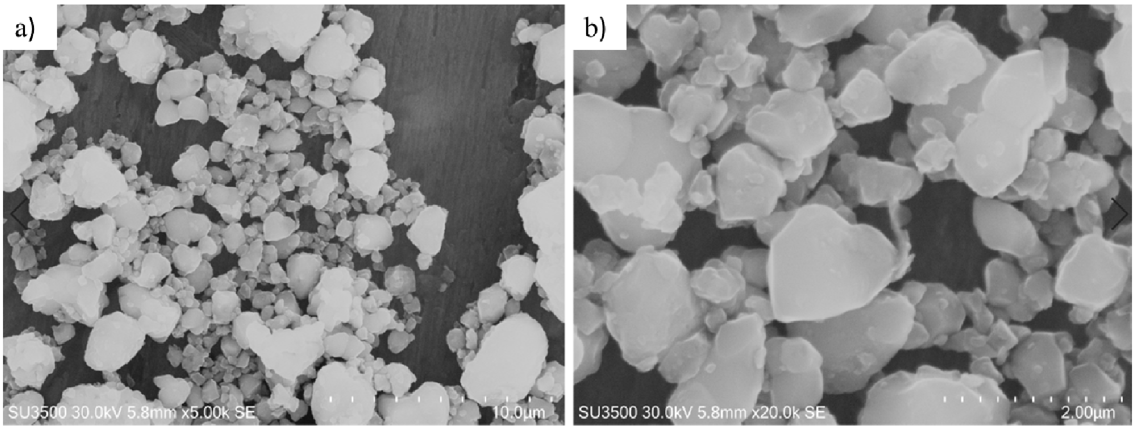

a) — magnification of 5k, b) — magnification of 20k

Figure 1. Micrographs of micron titanium dioxide powders

The X-ray diffraction pattern of a micron TiO_2 powder is shown in Figure 2, small peaks indicate the presence of permissible admixtures (Fe_2O_3, P_2O_5, SiO_2).

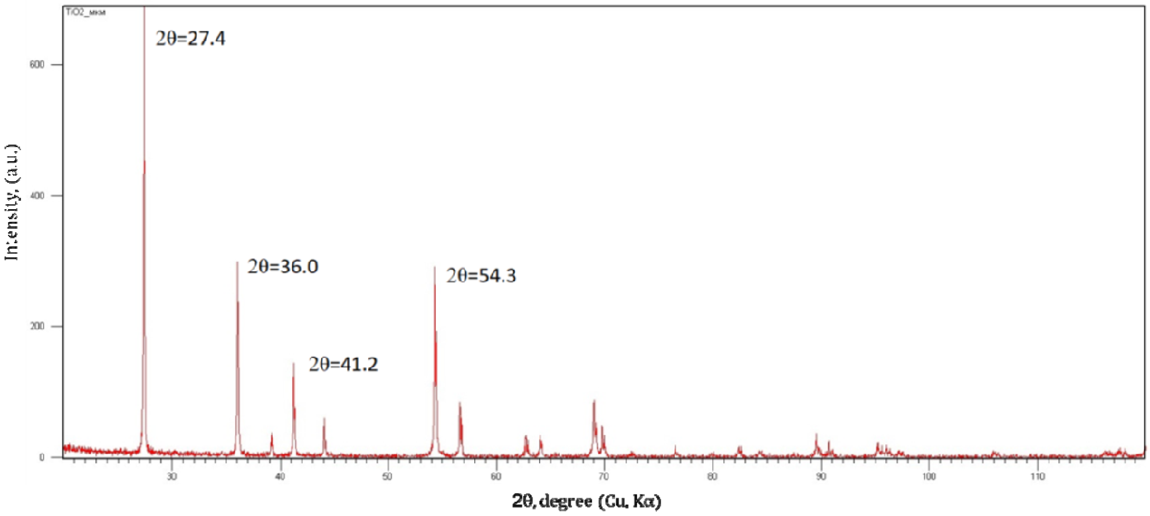

Figure 2. X-ray diffraction pattern from a titanium dioxide sample for 2θ values in the range from 0° to 120°. Deciphering the values of the angles (2θ=27,4; 2θ=36,0; 2θ=39,1 etc.) and peak intensities in the «Quantax 70» program indicates the complete compliance of the sample with the rutile modification of TiO_2

Thus, the micro-powder used in the research contains 99.53 wt%, which corresponds to TI 301–10–020–90. The element-wise content of impurities is also within the permissible values. The results of X-ray structural analysis indicate its full compliance with the rutile modification, which confirms the conditionality and the possibility of manufacturing serial ceramic products using factory technology.

Titanium dioxide nanopowder obtained by the method of electric explosion of a conductor (Fig. 3 a, b.) was used to manufacture experimental samples in order to study the methods of introduction and the effect of nanoparticles on the rheological properties of the foundry slip, their uniformity of distribution in the volume of the micron matrix. A nanopowder is a mixture of irregularly shaped particles ranging in size from 5 to 10 nm.

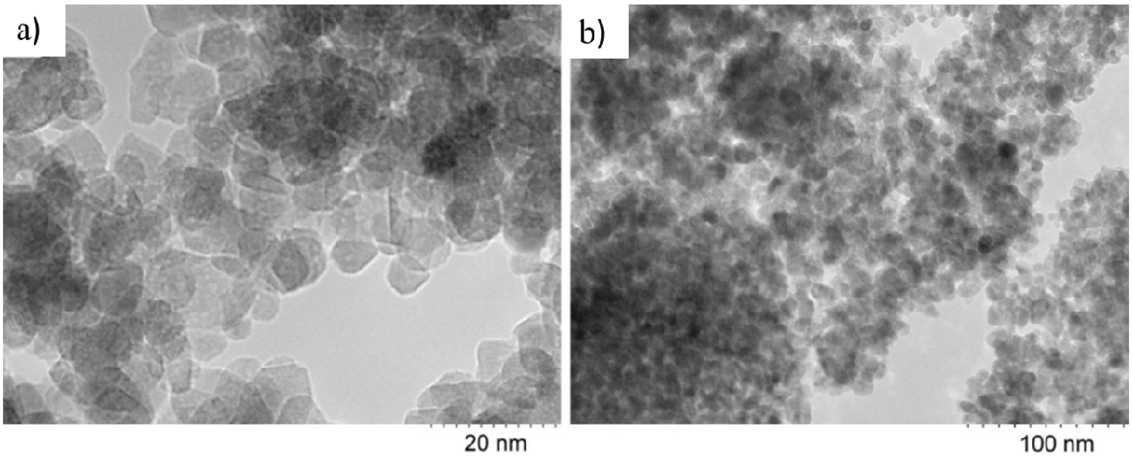

a) magnification 400k, b) magnification 100k

Figure 3. Micrograph of TiO_2 nanoparticles obtained by the method of electrical explosion of a conductor

Along with nanoparticles ≥10 nm, there are formations up to 15 nm in size, which, apparently, are agglomerates of smaller particles. As a rule, the shape of all particles is close to spherical. The research of the particle size distribution showed that the nanopowder has a logarithmically normal distribution with an average particle size of 10 nm. Deviation from the average size is no more than 20 %.

The research results by the XRF method are shown in Figure 4.

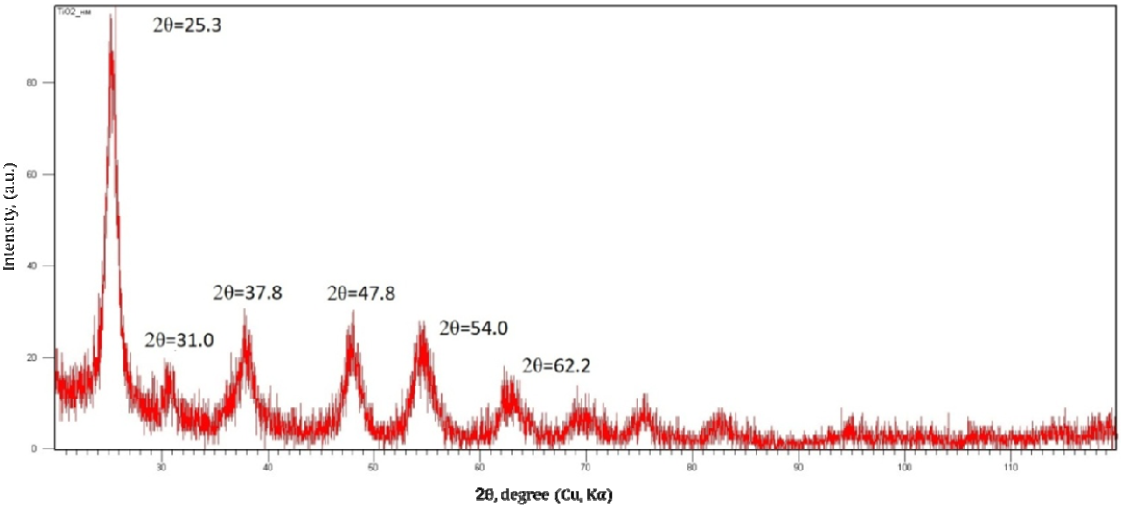

Figure 4. X-ray diffraction pattern from a TiO_2 nanopowder sample for 2θ values in the range from 0° to 120°. Deciphering the values of the angles (2θ = 25,3; 2θ = 31,0; 2θ = 37,8,0 and etc.) and peak intensities in the «Quantax 70» program indicates the complete compliance of the sample with the anatase modification of TiO_2

The insertion of nanoparticles into the composition of the charge is one of the most difficult tasks from the technological point of view [16]. Nanoparticles must be evenly distributed over the entire volume of the charge, to exclude their possible coagulation and agglomeration. The problem was solved in several ways: mixed dry and in a liquid medium in a roller mill; in a liquid medium in a specially designed impeller-type reactor with continuous bubbling with compressed air.

The dry mixing method failed to achieve a uniform distribution of particles in the volume of micron powders, due to the fact that the components of the charge are distributed mainly along the perimeter of the working chamber, under the action of centrifugal force, while mixing occurs only in the direction of rotation of the drum. The slip mass from the charge obtained by this technology was not prepared.

The method of introducing nanoparticles in which mixing of the charge components was carried out in a specially designed impeller-type reactor was the most effective. The installation is a cylindrical vertically located stainless steel tank on a rigid base, inside which a shaft with blades is installed, during the rotation of which the charge is mixed, and compressed air is continuously supplied in the lower part (Fig. 5).

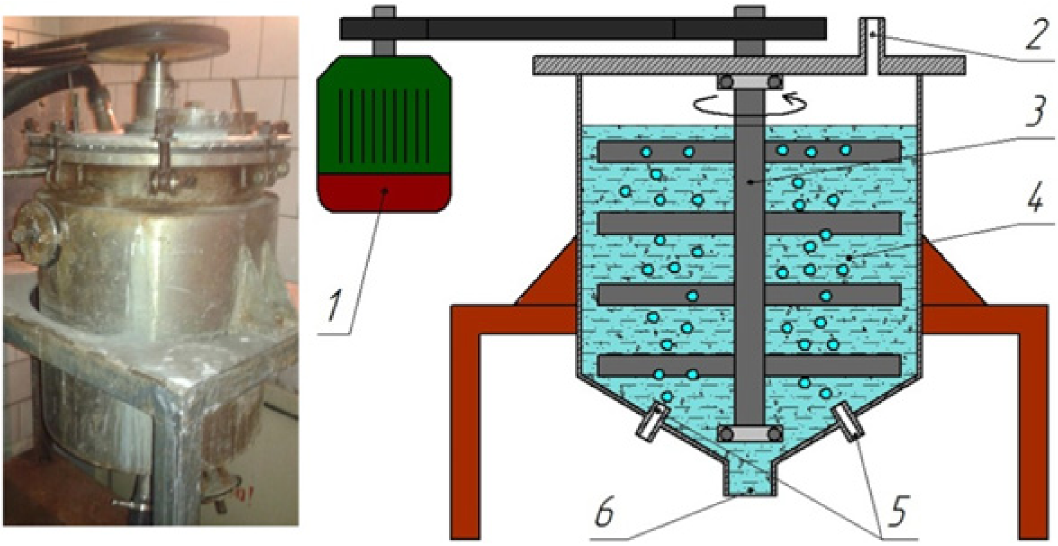

1 — electric motor; 2 — compressed air supply channel; 3 — shaft with blades; 4 — charge;
5 — supply of compressed air for bubbling the charge; 6 — drain hole.

Figure 5. Schematic diagram of the P-60 reactor operation

Air bubbles, rising up according to the Archimedes law through the entire volume of the charge, allow the movement of flows in the liquid not only in the horizontal, but also in the vertical direction.

Samples were obtained with additives 5; 10; 15; 20; 25; 30 wt.%.%TiO_2^{nano} rest of BeO and 0.1; 0.5; 1.0; 1.5; 2.0 wt.%TiO_2^{nano}+$TiO_2^{\mu m}$+70 wt% BeO to study the effect of the method of introducing nanoparticles into the micron matrix of beryllium and titanium oxides, on the uniformity of their distribution and the effect on the rheological properties of the casting slip.

The mixtures of the following composition (1-x)BeO+xTiO_2 were obtained by using the developed technology for introducing nanoparticles, Table 3.

Table 3

Values of the main parameters of the charge with the addition of TiO_2^{nano} nanoparticles

(1-)BeO+xTiO_2	x=0.05 (5 %)	x=0.1 (10 %)	x=0.15 (15 %)	x=0.2 (20 %)	x=0.25 (25 %)	x=0.3 (30 %)
Ssp., cm^2/g	16200	17000	17700	18000	18100	18400
Nat. weight., g/cm^3	0.76	0.74	0.70	0.67	0.63	0.60

As can be seen from the data in Table 3, the specific surface area predictably increases with an increase in the concentration of TiO_2 nanoparticles. It should be noted that the specific surface area of the beryllium oxide powder BeO used in this study was 11000 cm^2/g.

The indicator of the flowability of the charge is the bulk density, that is, its density in the unconsolidated state, which takes into account not only the volume of the material particles themselves, but also the space between them, also decreases with an increase in the concentration of nanoadditives. For both physical characteristics, there are tendencies of change inherent in the presence of nanoparticles.

Further, slip masses were prepared for each percentage composition on the basis of an organic binder — wax, paraffin, oleic acid at the rate of LOI (loss on ignition) — 9.5 %. The rheological properties of the obtained slip batches are presented in Table 4.

Table 4

Rheological properties of thermoplastic slips based on beryllium oxide with the addition of nanoparticles 5–30 wt.% TiO_2^{nano}

(1-x)BeO+xTiO_2	x=0.05 (5 %)	x=0.1 (10 %)	x=0.15 (15 %)	x=0.2 (20 %)	x=0.25 (25 %)	x=0.3 (30 %)
LOI, %	9,5	9,3	9,4	9,2	9,3	9,3
Viscosity, Pa·s	45	59	72	88	93	107
Casting capacity, mm	76	62	41	33	27	16

In the process of casting blanks using TiO_2 nanopowders it was noted that the rheological properties of the slip mass strongly changed with an increase in their concentration: the slip became viscous and difficult to mix (Table 4). This is due to the fact that nanoparticles, having a highly active surface, require the introduction of a much larger amount of organic binder, compared with micron-sized TiO_2 powders, which negatively affects the properties of slips (viscosity and castability) and the quality of sintered products in the form of the presence of shells, impurities and excessive porosity.

As it is known, the casting ability of a slip characterizes its suitability for casting articles of a given configuration. It is a conditional complex characteristic that depends on the viscosity and the rate of solidification. The lower the viscosity and speed of solidification of the slip, the higher its casting ability. In turn, the viscosity determines the ability of the foundry mass to continuously fill the mold during the casting process. It is possible to increase the casting ability indicator by adding a binder to the slip mass, however, the more binder in the slip, the worse the quality of the sintered product, since after the operation of burning the binder, the evaporated organic matter leaves behind defects in the form of various cavities and pores. Thus, for the purity of the experiment, it was decided not to increase the castability of the slip by adding a binder. Forming a billet by slip casting is possible by increasing the pressure applied to the slip in the case of a low casting capacity.

Work on forming the blanks was carried out on a micro-casting unit for casting thermoplastic slips of factory design (Fig. 6).

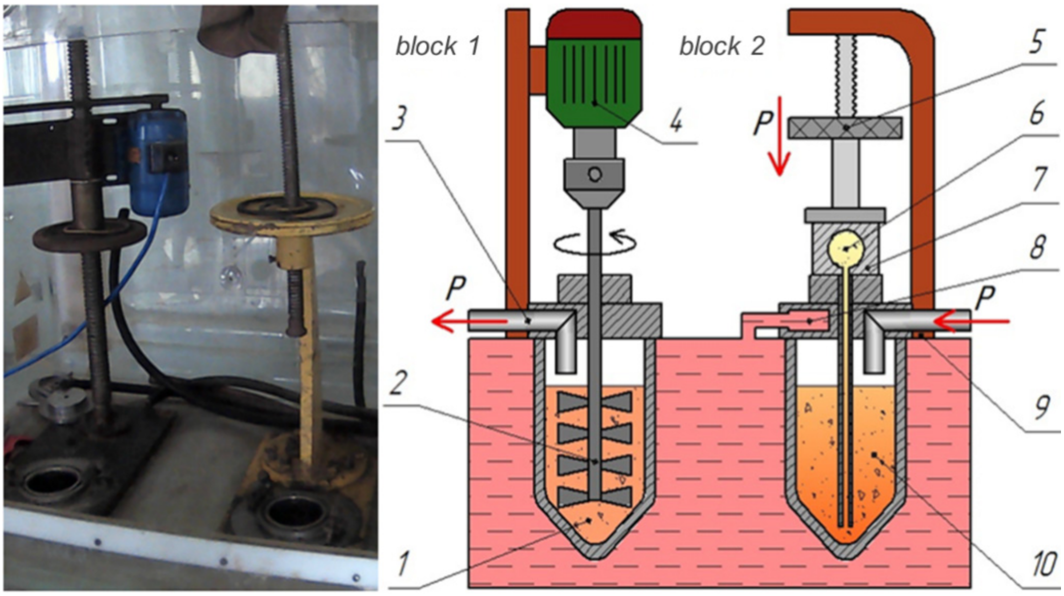

1 — slip mass in the evacuation reactor; 2 — shaft with blades; 3 — evacuation channel;
4 — electric motor; 5 — steering wheel for pressing the casting mold; 6 — formed blank; 7 — casting mold;
8 — heating circuit; 9 — compressed air supply channel; 10 — slip mass in a casting reactor.

Figure 6. Photo and schematic diagram of the micro-casting installation

The pressure on the slip was proportionally increased with an increase in the concentration of nanoparticles to maintain the required pouring rate, according to the graph shown in Figure 7.

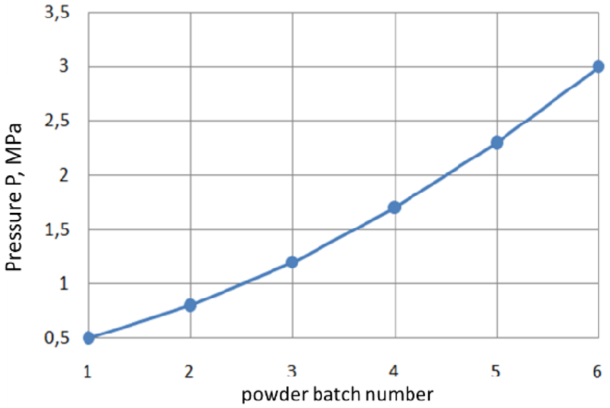

Figure 7. Graph of the dependence of the pressure change on the slip from the concentration of nanoparticles in the range of 5–30 wt.% TiO_2^{nano}, batches 1–6, respectively

Next, samples were obtained, the composition of which is shown in Table 5. In order to improve the rheological properties of the casting slip the amount of added nanoadditives was limited from 0.1 to 2.0 wt.% TiO_2^{nano}.

Table 5

Values of the main parameters of the charge with the addition of nanoparticles 0.1–2.0 wt%

№ batches	The composition of the charge	$S_{sp.}$, cm^2/g	Nat. weight., g/cm^3
P1	BeO + 29.9 wt.%$TiO_2^{μm}$ + 0.1 wt.%TiO_2^{nano}	12700	1.07
P 2	BeO + 29.5 wt.%$TiO_2^{μm}$+ 0.5 wt.%TiO_2^{nano}	13800	1.03
P 3	BeO + 29.0 wt.%$TiO_2^{μm}$+ 1.0 wt.%TiO_2^{nano}	14600	0.97
P 4	BeO + 28.5 wt.%$TiO_2^{μm}$+ 1.5 wt.%TiO_2^{nano}	15700	0.93
P 5	BeO + 28.0 wt.%$TiO_2^{μm}$+ 2.0 wt.%TiO_2^{nano}	16200	0.90

The specific surface area also increases with the introduction of nanoparticles up to 2.0 wt% into the volume of the charge. The specific surface area of the beryllium oxide powder BeO used in this study was also 11000 cm^2/g, and the specific surface area of the titanium dioxide powder was 10000 cm^2/g. The indicator of the flowability of the charge, the bulk density, also does not significantly decrease with an increase in the concentration of nanoadditives, remaining in the permissible range of values.

Further, slip masses were prepared for each percentage composition on the basis of an organic binder — wax, paraffin, oleic acid at the rate of LOI (loss on ignition) — 9.5 %. The composition of the wax paraffin components and the slips preparation technology are identical.

The rheological properties of the obtained slips batches are presented in Table 6.

Table 6

Rheological properties of thermoplastic slips with the addition of nanoparticles 0.1–2.0 wt.%

Characteristics	P1	P2	P3	P4	P5
LOI, %	9.6	9.4	9.2	9.2	9.2
Viscosity, Pa·s	49	48	44	43	40
Casting capacity, mm	63	65	71	78	83

As can be seen from Table 6, the rheological properties of slips with the introduction of nanoparticles in the range of 0.1–2.0 wt.% remain at an acceptable level. The casting ability of the slip increases with an increase in the concentration of nanoparticles, it becomes less viscous. Thus, a relatively small number of introduced nanoparticles allows maintaining a minimum volume of organic binder while maintaining the casting properties of the slip mass at an acceptable level.

Due to the increase in casting capacity, the pressure on the slip was decreased in proportion to the increase in the concentration of nanoparticles, according to the graph shown in Figure 8.

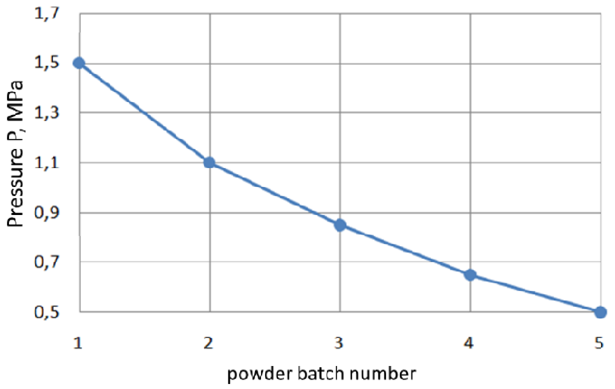

Figure 8. Graph of the dependence of the pressure change on the slip from the concentration of nanoparticles in the range from 0.1 to 2.0 wt.%, batches 1–5, respectively

The observed effect is explained by the filling of voids between solid and larger powder particles with particles of smaller fractions, as a result of which the density of the charge increases, and the reorientation of large grains contributes to a decrease in friction against the walls of the tooling.

On the obtained samples there are many fragments of the TiO_2 phase and pores after sintering, predominantly round form with the size up to 3 mm, indicating the processes of conglomeration of nanoparticles. The number of fragments increases in proportion to the introduced amount of TiO_2^{nano} in the case of the introduction of nanoparticles 5.0–30.0 wt.% (Fig. 9).

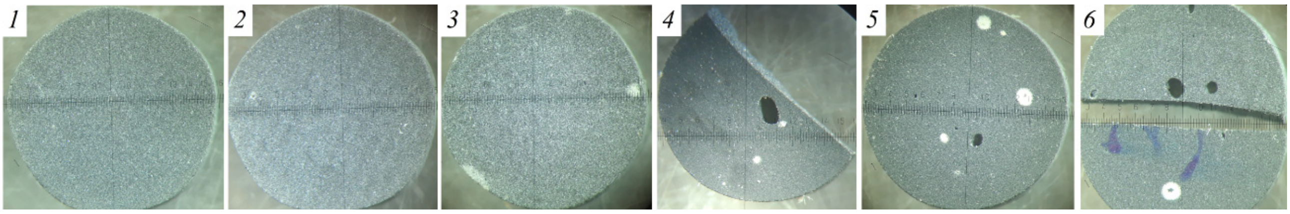

The figure signature number corresponds to the batch number according to: P1– 5wt.%TiO_2^{nano};
P2 — 10wt.%TiO_2^{nano}; P3 — 15wt.%TiO_2^{nano}; P4 –20wt.%TiO_2^{nano}; P5 –25wt.%$TiO_2^{nano}$and P6 — 30wt.%TiO_2^{nano}.

Figure 9. Macrostructure of samples containing TiO_2 nanoparticles. Magnification × 16

Thus, it is not possible to obtain a completely homogeneous sample without pores and impurities containing nanoparticles from 5 to 30 wt% TiO_2.

Figure 10 shows the macrostructure of samples containing nanoparticles of 0.5–2.0 wt%.

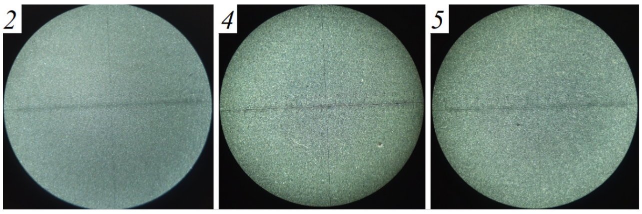

The figure signature number corresponds to the batch number according to:
P2 — 0.5wt.%TiO_2^{nano}; P4 — 1.5wt%$TiO_2^{nano}$and P5 — 2.0wt%TiO_2^{nano}

Figure 10. The macrostructure of samples with containing nanoparticles of TiO_2. Magnification × 16

As can be seen, the macrostructure of the samples with a nanoparticle content of up to 2.0 wt% is rather uniform with this method of introducing nanoparticles, there are practically no grouped fragments of the TiO_2 phase. Thus, it is not possible to obtain a homogeneous, dense sample with the introduction of nanoparticles in excess of 5 wt%.

Conclusions

1. In this work an effective method is proposed for introducing nanodispersed TiO_2 powders into a micron matrix of beryllium and titanium oxides, in which air bubbles, rising upward according to the Archimedes law through the entire volume of the charge, allow the movement of flows in the liquid not only horizontally, but also in the vertical direction.
2. It has been experimentally shown that the addition of nanoparticles from 5 to 30 wt% TiO_2^{nano} negatively affects the casting properties of slips (viscosity and casting ability) and, consequently to the quality of sintered products in the form of cavities, impurities and excessive porosity.
3. As a result of research, the effect of the concentration of nanoparticles on the main technological parameters, such as specific surface area, bulk density, viscosity, casting ability, pressure on the slip during billet molding, the optimal concentration of nanopowder of TiO_2, — 0.1 — 2.0 wt. % was established, providing normal indicators of technological parameters.

Acknowledgments

The work was carried out within the framework of grant funding for scientific research on 2021–2023 years by the Science Committee of the Ministry of Education and Science of the Republic of Kazakhstan (AP09058686).

References

1 Кийко В.С. Керамика на основе оксида бериллия: получение, физико-химические свойства и применение / В.С. Кийко, Ю.Н. Макурин, А.Л. Ивановский. — Екатеринбург: УрО РАН, 2006. — 440 с.

2 Кийко В.С. Получение, физико-химические свойства и пропускание СВЧ-излучения керамикой на основе BeO / В.С. Кийко, С.Н. Шабунин, Ю.Н. Макурин // Огнеупоры и техническая керамика. — 2004. — № 10. — С. 8–17.

3 Kiiko V.S. Microstructure and electrical conductivity of compositing ($BeO+TiO_2$) ceramics / V.S. Kiiko, M.A. Gorbunova, Y.N. Makurin, A.D. Neuimin, A.L. Ivanovskii // Refractories and Industrial Ceramics. — 2007. — Vol. 48, No. 6. — P. 429–434.

4 Кийко В.С. Композиционная ($BeO+TiO_2$)-керамика для электронной и других областей техники / В.С. Кийко, А.В. Павлов // Новые огнеупоры. — 2017. — № 12. — С. 64–70.

5 Кийко В.С. Влияние добавок диоксида титана на физико-химические и люминесцентные свойства бериллиевой керамики / В.С. Кийко // Неорган. материалы. — 1994. — Т. 30, № 5. — С. 688–693.

6 Дрокин Н.А. Электрофизические свойства керамики БТ-30 / Н.А. Дрокин, В.С. Кийко, А.В. Павлов, А.И Малкин // Новые огнеупоры. — 2020. — № 6. — С. 56–63.

7 Мальцев П. СВЧ-технологии — основа электроники будущего / П. Мальцев, И. Шахнович // Электроника наука /технология /бизнес. — 2015. — № 8 (00148). — С. 72–84.

8 Морозов А.Н. Синтез и каталитические свойства наноструктурированных покрытий диоксида титана: дис. ... канд. хим. наук: 05.17.01 / Морозов Александр Николаевич; Рос. хим.-техн. ун-т им. Д.И. Менделеева. — М., 2014. — 160 с.

9 Serpone N. Size effects on the photophysical properties of colloidal anatase TiO_2 particles: size quantization versus direct transitions in this indirect semiconductor / N. Serpone, D. Lawless, R. Khairutdinov // J. Phys. Chem. — 1995. — Vol. 99, No. 45. — 1995. — P. 16646–16654.

10 Sagdoldina Zh.B. Structural evolution of ceramic coatings by mechanical alloying / Zh.B. Sagdoldina, B.K. Rakhadilov, M.K. Skakov, O. Stepanova // Materials testing. — 2019. — Vol 61, No 4. — P. 304–308.

11 ГОСТ 23401–90. Порошки металлические. Катализаторы и носители. Определение удельной поверхности. — М.: Изд-во стандартов, 1991. — С. 10.

12 ГОСТ 19440–94. Металлические порошки. Определение насыпной плотности. — М. Изд-во стандартов, 1997. — С. 41.

13 Rakhadilov, B.K. Development of air-plasma technology for hardening cutting tools by applying wear-resistant coatings / B.K. Rakhadilov, A.B. Kenesbekov, P. Kowalevski, Y.A. Ocheredko, Zh.B. Sagdoldina // News of the National Academy of Sciences of the Republic of Kazakhstan, Series of Geology and Technical Sciences. — 2020. — No 3(441). — P. 54–62.

14 Rakhadilov B.K. Preparation of powder coatings on the surface of steel balls by mechanochemical synthesis / B.K. Rakhadilov, D.B. Buitkenov, Zh.B. Sagdoldina, L.G. Zhurerova, W. Wieleba // Bulletin of the university of Karaganda-Physics. — 2020. — Vol. 4 (100). — P. 8–13.

15 ГОСТ 2409–95. Огнеупоры. Способ определения кажущейся плотности, открытой, полной и закрытой пористости, водопоглощения. — М.: Изд-во стандартов, 2004. — С. 5.

16 Погожев Ю.С. Дисперсно-упрочненные наночастицами электродные материалы и покрытия на основе карбида титана: дис. ... канд.ист. наук. техн.: 05.16.06 / Погожев Юрий Сергеевич; Моск. гос. ин-т стали и сплавов. — М., 2006. — 184 с.

А.В. Павлов, Е.Е. Айымханов, Ж.Б. Сагдолдина, А.Б. Касымов, Д.Р. Байжан, М.С. Жапарова

TiO_2 нанобөлшектерін BeO және TiO_2 ұнтақтарының микрондық матрицасына енгізу әдістерін және олардың құю шликерінің реологиялық қасиеттеріне әсерін зерттеу

Мақалада нанодисперсті титан оксиді TiO_2 ұнтақтарын бериллий мен титан оксидтерінің микрон матрицасына енгізу әдістерінің зерттеу нәтижелері көрсетілген. 5 %-дан жоғары нанобөлшектердің болуы құю шликерінің реологиялық қасиеттеріне теріс әсер етеді және керісінше, 0,1–2,0 мас. % аралығында нанобөлшектердің қосылуы тұтқырлықты төмендетуге және жылжымалы массаның құю қабілетін арттыруға ықпал етеді. Агрегатталған дайындаманы макроқұрылымдық талдау нанобөлшектердің конгломераттары немесе нано- және микро- TiO_2 бөлшектері түрінде құрылымдық элементтердің толық болмауын көрсетеді. Нанобөлшектерді енгізудің дамыған әдісі өнімді шликерді құю арқылы дайындаманың бүкіл көлеміне біркелкі таратуға мүмкіндік береді. Ғылыми жұмыстың авторлары болашақта алынған нанобөлшектері бар керамиканың жылу физикалық және импеданс сипаттамаларына нанобөлшектердің әсерін зерттеуді жоспарлады. Ғылыми әлемде наноұнтақтардың бериллий керамикасының электрофизикалық қасиеттеріне әсерін зерттеу туралы белгісіз. Бериллий оксиді және титан оксидтері қоспасы BeO+TiO_2 керамикасының ең маңызды қасиеттерінің бірі — аса жоғарғы жиілікте сәулеленуді сіңіру қабілеті, ол аз қызуы керек, яғни жылуды жақсы өткізеді. Жоғары коэффициентті алу үшін BeO керамика құрамына TiO_2 фазасын мүмкіндігінше көп енгізу керек.

Кілт сөздер: TiO_2 нанобөлшектері, шихта, құю шликері, реологиялық қасиеттері, берилий оксиді, керамика, макроқұрылым.

А.В. Павлов, Е.Е. Айымханов, Ж.Б. Сагдолдина, А.Б. Касымов, Д.Р. Байжан, М.С. Жапарова

Исследование методов введения наночастиц TiO_2 в микронную матрицу порошков BeO и TiO_2 и их влияния на реологические свойства литейного шликера

В статье представлены результаты исследований методов введения нанодисперсных порошков TiO_2 в микронную матрицу оксидов бериллия и титана. Показано, что наличие наночастиц свыше 5,0 мас. % отрицательно влияет на реологические свойства литейного шликера, и, наоборот, добавление наночастиц в диапазоне 0,1–2,0 мас. % способствует снижению вязкости и повышению литейной способности шликерной массы. Макроструктурный анализ спеченной заготовки свидетельствует о полном отсутствии структурных элементов в виде конгломератов наночастиц или частиц нано- и микро-TiO_2. Разработанный способ введения наночастиц позволяет получать изделия с их равномерным распределением по всему объему заготовки методом шликерного литья под давлением. В дальнейшем авторы научной работы планировали исследовать влияние наночастиц на теплофизические и импедансные характеристики полученной керамики. Об исследованиях влияния нанопорошков на электрофизические свойства бериллиевой керамики в научном мире не известно. Самыми важными свойствами, которыми должна обладать керамика BeO+TiO_2, это способность поглощать СВЧ-излучение, при этом она должна мало нагреваться, т.е. хорошо проводить тепло. Для получения высокого коэффициента необходимо как можно больше вводить в состав керамики BeO фазу TiO_2.

Ключевые слова: наночастицы TiO_2, шихта, шликер, реологические свойства, оксид бериллия, керамика, макроструктура.

References

1 Kiiko, V.S., Makurin, Iu.N., & Ivanovskii, A.L. (2006). Keramika na osnove oksida berilliia: poluchenie, fiziko-khimicheskie svoistva i primenenie [Beryllium oxide-based ceramics: preparation, physical and chemical properties and application]. *Ekaterinburg: UrO RAN*, 440 [in Russian].

2 Kiiko, V.S., Shabunin, S.N., & Makurin, Yu.N. (2004). Poluchenie, fiziko-khimicheskie svoistva i propuskanie SVCh-izlucheniia keramikoi na osnove BeO [Production, physical and chemical properties and transmission of microwave radiation by BeO-based ceramics]. *Ogneupory i tekhnicheskaia keramika — Refractories and technical ceramics,* 10, 8–17 [in Russian].

3 Kiiko, V.S., Gorbunova, M.A., Makurin, Y.N., Neuimin, A.D., & Ivanovskii, A.L. (2007). Microstructure and electrical conductivity of compositing (BeO+TiO_2) ceramics, *Refractories and Industrial Ceramics*, 48(6), 429–434.

4 Kiiko, V.S., & Pavlov, A.V. (2017). Kompozitsionnaia (BeO+TiO_2)-keramika dlia elektronnoi i drugikh oblastei tekhniki [Composite (BeO+TiO_2)-ceramics for electronic and other fields of technology]. *Novye ogneupory — New refractories*, 12, 64–70 [in Russian].

5 Kiiko, V.S. (1994). Vliianie dobavok dioksida titana na fiziko-khimicheskie i liuminestsentnye svoistva berillievoi keramiki [Effect of titanium dioxide additives on the physicochemical and luminescent properties of beryllium ceramics]. *Neorganicheskie materialy — Inorganic Materials*, 30(5), 688–693 [in Russian].

6 Drokin, N.A., Kiiko, V.S., Pavlov, A.V., & Malkin, A.I (2020). Elektrofizicheskie svoistva keramiki BT-30 [Electrophysical properties of BT-30 ceramics]. *Novye ogneupory-New refractories,* 6, 56–63 [in Russian].

7 Maltsev, P., & Shakhnovich, I. (2015). SVCh-tekhnologii — osnova elektroniki budushchego [Microwave technologies-the basis of electronics of the future]. *Elektronika nauka /tekhnologiia /biznes — Electronics science /technology /business,* 8 (00148), 72–84 [in Russian].

8 Morozov, A.N. (2014). Sintez i kataliticheskie svoistva nanostrukturirovannykh pokrytii dioksida titana [Synthesis and catalytic properties of nanostructured titanium dioxide coatings]. *Candidate's thesis.* Moscow [in Russian].

9 Serpone, N., Lawless, D., & Khairutdinov, R. (1995). Size effects on the photophysical properties of colloidal anatase TiO_2 particles: size quantization versus direct transitions in this indirect semiconductor, *J. Phys. Chem.,* 99(45), 16646–16654.

10 Sagdoldina, Zh.B., Rakhadilov, B.K., Skakov, M.K., & Stepanova, O. (2019). Structural evolution of ceramic coatings by mechanical alloying, *Materials testing,* 61(4), 304–308.

11 GOST 23401–90. Poroshki metallicheskie. Katalizatory i nositeli. Opredelenie udelnoi poverkhnosti [State Standard 23401–90 Metal powders. Catalysts and carriers. Determination of the specific surface area]. (1991). Moscow: Izdatelstvo standartov [in Russian].

12 GOST 19440–94. Metallicheskie poroshki. Opredelenie nasypnoi plotnosti [State Standard 19440–94 Metal powders. Determination of bulk density]. (1997). Moscow: Izdatelstvo standartov [in Russian].

13 Rakhadilov, B.K., Kenesbekov, A.B., Kowalevski, P., Ocheredko, Y.A., & Sagdoldina, Zh.B. (2020). Development of air-plasma technology for hardening cutting tools by applying wear-resistant coatings, *News of the National Academy of Sciences of the Republic of Kazakhstan, Series of Geology and Technical Sciences,* 3(441), 54–62.

14 Rakhadilov, B.K., Buitkenov, D.B., Sagdoldina, Zh.B., Zhurerova, L.G., & Wieleba, W. (2020). Preparation of powder coatings on the surface of steel balls by mechanochemical synthesis, *Bulletin of the university of Karaganda-Physics*, 4 (100), 8–13.

15 GOST 2409–95. Ogneupory. Sposob opredeleniia kazhushcheisia plotnosti, otkrytoi, polnoi i zakrytoi poristosti, vodopogloshcheniia [State Standard 2409–95 Refractories. Method for determining the apparent density, open, full and closed porosity, water absorption]. (2004). Moscow: Izdatelstvo standartov [in Russian].

16 Pogozhev, Yu.S. (2006). Dispersno-uprochnennye nanochastitsami elektrodnye materialy i pokrytiia na osnove karbida titana [Nanoparticle-reinforced electrode materials and coatings based on titanium carbide*]. Candidate's thesis. Moskovskii gosudarstvennyi institut stali i splavov. Moscow* [in Russian].

КОНДЕНСАЦИЯЛАНҒАН КҮЙДІҢ ФИЗИКАСЫ
ФИЗИКА КОНДЕНСИРОВАННОГО СОСТОЯНИЯ
PHYSICS OF THE CONDENSED MATTER

DOI 10.31489/2021Ph3/83-92
UDC 68.004.05

N.I. Kosach[1], V.B. Bolshakov[2], I.T. Bohdanov[3], Y.O. Suchikova[3*]

[1]State Enterprise KHARKIV MACHINERY PLAN «FED», Kharkiv, Ukraine;
[2]Civil organization «Ukraienian Academy of Metrology», Kyiv, Ukraine;
[3]Berdyansk State Pedagogical University, Ukraine
([*]yanasuchikova@gmail.com)

Statistical evaluation of morphological parameters of porous nanostructures on the synthesized indium phosphide surface

A constructive method for estimating the surface morphology of nanostructured semiconductors, which consists in determining the main statistical characteristics of the aggregate structure of nanoscale objects on their synthesized surface is presented. In terms of the indium phosphide semiconductor with a synthesized porous layer on its surface, it is shown that the evaluation of the main statistical characteristics allows a deeper understanding of the kinetics of the pore formation process during typical electrochemical treatment of the crystal. The determination of the main statistical metrologically based characteristics (indicators of the distribution center, variation, and shape of the distribution) allows us to understand in more detail view the processes occurring during electrochemical processing of crystals. In the long run, this will make it possible to create nanostructures with predetermined properties, which will become the basis for the industrial production of high-quality nanostructured semiconductors.

Keywords: synthesis, semiconductors, surface morphology, measurement, aggregate structure, statistical analysis, indium phosphide, ImageJ.

Introduction

Currently, nanotechnology is the industry demonstrating the fastest development rates. It is widely used to create ultra-fast and super-powerful computers [1, 2], in electronics (lasers, photonics) [3], alternative energy [4, 5], information technologies (information transmission and storage) [6], environmental monitoring (wastewater, air, soil) [7], as well as in a number of other utmost relevant applied aspects of science and technology [8, 9].

The necessity for this is that nanomaterials are characterized, as a rule, by a much larger proportion of surface atoms, which determine the dominant features of the physical and chemical properties of materials [10]. Thus, structuring the surface of semiconductors leads to an increase of their effective area by tenfolds, which has an important practical consequence for improving the efficiency of photo-emmissive energy converters [11, 12]. In addition, quantum-dimensional effects begin to appear at the submicron level [13]. This property is possessed by quantum dots [14, 15], nanoconductors [16], nanowires [17], porous layers [18], etc.

In this regard, the synthesis of nanostructures with specified functional characteristics and, first of all, controlled sizes of nanoobjects remains as a crucial problem in recent decades. This is emphasized in such program documents as «Strategic Research and Innovation Agenda for Nanomedicine, European Technology Platform on Nanomedicine, 2016–2030» [19], «EU US Roadmap Nanoinformatics, 2017–2030» [20], «Continuing to Protect the Nanotechnology Workforce: NIOSH Nanotechnology Research Plan for 2018–2025» [21].

The complexity of solving this problem is due to the fact that two competing mechanisms always operate during the formation of surface nanostructures: the nanostructures generation with specified properties

[22] and the self-organization of nanoobjects [23]. Overcoming this contradiction is possible only with a complete, detailed analysis of the statistical characteristics of the synthesized surface morphology, the most promising tool for which is the analysis of microscopic images of the surface of nanomaterials using statistical methods [24].

The article presents the results of representative metrologically based studies of the surface morphology of a nanostructured semiconductor, namely, the establishment of statistical characteristics of the pore distribution over diameter in a typical process of nanostructure synthesis, which, along with previously obtained results of the trend of their dependence on etching time [25], allows creating crystals with a predetermined aggregate structure.

Methods and materials

The surface morphology of a nanostructured semiconductor during its synthesis was studied experimentally on the example of a sample of n-type single-crystal indium phosphide (por-InP) with surface orientation (111) [26]. Porous surface layers of indium phosphide were obtained by typical electrochemical etching of a sample in a hydrochloric acid solution ($10H_2O+1HCl$). The etching time $t = 20$ min, current density of $j = 150$ mA/cm^2. Plates of indium monocrystalline phosphide were polished before etching and cleaned with alcohol and vinegar. The pores on the plate were formed in a standard electrolytic cell with platinum at the cathode [27]. After this they were dried in air and subjected to short-term drawing in a nitrogen stream to stabilize the properties. The morphology of the synthesized nanoobjects was studied using a JEOL-6490 raster electron microscope with a resolution of up to 3.0 nm, accelerating voltage (0.3–30) kW; magnification from x5 to x300,000; types of contrast (secondary and reflected electrons): topographic, compositional, and shadow.

For representativeness of the experiment, 10 crystal plates were examined and 5 observations of the morphology of nanoobjects on the surface of each sample were made, the results of which were within the limits of confidence intervals of ± 5 % for the measured value $P = 0.95$.

Raster processing of photomicrographs under surface analysis based on selected morphological characteristics was performed using the ImageJ program. Statistical processing of results was performed using the Origin Pro program.

The main tasks of analyzing photomicrographs of the surface of nanostructured samples are:

- statistical processing of the obtained in the measurement process of objects parameters;
- determination of the average values of the values obtained;
- the construction of graphic dependences for visualization of the analysis process.

A two-dimensional image, obtained using a microscope, in a certain approximation could be considered as a matrix, the indexes of which describe the numbers of rows and columns, and the numerical values of elements characterize the color intensity. The main parameter that characterizes a digital image is its resolution (the number of pixels in the original image and the color depth).

The morphological parameter used for the analysis is the average pore diameter, despite the fact that the pores have a cone shape-the diameter of their Don is less than the diameter of the surface section, for simplicity of research, but without losing the generality and correctness of the results obtained, it was considered that they have a cylindrical shape in the lumbar section.

For statistical estimation of the pore distribution by diameter the values of the indicators of the average diameter series in ascending order were ranked and sorted. To estimate the distribution series the main statistical indicators of the distribution center are found: the mode, median, and simple arithmetic mean of its value, as well as indicators of variation in the pore distribution series over the diameter. The change in the variation of the distribution of the series over the diameter in the aggregate was carried out using absolute and relative indicators, which were determined by calculating the asymmetry coefficients, Pearson, and the access indicator.

Results and Discussion

Figure 1 shows a typical micrography obtained using a microscope of the studied fragment of one of the samples. Visual analysis of photomicrograph shows that the synthesized surface of indium phosphide is densely covered with pores. The pores shape the tracks. The nature of these tracks are micro-scratches on the surface of the plate [28]. They can also be caused by uneven impurity distribution and the crystallographic orientation of the semiconductor plate [29]. Along the track line, the pores tend to merge and form long channels [30]. Isolated pores are mostly cylindrical in cross-section. Some areas have massive etched pits, the appearance of which is most often associated with the release of dislocation to the surface [31, 32].

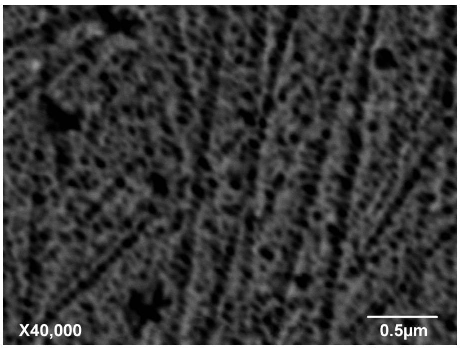

Figure 1. Morphology of *por-InP:*

Figure 2 shows the raster processing of microphotograph performed in the ImageJ program. To increase the contrast of the pore borders, a Bandpass filter based on Fourier transform is used allowing to remove both high and low spatial frequencies in the image [33]. The Watershed algorithm is used to separate adjacent crystallites and pores with indistinct boundaries [34].

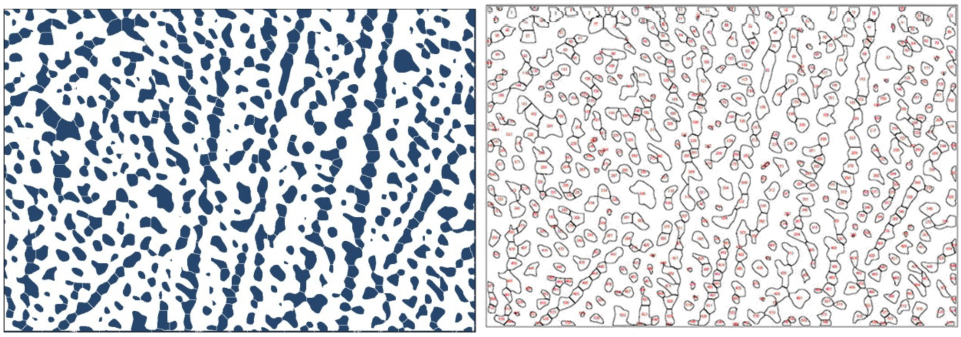

a) b)

Figure 2. Results of processing a microscopic image of the sample surface using the ImageJ program
a) after the binarization process, b) after using the Watershed algorithm

For the studied sample fragment the number of pores was calculated (there were 558 of them) and their size distribution $R_N = [d_{min}, d_{max}]$ (Fig. 3), where $N = 6$ is the number of distributions, $d_{\min}$ and $d_{\max}$ are the minimum and maximum pore diameter in microns. For statistical estimation of the pore distribution by diameter it is necessary to rank and sort the value of the indicators of the average diameter series in ascending order.

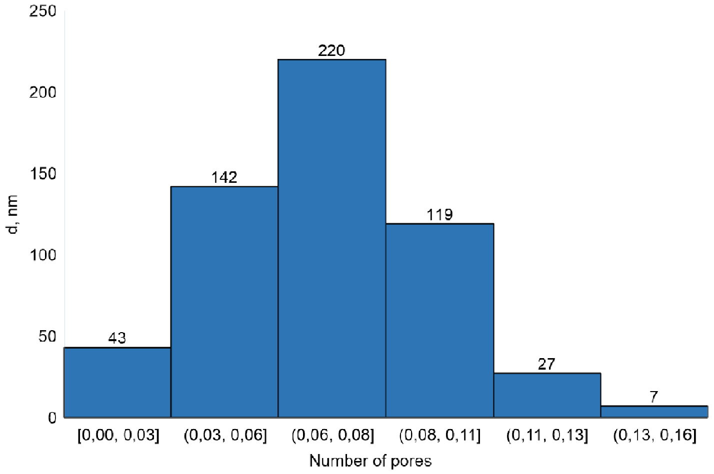

Figure 3. Histogram of pore distribution by size

To estimate the range of pore diameter distribution by size the above-mentioned indicators were defined as follows.

Indicators of the distribution center. This class of indicators includes: the simple arithmetic mean of pores — ($\bar{d}$); the most common value of the average diameter — the mode (M_o) and the diameter value that falls in the middle of an ordered population — the median (M_e), which serves as a good characteristic in an asymmetric distribution of data, because even in the presence of outliers of data it is more resistant to their influence. In symmetric distribution series the values of the mode and median coincide with the average pore value [35]:

$$\bar{d} = M_e = M_o, \tag{1}$$

and in moderately asymmetric ones, they correlate as follows [36]:

$$3(\bar{d} - M_e) \approx \bar{d} - M_o. \tag{2}$$

The indicators of the distribution center obtained from the results of the performed studies are presented in Table. 1.

Table 1

Indicators of the distribution center of a number of pore diameters

Indicator	Identification	Value, μm
Arithmetic mean of the diameter, $\bar{d}$	$\bar{d} = \frac{\sum_{i=1}^{n} d_i}{n}$	0.0683
Mode, M_o	The most common diameter value is the number of repetitions f = 86	0.07136
Median, M_e	the value of the diameter that divides the sizes of the pore distribution series by diameter into two parts	0.07136

Thus, you can state that the mode and median of the series coincide, but exceed the average value. Such a series is considered conditionally symmetric.

Variation indicators. This class of indicators is presented in Table 2. Its study is of great practical importance and is a necessary component in the variational analysis. This is due to the fact that the average, being equal in effect, performs its main task with different degrees of accuracy: the smaller the differences in individual values of the attribute to be averaged, the more homogeneous is its total value, and, consequently, the more accurate and reliable the average value is, and vice versa [37]. Therefore, by the degree of variation, we can judge the variation limits in the pore diameter, the homogeneity of the total value of diameter values.

Table 2

The variation indicators of the pore distribution series by the diameter

Indicator	Identification	Formula	Value
1	2	3	4
Invariable indicators of variation			
Variation span, μm	Difference between maximum and minimum pore diameter values	$R = d_{\max} - d_{\min}$	0.1564074
Mean deviation, μm^2	Arithmetic mean from absolute divergences of individual pore diameter values from the overall average	$\bar{D} = \frac{\sum \lvert d - \bar{d} \rvert f}{\sum f}$	0.0222
Dispersion, μm^2	The arithmetic mean of the deviation squares of each pore diameter value from the arithmetic mean value	$\sigma^2 = \frac{\sum \left(d - \bar{d}\right)^2 f}{\sum f}$	0.000821
Mean square deviation, μm	STD	$\sigma = \sqrt{\sigma^2}$	0.0286
Fixed dispersion, μm^2	Capable estimate of the variance	$s^2 = \frac{\sum \left(d_i - \bar{d}\right)^2}{n-1}$	0.00552
Estimation of the mean square deviation, μm	The square root of the fixed variance	$s = \sqrt{s^2}$	0.0743

1	2	3	4
Relative indicators of variation			
Coefficient of variation, %	Measure of the relative spread of total values: shows what percentage of the average pore diameter is its average spread	$v = \frac{\sigma}{d}$	41.92
Relative linear deflection, %	Characterizes the proportion of the average value of pore diameters of absolute divergences from the average quantity	$K_d = \frac{D}{\overline{d}}$	32.48

In Table: *f* — the sum of the frequencies of variation in the series, and *n* — the number of features.

Thus, the results of these studies allow us to conclude that since the coefficient of variation is greater than 30 %, but less than 70 %, there is a moderate variation in the pore diameters of the synthesized semiconductor surface.

Indicators of the distribution form. One of the main characteristics of the distribution form is its symmetry, that is, when the frequencies of any two variants equidistant on both sides of the distribution center are equal to each other; in any other case, the distribution is considered unbalanced. The criterion for the degree of symmetry of the distribution is the asymmetry coefficient [38]:

$$A_s = \frac{M_3}{s^3}, \tag{3}$$

where *M3* is the central moment of the third order of the pore diameter distribution series, *s* — mean-square deviation.

The central moments of the pore distribution series by diameter calculated from the results of the measurements performed are shown in Figure 4.

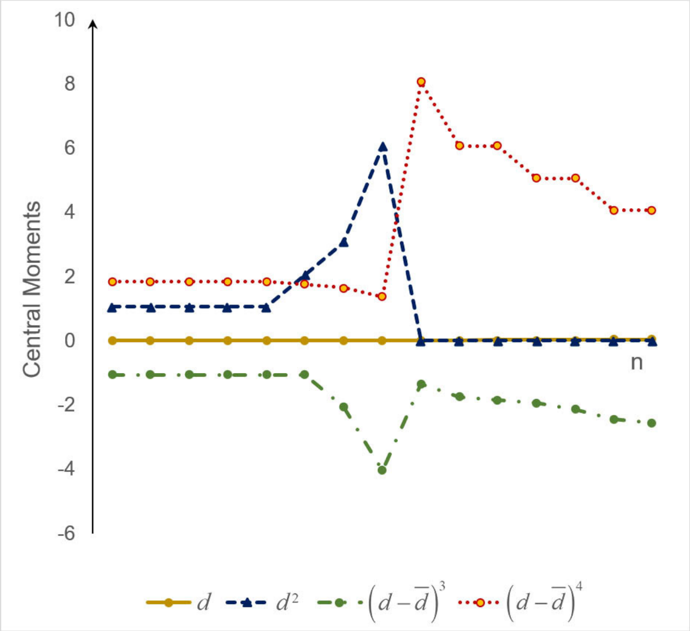

Figure 4. Diagram of the central moments distribution to determine the significance of the skewness of the pore diameter distribution series

It is determined that in our case $A_s = 4.254$, which indicates that there is a right-sided asymmetry in the resulting distribution.

The significance of the skewness indicator was determined using the mean square error of the skewness ratio [39, 40]:

$$s_{As} = \sqrt{\frac{6(n-2)}{(n+1)(n+3)}}. \tag{4}$$

In this case it is considered that if $|A_s|/s_{As} \prec 3$ then the asymmetry is insignificant, its presence is explained by random circumstances. If $|A_s|/s_{As} \succ 3$, then the asymmetry is considered significant and the distribution of the feature in the general population is not symmetric.

As a result of the analysis of the measurements performed it was found that s_{As} = 0.171, i.e., $|A_s|/s_{As} = 4.254 : 0.171 = 24.93 \succ 3$, and it can be argued that in the study there is a significant asymmetry of distribution: larger pores predominate in this fragment of the porous surface, and pores with dimensions smaller than the average diameter are much rarer. This correlates with the previously obtained result [25]: the number of pores and their size distribution depends on the time of crystal etching — the longer the processing of the crystal, the greater the number of primordial pores will appear on the surface. In general, the effect of the synthesis time (t, min) on the size (d, μm) of the pore mass of the corresponding trend equation has the following form [25]:

$$d = 0.143\,t^2 + 4.447\,t — 10.779. \qquad (5)$$

Obtained structural skewness indicators allow us to assess the skewness only in the central part of the distribution, that is, in the main mass of sizes, where they do not depend on the boundary values. However, despite this, such characteristics are an important element in the analysis of the pore distribution by size, as they help to analyze the main mass of the pores, and do not take into account those pores that are unprovable, such as germ pores, which are still very small in size, and massive pores, which are classified as etching pits, resulting from the digestion of surface defects and dislocations in a typical method of electrochemical synthesis.

Conclusions

Experimental studies of the surface morphology of nanostructured semiconductors are carried out on the example of a synthesized porous layer on an indium phosphide crystal. Representative metrologically capable results were obtained using the most efficient modern software tools for analyzing microscopic images and statistical methods.

As a result, the characteristics of one of the main parameters of the aggregate structure of the synthesized porous layer are determined — the pore diameter distribution on semiconductors during their electrical etching, namely the median (M_e = 0.07136 μm), mode (M_o = 0.07136 μm) and the arithmetic mean diameter ($\overline{d}$ = 0.0683 μm), on the basis of which it is concluded that the pore diameter distribution series is conditionally symmetric.

This variation was found to be moderate. Structural indicators of skewness allowed us to establish an important element of the pore growth mechanism which correlates with previously obtained results [25] — the longer the crystal is processed, the greater the number of primordial pores will appear on the surface, the greater the pore size spread.

Thus, the presented methodology can become an effective tool for the characterization of porous nanostructures on the crystal surface, and the results obtained are an important link in the structural analysis of nanostructured semiconductors. In the future they can ensure the formation of nanostructures with adjustable properties and quality levels, which is a solution to a complex technological problem of our time.

Acknowledgments

The work was carried out as part of the state budget research «Theoretical and methodological foundations of the systemic fundamentalization of the training of future specialists in the field of nanomaterials knowledge for productive professional activity» (state registration number 0121U109426).

References

1 Karoui F.S. Application of quantum mechanics for computing the vibrational spectra of nitrogen complexes in silicon nanomaterials / F.S. Karoui, A. Karoui // Some Applications of Quantum Mechanics. — 2012. — P. 131.

2 Ouyang J. Application of nanomaterials in two-terminal resistive-switching memory devices / J. Ouyang // Nano reviews. — 2010. — Vol. 1. — № . 1. — P. 5118.

3 Zhukovskii Y.F. Influence of F centres on structural and electronic properties of AlN single-walled nanotubes / Y.F. Zhukovskii et al. // Journal of Physics: Condensed Matter. — 2007. — 19: 39. — P. 395021.

4 Suchikova Y.O. Sulfide passivation of indium phosphide porous surfaces / Y.O. Suchikova // Journal of Nano-and Electronic Physics. — 2017. –9:1. — P. 1006–1.

5 Chernov S.A. Photo-and thermo-stimulated luminescence of CsI—Tl crystal after UV light irradiation at 80 K / S.A. Chernov, L. Trinkler, A.I. Popov // Radiation effects and defects in solids. — 1998. –143: № . 4. — P. 345–355.

6 Park K.D. Radiative control of dark excitons at room temperature by nano-optical antenna-tip Purcell effect / K.D. Park, T. Jiang, G. Clark, X. Xu, M.B. Raschke // Nature nanotechnology. — 2018. — 13: 1. — P. 59–64.

7 Yu G. Applications of Nanomaterials for Heavy Metal Removal from Water and Soil: A Review / G. Yu, X. Wang, J. Liu // Sustainability. — 2021. –13: 2. — P. 713.

8 Zhukovskii Y.F. Structural and electronic properties of single-walled AlN nanotubes of different chiralities and sizes / Y.F. Zhukovskii // Journal of Physics: Condensed Matter. — 2006. — Vol. 18. — № 33. — P. S2045.

9 Eglitis R.I. Semi-empirical simulations of the electron centers in MgO crystal / R.I. Eglitis // Computational materials science. — 1996. — Vol. 5. — № 4. — P. 298–306.

10 Bayati M. R. A photocatalytic approach in micro arc oxidation of WO3–TiO2 nano porous semiconductors under pulse current / M.R. Bayati, F. Golestani-Fard, A. Z.Moshfegh, R. Molaei // Materials Chemistry and Physics. — 2011. — Vol. 128. — № 3. — P. 427–432.

11 Zhan W. Recent progress on engineering highly efficient porous semiconductor photocatalysts derived from Metal–organic frameworks / W. Zhan, L. Sun, X. Han // Nano-micro letters. — 2019. — Vol. 11. — № 1. — P. 1.

12 Serikov T.M. The effect of electric transport properties of titanium dioxide nanostructures on their photocatalytic activity / T.M. Serikov // Bulletin of the university of Karaganda-Physics. — 2020. — 99(3). — 13 — 21.

13 BorodinY. V. Spectroscopy of nanoscale crystalline structural elements / Y.V. Borodin, K.V. Sysolov, V.R. Rande, G.V. Vavilova, O. Starý // Bulletin of the university of Karaganda-Physics. — 2020. — 99(3). — P. 46–53.

14 Alavi M. Functionalized carbon-based nanomaterials and quantum dots with antibacterial activity: a review / M. Alavi, E. Jabari, E. Jabbari // Expert Review of Anti-infective Therapy. — 2021. — Vol. 19. — № . 1. — P. 35–44.

15 Frieler M. Effects of Doxorubicin Delivery by Nitrogen-Doped Graphene Quantum Dots on Cancer Cell Growth: Experimental Study and Mathematical Modeling / M. Frieler, C. Pho, B.H. Lee // Nanomaterials. — 2021. — Vol. 11. — № 1. — P. 140.

16 Pan D. TiB nano-whiskers reinforced titanium matrix composites with novel nano-reticulated microstructure and high performance via composite powder by selective laser melting / D. Pan //Materials Science and Engineering: A. — 2021. — Vol. 799. — P. 140137.

17 Vambol S. O. Formation of filamentary structures of oxide on the surface of monocrystalline gallium arsenide / S.O. Vambol et al. // Journal of Nano-and Electronic Physics. — 2017. — V. 9. — № 6.

18 Suchikova J.A. Synthesis of indium nitride epitaxial layers on a substrate of porous indium phosphide / J.A. Suchikova // Journal of Nano-and Electronic Physics. — 2015. — Vol. 7. — № 3. — P. 3017–1.

19 Allon I.Building the European Nanomedicine Research and Innovation Area: EuroNanoMed. 10 years funding innovative research projects / I. Allon, N. Levine, I. Baanante // Precision Nanomedicine. — 2019. — Vol. 2. — № 2. — P. 270–277.

20 Lobaskin, V., Puzyn, T., & Verheyen, G. EU US roadmap nanoinformatics 2030. EU Nanosafety Cluster. — 2018.

21 Hodson, L., Geraci, C., & Schulte, P. Continuing to protect the nanotechnology workforce: NIOSH nanotechnology research plan for 2018–2025. — 2019.

22 Lazarenko A.S. Nanotopography and grain-boundary migration in the vicinity of triple junctions / A.S. Lazarenko et al. // Acta metallurgica et materialia. — 1995. — Vol. 43. — № 2. — P. 639–643.

23 Suchikova Y.A. Influence of dislocations on the process of pore formation in n-InP (111) single crystals / Y.A. Suchikova, V.V. Kidalov, G.A. Sukach // Semiconductors. — 2011. — Vol. 45. — № 1. — P. 121–124.

24 Boyd R.D. New approach to inter-technique comparisons for nanoparticle size measurements; using atomic force microscopy, nanoparticle tracking analysis and dynamic light scattering / R.D. Boyd, S.K. Pichaimuthu, A. Cuenat // Colloids and Surfaces A: Physicochemical and Engineering Aspects. — 2011. — Vol. 387. — № 1–3. — P. 35–42.

25 Suchikova Y. Synthesized nanostructures formation time effect on their morphological quality indicators–pore diameter increase in nanostructured coatings / Y. Suchikova, N. Kosach, V. Bolshakov, G. Shishkin // Ukrainian Metrological Journal. — 2020. — № . 4. — P. 43–49.

26 Suchikova Y.A. Influence of type anion of electrolit on morphology porous inp obtained by electrochemical etching / Y.A. Suchikova, V.V. Kidalov, G.A. Sukach // Journal of Nano- and Electronic Physics. — 2009. — Vol. 1. — № . 4. — P. 78–86.

27 Sychikova Y.A. Dependence of the threshold voltage in indium-phosphide pore formation on the electrolyte composition / Y.A. Sychikova, V. V.Kidalov, G.A. Sukach //Journal of Surface Investigation. X-ray, Synchrotron and Neutron Techniques. — 2013. — Vol. 7. — № . 4. — P. 626–630.

28 Li G. Ag quantum dots modified hierarchically porous and defective TiO2 nanoparticles for improved photocatalytic CO2 reduction / G.Li et al. //Chemical Engineering Journal. — 2021. — Vol. 410. — P. 128397.

29 Li Y. Bulk Si production from Si–Fe melts by directional-solidification, part II: Element distribution / Y. Li et al. // Materials Science in Semiconductor Processing. — 2021. — Vol. 128. — P. 105754.

30 Notthoff C. Swift heavy ion irradiation of GaSb: From ion tracks to nanoporous networks / C. Notthoff et al. // Physical Review Materials. — 2020. — Vol. 4. — № 4. — P. 046001.

31 Massabuau F. C.P. Dislocations as channels for the fabrication of sub-surface porous GaN by electrochemical etching / F.C.P. Massabuau et al. //APL Materials. — 2020. — Vol. 8. — № 3. — P. 031115.

32 Liang H. Solution growth of screw dislocation driven α-GaOOH nanorod arrays and their conversion to porous ZnGa2O4 nanotubes / H. Liang et al. // Chemistry of Materials. — 2017. — Vol. 29. — № 17. — P. 7278–7287.

33 Rueden C.T. et al. ImageJ2: ImageJ for the next generation of scientific image data / C.T. Rueden et al. //BMC bioinformatics. — 2017. — Vol. 18. — № 1. — P. 1–26.

34 Chen Y. A convenient method for quantifying collagen fibers in atherosclerotic lesions by ImageJ software / Y. Chen, Q. Yu, C.B. Xu // Int J Clin Exp Med. — 2017. — Vol. 10. — № 10. — P. 14904–14910.

35 Hoseinzadeh A. The Skew-Reflected-Gompertz distribution for analyzing symmetric and asymmetric data / A. Hoseinzadeh et al. // Journal of Computational and Applied Mathematics. — 2019. — Vol. 349. — P. 132–141.

36 Tsoukalas I. Simulation of stochastic processes exhibiting any-range dependence and arbitrary marginal distributions / I. Tsoukalas, C. Makropoulos, D. Koutsoyiannis // Water Resources Research. — 2018. — Vol. 54. — № 11. — P. 9484–9513.

37 Newey W.K. Asymmetric least squares estimation and testing / W.K. Newey, J.L. Powell // Econometrica: Journal of the Econometric Society. — 1987. — P. 819–847.

38 Jones M.C. Sinh-arcsinh distributions / M.C. Jones, A. Pewsey // Biometrika. — 2009. — Vol. 96. — № 4. — P. 761–780.

39 Zabolotnii S.V. et al. Polynomial estimates of measurand parameters for data from bimodal mixtures of exponential distributions / S.V. Zabolotnii, V.Y. Kucheruk, Z.L. Warsza, A.K. Khassenov // Bulletin of the university of Karaganda-Physics. — 2018. — Vol. 2. — № 90. — P. 71–80.

Н.И. Косач, В.Б. Большаков, И.Т. Богданов, Я.А. Сычикова

Индий фосфидінің синтезделген бетіндегі кеуекті наноқұрылымдардың морфологиялық параметрлерін статистикалық бағалау

Наноқұрылымды жартылай өткізгіштердің беттік морфологиясын бағалаудың конструктивті әдісі ұсынылған, ол олардың синтезделген бетіндегі наноөлшемді объектілердің жиынтық құрылымының негізгі статистикалық сипаттамаларын анықтаудан тұрады. Бетінде синтезделген кеуекті қабаты бар индий фосфидті жартылай өткізгіштің мысалын пайдаланып, негізгі статистикалық сипаттамаларды бағалау кристалды әдеттегі электрохимиялық өңдеу кезінде кеуектерді қалыптастыру процесінің кинетикасын тереңірек түсінуге мүмкіндік беретіндігі көрсетілген. Негізгі статистикалық метрологиялық негізделген сипаттамаларды анықтау (таралу орталығының көрсеткіштері, вариациясы және таралу формасы) кристалдарды электрохимиялық өңдеу кезінде болатын процестерді толығырақ түсінуге мүмкіндік береді. Болашақта бұл алдын ала анықталған қасиеттері бар наноқұрылымдарды құруға мүмкіндік береді және жоғары сапалы наноқұрылымды жартылай өткізгіштердің өнеркәсіптік өндірісіне негіз болады.

Кілт сөздер: синтез, жартылай өткізгіштер, беттік морфология, өлшемдер, агрегаттық құрылым, статистикалық талдау, индий фосфиді, ImageJ.

Н.И. Косач, В.Б. Большаков, И.Т. Богданов, Я.А. Сычикова

Статистическая оценка морфологических показателей пористых наноструктур на синтезированной поверхности фосфида индия

Представлен конструктивный метод оценки морфологии поверхности наноструктурированных полупроводников, который заключается в определении основных статистических характеристик агрегатной структуры наноразмерных объектов на их синтезированной поверхности. На примере полупроводника фосфида индия с синтезированным пористым слоем на его поверхности показано, что оценка основных статистических характеристик позволяет глубже понять кинетику процесса порообразования при типичной электрохимической обработке кристалла. Определение основных статистических метрологически обоснованных характеристик (показателей центра распределения, вариации и формы распределения) позволяет более детально понять процессы, происходящие во время электрохимической обработки кристаллов. В перспективе это позволит создавать наноструктуры с заранее определенными свойствами, станет основой для промышленного изготовления наноструктурированных полупроводников высокого уровня качества.

Ключевые слова: синтез, полупроводники, морфология поверхности, измерения, агрегатная структура, статистический анализ, фосфид индия, ImageJ.

References

1 Karoui, F.S., & Karoui, A. (2012). Application of quantum mechanics for computing the vibrational spectra of nitrogen complexes in silicon nanomaterials. *Some Applications of Quantum Mechanics*, 131.

2 Ouyang, J. (2010). Application of nanomaterials in two-terminal resistive-switching memory devices. *Nano reviews*, *1(1),* 5118.

3 Zhukovskii, Y.F., Pugno, N., Popov, A.I., Balasubramanian, C., & Bellucci, S. (2007). Influence of F centres on structural and electronic properties of AlN single-walled nanotubes. *Journal of Physics: Condensed Matter*, *19(39),* 395021.

4 Suchikova, Y.O. (2017). Sulfide Passivation of Indium Phosphide Porous Surfaces, *Journal of Nano- and Electronic Physics*, *9(1)*, 1006–1–1006–6.

5 Chernov, S.A., Trinkler, L., & Popov, A.I. (1998). Photo-and thermo-stimulated luminescence of CsI—Tl crystal after UV light irradiation at 80 K. *Radiation effects and defects in solids, 143(4)*, 345–355.

6 Park, K.D., Jiang, T., Clark, G., Xu, X., & Raschke, M.B. (2018). Radiative control of dark excitons at room temperature by nano-optical antenna-tip Purcell effect. *Nature nanotechnology, 13(1)*, 59–64.

7 Yu, G., Wang, X., Liu, J., Jiang, P., You, S., Ding, N., ... & Lin, F. (2021). Applications of Nanomaterials for Heavy Metal Removal from Water and Soil: *A Review. Sustainability, 13(2)*, 713.

8 Zhukovskii, Y.F., Popov, A.I., Balasubramanian, C., & Bellucci, S. (2006). Structural and electronic properties of single-walled AlN nanotubes of different chiralities and sizes. *Journal of Physics: Condensed Matter, 18(33),* S2045.

9 Eglitis, R.I., Kuklja, M.M., Kotomin, E.A., Stashans, A., & Popov, A.I. (1996). Semi-empirical simulations of the electron centers in MgO crystal. *Computational materials science, 5(4)*, 298–306.

10 Bayati, M.R., Golestani-Fard, F., Moshfegh, A.Z., & Molaei, R. (2011). A photocatalytic approach in micro arc oxidation of WO3–TiO2 nano porous semiconductors under pulse current. *Materials Chemistry and Physics, 128(3)*, 427–432.

11 Zhan, W., Sun, L., & Han, X. (2019). Recent progress on engineering highly efficient porous semiconductor photocatalysts derived from Metal–organic frameworks. *Nano-micro letters, 11(1),* 1.

12 Serikov, T.M. (2020). The effect of electric transport properties of titanium dioxide nanostructures on their photocatalytic activity. *Bulletin of the university of Karaganda-Physics, 99(3),* 13 — 21. DOI 10.31489/2020Ph3/13–21

13 Borodin, Y.V., Sysolov, K.V., Rande, V.R., Vavilova, G.V., & Starý, O. (2020). Spectroscopy of nanoscale crystalline structural elements. *Bulletin of the university of Karaganda-Physics, 99(3)* 46 — 53. DOI 10.31489/2020Ph3/46–53

14 Alavi, M., Jabari, E., & Jabbari, E. (2021). Functionalized carbon-based nanomaterials and quantum dots with antibacterial activity: a review. *Expert Review of Anti-infective Therapy, 19(1)*, 35–44.

15 Frieler, M., Pho, C., Lee, B.H., Dobrovolny, H., Akkaraju, G.R., & Naumov, A.V. (2021). Effects of Doxorubicin Delivery by Nitrogen-Doped Graphene Quantum Dots on Cancer Cell Growth: Experimental Study and Mathematical Modeling. *Nanomaterials, 11*, 140.

16 Pan, D., Zhang, X., Hou, X., Han, Y., Chu, M., Chen, B., ... & Li, S. (2021). TiB nano-whiskers reinforced titanium matrix composites with novel nano-reticulated microstructure and high performance via composite powder by selective laser melting. *Materials Science and Engineering: A, 799,* 140137.

17 Vambol, S.O., Bohdanov, I.T., Vambol, V.V. & Onyschenko, S.V. (2017). Formation of filamentary structures of oxide on the surface of monocrystalline gallium arsenide. *Journal of Nano-and Electronic Physics, 9(6)*. 06016

18 Suchikova, J.A. (2015). Synthesis of indium nitride epitaxial layers on a substrate of porous indium phosphide. *Journal of Nano-and Electronic Physics, 7(3)*, 3017–1.

19 Allon, I., Levine, N., & Baanante, I. (2019). Building the European Nanomedicine Research and Innovation Area: EuroNanoMed. *10 years funding innovative research projects.* DOI:10.33218/PRNANO2(1).190404.1

20 Lobaskin, V., Puzyn, T., & Verheyen, G. (2018). EU US roadmap nanoinformatics 2030. *EU Nanosafety Cluster.*

21 Hodson, L., Geraci, C., & Schulte, P. (2019). Continuing to protect the nanotechnology workforce: NIOSH nanotechnology research plan for 2018–2025.

22 Lazarenko, A.S., Mikhailovskij, I.M., Rabukhin, V.B., & Velikodnaya, O.A. (1995). Nanotopography and grain-boundary migration in the vicinity of triple junctions. *Acta metallurgica et materialia, 43(2), 639–643.*

23 Suchikova, Y.A., Kidalov, V.V., & Sukach, G.A. (2011). Influence of dislocations on the process of pore formation in n-InP (111) single crystals. *Semiconductors, 45(1),* 121–124.

24 Boyd, R.D., Pichaimuthu, S.K., & Cuenat, A. (2011). New approach to inter-technique comparisons for nanoparticle size measurements; using atomic force microscopy, nanoparticle tracking analysis and dynamic light scattering. *Colloids and Surfaces A: Physicochemical and Engineering Aspects, 387(1–3)*, 35–42.

25 Suchikova, Y., Kosach, N., Bolshakov, V., & Shishkin, G. (2020). Synthesized nanostructures formation time effect on their morphological quality indicators–pore diameter increase in nanostructured coatings. *Ukrainian Metrological Journal, 4,* 43–49.

26 Suchikova, Y.A., Kidalov, V.V., & Sukach, G.A. (2009). Influence of type anion of electrolit on morphology porous inp obtained by electrochemical etching. *Journal of Nano- and Electronic Physics, 1(4),* 78–86.

27 Sychikova, Y.A., Kidalov, V.V., & Sukach, G.A. (2013). Dependence of the threshold voltage in indium-phosphide pore formation on the electrolyte composition. *Journal of Surface Investigation. X-ray, Synchrotron and Neutron Techniques, 7(4),* 626–630.

28 Li, G., Sun, Y., Zhang, Q., Gao, Z., Sun, W., & Zhou, X. (2021). Ag quantum dots modified hierarchically porous and defective TiO2 nanoparticles for improved photocatalytic CO$_2$ reduction. *Chemical Engineering Journal, 410,* 128397.

29 Li, Y., Lei, X., Liu, C., & Zhang, L. (2021). Bulk Si production from Si–Fe melts by directional-solidification, part II: Element distribution. *Materials Science in Semiconductor Processing, 128,* 105754.

30 Notthoff, C., Jordan, S., Hadley, A., Mota-Santiago, P., Elliman, R.G., Lei, W., & Kluth, P. (2020). Swift heavy ion irradiation of GaSb: From ion tracks to nanoporous networks. *Physical Review Materials, 4(4),* 046001.

31 Massabuau, F.C.P., Griffin, P.H., Springbett, H.P., Liu, Y., Kumar, R.V., Zhu, T., & Oliver, R.A. (2020). Dislocations as channels for the fabrication of sub-surface porous GaN by electrochemical etching. *APL Materials, 8(3),* 031115.

32 Liang, H., Meng, F., Lamb, B. K., Ding, Q., Li, L., Wang, Z., & Jin, S. (2017). Solution growth of screw dislocation driven α-GaOOH nanorod arrays and their conversion to porous $ZnGa_2O_4$ nanotubes. *Chemistry of Materials, 29(17),* 7278–7287.

33 Rueden, C.T., Schindelin, J., Hiner, M.C., DeZonia, B.E., Walter, A.E., Arena, E.T., & Eliceiri, K.W. (2017). ImageJ2: ImageJ for the next generation of scientific image data. *BMC bioinformatics, 18(1),* 1–26.

34 Chen, Y., Yu, Q., & Xu, C.B. (2017). A convenient method for quantifying collagen fibers in atherosclerotic lesions by ImageJ software. *Int J Clin Exp Med, 10(10),* 14904–14910.

35 Hoseinzadeh, A., Maleki, M., Khodadadi, Z., & Contreras-Reyes, J. E. (2019). The Skew-Reflected-Gompertz distribution for analyzing symmetric and asymmetric data. *Journal of Computational and Applied Mathematics, 349,* 132–141.

36 Tsoukalas, I., Makropoulos, C., & Koutsoyiannis, D. (2018). Simulation of stochastic processes exhibiting any-range dependence and arbitrary marginal distributions. *Water Resources Research, 54(11),* 9484–9513.

37 Carstensen, J., & Lindegarth, M. (2016). Confidence in ecological indicators: a framework for quantifying uncertainty components from monitoring data. *Ecological indicators, 67,* 306–317.

38 Newey, W.K., & Powell, J.L. (1987). Asymmetric least squares estimation and testing. Econometrica: *Journal of the Econometric Society*, 819–847.

39 Jones, M.C., & Pewsey, A. (2009). Sinh-arcsinh distributions. *Biometrika, 96(4),* 761–780.

40 Zabolotnii, S.V., Kucheruk, V.Y., Warsza, Z.L., & Khassenov, A.K. (2018). Polynomial estimates of measurand parameters for data from bimodal mixtures of exponential distributions. *Bulletin of the university of Karaganda-Physics, 2(90),* 71–80.

DOI 10.31489/2021Ph3/93-100
UDC 535.215; 535.3

A.K. Aimukhanov, X.S. Rozhkova*, A.K. Zeinidenov, T.E. Seisembekova

Karagandy University of the name of academician E.A. Buketov,
Scientific Center for Nanotechnology and Functional Nanomaterials, Kazakhstan
*(*E-mail: ksusharogovaya@mail.ru)*

Influence of surface structure and morphology of PEDOT: PSS on its optical and electrophysical characteristics

This paper presents the results of a study of the effect of modification of the structure of the PEDOT: PSS polymer with hole conductivity on the optical and electrophysical properties of an organic solar cell. It was found that the modification of a polymer film with ethyl and isopropyl alcohols leads to a change in the morphology and roughness of the film surface. It has been determined that annealing of films in alcohol vapor promotes the formation of more uniform films. It is shown that upon modification of the PEDOT: PSS film in alcohol vapor the absorption spectrum shifts the absorption maximum of PEDOT to the short-wavelength region of the spectrum, the absorption of the aromatic PSS fragment decrease. X-ray phase analysis showed that after surface modification with alcohol vapor, the PEDOT and PSS chains change their structure. It is shown that the structural features of the surface morphology of PEDOT: PSS affect the electrophysical parameters of the films, such as the effective extraction rate and the effective time of flight of charge carriers. It was found that the modification of the surface of the PEDOT: PSS film leads to an improvement in the electrical transport properties of the films.

Keywords: PEDOT: PSS, Izopropanol, Ethanol, surface morphology, thermal annealing, aromatic fragment PSS, optical spectroscopy, impedance spectroscopy.

Introduction

PEDOT is a relatively new member of the conductive polymer family. It has a fairly high electrochemical and thermal stability of electrical properties [1]. PEDOT is composed of ethylenedioxythiophene monomers (EDOT). However, EDOT is insoluble in many common solvents and is unstable in the neutral state as it rapidly oxidizes in the atmosphere. To improve its properties a polyelectrolyte solution (PSS) is added to EDOT, resulting in an aqueous suspension of PEDOT: PSS. Each phenyl ring of PSS monomer has one acidic SO_3H (sulfonate) group. Films with different properties can be obtained depending on the content of components, doping concentration, and particle size. The work function of the electron is approximately 5.2 eV. Due to the PSS content, the pH is between 1.5 and 2.5 at room temperature [2].

Morphology has a strong effect on the efficiency of generation and transport of charge carriers in PEDOT: PSS. The reason for this effect was the inhomogeneity of the films, which sharply reduces the efficiency of charge transport [3]. Thus, the main reason for the low indicators of transport characteristics is the tendency to aggregation and low solubility of active compounds, since crystallization of the components in PEDOT: PSS leads to the formation of polycrystalline domains, which are characterized by undesirable grain size and suboptimal crystalline ordering [4, 5]. However, the problems associated with the influence of the structural feature of PEDOT: PSS on fundamental parameters, such as the efficiency of electron transport of charge carriers, are still completely unsolved.

In this article studies were carried out on the effect of structural changes in the PEDOT: PSS polymer on the morphological, optical, and electrophysical parameters of the films. To change the structure, the hole-conducting polymer PEDOT: PSS was annealed in vapors with a certain concentration of alcohols. The results were analyzed by comparing the surface morphology, optical and impedance spectra of PEDOT: PSS films.

Experimental

To change the surface morphology PEDOT: PSS was subjected to heat treatment at a certain ratio of ethyl and isopropyl alcohol vapors. The structural formulas of the compounds are shown in Figure 1. The preparation of the substrates was carried out according to the procedure [6, 7]. We used PEDOT: PSS (1 %, Ossila Al4083), Izopropanol, Ethanol (pure 99.9 % Sigma Aldrich). Before starting the experiments, the PEDOT: PSS solution was filtered through a 0.45 micron filter. Films PEDOT: PSS were obtained on a silica glass surface by centrifugation (on a SPIN150i centrifuge manufactured by Semiconductor Production System) at a rotation speed of 5000 rpm.

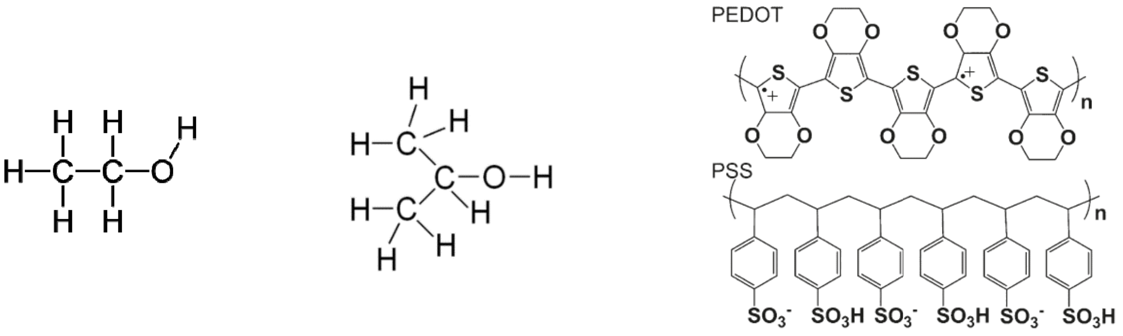

Ethanol Izopropanol PEDOT and PSS

Figure 1. Chemical structure of Ethanol, Izopropanol, PEDOT and PSS

The topography of the film surface was studied using a JSPM-5400 atomic force microscope (AFM) (JEOL, Japan). A special modular program for analyzing scanning probe microscopy data (Win SPMII Data-Processing Software) was used to process the images obtained with AFM. Surface morphology and roughness of PEDOT: PSS thin films were analyzed from AFM images. The images of the surface of the PEDOT: PSS films were obtained in the semicontact scanning mode. The absorption spectra of the samples under study were recorded on an AvaSpec-ULS2048CL-EVO spectrometer (Avantes). The impedance spectra were measured using a P45X potentiostat-galvanostat in the impedance mode. The X-ray diffraction patterns of the films were obtained on a Rigaku SmartLab X-ray diffraction. To measure the impedance spectra on a CY-1700x-spc-2 sputtering apparatus (Zhengzhou CY Scientific Instruments Co., Ltd) an aluminum electrode 200 nm thick was applied to the surface of the films in a vacuum at a pressure of 10^5 Torr. Fitting of impedance spectra was carried out using the EIS-analyzer software package.

Results and Discussion

Images of the surface morphology of the PEDOT: PSS films are shown in Figure 2. Figure 2 shows that the PEDOT: PSS film has a granular structure. At the same time, large formations are observed against the background of a fine granular structure, the surface roughness is 0.63 nm.

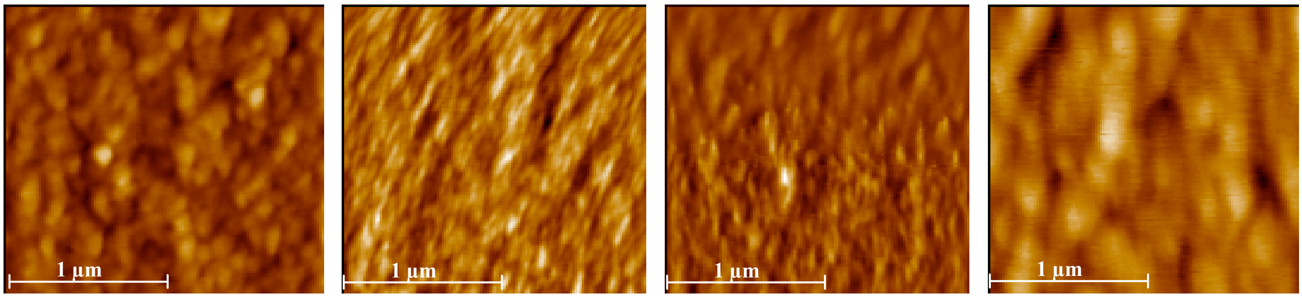

PEDOT: PSS 80 % PEDOT: PSS/ 20 % ethanol 70 % PEDOT: PSS/ 30 % ethanol 50 % PEDOT: PSS/ 50 % ethanol

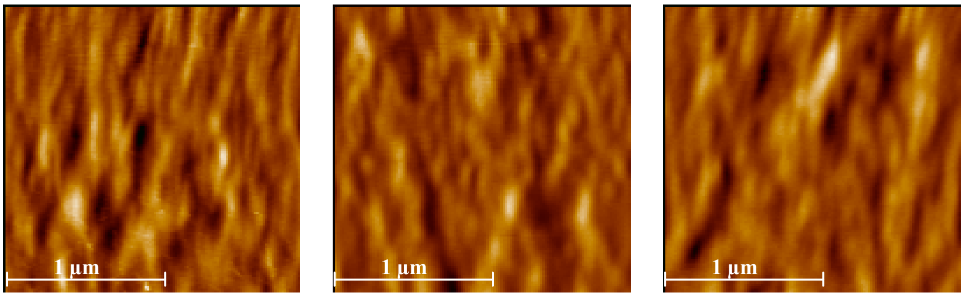

80 % PEDOT: PSS/ 20 % isopropanol 70 % PEDOT: PSS/ 30 % isopropanol 50 % PEDOT: PSS/ 50 % isopropanol

Figure 2. Pictures of the surface morphology of films

After treatment with alcohol vapor for 10 minutes the proportion of large particles decreases significantly, the film surface becomes smooth, the surface roughness becomes 0.56 nm for ethyl alcohol, and 0.49 nm for isopropyl alcohol. A further increase in the concentration of alcohols in vapors leads to a smoothing of the film surface. Table 1 shows the roughness values of PEDOT: PSS films at different ratios of alcohols.

Table 1

Surface roughness of PEDOT: PSS films

Sample	R_a, nm
PEDOT: PSS	0,63
80 % PEDOT: PSS/20 % ethanol	0,56
70 % PEDOT: PSS/30 % ethanol	0,53
50 % PEDOT: PSS/50 % ethanol	0,48
80 % PEDOT: PSS/20 % isopropanol	0,49
70 % PEDOT: PSS/30 % isopropanol	0,47
50 % PEDOT: PSS/50 % isopropanol	0,45

X-ray diffraction patterns (XRD) of PEDOT: PSS thin films modified in ethyl and isopropyl alcohol vapors are shown in Figure 3. Two separate peaks observed at 2Θ at 3.5° and 25.6° in the original PEDOT: PSS film correspond to spatial lattices parameters d 25.2 Å and 3.5 Å, calculated according to Bragg's law 2dsinθ = λ.

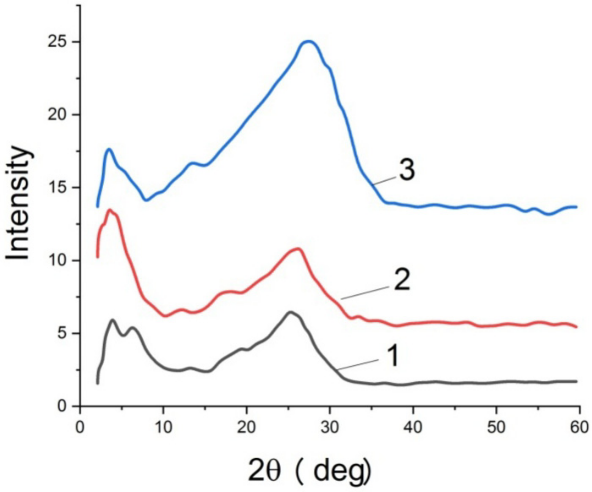

Figure 3. X-ray diffraction patterns (XRD) of PEDOT: PSS thin films:
1 — PEDOT: PSS, 2 — 50 % PEDOT: PSS/50 % ethanol, 3 — 50 % PEDOT: PSS/50 % isopropanol

The diffraction maximum observed at 3.5 °, with a spatial lattice of 25.2 Å, can be attributed to the distance between the lamellae (d 100 Å) of the PEDOT and PSS chains. After treatment in vapors of ethyl and isopropyl alcohols a slight change in the distance between the lamellae from 25.2 to 23.2 Å is observed (Fig. 3). A decrease in the distance between two points in the X-ray diffractogram indicates that the PEDOT and PSS chains pass from the benzoid structure to the quinoid structure; therefore, after modification in ethyl and isopropyl alcohol vapors, the structure becomes more planar.

Figure 4 shows the absorption spectra of the standart PEDOT: PSS films and films held for 10 minutes in alcohol vapor. The semiconducting polymer film PEDOT: PSS has a maximum at a wavelength of λ_1 = 224 nm with a spectral half-width of 28 nm (Fig. 4). In the absorption spectra of all PEDOT: PSS films, a shoulder with a maximum at 260 nm is observed, which is associated with the absorption of the aromatic fragment of PSS [8]. The position of the absorption maxima of the films obtained by holding PEDOT: PSS in alcohol vapor does not change, the half-width of the spectra increases. Table 2 shows the characteristics of the absorption spectra of the PEDOT: PSS films.

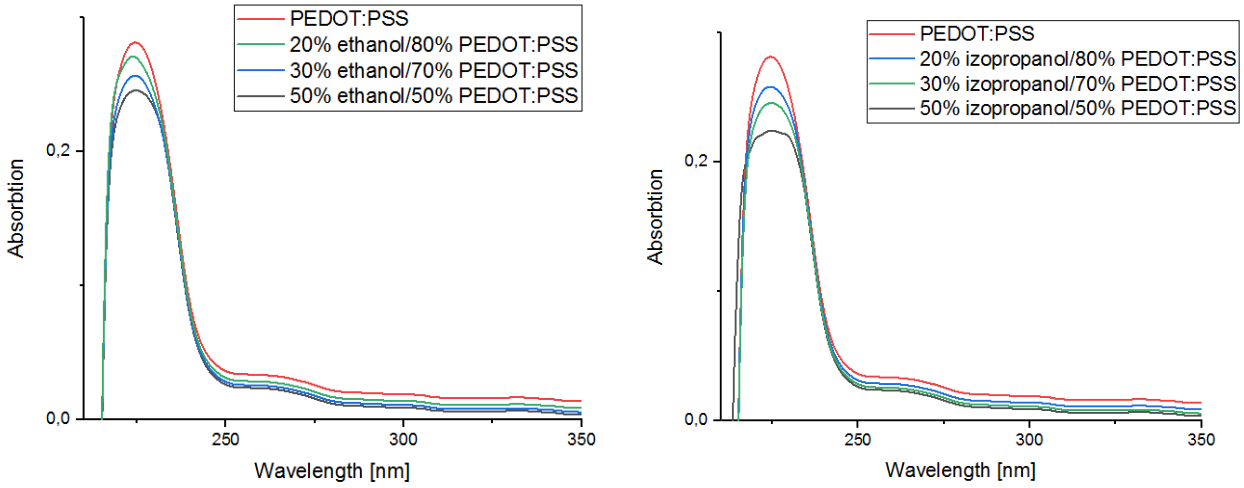

a b

a) spectra of PEDOT: PSS/ethanol films; b) spectra of PEDOT: PSS/isopropanol films

Figure 4. Absorption spectra of PEDOT: PSS films

The absorbance value at the absorption maximum does not undergo significant changes. The treatment with alcohol vapor leads to a decrease in the values at the short-wave and long-wave maxima. It is known that, due to its hydrophobic properties, the PEDOT polymer does not dissolve in ethyl and isopropyl alcohols; in turn, PSS has a high degree of hydrophilic properties [9]. The treatment with alcohol vapor of the PEDOT: PSS film leads to a decrease in the absorption spectrum of the aromatic PSS fragment [10].

Table 2

Characteristics of the absorption spectra of PEDOT: PSS films upon annealing in the atmosphere

Sample	Adsorption peak		D_1	D_2	FWHM, пм
	λ_1, nm	λ_2, nm			
PEDOT: PSS	224	260	0,28	0,03	28
Ethanol					
80 % PEDOT: PSS/20 % ethanol	224	260	0,27	0,03	29
70 % PEDOT: PSS/30 % ethanol	224	260	0,26	0,03	29,4
50 % PEDOT: PSS/50 % ethanol	224	260	0,25	0,02	32
Isopropanol					
80 % PEDOT: PSS/20 % isopropanol	224	260	0,26	0,03	29
70 % PEDOT: PSS/30 % isopropanol	224	260	0,24	0,03	31
50 % PEDOT: PSS/50 % isopropanol	224	260	0,22	0,02	32

The observed changes in the absorption spectra of the films are associated with the structural features of PEDOT: PSS. Initially, without preliminary exposure to alcohol vapors, the film has a granular structure, with intense absorption of the aromatic PSS fragment in the spectrum. After keeping the film in alcohol vapor, the graininess of the film decreases, and the optical absorption density of PSS also decreases. Subsequent treatment with alcohol vapor leads to a further drop in the absorption of the aromatic fragment in the film. Thus, treatment with alcohol vapor leads to a change in the optical absorption spectra associated with the structural features of the film, due to a decrease in the amount of the aromatic PSS fragment.

The analysis of the impedance measurement results was carried out according to the diffusion-recombination model and for the fitting an equivalent circuit was used, shown in Figure 5 (a) [11]. Figure 5 (b) shows a diagram of the movement of charge carriers in a PEDOT: PSS film.

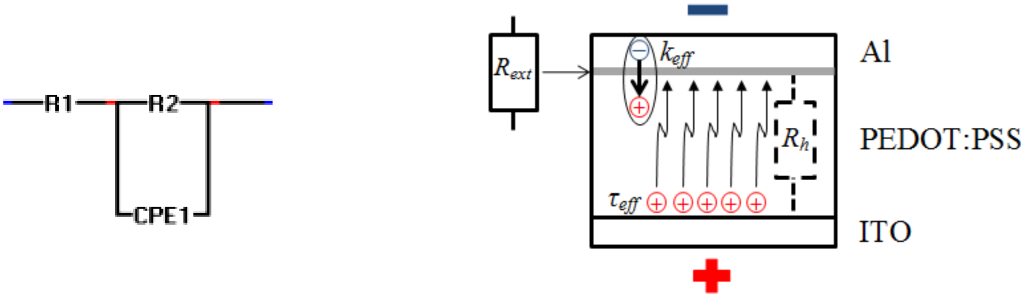

a b

a) equivalent electrical circuit; b) diagram of the movement of charge carriers in the film

Figure 5. Scheme of the transport of charge carriers in the film.

Figure 5 (a) shows the following parameters of the equivalent circuit for obtaining the hodograph of semiconductor films: R1 and R2 are the resistances corresponding to the resistances R_h and R_{ext}; CPE1, a constant phase element, is an equivalent circuit component that simulates the behavior of a double layer, but is an imperfect capacitor.

Figure 6 shows the impedance spectra of the standart PEDOT: PSS films and films treated in isopropyl alcohol vapor in a 50/50 ratio. Table 3 shows the values of the electrophysical parameters of the films, where k_{eff} is the effective rate of carrier extraction with PEDOT: PSS, τ_{eff} is the effective time of flight of charge carriers through the PEDOT: PSS, R_h is the resistance of the PEDOT: PSS film, R_{ext} is the resistance of charge carrier transfer to boundary PEDOT: PSS/electrode associated with the extraction of charge carriers with PEDOT: PSS. As can be seen from the data in Table 3, annealing in isopropyl alcohol vapor affects the resistance of the PEDOT: PSS film (R_h) and the resistance of charge carrier transfer at the PEDOT: PSS/electrode interface (R_{ext}). The resistance of the PEDOT: PSS film is rather high; after annealing at a temperature of 120 °C, a decrease in the resistance of the film by more than two times is observed. Aging in isopropyl alcohol vapor leads to a twofold decrease in the resistance of the PEDOT: PSS film without thermal annealing. Subsequent annealing slightly decreases the film resistance.

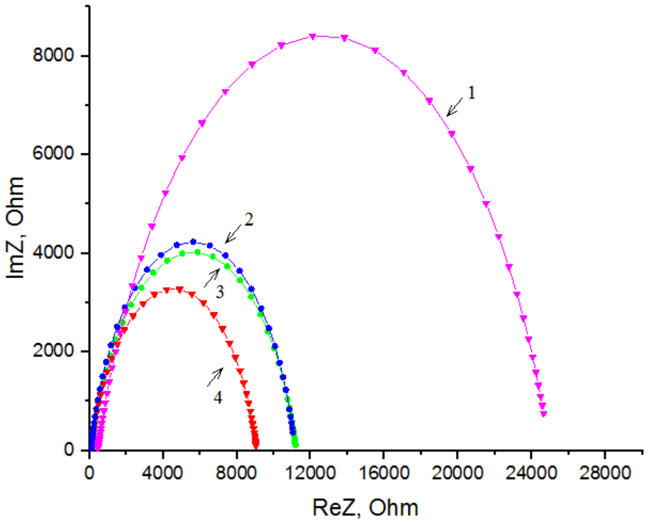

1 — PEDOT: PSS; 2 — PEDOT: PSS after thermal annealing; 3 — 50 % PEDOT: PSS/50 % isopropanol; 4 — 50 % PEDOT: PSS/50 % isopropanol after thermal annealing.

Figure 6. Light impedance spectra of PEDOT: PSS films at voltage parameters -500 mV and frequency from 100 kHz to 0.5 Hz

Changes are observed in the value of the resistance of charge carrier transfer at the interface PEDOT: PSS/electrode (R_{ext}). The R_{ext} resistance is most important for the unannealed PEDOT: PSS film. Upon thermal treatment of the film, R_{ext} is more than halved. At the same time, when the film is treated with alcohol vapors, R_h and R_{ext} are halved.

Table 3

The value of the electrophysical parameters of the films

Sample	R_h, Ohm	R_{ext}, Ohm	k_{eff}, s^{-1}	τ_{eff}, ms
Standart PEDOT: PSS	145,9	24532	44,3	22,57
Annealed film of standart PEDOT: PSS	65,5	11097	56,8	17,61
50 % PEDOT: PSS/50 % isopropanol	66,2	11161	92,5	10,81
Annealed film of 50 % PEDOT: PSS/50 % isopropanol	63,7	9010,6	93,5	10,70

It should be noted that the value of R_{ext} determines the efficiency of carrier injection from PEDOT: PSS films, and the smaller the value of R_{ext}, the greater the efficiency of accumulation of charge carriers in the cell. The quantities k_{eff} and τ_{eff} characterize the efficiency of carrier extraction from the PEDOT: PSS film and the effective time of flight of charge carriers along the PEDOT: PSS. Annealing the film insignificantly affects k_{eff} and τ_{eff}; at the same time, treatment with isopropyl alcohol vapor increases the efficiency of carrier extraction from PEDOT: PSS films by a factor of two and decreases the effective time of flight of charge carriers. The holes injected into the PEDOT: PSS diffuse to the electrode where they recombine with the electrons. The fast transport of the injected holes to the outer electrode is very important, since this reduces the likelihood of their reverse recombination. In our case, the fast transport of holes is ensured by changing the structure of PEDOT: PSS after treatment with isopropyl alcohol vapor; as a result, the efficiency of charge transport at the PEDOT: PSS/electrode interface increases.

Conclusions

An analysis of the experiments showed that a change in the structural features of PEDOT: PSS affects the generation and transport of charge carriers. It was found that thermal annealing of PEDOT: PSS films in isopropyl alcohol vapor leads to a change in the morphology and structure of the film, to an increase in the degree of domain homogeneity, and a decrease in roughness. X-ray phase analysis showed that after surface modification in ethyl and isopropyl alcohol vapors, the PEDOT and PSS chains pass from the benzoid structure to the quinoid structure. Upon modification of the PEDOT: PSS surface, a decrease in the absorption of the aromatic PSS fragment is observed in the absorption spectrum. It is shown that changes in the structure and morphology of the PEDOT: PSS surface affect the electrophysical parameters of the films. It was found that the modification of the surface of the PEDOT: PSS film leads to the optimization of the electrical transport characteristics of the film. Fast transport of holes is ensured by changing the structure of PEDOT: PSS after treatment with isopropyl alcohol vapor, as a result of which the efficiency of charge transport at the PEDOT: PSS/electrode interface increases.

This research is funded by the Science Committee of the Ministry of Education and Science of the Republic of Kazakhstan (Grant No. AP08856176).

References

1 Skotheim T.A. Handbook of Conducting Polymers / T.A. Skotheim, J. Reynolds. — New York: CRC Press, 2007.

2 Kok M.M. Modification of PEDOT: PSS as Hole Injection Layer in Polymer LEDs / M.M. Kok, M. Buechel, S.I.E. Vulto, P. Weijer, E.A. Meulenkamp, S.H.P.M. Winter, et.al // Physica Status Solidi (A). — 2004. — Vol. 201. — P. 1342. DOI: 10.1002/3527606637.ch16.

3 Hoppe H. Organic solar cells: An overview / H. Hoppe, N.S. Sariciftci // Journal of Materials Research — 2004. — Vol. 19. — P. 1924–1945. DOI: https://doi.org/10.1557/JMR.2004.0252

4 Ma W. Thermally stable, efficient polymer solar cells with nanoscale control of the interpenetrating network morphology / W. Ma, C. Yang, X. Gong, K. Lee, A.J. Heeger // Advanced Functional Materials. — 2005. — Vol. 15. — P. 1617–1622. DOI: 10.1002/adfm.200500211.

5 amkoong G. Aging process of PEDOT: PSS dispersion and robust recovery of aged PEDOT: PSS as a hole transport layer for organic solar cells / G. Namkoong, E.M. Younes, T.M. Abdel-Fattah, E.M. El-Maghraby, A.H. Elsayed, A.H. Abo Elazm // Organic Electronics. — 2015. — Vol.25. — P. 1566–1199. DOI: 10.1016/j.orgel.2015.06.049.

6 Kim K. Surface Property of Indium Tin Oxide (ITO) After Various Methods of Cleaning / K. Kim, K. Ihm, B. Kim // Acta Physica Polonica A. — 2014. — Vol. 127, № 4. — P. 1176–1179. DOI: 10.12693/APhysPolA.127.1176.

7 einidenov A.K. Photovoltaic and electrophysical properties of plasmon-enhanced organic solar cells / A.K. Zeinidenov, N.Kh. Ibrayev // Bulletin of the university of Karaganda-Physics. — 2017. — Vol. 88, № 4. — P. 18–23.

8 Xia Y. Highly conductive poly (3,4-ethylenedioxythiophene): poly(styrene sulfonate) films treated with an amphiphilic fluoro compound as the transparent electrode of polymer solar cells / Y. Xia, K. Sun and J. Ouyang // Energy and Environmental Science. — 2012. — Vol. 5. — P. 5325–5332. DOI: 10.1039/c1ee02475b.

9 Kim Y.H. Highly conductive PEDOT: PSS electrode with optimized solvent and thermal post-treatment for ITO-free organic solar cells / Y.H. Kim, C. Sachse, M.L. Machala, C. May, L. Muller-Meskamp, K. Leo // Advanced Functional Materials. — 2011. — Vol. 21. — P. 1076–1081. DOI: https://doi.org/10.1002/adfm.201002290.

10 Alemu D. Highly conductive PEDOT: PSS electrode by simple film treatment with methanol for ITO-free polymer solar cells / D. Alemu, H.Y. Wei, K.C. Ho, C.W. Chu // Energy and Environmental Science. — 2012. Vol. 5. P. 9662–9671. DOI: https://doi.org/10.1039/C2EE22595F.

11 Yuan X. EIS Equivalent Circuits In Electrochemical Impedance Spectroscopy in PEM Fuel Cells / X. Yuan, C. Song, H. Wang, J. Zhang. — California: Springer, 2010.

А.К. Аймуханов, К.С. Рожкова, А.К. Зейниденов, Т.Е. Сейсембекова

PEDOT: PSS құрылымы мен беттік морфологиясының оның оптикалық және электрофизикалық сипаттамаларына әсері

Мақалада кемтіктік өткізгіштігі бар PEDOT: PSS полимерінің құрылымын органикалық күн ұяшықтарының оптикалық және электрофизикалық қасиеттеріне модификациялаудың әсерін зерттеу нәтижелері келтірілген. Полимерлі қабықшаны этил және изопропил спирттерімен модификациялау қабықша бетінің морфологиясы мен кедір-бұдырлығының өзгеруіне әкелетіні анықталды. Спирттер буларындағы пленкаларды күйдіру біртекті пленкалардың түзілуіне ықпал ететіні дәлелденді. PEDOT: PSS қабықшасын спирттер буларында модификациялау кезінде, жұтылу спектрінде PEDOT максималды жұтылуы спектрдің қысқа толқындық аймағына ауысуы, сондай-ақ PSS хош иісті фрагментінің жұтылуының төмендеуі байқалады. Рентгендік фазалық талдау PEDOT және PSS тізбектерінің спирт буларының бетін өзгерткеннен кейін олардың құрылымын өзгертетінін көрсетті. PEDOT: PSS беттік морфологиясының құрылымдық ерекшеліктері, қабықшалардың тиімді шығару жылдамдығы және заряд тасымалдаушылардың тиімді ұшу уақыты сияқты электрофизикалық параметрлеріне әсер етеді. PEDOT: PSS қабықшасының бетін модификациялау қабықшалардың электрлік-транспорттық қасиеттерін жақсартуға әкелетіні анықталды.

Кілт сөздер: PEDOT: PSS, Izopropanol, Ethanol, беттік морфология, термиялық күйдіру, хош иісті PSS фрагменті, оптикалық спектроскопия, импеданс спектроскопиясы.

А.К. Аймуханов, К.С. Рожкова, А.К. Зейниденов, Т.Е. Сейсембекова

Влияние структуры и морфологии поверхности PEDOT: PSS на его оптические электрофизические характеристики

Представлены результаты исследования влияния модификации структуры полимера PEDOT: PSS с дырочной проводимостью на оптические и электрофизические свойства органической солнечной ячейки. Установлено, что модификация полимерной пленки этиловым и изопропиловым спиртами приводит к изменению морфологии и шероховатости поверхности пленки. Доказано, что отжиг пленок в парах спиртов способствует формированию более однородных пленок. Показано, что при модификации пленки PEDOT: PSS в парах спиртов, в спектре поглощения наблюдается сдвиг максимума поглощения PEDOT в коротковолновую область спектра, а также уменьшение поглощения ароматического фрагмента PSS. Рентгенофазовый анализ показал, что после модификации поверхности парами спиртов цепи PEDOT и PSS меняют свою структуру. Показано, что структурные особенности морфологии поверхности PEDOT: PSS оказывают влияние на электрофизические параметры пленок, такие как эффективная скорость извлечения и эффективное время пролета носителей заряда. Установлено, что модификация поверхности пленки PEDOT: PSS приводит к улучшению электротранспортных свойств пленок.

Ключевые слова: PEDOT: PSS, Izopropanol, Ethanol, морфология поверхности, термический отжиг, ароматический фрагмент PSS, оптическая спектроскопия, импедансная спектроскопия.

References

1 Skotheim, T.A. & Reynolds, J. (2007). *Handbook of Conducting Polymers*. New York: CRC Press.

2 Kok, M.M., Buechel, M., Vulto, S.I.E., Weijer, P., Meulenkamp E.A., Winter, S.H.P.M., & et al. (2004). Modification of PEDOT: PSS as Hole Injection Layer in Polymer LEDs. *Physica Status Solidi (A),* 201, 1342.

3 Hoppe, H. & Sariciftci, N.S. (2004). Organic solar cells: An overview. *Journal of Materials Research*, 19, 1924–1945.

4 Ma, W., Yang, C., Gong, X., Lee, K. & Heeger, A.J. (2005). Thermally stable, efficient polymer solar cells with nanoscale control of the interpenetrating network morphology. *Advanced Functional Materials*, 15, 1617–1622.

5 Namkoong, G., Younes, E.M., Abdel-Fattah, T.M., El-Maghraby, E.M., Elsayed, A.H. & Abo Elazm, A.H. (2015). Aging process of PEDOT: PSS dispersion and robust recovery of aged PEDOT: PSS as a hole transport layer for organic solar cells. *Organic Electronics*, 25, 1566–1199.

6 Kim, K., Ihm, K. & Kim B. (2014). Surface Property of Indium Tin Oxide (ITO) After Various Methods of Cleaning. *Acta Physica Polonica A,* 127(4), 1176–1179.

7 Zeinidenov, A.K., & Ibrayev, N.Kh. (2017). Photovoltaic and electrophysical properties of plasmon-enhanced organic solar cells // Bulletin of the university of Karaganda-Physics. — 2017. — Vol. 88, № 4. — P. 18–23.

8 Xia Y. Highly conductive poly (3,4-ethylenedioxythiophene): poly(styrene sulfonate) films treated with an amphiphilic fluoro compound as the transparent electrode of polymer solar cells / Y. Xia, K. Sun and J. Ouyang // Energy and Environmental Science. — 2012. — Vol. 5. — P. 5325–5332. DOI: 10.1039/c1ee02475b.

9 Kim Y.H. Highly conductive PEDOT: PSS electrode with optimized solvent and thermal post-treatment for ITO-free organic solar cells / Y.H. Kim, C. Sachse, M.L. Machala, C. May, L. Muller-Meskamp, K. Leo // Advanced Functional Materials. — 2011. — Vol. 21. — P. 1076–1081. DOI: https://doi.org/10.1002/adfm.201002290.

10 Alemu D. Highly conductive PEDOT: PSS electrode by simple film treatment with methanol for ITO-free polymer solar cells / D. Alemu, H.Y. Wei, K.C. Ho, C.W. Chu // Energy and Environmental Science. — 2012. Vol. 5. P. 9662–9671. DOI: https://doi.org/10.1039/C2EE22595F.

11 Yuan X. EIS Equivalent Circuits In Electrochemical Impedance Spectroscopy in PEM Fuel Cells / X. Yuan, C. Song, H. Wang, J. Zhang. — California: Springer, 2010.

DOI 10.31489/2021Ph3/101-114
UDC 669.295:539.214

[1]V.M. Yurov*, [2]A.T. Berdibekov, [3]N.A. Belgibekov, [1]K.M. Makhanov

[1]Karagandy University of the name of academician E.A. Buketov, Kazakhstan;
[2]MTO of the National University of Defense named after the First President of the Republic of Kazakhstan — Elbasy
[3]LLC «Research & Development Center» Kazakhstan Engineering»
*(*e-mail: exciton@list.ru)*

High entropic coatings FeCrNiTiZrAl and their properties

In our proposed empirical model the anisotropy of the surface energy and the thickness of the surface layer of the high-entropy FeCrNiTiZrAl alloy are calculated. The thickness of the surface layer of this alloy is about 2 nm, which is an order of magnitude greater than the thickness of the surface layer of complex crystals, but is of the same order of magnitude as that of metallic glasses. The hardness and other properties of the high-entropy alloy are the same as for metallic glasses, but are 2-3 times higher than the hardness of stainless steels. The surface energy of the high-entropy FeCrNiTiZrAl alloy is about 2 J/m2, which corresponds to the surface energy of magnesium oxide and other crystals with a high melting point. But unlike these crystals, the friction coefficients of a high-entropy alloy (~ 0.06) are much lower than that of ordinary steels (~ 0.8). We have theoretically shown that the friction coefficient is proportionally dependent on the surface energy and inversely proportional to the Gibbs energy, which significantly decreases for a high-entropy alloy, leading to low friction. The high hardness and low coefficient of friction of the high-entropy alloy facilitates the deposition of coatings from them on structural metal products, which contributes to their widespread use.

Keywords: high-entropy coatings, hardness, friction, wear resistance, nanostructure, microhardness.

Introduction

In high-entropy alloys, as a result of the effect of intense mixing, the entropy contribution increases, which stabilizes the formation of a solid solution with a simple structure [1-3]. Based on Boltzmann's hypothesis on the relationship between entropy and system complexity, the configurational change in entropy ΔS_{conf} during the formation of a solid solution of n elements with equiatomic content can be calculated using the following formula:

$$\Delta S_{conf} = -R\ln(1/n) = R\ln(n), \qquad (1)$$

where R is the universal gas constant, n is the number of mixing elements.

At n = 5, $\Delta S_{conf} = 1.61R$ approaches the value of the melting entropy of most intermetallics (about 2R). However, it was later shown that a high entropy of mixing is not a necessary condition for the formation of a single-phase solid solution, but the very term for the name of such an alloy continues to remain in use [4-9]. There are foreign reviews and some dissertations on high-entropy alloys [10-12], but research in this direction is only gaining momentum. We also investigated some high-entropy alloys and coatings obtained by mechanical alloying and magnetron sputtering of targets [13-15].

In our proposed empirical model, not only the anisotropy is calculated, but also the thickness of the surface layer of the high-entropy alloy [16-18].

Objects and research methods

To prepare the FeCrNiTiZrAl target the corresponding equiatomic metal micropowders were used. Further, the obtained metal composition was loaded into a mill glass, which was made of tungsten carbide, and grinding balls with a diameter of 5-10 mm were also made of tungsten carbide. Having filled the glass of the mill with Galosha gasoline, the mill was connected to the rotation connector at a speed of 500 revolutions/minute for 5 hours. Then the metal composition was dried, pressed into a disc 100 mm in diameter and 5 mm thick, and placed in a thermal furnace in which the required vacuum was maintained. The process itself took 3 hours. The FeCrNiTiZrAl target was used in the deposition of coatings (Fig. 1).

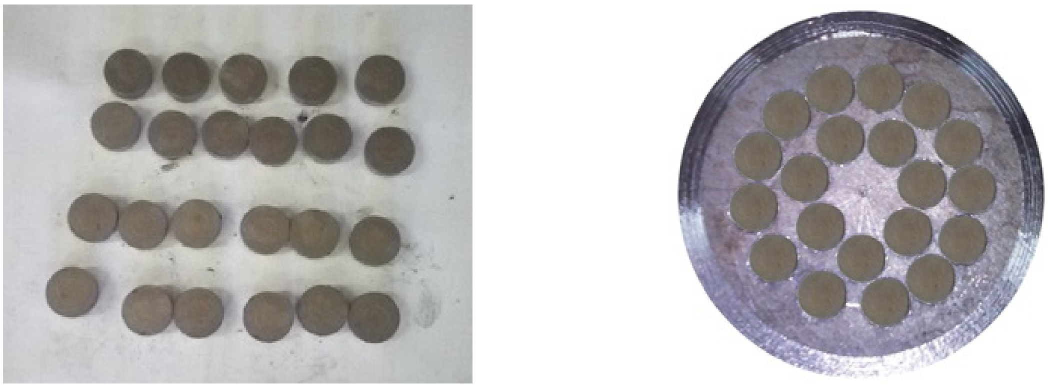

a) b)

Figure 1. Tablets from FeCrNiTiZrAl alloy (a), target with tablets from FeCrNiTiZrAl alloy (b)

Electron microscopic examination was carried out on a scanning electron microscope (SEM) MIRA 3 from TESCAN (Fig. 2).

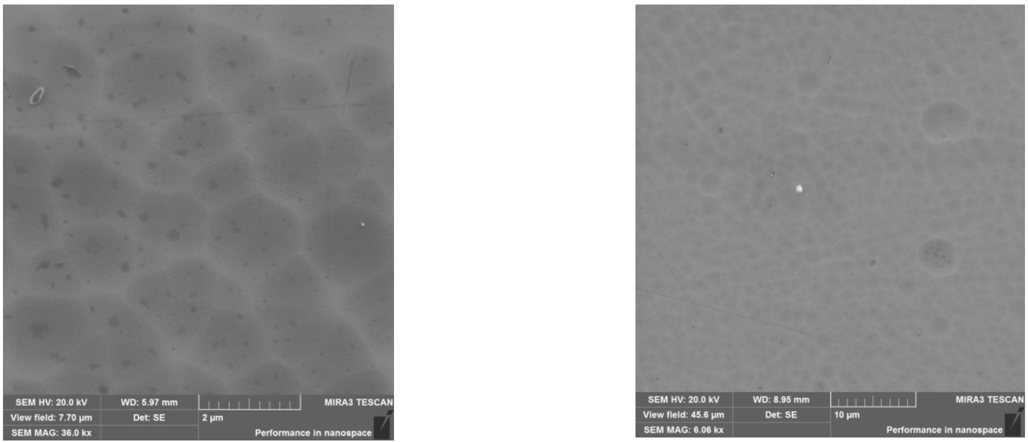

a) b)

Figure 2. SEM image of the FeCrNiTiZrAl coating in argon 2 μm (a) and 10 μm (b)

X-ray fluorescence electron spectroscopy (XPS) of FeCrNiTiZrAl coatings for argon is shown in Figure 3, and the chemical composition is presented in Table 1.

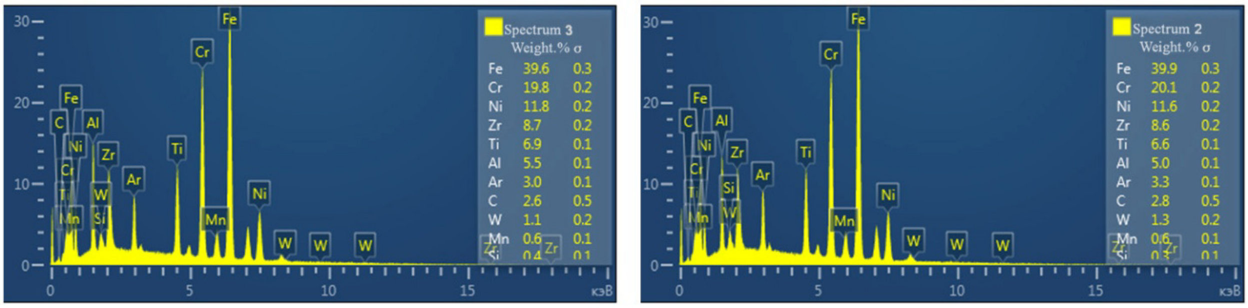

Figure 3. XPS of FeCrNiTiZrAl coatings at two points

Table 1

Chemical composition of the target (at.%)

Alloy	Fe	Cr	Ni	Ti	Zr	Al
FeCrNiTiZrAl	39,6	19,8	11,8	6,9	8,7	5,5

The chemical composition (Table 1) indicates that we have a high-entropy alloy (5-40 at.%). The obtained values of the mass concentration of the elements of the composite cathodes were used to calculate their stoichiometry in the analyzed compound. The values of mass concentration at. % of elements are taken from the experimental data (Fig. 3 and Table 1) — $Fe_{39.6}Cr_{19.8}Ni_{11.8}Ti_{6.9}Zr_{8.7}Al_{5.5}$.

Investigations of the morphology (Fig. 4) of the FeCrNiTiZrAl surface obtained by magnetron sputtering in vacuum were carried out on a JSPM-5400 atomic force microscope (AFM) manufactured by JEOL.

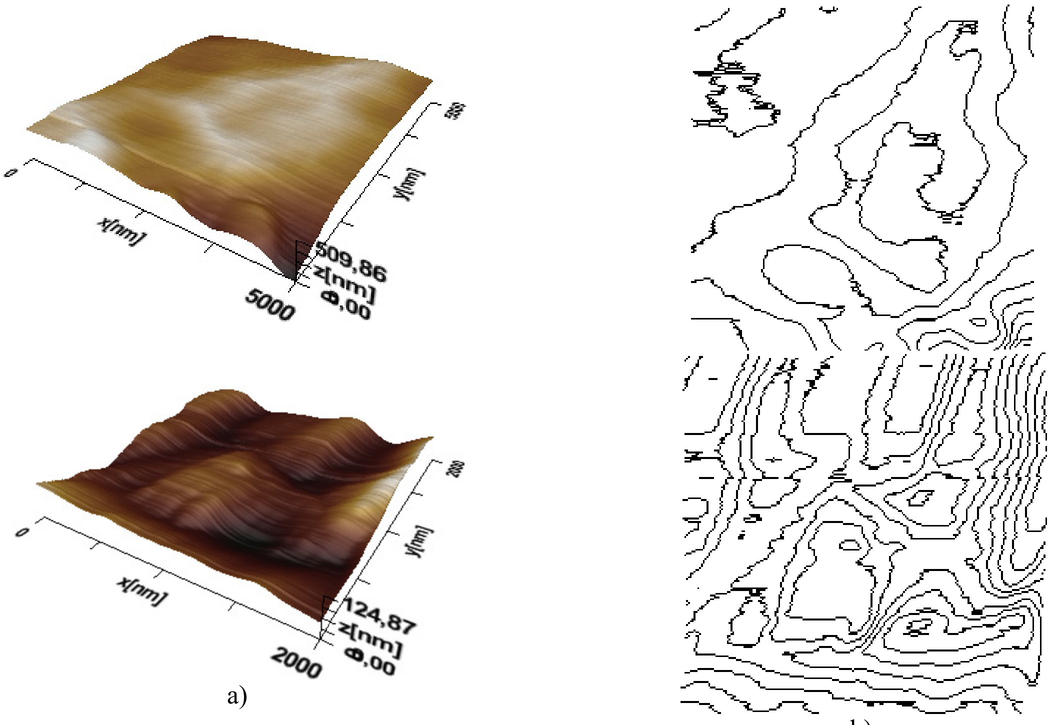

a)

b)

Figure 4. AFM image of the FeCrNiTiZrAl surface (a) and its fractal structure (b) at two points

We used a HVS-1000A microhardness tester (Fig. 5a). This instrument is designed using the latest advances in mechanics, optics, electronics and computer technology to test the hardness of metallic and nonmetallic materials, especially small parts or thin hardened layers. The general scheme of the installation for determining the friction coefficients is shown in Figure 5b and includes: 1 — known clamping weight (15-25 mg), 2 — sample, 3 — sliding surface, 4 — measuring table, 5 — force transducer, 6 — electronics unit and drive.

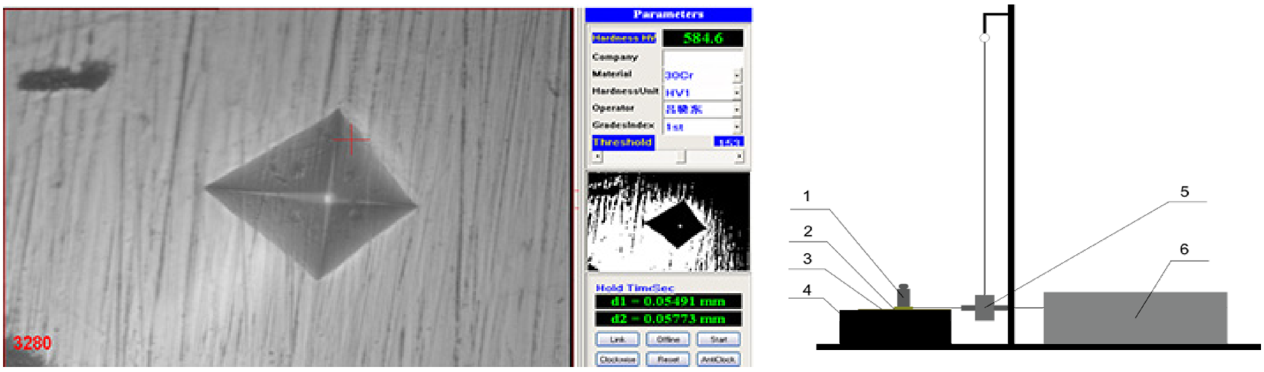

Parameters
Hardness HV 584.6
Company
Material 30Cr
Hardness/Unit HV1
Operator [illegible]
GradesIndex 1st
Threshold [illegible]
Hold Time/Sec
d1 = 0.05491 mm
d2 = 0.05773 mm

a)

b)

Figure 5. Microhardness tester HVC-1000A (a) and installation
diagram for determining the friction coefficients (b)

Calculations of the surface energy will be carried out according to the formula derived under the assumption that there are no first-order phase transitions in these substances up to their melting point [16]:

$$\sigma_{hkl} = \left(\frac{\rho l_{hkl}}{M}\right)\int_{o}^{T_m} c_p dT, \tag{2}$$

where ρ is the density of the crystalline substance, and M is its molecular weight, Tm is the melting point, cp is the molar heat capacity, l_{hkl} is the thickness of the first coordination sphere in the [hkl] direction, which for crystals with body-centered (bcc) and face-centered (fcc)) is given by the relations [19, 20]:

$$\begin{aligned} &\mathrm{Im3m},\ Z=2;\ l_{100}=a;\ l_{110}=a\sqrt{2};\ l_{111}=a/\sqrt{3}, \\ &\mathrm{Fd3m},\ Z=4;\ l_{100}=a;\ l_{110}-a/\sqrt{2};\ l_{111}=2a/\sqrt{3}. \end{aligned} \tag{3}$$

The parameter R(I) is related to the surface energy σ. In [18] we showed that the following relation is fulfilled with an accuracy of 3%:

$$\sigma = 10^{-3}\cdot T_{\mathrm{m}}, \tag{4}$$

where T_m is the melting point of the solid (K). The ratio is fulfilled for all metals and for other crystalline compounds. For $T = T_m$ from [18] we get:

$$R(I)_i = 0.24\cdot 10^{-9}\upsilon. \tag{5}$$

Equation (5) shows that the surface layer of thickness R(I) is determined by the molar (atomic) volume of the element υ = M/ρ, M is the molar mass (g/mol), ρ is the density (g/cm^3), which periodically changes in accordance with the table D.I. Mendeleev. For HEAs, the following ratios are valid:

$$\begin{aligned} T_m &= \sum_{i=1}^{n} c_i (T_m)_i, \\ M &= \sum_{i=1}^{n} c_i (M)_i, \\ \rho &= \sum_{i=1}^{n} c_i (\rho)_i, \end{aligned} \tag{6}$$

where $(T_m)_i$ is the melting point of each alloy element (K), $(M)_i$ is the molar mass of each alloy element (g/mol), ρ is the density of each alloy element (g/cm^3), ci is the concentration of each alloy element, n is the number of alloy elements. All these calculations are carried out using Table 1. Equation (4) can be rewritten as:

$$\sigma(\mathrm{hkl}) = 10^{-3}\cdot T_{\mathrm{m}}\cdot \mathrm{l(hkl)}, \tag{7}$$

where l (hkl) for crystals with body-centered (bcc) and face-centered (fcc) cubic structures is given by relations (3) at a = 1.

Experimental results and their discussion

Let's make calculations according to (5), (6) and (7), taking reference data on T_m, M, ρ [21].

Table 2

Surface layer thickness and surface energy anisotropy FeCrNiTiZrAl

Alloy	(hkl)	Structure	T_m, K	R(I), nm	σ_{hkl} mJ/m^2
FeCrNiTiZrAl	100	Fd3m	1644	1,9	1644
	110			1,4	1174
	111			2,2	1934

Our proposed empirical model is schematically shown in Figure 6. It is an ideal atomically smooth single crystal without vacancies, dislocations and other defects.

The de Broglie layer $R_0 = \lambda dB = \hbar/p$ for metals ranges from 0.01 nm to 0.1 nm. Quantum dimensional effects begin in this layer. The main quantum-dimensional structures include structures with a two-dimensional electron gas — epitaxial films, MIS structures, heterostructures, etc.; structures with one-dimensional gas — quantum threads or wires; structures with zero-dimensional gas — quantum dots, boxes, crystallites [22].

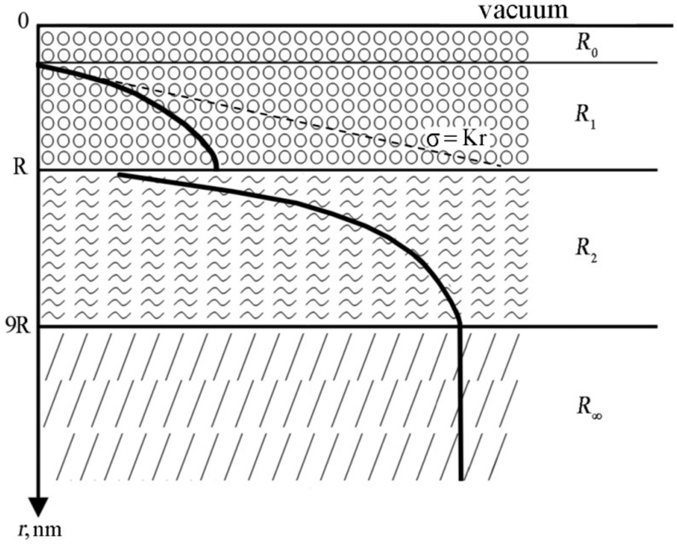

R_0 — de Broglie layer; R_1 — layer R(I); R_2 is the R(II) layer; R_∞ — solid sample layer

Figure 6. Schematic representation of the surface layer [18].

In the R(I) layer with pure metal atoms, there is a reconstruction and relaxation associated with the rearrangement of the surface [23]. For gold, the lattice constant is equal to a = 0.41 nm and the surface is rearranged at a distance $R(I)_{Au} = 1.2/0.41 \approx 3$ three atomic monolayers. The size effects in the R(I) layer are determined by the entire collective of atoms in the system (collective processes). Such «semiclassical» size effects are observed only in nanoparticles and nanostructures [24]. Experimentally, they can be observed in very pure single crystals, when the regime of grazing incidence of X-ray radiation is observed and in the case of an angle of incidence equal to or obviously smaller than the critical angle with total internal reflection [25]. In this case, the refractive wave decays exponentially at sizes on the order of a nanometer. For example, this dimension is 3.1 nm for silicon and 1.2 nm for gold. The result of this process is wave motion, which propagates along the surface and reflects the thickness of the surface layer [23].

The R(II) layer extends approximately to the size $R(II) \approx 9R = R_\infty$, where the bulk phase begins. Dimensional properties begin from this size. By nanomaterials it is customary to understand materials, the main structural elements of which do not exceed the nanotechnological boundary of ~ 100 nm, at least in one direction [25-27].

Table 2 shows that the structure of FeCrNiTiZrAl has a surface layer thickness of about 2 nm on average, which is 5-6 monolayers and is a nanostructure.

Considering the case when the alloy is formed from its constituent elements under isobaric conditions, the change ΔGmix of mixing from the initial element-by-element state to the state after fusion can be expressed as:

$$\Delta G_{mix} = \Delta H_{mix} - T\Delta S_{mix} . \tag{8}$$

An equilibrium state is a state with a minimum of free energy. Figure 7a (according to equation 1) shows an increase in the entropy of mixing with an increase in the number of elements for equimolar alloys. It is seen that the entropy of mixing for the phases of the solid solution increases from a small value for conventional alloys to a large value for high-entropy alloys of the composition [2].

Based on the effect of entropy of mixing, it is possible to divide the variety of alloys into three fields, as shown in Figure 7b. Low entropy alloys are traditional alloys. High-entropy alloys are alloys with at least five basic elements. Medium entropy alloys are alloys with 2–4 basic elements. The high-entropy effect of activation of the formation of a disordered solid phase occurs in essence in the field of high-entropy alloys and should be present to a lesser extent in medium-entropy alloys. Stabilization of a simple solid solution phase is important for the microstructure and properties that can be obtained in these materials [2].

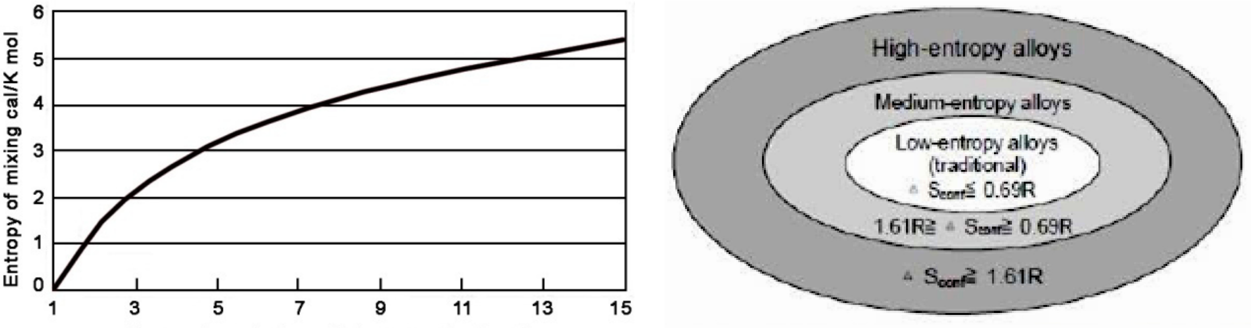

a) b)

Figure 7. The increase in the entropy of mixing to the number of elements in equimolar alloys in a disordered state (a), the division of the world of alloys by the entropy of mixing (b) [2].

It should be noted that the thickness of the surface layer equal to R(I) = M / ρ for high-entropy alloys is significantly lower than for structures of 4-5 and more elemental composition (Table 3) [18]. Table 3 shows that the thickness of the surface layer R(I) of the most common crystals is an order of magnitude greater than the thickness of the surface layer of high-entropy alloys.

Table 3

Thickness of the surface layer of complex crystals [18]

Group of pomegranate	R(I), nm	Group of pomegranate	R(I), nm
$Mg_3Al_2(SiO_4)_3$	25,9	$Ca_3Fe_2Si_3O_{12}$	21,1
$Fe_3Al_2(SiO_4)_3$	19,7	$Ca_3Ti_2(Fe_2Si)O_{12}$	22,7
$Mn_3Al_2[SiO_4]_3$	19,6	$Ca_3Fe_2(SiO_4)_3$	18,8
$Ca_3Al_2[SiO_4]_3$	21,7	$Ca_3(VAlFe)_2(SiO_4)_3$	26,2

This indicates a strong compression of the crystal lattice, reducing its molar (atomic) volume according to equation (5).

Comparing the thickness of the surface layer of high-entropy alloys from Table 2 with the thickness of the surface layer of metallic glasses, we found a great similarity (Table 4), R(I) is not more than 2 nm [28].

In our opinion, there is a lot in common between high-entropy alloys and metallic glasses. Let's compare the mechanical properties of high-entropy alloys, metallic glasses and traditional stainless steels. Table 5 shows that the microhardness of high-entropy alloys and metallic glasses is approximately the same, but 2-3 times higher than that of stainless alloys. This means that the mechanisms for the formation of high-entropy alloys are similar to those for the formation of metallic glasses.

The first metallic glass $Au_{75}Si_{25}$ was obtained by group in the USA in 1960 [29], and the first high-entropy alloy was obtained by Chinese researchers in 2004 [1-3], that is, 40 years later than metallic glasses.

Table 4

Thickness of the surface layer of metallic glass [28]

Glass	M, g/mol	ρ, g/sm^3	R(I), nm
$Mg_{65}Cu_{25}Y_{10}$	40,7	3,8	1,8
$Pd_{40}Ni_{40}P_{20}$	72,3	8,9	1,4
$Fe_{78}Si_{10}B_{12}$	47,6	6,7	1,2
$Ti_{50}Be_{50}Zr_{10}$	36,6	3,7	1,7
$Fe_{40}Ni_{40}P_{14}B_6$	50,8	7,2	1,2
$Ni_{49}Fe_{29}P_{14}B_6Al_2$	56,7	7,8	1,2
$Zr_{62}Cu_{22}Al_{10}Fe_5Dy_1$	77,6	7,0	1,9
$Zr_{41.2}Ti_{13.8}Cu_{12.5}Ni_{10}Be_{22.5}$	53,8	5,7	1,6

Table 5

Microhardness μ of high-entropy alloys (HEA), metallic glasses (MS) and stainless steels (NS)

HEA	μ, HV [10]	MS	μ, HV [30]	NS	μ, HV [21]
FeCrNiTiZrAl (our alloy)	585	$Fe_{80}B_{20}$	1100	316 Stainless steel	189
CoCrFeNiMn	659	$Fe_{78}Mo_2B_{20}$	1015	17-4 PH Stainless steel	410
CrNiTiZrCu	890	$Fe_{40}Ni_{40}P_{14}B_6$	640	Stellite 6 (base Co-Cr)	413
AlTiVFeNiZr	800	$Fe_{78}P_{13}C_7$	760	Hastelloy C (based on Ni-Mo-Fe)	236
MoTiVFeNiZr	740	$Fe_{78}Si_{10}B_{12}$	890	18Х2Н4МА	269
CuTiVFeNiZrCo	630	$Ni_{75}Si_8B_{17}$	860	15ХСНД	335
MoTiVFeNiZrCo	790	$Co_{75}Si_{15}B_{10}$	910	20ХГНР	197

Let us now turn to Table 2 and consider the anisotropy of the surface energy of FeCrNiTiZrAl. Table 2 shows that the maximum surface energy σhkl is achieved in the [111] plane. Metals with a face-centered cubic (fcc) lattice are deformed along close-packed octahedral [111] planes in close-packed <110> directions. In cube-shaped lattices along the direction of the edge there are fewer atomic units than the diagonal of the cube in the bcc lattices or the diagonal of the fcc face, where there are more atomic units. The same is true for the planes that intersect the faces of the bcc and fcc lattices. Since atomic units differ in different crystallographic directions, and hence their density differs, this leads to the fact that the physical and chemical properties exhibit anisotropy of these properties in crystalline solids.

It is rather difficult to experimentally study the energy of the surface of a solid, because the atoms are not in a liquid, where they are mobile, but rather strongly linked by intermolecular interactions. They become mobile only at a temperature close to the melting point of a solid. At room and lower temperatures, the surface energy of a crystal can be determined only by knowing its crystal structure, that is, only in the case when it is possible to do the work of splitting the crystal in one direction or another, if the destruction of the solid itself was brittle [31]. This method was developed in 1930 by Obreimov [32] and consisted of splitting the crystal along the cleavage plane, which bends and the connected dynamometer measures the force preventing this. The work of this force gives the value of surface energy. Gilman [33] (Table 6) measured the surface energy of a number of crystals using this method at the temperature of liquid nitrogen (T = -196 ºC). The error obtained in determining the surface energy by the method of splitting a crystal is from 10 to 20%. Comparing tables 6 and 2, we find that magnesium oxide and silicon oxide have similar values of surface energy for HEAs if we take into account that these values were obtained in experiments at T = -196 ºC.

Table 6

Surface energy of some crystals [33]

Crystal	LiF (100)	MgO (100)	CaF_2 (111)	$CaCO_3$ (100)	Si (111)	Zn (0001)
σ_s, mJ/m^2	340	1200	450	230	1240	105

The anisotropy of the surface energy leads to the fact that the melting temperature of various faces becomes different and, with a decrease in the particle size, it changes according to the law [34]:

$$T(r) = T_0\left(1 - \frac{R(I)}{r}\right), \tag{9}$$

where T_0 is the melting point of the bulk sample.

Table 7 shows the coefficients of friction FeCrNiTiZrAl, measured by us on the installation in Figure 5b. The average values are ~ 0.06, which noticeably distinguishes them from traditional steels, where the steel-steel friction coefficients are ~ 0.8.

Table 7

Coefficients of friction of samples sprayed for 2 hours in argon

Number of measurements	Coefficients of friction of samples with FeCrNiTiZrAl sputtering	
	over copper plate	over aluminum plate
1	0,075	0,044
2	0,067	0,091
3	0,092	0,044
4	0,076	0,059
5	0,074	0,062
6	0,072	0,047
7	0,086	0,054
8	0,074	0,050
9	0,092	0,055
10	0,109	0,050
Average	**0,081**	**0,055**

Within the framework of the thermodynamic approach for the dry friction coefficient, we obtained the following formula [34]:

$$k = \tilde{N}\cdot\grave{O}\cdot\frac{\sigma\cdot S}{\Delta G^0}\cdot\overline{N}, \qquad (10)$$

where σ is the specific surface energy of the material, S is the contact area, T is the temperature, ΔG^0 is the Gibbs energy, $\overline{N}$ is the average number of elementary fracture carriers (proportional to the number of defects), C is a constant.

But according to the molecular kinetic theory, the friction force F ~ k is equal to:

$$F = \int \sigma dL \approx \sigma\cdot L, \qquad (11)$$

where σ is the surface energy (table 2), L is the length of the traveled path.

Equation (10) shows that the coefficient of friction is proportional and increases with increasing surface energy according to (11), that is, the value of σ from Table 2 should lead to an increase in the coefficient of friction. But the opposite picture is observed experimentally, the friction coefficient decreases, which contradicts the molecular kinetic theory but becomes explainable from the point of view of our formula (10), which contains the Gibbs formula in the denominators and significantly decreases for a high-entropy alloy according to formulas (8) and (1). Since tribological properties play an essential role in technology, high-entropy alloys and coatings will take a worthy place among structural materials.

Let us now turn to Figure 4, where AFM images show the waviness of the surface. We measured the microhardness multiple times every 0.5 mm on an electronic microhardness tester HVS-1000A. The results are shown in Figure 8.

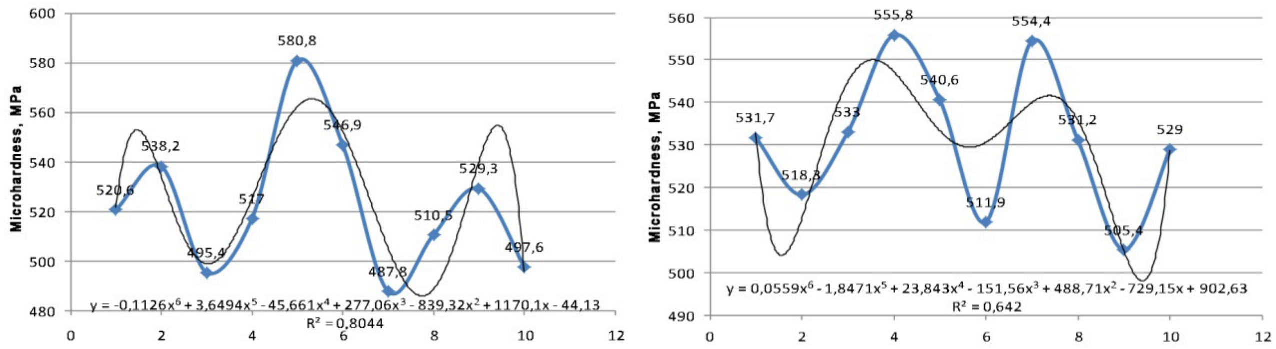

Figure 8. Autowaves in the FeCrNiTiZrAl coating [35]

In both cases, a quasiperiodic structure is observed, i.e., wave process. Figure 8 shows that the wavelength is about 10^{-4} m, i.e., the mass transfer rate is ~ 10^{-4} m/s. Since the rate of mass transfer $V \approx \sqrt{D/t}$, then for the diffusion coefficient we obtain the estimate $D \sim 10^{-8}$ m^2/s. This corresponds to the low diffusion regime [36].

We considered the problem of crystallization of a deposited coating in the form of a cylinder of finite dimensions with a movable interface. The non-stationary equation describing this process in a movable cylindrical coordinate system moving according to the law β(t) has the form [37-39]:

$$\frac{\partial T}{\partial t} = \alpha\left[\frac{\partial^2 T}{\partial z^2} + \frac{1}{r}\frac{\partial}{\partial r}\left(r\frac{\partial T}{\partial r}\right)\right], \qquad (12)$$

where α is the coefficient of thermal diffusivity.

As a result, the solution is obtained in the form:

$$T(r,z) = \frac{T_0 R}{\sqrt{\pi z}} I_0\left(\frac{2r}{R}\right).$$

The radial and axial components of the temperature gradient are equal:

$$\frac{\partial T}{\partial r} = \frac{2}{z}\frac{T_0}{\sqrt{\pi}} I_1\left(\frac{2r}{R}\right),$$

$$\frac{\partial T}{\partial z} = \frac{RT_0}{\sqrt{\pi z^2}} I_0\left(\frac{2r}{R}\right).$$

Both equations containing the Bessel functions $I_0(2r/R)$ and $I_1(2r/R)$ show the wave character of the coating solidification (Fig. 9).

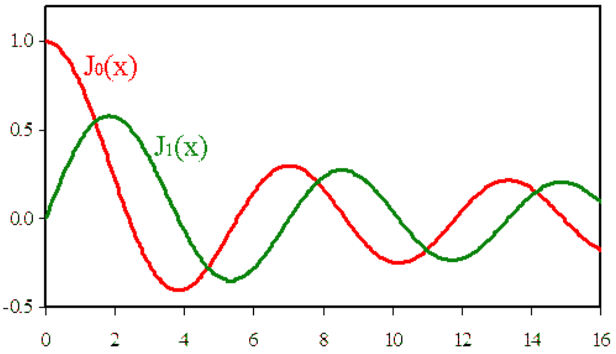

Figure 9. Graphs of Bessel functions (compare with Figure 8)

The theory of crystallization of a cylinder of finite dimensions developed by us belongs to problems with a moving phase interface and is called the Stefan problem [40]. Boundary value problems of this type differ significantly from the classical problems of heat conduction or diffusion. This difference is associated with the motion of the phase separation according to an arbitrary law, so that the separation of variables by classical methods is not feasible. The method of integral Fourier transforms is also not allowed. The motion of the phase boundary leads to nonlinearity of the system of equations, which causes the appearance of autowaves.

Industrial testing of high-entropy coating

At Karaganda CHPP-3, a hammer mill that has high economic indicators is used in systems with direct fuel injection and can work under pressure. In these mills the fuel is crushed mainly by the impact of hammers (beats), and partially also abrades between the beaters and the mill body. The main problem in the operation of coal grinding mills is the high abrasive wear of the beaters, the service life of which averages 500 hours.

In this work, an attempt is made to increase the service life of the beaters of coal grinding mills by mechanically activating them in a tumbling drum, followed by the application of hardening coatings from high-entropy FeCrNiTiZrAl alloys (Fig.10a). Studies have shown that with the FeCrNiTiZrAl coating the microhardness increases by about 1.6 times; wear resistance increases 7.5 times; the coefficient of friction decreases almost 10 times, and the resource of the beater increases almost three times, which is economically very significant.

The turbomechanical plant in Karaganda mastered the blades for the T-100/120-130-2 TMZ steam turbine. It is a single-shaft three-cylinder unit with two cogeneration steam extractions (upper and lower) and two exhausts. The main cause of erosive wear of the blades of low-pressure stages of steam turbines is cavitation phenomena during the shock-droplet effect of wet steam on certain zones of the blades during the operation of the turbine. Coating was carried out on prepared turbine blades made of steel grade 20X13. The vacuum chamber was evacuated to a pressure of 0.003 Pa, then the PINK was switched on, Ar was injected to a pressure of 1 Pa, a negative bias potential of 1000 V was applied to the substrate, and the blade surface was cleaned and heated for 10 min. Then the argon pressure was lowered to 0.1 Pa, and the magnetron was turned on. The displacement on the blades was reduced to 150 V, the magnetron current was kept constant 3 A. The blades were located in the chamber at a distance of 15 cm, the spraying time was 1 hour. Turbine blades with spraying are shown in Figure 10 b.

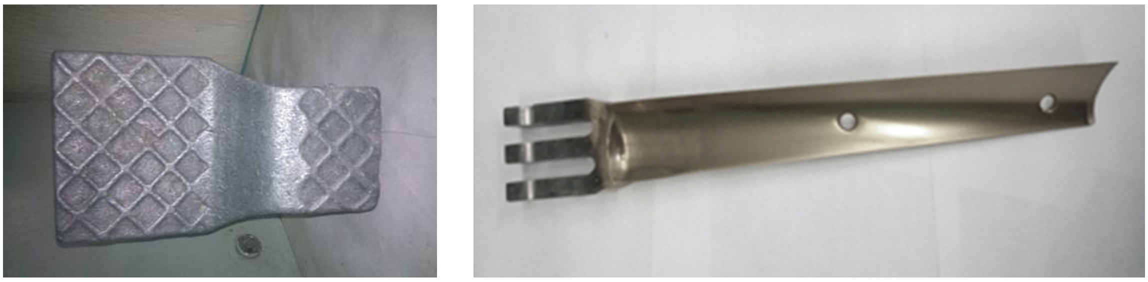
a) b)

Figure 10. Beater for coal grinding mills coated with FeCrNiTiZrAl (a), turbine blades coated with FeCrNiTiZrAl (b).

Conclusion

In our proposed empirical model, the surface anisotropy and the thickness of the surface layer of the high-entropy FeCrNiTiZrAl alloy are calculated. X-ray fluorescence electron spectroscopy of FeCrNiTiZrAl coatings for argon and chemical composition showed that we have formed a high-entropy alloy, the thickness of the surface layer of which was 2 nm. In our opinion, there is a lot in common between high-entropy alloys and metallic glasses. Comparison shows that the microhardness of high-entropy alloys and metallic glasses is approximately the same, but 2-3 times higher than that of stainless alloys. This means that the mechanisms for the formation of high-entropy alloys are similar to those for the formation of metallic glasses.

Studies have shown that the maximum surface energy σhkl is reached in the [111] plane. Metals with a face-centered cubic (fcc) lattice are deformed along close-packed octahedral [111] planes in close-packed <110> directions. The anisotropy of the surface energy leads to the fact that the melting point of different faces becomes different and with a decrease in the size of the coating, it changes according to the hyperbolic law.

The equation (10) we obtained shows that the friction coefficient is proportional and increases with an increase in the surface energy according to (11), that is, the value of σ should lead to an increase in the friction coefficient. But the opposite picture is observed experimentally, the friction coefficient decreases, which contradicts the molecular-kinetic theory but becomes explainable from the point of view of our formula (10), which contains the Gibbs formula in the denominators and decreases significantly for the high-entropy one. Since tribological properties play an essential role in technology, high-entropy alloys and coatings will take a worthy place among structural materials.

The wear of the Hadfield steel used at CHPP-3 occurs in (500-550) hours of continuous operation. That is, after the high-entropy coating of FeCrNiTiZrAl, the resource of the mill increases almost 3 times, which is economically very significant.

The microhardness of our FeCrNiTiZrAl coating is not inferior to high-entropy equiatomic alloys. Such wear resistance of the FeCrNiTiZrCu coating means that the structure of the coating is not only high-entropy, as evidenced by the chemical composition, but also ordered. The ordering of the coating corresponds, as a rule, to dissipative structures. They differ from equilibrium structures in that for their existence they require a constant influx of energy from the outside (magnetron deposition of a coating).

The work was performed under the program of the Ministry of Education and Science of the Republic of Kazakhstan. Grants No. 0118RK000063 and No. F.0781.

References

1 Yeh J.-W. Nanostructured High-Entropy Alloys with Multiple Principle Elements: Novel Alloy Design Concepts and Outcomes / J.-W. Yeh, S.-K. Chen, S.-J. Lin, Sh.-Y. Chang// Advanced Engineering Materials. — 2004. — Vol. 6, №8. — P. 299-303.

2 Yeh J.W. High-entropy alloys — a new era of exploitation / J.W. Yeh, Y.L. Chen, S.J. Lin // Materials Science Forum. — 2007. — Vol. 560. — P. 1-9.

3 Wang Y.P. Solid Solution or Intermetallics in a High-Entropy Alloy / Y.P. Wang, B.Sh. Li, Zh.F. Heng // Advanced Engineering Materials. — 2009. — Vol. 11, № 8. — P. 641-644.

4 Firstov S.A. A new class of materials — high-entropy alloys and coatings / S.A. Firstov, V.F. Gorban, N.A. Krapivka, E.P. Pechkovsky // Vestnik TSU, — 2013. — Vol. 18. — P. 1938-1940.

5 Shaginyan L.R. Properties of coatings from high-entropy alloy Al–Cr–Fe–Co–Ni–Cu–V obtained by magnetron sputtering / L.R. Shaginyan, V.F. Gorban, N.A. Krapivka, S.A. Firstov, I.F. Kopylov // Superhard materials. — 2016. — No. 1. — P. 33-43.

6 Kostyuk G.I. Scientific foundations for the creation of high-entropy nitride, carbide, boride and oxide nanocoatings on T12A hard alloy / G.I. Kostyuk, Yu, A. Sysoev, O.M. Melkozerova // Open information and computer integrated technologies. — 2017. — No. 75. — P. 121-131.

7 Gorban V.F. Obtaining and physical and mechanical properties of high-entropy oxide based on equiatomic alloy CrFeCoNiMn / V.F. Gorban, A.A. Andreev, A.M. Chikryzhov, M.V. Karpets, A.A. Ostroverkh // Superhard materials. — 2019. — No. 1. — P. 51-57.

8 Sanin V.N. SHS metallurgy of cast high-entropy alloys based on transition metals / V.N. Sanin, V.I. Yukhvid, D.N. Ikornikov // *DAN NAN.* — 2016. — Vol. 470. — No. 4. — P. 421-426.

9 Miracle D.B. A critical review of high entropy alloys and related concepts / D.B. Miracle, O.N. Senkov // Acta Mater. — 2017. — Vol. 122. — P. 448–511.

10 Шайсултанов Д.Г. Структура и механические свойства высокоэнтропийных сплавов системы CoCrFeNiX (X = Mn, V, Mn и V, Al и Cu): дис. ... канд. техн. наук // Д.Г. Шайсултанов. — Белгород, 2015. — 142 с.

11 Ивченко М.В. Структура, фазовые превращения и свойства высокоэнтропийных эквиатомных металлических сплавов на основе AlCrFeCoNiCu: дис. ... канд. физ.-мат. наук // М.В. Ивченко. — Екатеринбург, 2015. — 167 с.

12 Юрченко Н.Ю. Разработка и исследование высокоэнтропийных сплавов с высокой удельной прочностью на основе системы Al-Cr-Nb-Ti-V-Zr: дис. ... канд. тех. наук // Н.Ю. Юрченко. — Белгород, 2019. — 187 с.

13 Yurov V.M. Wear resistance and tribological properties of high entropy coatings CrNiTiZrCu / V.M. Yurov, E.N. Eremin, S.A. Guchenko // Eurasian Physical Technical Journal. — 2020. — Vol. 17. — No. 1 (33). — P. 13–18.

14 Yurov V.M. Structural properties of the high-entropy TiNiZrCuCr coating / V.M. Yurov, S.A. Guchenko, K.M. Makhanov // Modern science-intensive technol. — 2020. — No. 4. — P. 78-83.

15 Yurov V.M. Application of high-entropy coatings on turbine blades / V.M. Yurov, B.N. Shelpyakov, S.A. Guchenko, A.N. Tvardovsky // Trends in the development of science and education. — 2020. No. 59, Part 1. — P. 49-54.

16 Yurov V.M. Anisotropy of surface energy and thickness of the surface layer of magnetic nanostructures / V.M. Yurov, V.I. Goncharenko, V.S. Oleshko // Nano- and microsystem technology. — 2021. — V. 23, No. 2. — P. 59-62.

17 Yurov V.M. Anisotropy of the surface energy of silicon. Bulletin of KazNU im. al Farabi // V.M. Yurov. — 2021. — No. 1(76). — P. 51-58.

18 Yurov V.M. Surface layer thickness, surface energy, and atomic volume of an element / V.M. Yurov, S.A. Guchenko, V.Ch. Laurinas // Physicochemical aspects of the study of clusters, nanostructures and nanomaterials. — 2018. Issue. 10. — P. 691-699.

19 Bokarev V.P. Anisotropy of physicochemical properties of single-crystal surfaces / V.P. Bokarev, G.Ya. Krasnikov // Electronic engineering. Series 3. Microelectronics. — 2016. — No. 4 (164). — P. 25-30.

20 Бочкарев В.П. Развитие физико-химических принципов оценки влияния поверхностной энергии на свойства материалов и процессы для технологии микроэлектроники: дис. ... д-ра техн. наук // В.П. Бочкарев. — М., 2020. — 299 с.

21 Солнцев Ю.П. Металлы. Справочник / Ю.П. Солнцев. — СПб.: Рубин, 2000. — 614 с.

22 Arutyunov K.Yu. Quantum size effects in metallic nanostructures / K.Yu. Arutyunov // DAN VSH RAS. — 2015. — No. 3(28). — P. 7-16.

23 Оура К. Введение в физику поверхности / К. Оура, В.Г. Лифшиц, А.А. Саранин, А.В. Зотов, М. Катаяма. — М.: Наука, 2006. — 490 с.

24 Uvarov N.F. Size effects in the chemistry of heterogeneous systems / N.F. Uvarov, V.V. Boldyrev // Uspekhi khimii. — 2001. — V. 70 (4). — P. 307-329.

25 Gusev A.I. Nanomaterials, nanostructures, nanotechnology / A.I. Gusev. — Moscow: Fizmatlit, 2005. — p. 96.

26 Андриевский Р.А. Наноструктурные материалы / Р.А. Андриевский, А.В. Рагуля. — М.: Академия, 2005. — 192 с.

27 Суздалев И.П. Нанотехнология: физико-химия нанокластеров, наноструктур и наноматериалов / И.П. Суздалев. — М.: КомКнига, 2006. — 592 с.

28 Yurov V.M. Surface and surface energy of metal glasses / V.M. Yurov, D.A. Kaykenov // Sciences of Europe. — 2020. — No. 51. — Vol. 1. — P. 71-74.

29 Cheng Y.Q. Atomic-level structure and structure–property relationship in metallic glasses / Y.Q. Cheng, E. Ma // Progress in Materials Science. — 2011. — Vol. 56. — P. 379 — 473.

30 Абросимова Г.Е. Эволюция структуры металлических стекол при внешних воздействиях: дис. д-ра физ.-мат. наук // Г.Е. Абросимова. — Черноголовка, 2012. — 296 с.

31 Kudrya A.V. The role of different-scale structures in ensuring the plasticity and toughness of structurally inhomogeneous steels / A.V. Kudrya // Metallurgy and heat treatment of metals. — 2005. — No. 5. — P. 18-23.

32 Obreimoff, J.W. The splitting reigth of mica / J.W. Obreimoff // Proc. Roy. — 1930. — V. 127. — P. 290-293.

33 Gilman J. Direct Measurements of the surface energies of crystals / J. Gilman // J. Appl. Phys., — 1960. — Vol. 31, № 2. — P. 2208-2216.

34 Yurov V.M. Estimation of the melting temperature of nanostructures of solids / V.M. Yurov, K.M. Makhanov // Nano- and microsystem technology. — 2020. — Vol. 22, No. 7. — P. 347-351.

35 Yurov V.M. Superfecial tension of pure metals / V.M. Yurov // Eurasian Physical Technical journal. — 2011. — Vol. 8, № 1(15). — P. 10-14.

36 Мищенко Е.Ф. Автоволновые процессы в нелинейных средах с диффузией / Е.Ф. Мищенко, В.А. Садовничий, А.Ю. Колесов, Н.Х. Розов. — М.: Физматлит, 2010. — 395 с.

37 Yurov V.M. Thermodynamics of luminescent systems / V.M. Yurov // Bulletin of the university of Karaganda-Physics. — 2005. — № 3 (39). — P. 13-15.

38 Yurov V.M. The thickness of the surface layer and autowave processes in high-entropy coatings / V.M. Yurov, S.V. Guchenko, K.M. Makhanov // Matrix of scientific knowledge. — 2020. — №. 7. — P. 9-16.

39 Yurov V.M. Application of high entropy coatings simultaneous in one cycle spraying three cathodes / V.M. Yurov, E.N. Eremin, S.A. Guchenko // Bulletin of the university of Karaganda-Physics. — 2020. — № 1 (97). — P. 7-17.

40 Gupta S.C. The Classical Stefan Problem: Basic Concepts, Modelling and Analysis with Quasi-Analytical Solutions and Methods / S.C. Gupta // New Edition: Elsevier. — 2018. — 732 p.

В.М. Юров, А.Т. Бердібеков, Н.А. Белгібеков, Қ.М. Маханов

Жоғарыэнтропиялы FeCrNiTiZrAl жабындары және олардың қасиеттері

Авторлар ұсынған эмпирикалық модельде жоғарыэнтропиялы FeCrNiTiZrAl қорытпасының беткі энергия анизотропиясы және беткі қабаттың қалыңдығы есептелген. Қорытпаның беткі қабатының қалыңдығы шамамен 2 нм құрайды, бұл күрделі кристалдардың беткі қабатының қалыңдығынан үлкен болса да, дегенмен, реті бойынша металл шыныларымен сәйкес келеді. Жоғарыэнтропиялы қорытпаның қаттылығы және басқа да қасиеттері металл шынылардікімен бірдей, бірақ тотығуға төзімді болаттардың қаттылығынан 2-3 есе жоғары. Жоғарыэнтропиялы FeCrNiTiZrAl қорытпасының беттік энергиясы шамамен 2 Дж/м^2 құрайды, бұл магний оксиді мен балқу температурасы жоғары басқа кристалдардың беткі энергиясына сәйкес келеді. Бірақ бұл кристалдардан айырмашылығы, жоғарыэнтропиялы қорытпаның үйкеліс коэффициенттері қарапайым болаттарға қарағанда (~ 0,8) әлдеқайда төмен (~ 0,06). Үйкеліс коэффициенті беткі энергияға пропорционал түрде тәуелді екенін және жоғарыэнтропиялы қорытпа үшін едәуір азайып төменгі үйкеліске әкелетін Гиббс энергиясынан тәуелділігі кері пропорционал екенін теориялық тұрғыдан көрсетілген, жоғарыэнтропиялы қорытпаның жоғары қаттылығымен үйкеліс коэффициентінің төмендігі оларды металдан жасалған конструкциялық бұйымдардың бетіне қалыптастыруға ықпал етіп, осы бұйымдардың қолданысын кеңейтуге оң әсерін тигізеді.

Кілт сөздер: жоғарыэнтропиялық жабындар, қаттылық, үйкеліс, тозуға төзімділік, наноқұрылым, микроқаттылық.

В.М. Юров, А.Т. Бердибеков, Н.А. Бельгибеков, К.М. Маханов

Высокоэнтропийные покрытия FeCrNiTiZrAl и их свойства

В предложенной авторами эмпирической модели рассчитаны анизотропия поверхностной энергии и толщина поверхностного слоя высокоэнтропийного сплава FeCrNiTiZrAl. Толщина слоя поверхности этого сплава составляет около 2 нм, которая на порядок превышает толщину поверхностного слоя сложных кристаллов, но имеет такой же порядок, как и металлические стекла. Твердость и другие свойства высокоэнтропийного сплава одинаковы с металлическими стеклами, но в 2–3 раза превышают твердость нержавеющих сталей. Поверхностная энергия высокоэнтропийного сплава FeCrNiTiZrAl составляет около 2 Дж/м^2, что соответствует поверхностной энергии окиси магния и другим кристаллам с высокой температурой плавления. Но, в отличие от этих кристаллов, коэффициенты трения у высокоэнтропийного сплава значительно ниже (~ 0,06), чем у обычных сталей (~ 0,8). Теоретически нами показано, что коэффициент трения пропорционально зависит от поверхностной энергии и обратно пропорционально зависит от энергии Гиббса, которая значительно уменьшается для высокоэнтропийного сплава, приводя к низкому трению. Высокая твердость и низкий коэффициент трения высокоэнтропийного сплава способствуют нанесению покрытий из них на конструкционные изделия из металлов, что способствует их широкому применению.

Ключевые слова: высокоэнтропийные покрытия, твердость, трение, износостойкость, наноструктура, микротвердость.

References

1 Yeh, J. -W., Chen, S. -K., Lin, S. -J., & Chang, Sh. -Y. (2004). Nanostructured High-Entropy Alloys with Multiple Principle Elements: Novel Alloy Design Concepts and Outcomes. *Advanced Engineering Materials*, 6, № 8, 299-303.

2 Yeh, J.W., Chen, Y.L., Lin, S.J. (2007). High-entropy alloys — a new era of exploitation. *Materials Science Forum*, 560, 1-9.

3 Wang, Y.P., Li, B.Sh., Heng, Zh.F. (2009). Solid Solution or Intermetallics in a High-Entropy Alloy. *Advanced Engineering Materials*, 11, № 8, 641-644.

4 Firstov, S.A., Gorban, V.F., Krapivka, N.A., & Pechkovsky E.P. (2013). A new class of materials — high-entropy alloys and coatings. *Vestnik TSU*, 18, 1938-1940.

5 Shaginyan, L.R., Gorban, V.F., Krapivka, N.A., Firstov, S.A. ,& Kopylov, I.F. (2016). Properties of coatings from high-entropy alloy Al–Cr–Fe–Co–Ni–Cu–V obtained by magnetron sputtering. *Superhard materials*, 1, 33-43.

6 Kostyuk, G.I., Sysoev, Yu, A., Melkozerova O.M. (2017). Scientific foundations for the creation of high-entropy nitride, carbide, boride and oxide nanocoatings on T12A hard alloy. *Open information and computer integrated technologies*, 75, 121-131.

7 Gorban, V.F., Andreev, A.A., Chikryzhov, A.M., Karpets, M.V. & Ostroverkh A.A. (2019). Obtaining and physical and mechanical properties of high-entropy oxide based on equiatomic alloy CrFeCoNiMn. *Superhard materials*, 1, 51-57.

8 Sanin, V.N., Yukhvid, V.I., Ikornikov, D.N. (2016). SHS metallurgy of cast high-entropy alloys based on transition metals. *DAN NAN*, 470, 4, 421-426.

9 Miracle, D.B., Senkov, O.N. (2017). A critical review of high entropy alloys and related concepts. *Acta Mater.*, 122, 448–511.

10 Shaisultanov, D.G. (2015). Struktura i mekhanicheskie svoistva vysokoentropiinykh splavov sistemy CoCrFeNiX (X = Mn, V, Mn i V, Al i Cu) [Structure and mechanical properties of high-entropy alloys of the CoCrFeNiX system (X = Mn, V, Mn and V, Al and Cu)]. *Candidate's thesis*. Belgorod [in Russian].

11 Ivchenko, M.V. (2015). Struktura, fazovye prevrashcheniia i svoistva vysokoentropiinykh ekviatomnykh metallicheskikh splavov na osnove AlCrFeCoNiCu [Structure, phase transformations and properties of high-entropy equiatomic metal alloys based on AlCrFeCoNiCu]. *Candidate's thesis*. Yekaterinburg [in Russian].

12 Yurchenko, N.Yu. (2019). Razrabotka i issledovanie vysokoentropiinykh splavov s vysokoi udelnoi prochnostiu na osnove sistemy Al-Cr-Nb-Ti-V-Zr [Development and research of high-entropy alloys with high specific strength based on the Al-Cr-Nb-Ti-V-Zr system]. *Candidate's thesis*. Belgorod [in Russian].

13 Yurov, V.M., Eremin, E.N., Guchenko, S.A. (2020). Wear resistance and tribological properties of high entropy coatings CrNiTiZrCu. *Eurasian Physical Technical Journal*, 17, 1 (33), 13-18.

14 Yurov, V.M., Guchenko, S.A., Makhanov, K.M. (2020). Structural properties of the high-entropy TiNiZrCuCr coating. *Modern science-intensive technol*, 4, 78-83.

15 Yurov, V.M., Shelpyakov, B.N., Guchenko, S.A.,& Tvardovsky, A.N. (2020). Application of high-entropy coatings on turbine blades. *Trends in the development of science and education*, 59, 1, 49-54.

16 Yurov, V.M., Goncharenko, V.I., Oleshko, V.S. (2021). Anisotropy of surface energy and thickness of the surface layer of magnetic nanostructures. *Nano- and microsystem technology*, 23, 2, 59-62.

17 Yurov, V.M. (2021). Anisotropy of the surface energy of silicon. *Bulletin of KazNU im. al Farab*i, 1(76), 51-58.

18 Yurov, V.M., Guchenko, S.A., Laurinas, V.Ch. (2018). Surface layer thickness, surface energy, and atomic volume of an element. *Physicochemical aspects of the study of clusters, nanostructures and nanomaterials,* Issue. 10, 691-699.

19 Bokarev, V.P., Krasnikov, G.Ya. (2016). Anisotropy of physicochemical properties of single-crystal surfaces. *Electronic engineering. Series 3. Microelectronics*, 4 (164), 25-30.

20 Bochkarev, V.P. (2020). Razvitie fiziko-khimicheskikh printsipov otsenki vliianiia poverkhnostnoi energii na svoistva materialov i protsessy dlia tekhnologii mikroelektroniki [Development of physicochemical principles for assessing the effect of surface energy on the properties of materials and processes for microelectronic technology]. *Doctor's thesis*. Moscow [in Russian].

21 Solntsev, Yu.P. (2000). *Metally: Spravochnik [Metals. Directory]*. Saint Petersburg: Rubin [in Russian].

22 Arutyunov, K.Yu. (2015). Quantum size effects in metallic nanostructures. *DAN VSH RAS*, 3(28), 7-16.

23 Oura, K., Lifshits, V.G., Saranin, A.A., Zotov, A.V., & Kataiama, M. (2006). *Vvedenie v fiziku poverkhnosti [Introduction to surface physics]*. Moscow: Nauka [in Russian].

24 Uvarov, N.F., Boldyrev, V.V. (2001). Size effects in the chemistry of heterogeneous systems. *Uspekhi khimii*, 70 (4), 307-329.

25 Gusev, A.I. (2005). *Nanomaterials, nanostructures, nanotechnology*. Moscow: Fizmatlit.

26 Andrievskii, R.A., & Ragulia, A.V. (2005). *Nanostrukturnye materialy [Nanostructured materials]*. Moscow: Akademiia [in Russian].

27 Suzdalev, I.P. (2006). *Nanotekhnologiia: fiziko-khimiia nanoklasterov, nanostruktur i nanomaterialov [Nanotechnology: physical chemistry of nanoclusters, nanostructures and nanomaterials]*. Moscow: KomKniga [in Russian].

28 Yurov, V.M., Kaykenov, D.A. (2020). Surface and surface energy of metal glasses. *Sciences of Europe*, 51, 1, 71-74.

29 Cheng, Y.Q., Ma, E. (2011). Atomic-level structure and structure–property relationship in metallic glasses. *Progress in Materials Science*, 56, 379–473.

30 Abrosimova, G.E. (2012). Evoliutsiia struktury metallicheskikh stekol pri vneshnikh vozdeistviiakh [Evolution of the structure of metallic glasses under external influences] *Doctor's thesis*. Chernogolovka [in Russian].

31 Kudrya, A.V. (2005). The role of different-scale structures in ensuring the plasticity and toughness of structurally inhomogeneous steels. *Metallurgy and heat treatment of metals*, 5, 18-23.

32 Obreimoff, J.W. (1930). The splitting reigth of mica. *Proc. Roy,* 127, 290-293.

33 Gilman, J. (1960). Direct Measurements of the surface energies of crystals. *J. Appl. Phys.*, 31, № 2, 2208-2216.

34 Yurov, V.M., Makhanov, K.M. (2020). Estimation of the melting temperature of nanostructures of solids. *Nano- and microsystem technology*, 22, 7, 347-351.

35 Yurov, V.M. (2011). Superfecial tension of pure metals. *Eurasian Physical Technical journal*, 8, № 1 (15), 10-14.

36 Mishchenko, E.F., Sadovnichii, V.A., Kolesov, A.Yu., & Rozov, N.Kh. (2010). *Avtovolnovye protsessy v nelineinykh sredakh s diffuziei [Autowave processes in nonlinear media with diffusion]*. Moscow: Fizmatlit [in Russian].

37 Yurov, V.M. (2005). Thermodynamics of luminescent systems // *Bulletin of the university of Karaganda-Physics*, 3 (39), 13-15.

38 Yurov, V.M., Guchenko, K.M., Makhanov, K.M. (2020). The thickness of the surface layer and autowave processes in high-entropy coatings. Matrix of scientific knowledge. 7, 9-16.

39 Yurov ,V.M., Eremin, E.N., & Guchenko, S.A. (2020). Application of high entropy coatings simultaneous in one cycle spraying three cathodes. *Bulletin of the university of Karaganda-Physics*, 1 (97), 7-17.

40 Gupta, S.C. (2018). The Classical Stefan Problem: Basic Concepts, Modelling and Analysis with Quasi-Analytical Solutions and Methods. New Edition: Elsevier.

DOI 10.31489/2021Ph3/115-121
UDC 544.14

T.M. Serikov*, A.E. Sadykova, P.A. Zhanbirbayeva, A.S. Baltabekov, A.S. Kayumova

Karagandy University of the name of academician E.A. Buketov, Kazakhstan
*(*E-mail: Serikov-timur@mail.ru)*

Photocatalytic water splitting of nanocomposite materials based on TiO_2 and rGO nanorods

The paper presents the results of a study of films formed by titanium dioxide nanorods and deposited on their surface of reduced graphene oxide by electrochemical deposition. Nanostructured films based on TiO_2 nanorods were prepared in a 100 ml stainless steel autoclave with a fluoroplastic insert from a solution containing 35 ml of deionized water (H_2O), 35 ml of hydrochloric acid (HCl) (36.5 %, Sigma–Aldrich) and 0.25 ml of titanium butylate $C_{16}H_{36}O_4Ti$ (97 %, Sigma–Aldrich). The addition of reduced graphene oxide to the structure of titanium dioxide nanorods increases the specific surface area of nanostructures from 29.3 m^2/g to 63.1 m^2/g. Calculations based on the film impedance spectra have shown that the optimal deposition time of reduced graphene oxide on the surface of TiO_2 nanorods is 3 minutes, since it has a low recombination coefficient and a long electron lifetime. Studies of the photocatalytic activity of nanomaterials and registration of the released hydrogen and oxygen gases have shown that when the films are irradiated for 5 hours, the amount of hydrogen released varies from 50 to 225 $mmol/cm^2$.

Keywords: nanorods, graphene oxide, specific surface area, photo-splitting of water.

Introduction

Hydrogen is practically not found on Earth in its pure form and must be extracted from other compounds using various chemical methods. According to the source [1], 75 million tons of hydrogen are consumed annually in the world. Moreover, three-quarters of it is carried out by steam conversion of methane and natural gas, and this consumes about 205 billion m^3 of gas. Almost everything else is obtained from coal and only 0.1 % (~100 thousand tons) is extracted by splitting water by electrolysis or in photoelectrochemical cells and solar thermochemical systems. Sunlight can be used to directly produce hydrogen from water using modern photoelectrochemical, thermochemical, and photobiological processes. Direct use of sunlight is the most efficient way to produce hydrogen, as it avoids energy losses. According to the European Commission, the main investors in the development of hydrogen energy were the United States (~\$500 million), Japan (~\$300 million) and the EU countries (~\$230 million). The leading countries also include South Korea (~\$100 million) and China (~\$60 million). In the future, the main regions for fuel cell sales are India, China, and Africa, where the development of the telecommunications market is largely constrained by an imperfect power supply system. In the countries of the former USSR, including Kazakhstan, investments in the development of hydrogen energy are very small. Therefore, conducting fundamental research that will generate new scientific information can contribute to the development of hydrogen production technologies in our country.

In the process of photodegradation of water, there is a need to create highly efficient photocatalysts that can absorb solar radiation and divide the water molecule into hydrogen gas and oxygen.

For effective photocatalytic splitting of water, photocatalysts are used, the band gap of which should cover the oxidation potentials of water, which are +0 and +1.23 V with respect to the normal hydrogen electrode (NHE) at pH= 0. Such photocatalysts include wide-band semiconductors such as ZrO_2, ZnO, TiO_2, WO_3 [2, 3], perovskite materials of the composition $CaTi_{0.98}Cu_{0.02}O_3$, Rh/Ta/F: $SrTiO_3$, Cr/Ta/F: $SrTiO_3$, etc. [4].

Among the listed photocatalysts, titanium dioxide (TiO_2) occupies a special place due to its physical, optical, electrical and photocatalytic properties. Using various synthetic approaches, it is possible to obtain zero-dimensional, one-dimensional and two-dimensional nanostructures of titanium dioxide [5–7]. Its one-dimensional formations, such as nanorods, have a number of advantages over zero-dimensional and two-dimensional ones. 3–dimensional electron transport is carried out in films made of TiO_2 nanoparticles. The features of agglomeration of dioxide nanoparticles during thermal annealing significantly affect the possibilities of electronic transitions between them. Non-intensive chemical binding leads to a decrease in the efficiency of electron transport. In view of this, when using TiO_2 nanorods in the process of photocatalytic decomposition of water it is possible to expect a preferential transport of electrons along their walls, which will reduce the transfer time from the charge carrier generation centers to the chemical reaction boundary, and also, when optimizing the design will allow to achieve a smaller number of surface defects. In addition, TiO_2 nanorods in controlled synthesis may have a higher specific surface area than spherical nanoparticles. However, a significant disadvantage of TiO_2 nanorods is its wide band gap (about 3.2 eV), which indicates the absorption band only in the ultraviolet region of the electromagnetic wave. Increasing the sensitivity of such films in the visible region can be achieved by using hybrid nanostructures, for example, in combination with graphene. To date, graphene (a monatomic layer of graphite) nanostructures are promising materials for use in photovoltaics, electronics, photocatalytic water splitting and in systems for cleaning from organic pollutants [8–11]. Grapheme is optically transparent, chemically functional, has a high mobility of charge carriers and the value of the specific surface area. The production of graphene nanostructures is well studied and it can be easily obtained by the well-known Hammer method [12]. In practice, graphene oxide is often synthesized. But for the transport of electrons through the material, it is necessary to restore the sp^2 aromatic structure of graphene oxide, which results in reduced graphene oxide. Often, recovery occurs by chemical, photochemical, and hydrothermal methods [13–15]. The use of graphene nanostructures in semiconductor films made of titanium dioxide nanorods will improve the separation of electron-hole pairs, increase the absorption capacity of semiconductor films in the visible region of the electromagnetic wave, and lead to an increase in the specific surface area of nanostructures as a whole. These factors are expected to significantly improve the photocatalytic activity of the films.

Experimental

Nanostructured films based on TiO_2 nanorods were prepared in a stainless steel autoclave with a fluoroplastic insert. A solution containing 15 ml of deionized water, 15 ml of HCl (36.5 %, No. 320331, Sigma–Aldrich) and 0.25 ml of titanium butylate $C_{16}H_{36}O_4Ti$ (97 %, No. 244112, Sigma–Aldrich) was poured into a 50 ml fluoroplast insert. TiO_2 nanorods were synthesized on FTO substrates (7 ohms/cm^2, No. 735167, Sigma–Aldrich), previously purified by ultrasound treatment in a mixture of deionized water, acetone and 2-propanol (volume ratio 1 : 1 : 1) for 30 min. The prepared FTO substrates were then placed in the autoclave with the conductive side down. The temperature treatment was carried out in a convective furnace (8,2/1100, SNOL). The furnace temperature and the synthesis duration are 200 ^{0}C in the range from 100 ^{0}C to 200 ^{0}C and from 6 to 24 hours, respectively. The resulting samples were washed with deionized water and dried at room temperature. The samples were then calcined at a temperature of 500 ^{0}C for 2 hours in air.

Further, to obtain the NR TiO_2/rGO composite material, commercial rGO powder (Reduced Graphen Oxide, Cheaptubes Inc.) was delaminated in 0.1 M pH 9.32. phosphate buffer solution (PBS, Na_2HPO_4, and NaH_2PO_4) and treated in an ultrasonic bath for 90 min to form a brown colloidal RGO dispersion with a concentration of 0.5 mg/ml. The deposition was carried out using a three-electrode system (HC TiO_2 as the working electrode, Pt foil as the counter electrode, and Ag/AgCl electrode as the reference electrode) at the ELINS electrochemical plant (R-20XV, Russia). The number of graphene oxide sheets deposited was controlled by a deposition time of 1 to 15 minutes. After precipitation the NR TiO_2/rGO composite material was washed with ethylene glycol and deionized water and then dried at room temperature.

Images of the sample surface were obtained using a scanning electron microscope (SEM) (MIRA 3 LMU, Tescan). The voltage at the accelerating electrode was 20 keV.

Spectrophotometric measurements were carried out on an automatic scanning spectrophotometer Solar CM 2203 (Solar) in the wavelength range of 250–800 nm with a spectral resolution of 0.5 nm.

The textural characteristics of synthesized samples were calculated on the basis of nitrogen adsorption and desorption isotherms at a temperature of 77K obtained at the quantachrome volumetric unit («Sorbi», USA). The specific surface area of the samples was estimated by the Brunauer-Emmett–Taylor method (BET).

A photoelectrochemical cell was used to record the released hydrogen. The cell window is quartz (Minihua Store). The opposite electrode is platinum. The solutions were separated using a Nafion filter. Nanostructures of titanium dioxide and graphene oxide were used as the working electrode. Both sides of the cell were pre-purged with a stream of argon gas. Then, when the sample was irradiated, samples were taken and identified on an Agilent gas chromatograph (Lomonosov Moscow State University).

Based on the obtained impedance spectra for the films the electrophysical parameters of the Z-500PRO impedance meter (Elins, Russia) were calculated when irradiated with a xenon lamp with a power of 100 MW/cm^2. The amplitude of the applied signal was up to 25 mV, and the frequency range was from 1 MHz to 100 MHz. Platinum coatings used as the opposite electrode were deposited from an ethanol solution of H2PtCl6 by electrochemical method on glass substrates with a conductive layer of FTO. The electrodes were glued together. A polymer film Meltonix (Solaronix, Switzerland) with a thickness of 25 microns served as a spacer between the working electrode and the removal electrode in the solar cell.

Results and discussions

Figure 1 shows the surface morphology of NR TiO_2 films. As can be seen from the figure, before the deposition of graphene oxide nanolayers, the film consists of titanium dioxide nanorods. The average length of the nanorods disoriented with respect to the substrate surface in this case was ~120 nm and the average diameter ~ 43 nm (Fig. 1a).

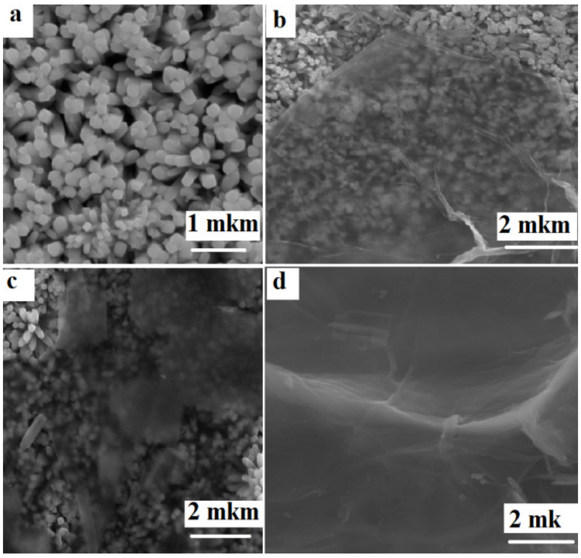

A-clean; b-1 min.; c-3 min.; d-5 min..

Figure 1. SEM images of the NR TiO_2/rGO nanocomposite

When the deposition time is about 1 minute, graphene oxide sheets are formed on the surface of the NR. Graphene oxide is dispersed over the entire surface of the TiO_2 NR, which can form a conducting network between them. With an increase in the duration of the deposition process to 3 and 5 minutes, the number of deposited sheets increases, and with a 5 minute deposition the surface is completely covered with graphene oxide flakes. This will allow the TiO_2 NR to inject its photogenerated electrons into the graphene oxide sheets under the action of light, ensuring their efficient transport to the FTO layer and further registration of the photocurrent.

The study of the specific surface area of nanocomposite materials was carried out by the method of low-temperature nitrogen adsorption. To do this the nanocomposite material is separated from the substrate. If necessary, the process was repeated until sufficient mass was obtained to change its specific surface area. The samples were thermotrained at a temperature of 95^0C for 180 minutes in the «SorbiPrep» pretreatment unit with a constant flow of adsorbate gas at a speed of 2 l/min. The measurement was carried out at a liquid nitrogen temperature of 77 K. Nitrogen was used as an adsorbate. Table 1 shows the dynamics of measuring the specific surface area of nanocomposite materials of the composition NR TiO_2/rGO as a function of the electrochemical deposition time.

Table 1

Specific surface area of nanocomposite materials of the composition NR TiO_2/rGO and NT TiO_2/rGO

№	Sample	Specific surface area S_{BET}, m^2/g	Full pore volume Vp, cm^3/g
1	rGO	600	0.416
2	NR TiO_2	29,3	0,165
3	NR TiO_2/ rGO_1 min	45,1	0,213
4	NR TiO_2/ rGO_3 min	52,8	0,231
5	NR TiO_2/ rGO_5 min	63,1	0,249

From the presented data it can be seen that the addition of TiO2/mgo to the HC structure significantly increases the specific surface area of the nanostructures. Thus, for HC films the specific area before the deposition of graphene oxide was 29.3 m^2/g, after which it increased to 63.1 m^2/g, as well as the volume of the adsorbed gas.

The nitrogen adsorption-desorption isotherms for all samples have the same appearance, except for the volume of adsorbed nitrogen. At low relative pressures (P/P_0 less than 0.1) an increase in nitrogen adsorption is observed on the isotherms, which indicates the presence of micropores. With an increase in the relative partial pressure for the samples, the volume of adsorbed nitrogen increases. In accordance with the IUPAC nomenclature, the obtained isotherms belong to the type IV isotherms with a hysteresis loop, reflecting the process of capillary condensation in mesopores.

The electric transport properties of nanocomposite materials were studied by the method of impedance spectroscopy. From the central arc of the impedance spectra, the effective recombination rate keff, the effective electron lifetime teff, the electron transport resistance in titanium dioxide films Rw, and the charge transfer resistance Rk associated with electron recombination were calculated according to the above method. Figure 2 shows the hodographs in Nyquist coordinates for the synthesized samples.

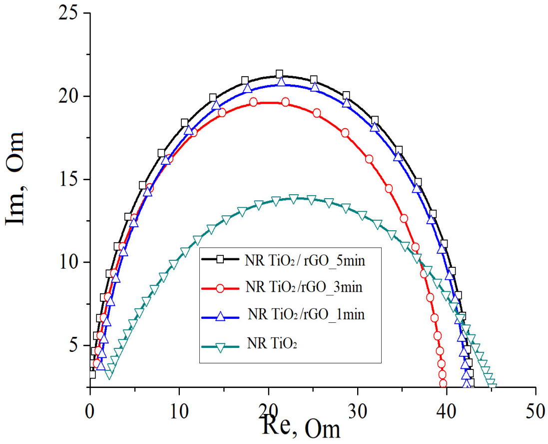

Figure 2. Impedance spectra of nanocomposite materials

The electron transport resistance in the nanocomposite R_w and the charge transfer resistance R_k will depend directly on the number of electrons received from the number of free electrons. If we take into account that the size and thickness of the semiconductor film are identical for all systems only the deposited layers of graphene oxide will affect the resistance value. The brief calculations are presented in Table 2.

Table 2

Electric transport properties of films based on nanocomposite materials

Sample	k_{eff}, c^{-1}	τ_{eff}, c	R_k. Om	R_w, Om
NR TiO_2	15	0,06	45	3
NR TiO_2/ rGO_1 min	12	0,08	42	2
NR TiO_2/ rGO_3 min	11	0,09	39	2
NR TiO_2/ rGO_5 min	14	0,07	41	2

The method allows us to calculate the main electric transport properties of nanocomposite films. However, a number of conclusions can be drawn from the results obtained. From the tabular data it can be seen that in the TiO_2 / mgo_3 min NR a low recombination coefficient and a long electron lifetime are observed. This indirectly indicates that in these cells the recovery of the electrolyte at the electrolyte/catalyst interface (graphene oxide) is more efficient than in the others.

The edge of the absorption spectrum of HC TiO_2 appears in the UV region of the spectrum around 380 nm. RGO also absorbs in the UV zone, the maximum of its absorption spectrum is at 230 nm. At the same time, the RGO film is almost transparent in the wavelength range from 400 to 800 nm. SiO_2-GO nanocomposites also actively absorb light in the UV region of the spectrum. Along with this, there is a broadening of the absorption band in the visible range of the spectrum.

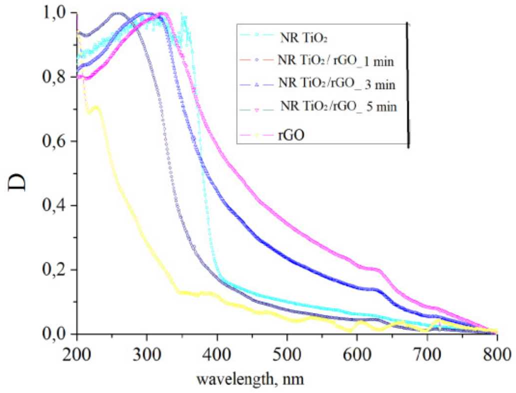

Figure 3. Absorption spectra of a nanocomposite of the composition NR TiO_2/rGO

Next, the photocatalytic activity of nanomaterials was investigated. The results of the experiments are shown in Figure 3.

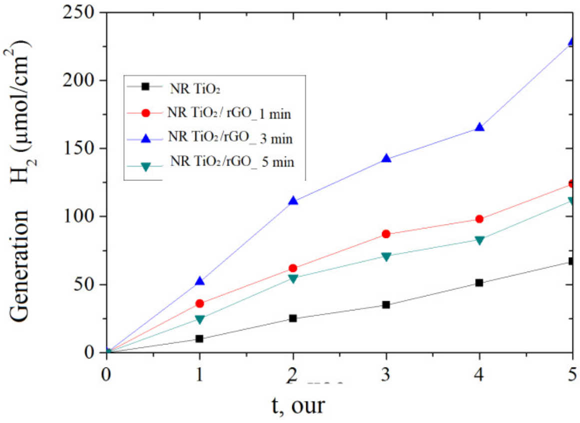

Figure 4. Photocatalytic cleavage of NR TiO_2/rGO water

From the presented data it can be seen that the addition of TiO_2 to the HC structures in various concentrations leads to an increase in their photocatalytic activity and water splitting. Moreover, it is necessary to determine the optimal concentration of graphene oxide. In this case, the best generation of hydrogen is observed by electrochemical deposition within 3 minutes, compared to other nanocomposite layers.

Conclusion

Electrochemically, sheets of reduced graphene oxide were deposited on the surface of the TiO_2 NR at a deposition time of 1, 3, and 5 minutes. The influence of the preparation conditions of nanostructured materials on their specific surface area, structure, electrophysical, optical and photocatalytic properties is investigated. The addition of TiO_2 rGO to the NR structure significantly increases the specific surface area of the nanostructures. Thus, for NR films the specific area before the deposition of graphene oxide was 29.3 m^2/g, after which it increased to 63.1 m^2/g, as well as the volume of the adsorbed gas. Low recombination coefficient and long electron lifetime are observed in films made of HC TiO_2 / rGO 3 min.

References

1 Serikov T.M. The effect of electric transport properties of titanium dioxide nanostructures on their photocatalytic activity / T.M. Serikov // Bulletin of the university of Karaganda. — Physics. — 2020. — № 3. — P. 13–21.

2 Kang Z Interface Engineering for Modulation of Charge Carrier Behavior in ZnO Photoelectrochemical Water Splitting / H. Kang, Z, Si, S. Zhang // Advanced functional materials. — 2019. — № 29. — P. 15.

3 Zhai K., Li K., Zhu X. Oxygen Exchange Materials Used in Two-Steps Thermochemical Water Splitting for Hydrogen Production / K. Zhai, K. Li, X. Zhu // Progress in chemistry. — 2015. — № 27, T 10. — P. 1481–1499.

4 Muhamad A. Titanate-based perovskites for photochemical and photoelectrochemical water splitting applications: A review / A. Muhamad, A. Khuzaimah, J. Lorna // International journal of hydrogen energy. — 2018. — № 43. — P. 23209–23220.

5 Fujishima A. Electrochemical photolysis of water at a semiconductor electrode / A. Fujishima, K. Honda // Nature. — 1972. — Vol. 238. — P. 37–38.

6 Pereira L. UV/TiO_2 Photocatalytic Degradation of Xanthene Dyes / L. Pereira, R. Pereira, K.S. Oliveira, L. Apostol // Photochemistry and Photobiology. — 2013. — Vol. 89. — P. 33–39.

7 Akinobu M. Water Splitting on Rutile TiO_2-Based Photocatalysts / M. Akinobu, N. Shunta // Chemistry A European Journal. — 2018. — № 24. — P. 204–219.

8 Kamat P.V. Graphene-based nanoassemblies for energy conversion / P.V. Kamat // The Journal of Physical Chemistry Letters. — 2010. — № 2. — P. 242 — 251.

9 Wang D.H. Self-assembled TiO_2-graphene hybrid nanostructures for enhanced Li-Ion insertion / D.H. Wang, D.W. Choi, J. Li, Z.G. Yang, Z.M. Nie, R. Kou, et al. // ACS Nano. — 2009. — № 3. — P. 907–914.

10 Wang X. Transparent, Conductive graphene electrodes for dye-sensitized solar cells / X. Wang, L. Zhi, K. Muellen // Nano Letters. — 2008. — № 8. — P. 323–327.

11 Serp P. *Carbon Materials for Catalysis* / P. Serp, J.L. Figueiredo, etc. — Hoboken, N.J.: John Wiley & Sons, 2009.

12 Hummers Jr W.S. Preparation of graphitic oxide / Jr W.S. Hummers, R.E. Offeman // Journal of the American Chemical Society. — 1958. — № 80. — P. 1339.

13 Li D. Processable aqueous dispersions of graphene nanosheets / D. Li, M.B. Muller, S. Gilje, R.B. Kaner, G.G. Wallace // Nature Nanotechnology. — 2008. — № 3. — P. 101–105.

14 Williams G. TiO2-graphene nanocomposites. UV-assisted photocatalytic reduction of graphene oxide / G.Williams, B. Seger, P.V. Kamat // ACS Nano. — 2008. — № 2. — P. 1487–1491.

15 Zhou Y. Hydrothermal dehydration for the «green» reduction of exfoliated graphene oxide to graphene and demonstration of tunable optical limiting properties / Y. Zhou, Q.L. Bao, L.A.L. Tang, Y.L. Zhong, K.P. Loh // Chemistry of Materials. — 2009. — № 21. — P. 2950–2956.

Т.М. Сериков, А.Е. Садыкова, П.А. Жанбирбаева, А.С. Балтабеков, А.С. Каюмова

TiO_2 және rGO негізіндегі нанокомпозитті материалдарда фотокатализ арқылы суды ыдырату

Мақалада титан диоксиді наноөзекшелері және оның бетіне электрохимиялық әдісімен тұндырылған графен оксидінен қалыптасқан қабыршақтарды зерттеу нәтижелері келтірілген. TiO_2 наноөзекшелері негізінде жасалған наноқұрылымды қабыршақтар көлемі 100 мл тот баспайтын болаттан және фторопласттан жасалған автоклав ішінде синтезделеді. Автоклавтың ішіне 35 мл ионсыздандырылған су (H_2O), 35 мл тұз қышқылы (HCl) (36,5 %, Sigma-Aldrich) және 0,25 мл титан бутилатының $C_{16}H_{36}O_4Ti$ (97 %, Sigma–Aldrich) қосындысы бар сұйықтық дайындалады. Титан диоксиді наноөзекшелерінің құрамына графен оксидін қосу, наноқұрылымдардың меншікті бетінің аумағын 29,3 $м^2$/ г-нан 63,1 $м^2$ / г-ға дейін арттырады. Қабыршақтардың импеданс спектрлерін қолдана отырып, жүргізілген есептеулер TiO_2 наноөзекшелерінің бетіне графен оксидінің оңтайлы тұндыру уақыты 3 минутты құрайтындығын көрсетті, себебі оның рекомбинация коэффициенті өзге үлгілерге қарағанда төмен және электрондардың өмір сүру уақыты жоғары. Наноматериалдардың фотокаталитикалық белсенділігі мен сутегі және оттегінің бөлінген газдарын тіркелу барысында, қабыршақтарды 5 сағат сәулелендіру кезінде бөлінетін сутектің мөлшері 50-ден 225 ммоль / $см^2$-ге дейін өзгеретінін көрсетті.

Кілт сөздер: наностержень, графен оксиді, беттік аудан, судың фотоыдырауы.

Т.М. Сериков, А.Е. Садыкова, П.А. Жанбирбаева, А.С. Балтабеков, А.С. Каюмова

Фотокаталитическое расщепление воды нанокомпозитных материалов на основе наностержней TiO_2 и rGO

Представлены результаты исследования пленок, образованных наностержнями диоксида титана и осажденных на их поверхность восстановленного оксида графена, методом электрохимического осаждения. Наноструктурированные пленки на основе наностержней TiO_2 получали в автоклаве из нержавеющей стали с фторопластовой вставкой объемом 100 мл из раствора, содержащего 35 мл деионизованной воды (H_2O), 35 мл соляной кислоты (HCl) (36,5 %, Sigma–Aldrich) и 0,25 мл бутилата титана $C_{16}H_{36}O_4Ti$ (97 %, Sigma–Aldrich). Добавление в структуру наностержней диоксида титана восстановленного оксида графена увеличивает удельную площадь поверхности наноструктур от 29,3 $м^2$/г до 63,1 $м^2$/г. Проведенные расчеты по спектрам импеданса пленок показали, что оптимальное время осаждения восстановленного оксида графена на поверхность наностержней TiO_2 составляет 3 мин, так как для него наблюдается низкий коэффициент рекомбинации и длительное время жизни электронов. Исследования фотокаталитической активности наноматериалов и регистрация выделяемых газов водорода и кислорода показали, что при облучении пленок в течение 5 ч количество выделяемого водорода варьируется от 50 до 225 ммоль/см^2.

Ключевые слова: наностержень, оксид графена, удельная поверхность, фоторасщепление воды, облучение.

References

1 Serikov, T.M. (2020). The effect of electric transport properties of titanium dioxide nanostructures on their photocatalytic activity. *Bulletin of the university of Karaganda. Physics, 3,* 13–21.

2 Kang, Z, Si H., & Zhang, S. (2019). Interface Engineering for Modulation of Charge Carrier Behavior in ZnO Photoelectrochemical Water Splitting. *Advanced functional materials, 29,* P.15.

3 Zhai, K., Li, K., & Zhu, X. (2015). Oxygen Exchange Materials Used in Two-Steps Thermochemical Water Splitting for Hydrogen Production. *Progress in chemistry, 27(10),* 1481–1499.

4 Muhamad, A., Khuzaimah, A., & Lorna, J. (2018). Titanate-based perovskites for photochemical and photoelectrochemical water splitting applications: A review. *International journal of hydrogen energy, 43,* 23209–23220.

5 Fujishima, A., & Honda, K. (1972). Electrochemical photolysis of water at a semiconductor electrode. *Nature, 238,* 37–38.

6 Pereira, L., Pereira, R., Oliveira, K.S., & Apostol, L. (2013). UV/TiO_2 Photocatalytic Degradation of Xanthene Dyes. *Photochemistry and Photobiology, 89,* 33–39.

7 Akinobu, M., & Shunta, N. (2018). Water Splitting on Rutile TiO2-Based Photocatalysts. *Chemistry A European Journal, 24,* 204–219.

8 Kamat, P.V. (2010). Graphene-based nanoassemblies for energy conversion. *The Journal of Physical Chemistry Letters*, 2, 242–251.

9 Wang, D.H., Choi, D.W., Li, J., Yang, Z.G., Nie, Z.M., Kou, R., et al. (2009). Self-assembled TiO_2-graphene hybrid nanostructures for enhanced Li-Ion insertion. *ACS Nano*, 3, 907–914.

10 Wang, X., Zhi, L., & Muellen, K. (2008). Transparent, Conductive graphene electrodes for dye-sensitized solar cells. *Nano Letters*, 8, 323–327.

11 Serp, P., & Figueiredo, J.L. (2009). *Carbon Materials for Catalysis*. Hoboken, N.J.: John Wiley & Sons.

12 Hummers, Jr W.S., & Offeman, R.E. (1958). Preparation of graphitic oxide. Journal of the American Chemical Society, 80, 1339.

13 Li, D., Muller, M.B., Gilje, S., Kaner, R.B., & Wallace, G.G. (2008). Processable aqueous dispersions of graphene nanosheets. *Nature Nanotechnology, 3,* 101–105.

14 Williams, G., Seger, B., & Kamat, P.V. (2008). TiO_2-graphene nanocomposites. UV-assisted photocatalytic reduction of graphene oxide. ACS Nano, 2. 1487 — 1491.

15 Zhou, Y., Bao, Q.L., Tang, L.A.L., Zhong, Y.L., & Loh, K.P. (2009). Hydrothermal dehydration for the «green» reduction of exfoliated graphene oxide to graphene and demonstration of tunable optical limiting properties. Chemistry of Materials, 21, 2950–2956.

АВТОРЛАР ТУРАЛЫ МӘЛІМЕТТЕР
СВЕДЕНИЯ ОБ АВТОРАХ
INFORMATION ABOUT AUTHORS

Aimukhanov, A.К. — Candidate of Physical and Mathematical Sciences, associate professor, Professor of the Department of Radiophysics and Electronics, Leading Researcher, Buketov University, Scientific Center for Nanotechnology and Functional Nanomaterials, Karaganda, Kazakhstan; e-mail: a_k_aitbek@mail.ru

Akhazhanov, S.B. — PhD, Associate Professor at the Buketov Karaganda University, Kazakhstan; e-mail: stjg@mail.ru

Akildinova, A.K. — Master of science, 3rdyear PhD student of KazNU named after al-Farabi, research officer, Institute of Applied Science and Information Technologies, Almaty, Kazakhstan;

Aymkhanov, Ermek Eerulanuly — Engineer of the Ceramic plant, Ust-Kamenogorsk; Ust-Kamenogorsk, Kazakhstan.

Baizhan, Daryn Rashiduly — Engineer, Research Center « Surface Engineering and Tribology»; Sarsen Amanzholov East Kazakhstan University; Ust-Kamenogorsk, Kazakhstan; e-mail: daryn.baizhan@mail.ru

Bakhtybekova, A.R. — 1st year PhD student, E.A. Buketov Karaganda University, Karaganda, Kazakhstan; e-mail: abskargu@mail.ru

Baltabekov, A.S. — candidate of physical and mathematical sciences, Buketov Karaganda University, Karaganda, Kazakhstan.

Bazarbayev, D. — PhD, Associate Professor at the L.N. Gumilyov Eurasian National University, Nur-Sultan, Kazakhstan; e-mail: phd84@mail.ru

Belgibekov, N. A. — Master, Director of the Department of Military-Technical Projects at Research & Development Center Kazakhstan Engineering LLP, Captain 2nd Rank, Nur Sultan, Kazakhstan, e-mail: exciton@list.ru

Berdibekov, A.T. — Doctor of Philosophy (PhD), Deputy Head of the Faculty of the Ministry of Defense of the National University of Defense named after the First President of the Republic of Kazakhstan — Elbasy, Colonel, Nur Sultan, Kazakhstan, e-mail: exciton@list.ru

Bespalko, A.A. — Doctor of Technical Sciences, Leading Researcher, Problem Research Laboratory of Electronics, Dielectrics and Semiconductors, Research School of High Energy Process Physics, Tomsk Polytechnic University, Russia; besko48@tpu.ru

Bolegenova, S.A. — Doctor of physical and mathematical sciences, Professor, head of the Department of Thermophysics and Technical Physics, Al Farabi Kazakh National University, Almaty, Kazakhstan

Dann Denis D. — Ph.D., Researcher, Problem Research Laboratory of Electronics, Dielectrics and Semiconductors, Research School of High Energy Process Physics, Tomsk Polytechnic University, Russia; dddann@tpu.ru

Dosbolayev, M.K. — candidate of physico-mathematical Sciences, docent, senior research officer, KazNU named after al—Farabi, Almaty, Kazakhstan.

Gabdullin, M.T. — candidate of physico-mathematical Sciences, PhD, professor, leading researcherof KazNU named after al —Farabi, Almaty, Kazakhstan.

Ihor, Bohdanov — Doctor of Sciences (Education), Professor, Rector of Berdyansk State Pedagogical University, Doctor of Sciences (Technical), associate professor, rector@bdpu.org.ua

Jaichibekov, Nurbulat Zhumabekovich — Doctor of Physical and Mathematical Sciences; Professor of the Department of Mechanics; L.N. Gumilyov Eurasian National University, Nur-Sultan, Kazakhstan; jaich@mail.ru

Kasymov, Askar Bagdatovich — PhD; Acting Associate Professor, Department of Technical Physics and Thermal Power Engineering; NAO «Shakarim University of Semey»; Semey, Kazakhstan; festland2@yandex.kz

Kayumova, A.S. — Master of science, senior lecturer, Buketov Karaganda University, Kazakhstan; aneka.08@mail.ru

Kengesbekov, Aidar Bakytbekuly — PhD student; Junior researcherof [1]Research Center «Surface Engineering and Tribology», [2]Institute of Composite Materials; [1]Sarsen Amanzholov East Kazakhstan University, [3]Institute of Composite Materials LLP; Ust-Kamenogorsk, Kazakhstan; aidar.94.01@mail.ru

Kireev, Victor Nikolaevich — Candidate of Physical and Mathematical Sciences; Associate Professor of the Department of Applied Physics; Physical-Technical Institute of the Bashkir State University, Ufa, Russia; kireev@anrb.ru

Kylyshkanov, Manarbek Kalymovich — Doctor of Ph. D., Professor; [1]Head of the Research Center, [2]professor of the Department of Physics; [1]Ulba Metallurgical Plant, Sarsen Amanzholov East Kazakhstan University, Ust-Kamenogorsk; Kazakhstan; kylyshkanov@mail.ru

Makhanov, K.M. (contact person) — Candidate of Physical and Mathematical Sciences, Professor of the Department of Radiophysics and Electronics, Ye. A. Buketov Karaganda University, Karaganda, Kazakhstan, e-mail: makanov@inbox.ru

Minkov, L.L. — Doctor of physical and mathematical sciences, Professor, National Research Tomsk State University, Tomsk, Russia

Mutalip, A.A. — 1st year undergraduate studentof KazNU named after al —Farabi, research assistant, Institute of Applied Science and Information Technologies, Almaty, Kazakhstan, e-mail: mutalip.abdurashid@gmail.com;

Nataliia, Kosach — Doctor of Sciences (Technical), Professor, Head of Department the Quality Management State Enterprise KHARKIV MACHINERY PLANT «FED», Kharkiv, Ukraine, kosach.nata@gmail.com

Pavlov, Alexander Viktorovich — Senior Lecturer of the Department « Department of Physics»; Sarsen Amanzholov East Kazakhstan University; Ust-Kamenogorsk, Kazakhstan, alexandr_pavlov_1988@mail.ru

Petrov, Maxim V. — Junior Researcher, Problem Research Laboratory of Electronics, Dielectrics and Semiconductors, Research School of High Energy Process Physics, Tomsk Polytechnic University, Russia; mvp17@tpu.ru

Pomishin E.K., Graduate student, Problem Research Laboratory of Electronics, Dielectrics and Semiconductors, Research School of High Energy Process Physics, Tomsk Polytechnic University, Russia; pomek@tpu.ru

Rakhadilov, Bauyrzhan Korabaevich — PhD, associate professor; Senior Researcher of Research Center «Surface Engineering and Tribology»; Sarsen Amanzholov East Kazakhstan University, Ust-Kamenogorsk; Kazakhstan; rakhadilovb@mail.ru

Ramazanov, T.S. — academic, chief researcher, professor, doctor of Physico-mathematical Sciences, Vice-rector for scientific and innovative activities of KazNU named after al — Farabi, Almaty, Kazakhstan;

Rozhkova, X.S. (contact person) — 2nd year PhD student, Junior Researcher, Buketov University, Scientific Center for Nanotechnology and Functional Nanomaterials, Karaganda, Kazakhstan; e-mail: ksusharogovaya@mail.ru

Sadykova, A.E. — master of Science, тeacher, Buketov Karaganda University, Karaganda, Kazakhstan; ainura_1457@mail.ru

Sagdoldina, Zhuldyz Bolatkyzy — PhD, associate professor; Leading Researcherof Research Center «Surface Engineering and Tribology»; Sarsen Amanzholov East Kazakhstan University, Ust-Kamenogorsk, Kazakhstan; sagdoldina@mail.ru

Seisembekova, T.E. — 1st year PhD student, Buketov University, Scientific Center for Nanotechnology and Functional Nanomaterials, Karaganda, Kazakhstan; tosh_0809@mail.ru

Serikov, T.M. (contact person) — PhD, Buketov Karaganda University, Karaganda, Kazakhstan, Serikov-timur@mail.ru

Shalabayeva, Bakyt Salamatovna — Candidate of Physical and Mathematical Sciences; Associate Professor of the Department of Mathematical and Computer Modeling; L.N. Gumilyov Eurasian National University, Nur-Sultan, Kazakhstan; shalabaeva.b.s@mail.ru

Shestakov, Konstantin Alexandrovich — Head of the Laboratory for Innovative Research and Development; Ulba Metallurgical Plant, Ust-Kamenogorsk, Kazakhstan; shestakovka@ulba.kz

Shevelev Sergei Anatolienvich — Senior Lecturer, School of Energy Engineering, Tomsk Polytechnic University, Tomsk, Russia; wevelev@tpu.ru

Sheveleva, Elena Alexandrovna — PhD, Associate Professor, School of Non-Destructive Testing, Tomsk Polytechnic University, Tomsk, Russia; vasendina@tpu.ru

Shuyushbaeva, N.N. — PhD, Associate Professor, Sh.Ualikhanov Kokshetau University, Kokshetau, Kazakhstan; nn_shuish@mail.ru

Starý, O. — PhD, Professor Assistant, Czech Technical University in Prague, Prague, Czech Republic, oldStar@centrum.cz

Tanasheva, N.K. (contact person) — PhD, Associate Professor, E.A. Buketov Karaganda University, Karaganda, Kazakhstan, e-mail: nazgulya_tans@mail.ru

Tleubergenova, A.Zh. — lecturer, E.A. Buketov Karaganda University, Karaganda, Kazakhstan

Toktarbaev, B.A. — 2nd year master student, Sh.Ualikhanov Kokshetau University, Kokshetau, Kazakhstan; shymkent.a7@mail.ru

Tulebekova, A.S. — PhD, Senior researcher at the CSI Research & Lab (LLP), Associate Professor at the L.N. Gumilyov Eurasian National University, Nur-Sultan, Kazakhstan; e-mail: krasavka5@mail.ru

Ussenov, Y.A. — PhD, postdoctoral student of KazNU named after al —Farabi, research officer, Institute of Applied Science and Information Technologies, Almaty, Kazakhstan; **Utepov, Ye.B.** — PhD, Head of R&D at the CSI Research & Lab (LLP), Associate Professor at the L.N. Gumilyov Eurasian National University, Nur-Sultan, Kazakhstan; e-mail: utepov-elbek@mail.ru

Volodymyr, Bolshakov — Doctor of Sciences (Technical), Senior researcher, Vice-President, Public organization «Ukrainian Academy of Metrology», Kharkiv, Ukraine, v_bolshakov@ukr.net

Yana, Suchikova — Doctor of Sciences (Technical), associate professor, Head of the Department of Physics and Methods of Teaching Physics, Berdyansk State Pedagogical University, Berdyansk, Ukraine, yanasuchikova@gmail.com

Yurov, V.M. (contact person) — Candidate of phys. -math. sciences, Professor, Director of the Scientific Research Center, Ye. A. Buketov Karaganda University, Karaganda, Kazakhstan, e-mail: exciton@list.ru

Zeinidenov, A.К. — PhD, associate professor, Dean of the Physical-Technical Faculty, Leading Researcher, Buketov University, Scientific Center for Nanotechnology and Functional Nanomaterials, Karaganda, Kazakhstan; asyl-zeinidenov@mail.ru

Zhanbirbayeva, P.A. — engineer, Buketov Karaganda University, Karaganda, Kazakhstan

Zhaparova, Mira Serikanovna — Senior Lecturer of the Department « Department of Physics»; Sarsen Amanzholov East Kazakhstan University; Ust-Kamenogorsk, Kazakhstan

Zharassov, Sh.Zh. — PhD Student at the L.N. Gumilyov Eurasian National University, Nur-Sultan, Kazakhstan; e-mail: zhshzh@mail.ru